STUDIES OF ZnSe AND INDIUM TIN OXIDE BASED THIN FILM SCHOTTKY BARRIERS AND HETEROJUNCTIONS FOR THEIR ELECTRICAL AND OPTICAL PROPERTIES

Thesis
Submitted to the
Gauhati University
for
The Degree of Doctor of Philosophy
in
the Faculty of Science in Physics

By

Sumbit Chaliha

2008

Dr. Atowar Rahman,
Professor,
Department of Physics
Gauhati University
Guwahati-781014 (India)

Phone: 0361-2570531 (Off)
0361-2571914 (Res)
Fax: 0361-2570133
Email: atowar6@rediffmail.com

Date ……

CERTIFICATE

Certified that Mr. Sumbit Chaliha, Lecturer, Department of Physics, Bahona College, Jorhat (India) has carried out research work under my personal supervision and guidance in the Department of Physics, Gauhati University. The results of research work have been presented by Mr Sumbit Chaliha in this thesis with the title "Studies of ZnSe and Indium Tin Oxide based thin film Schottky barriers and heterojunctions for their electrical and optical properties". The same has been submitted by him to the Gauhati University, Guwahait, for the degree of Doctor of Philosophy.

Mr. Chaliha has fulfilled all the requirements under the Ph. D. regulations of the Gauhati University. To the best of my knowledge, this thesis as a whole or any part thereof has not been submitted to any other University or institution for any other degree or diploma.

(A. Rahman)
Professor,
Department of Physics
Gauhati University,
Supervisor.

DECLARATION

I hereby declare that this thesis entitled "Studies of ZnSe and Indium Tin Oxide based thin film Schottky barriers and heterojunctions for their electrical and optical properties" is the result of my own investigations, which have been carried out by me under the supervision of my research guide Dr. A. Rahman, Professor, Department of Physics, Gauhati University. The results quoted from other workers have properly been referred to. I further declare that this thesis as a whole or any part thereof has not been submitted by me for the award of any research degree, to this university or any other University or Institution.

Date: 25/06/08 **(Sumbit Chaliha)**

Dedicated

to

my Parents

ACKNOWLEDGEMENT

It is my privilege to express my deep sense of gratitude to my research supervisor, Dr. A. Rahman, Professor, Department of Physics, Gauhati University, for his constant persuasion, affectionate guidance and efficient supervision at each and every stage of this research work.

I wish to express my gratefulness to University Grant Commission, North Eastern Regional Office, for granting me teachers' fellowship to carry out this research work. I express my gratefulness to Gauhati University, for providing me the necessary facilities in the University for my research work.

I express my sincere thanks to all the faculty members of the Department of Physics, Gauhati Universty especially to Prof H. L. Das, Prof. S. A. S. Ahmed, Prof. H. L. Duorah, Prof D. K. Chaudhury, Prof. M. Devi, Prof. K. Barua, Prof. B. K. Sarma, Dr. K. Duorah, Dr. M. P. Bora, Dr. A. G. Barua and Dr. Nimai Singh for their valuable suggestions at different stages of my research work.

I would like to express my special thanks to Dr. P. C. Sarmah, Scientist, North East Institute of Technology, Jorhat, whose invaluable guidance has been of great help to me in this research work. I express my heartiest thanks to all my research colleagues Dr. Ganesh Wary, Mothura Nath Borah and Tapan Kachary for being very supportive and co-operative all throughout my research work.

I offer my special thanks to the authority of Indian Institute of Technology (IIT), Guwahati, for providing me XRD and SEM facilities.

At this time I should remember my friends and colleagues Mr. Kangkan Sarmah, Dr. Pratyush Purkayastha, Dr. Ranjan Sarma, Ms. Ranjita Devi, Dr. Ranjan Bordoloi, Rofique Ahmed, Dr. Prasanna Kr. Dutta and many others for their encouragement, suggestions and valuable help. I am grateful to all my younger friends Nitya, Simanta, Naba, Hori, Monoj of V. V. Rao Research Scholars' Hostel (RCC5), Gauhati University, for their support and continued help that they provided during my

stay there. I express my thanks to all staff of Physics Department, Gauhati University, for their various services.

My sincere thanks are due to Dr. C. R. Dutta, Principal, Mr. P. K. Barooah Head, Department of Physics, and all my colleagues of Bahona College, Jorhat (India) for their constant motivation, support and cooperation during the period of my research work.

At last but not the least, I am forever indebted to my parents and family members Dada, Dhuni bow, Maina (dada), Kum (bow), Mom (Dipalima), Rubu, Momy and Monon for their continuous support, understanding, endless patience, encouragement and all other possible help throughout the work. Without their help and understanding this work could not have been completed.

Sumbit Chaliha
Department of Physics,
Bahona College,
Jorhat (India)

Dated Jorhat, the 25th June, 2008

SYNOPSIS

The studies of semiconductor thin films and their junctions such as metal-semiconductor junctions (Schottky Barriers) and heterojunctions have received much attention due to their applications in various electronic and optoelectronic devices including solar cells. In the present work, studies were carried out on electrical and optical properties of (n)ZnSe and ITO based thin film Schottky barriers and heterojunctions with an aim for their possible use in optoelectronic devices. Among the compound semiconductors of group II-VI, Zinc Selenide (ZnSe) is one of the most interesting semiconductors due to its wide band gap. One of the transparent oxide semiconductors, Indium Tin Oxide is most demanding because of its wide band gap, high transparency and high electrical conductivity. Considering their availability and easy of preparation, it was proposed in the present case to study these materials in the forms of thin films and their junctions. The results of the studies have been presented in the thesis written in nine chapters.

Chapter 1: General Introduction

This chapter contains introduction to thin films and thin film devices along with a brief discussion on their importance in various fields. A general introduction to the two types of semiconductor junctions, metal-semiconductor (Schottky barrier) junctions and heterojunctions in thin film form has also been given. A comprehensive discussion on the importance of Zinc Selenide (ZnSe) and Indium Tin Oxide (ITO) for the fabrication of different optoelectronic devices has been made. A brief review of research activities on ZnSe along with various techniques used for preparation of ZnSe films by different workers has been given. Also, a brief review of research works on Schottky barriers and heterojunctions with ZnSe has been given. The properties of Indium Tin Oxide (ITO) films have been briefly discussed and research works on ITO films have been reviewed in this chapter. At the end, comparative analysis on the properties of ITO films prepared by different methods has been given.

Chapter 2: Preparation methods and growth processes of thin films

This chapter deals with the different methods of preparation of thin films and the processes involved in the formation of thin films. Brief outlines of different methods like, physical vapour deposition (PVD), sputtering, chemical vapor deposition (CVD) and chemical deposition have been given. The mechanism of

thermal evaporation method has been discussed in some detail, as this method was used for preparing different samples for studying in the present case. The different processes viz. condensation, nucleation and growth in the formation of thin films have also been discussed in this chapter. The different factors which affect the growth, structure and film properties have also been mentioned at the end of this chapter.

Chapter 3: Theoretical background

In this chapter, theoretical background related to the present work has been briefly given. Theories used for the studies of structural properties, electrical and optical properties of semiconducting films and junctions are described. The different relations used to calculate the structural parameters like lattice constants, grain size, stress, strain, dislocation density have been given. The relations to measure different optical constants like absorption coefficient, optical band gap, refractive index, extinction coefficient, dielectric constants of the semiconducting films have also been discussed in the chapter. The photoconduction of a semiconductor has been discussed. The basic theories of different current transport mechanisms of metal-semiconductor Schottky barriers and semiconductor heterojunctions have been discussed in detail. The working principle of photovoltaic solar cell has been explained. The simplified relations used to calculate the different photovoltaic parameters have also been given in this chapter.

Chapter 4: Experimental Techniques

In this chapter details of sample preparation, vacuum evaporation techniques, structural characterization of samples, experimental techniques to study different electrical and optical properties have been discussed. In the present work thin films of ZnSe and ITO and different metal electrodes were deposited by vacuum evaporation method. Details of the vacuum coating unit used in the present study have been described in this chapter. The different steps of preparation processes of semiconductor films and Au-(n)ZnSe and Ni-(n)ZnSe Schootky barrier junctions and (n)ITO-(p)Si, (n)ZnSe-(p)CdTe and (n)ZnSe-(p)Si heterojunctions have been described here. The experimental set-up for measurement of film thickness by multiple interferometry method has been described. To measure the different optical constants of the films the transmittance and absorption spectra were recorded with the help of the UV-Visible spectrophotometer *CARY 300* (Varian, Australia). The detail of the spectrophotometer fitted with an integrating sphere was described in this chapter. XRD (X-ray diffractogram), SEM(Scanning electron micrograph) and EDAX

(Energy dispersive X-ray analysis) were used for structural, morphological and compositional studies. A brief discussion on these topics has also been incorporated in this chapter. The experimental arrangements and equipments used for various measurements such as current-voltage study of films and different junctions in dark and under illumination, variation of conductivity with temperature, photovoltaic characteristics, capacitance-voltage study etc. have been described in detail in this chapter.

Chapter 5: Studies of ZnSe films

The electrical and optical properties of ZnSe films are very sensitive to the structural properties of the films. Again the structural properties depend on the methods of preparation and deposition conditions. An attempt has been made to obtain the optimum growth condition of ZnSe films, so as to prepare Schottky barriers and heterojunctions with these films. In this chapter, the results of the structural, electrical and optical properties of ZnSe films prepared at different substrate temperatures are presented in detail.

The structural, morphological and compositional properties of thermally deposited ZnSe films have been discussed in the first section of this chapter. From X-ray diffractograms, it was found that, the films deposited at elevated temperatures were polycrystalline in nature. The crystallinity was improved on increase of substrate temperature during deposition and on annealing. From the XRD data, lattice constants, grain size, stress, strain and dislocation density of the films were calculated. It was observed from the calculation that the crystallite size increases but the internal strain of ZnSe films on glass substrates decreased with increase of substrate temperature during deposition and on annealing thereafter. The stress and dislocation density were found to decrease on deposition at higher substrate temperature and then on annealing. Since the dislocation density and strain are the manifestation of dislocation network in the films, the decrease in the dislocation density and strain indicates the formation of higher quality films at higher substrate temperatures and on annealing. From the structural study it was concluded that the elevated substrate temperatures 453K to 573K and annealing of the films at 473K for 1 hour after deposition, are the suitable optimum growth conditions for preparation of good quality polycrystalline ZnSe thin films. The films prepared at this range of temperature were found nearly stoichiometric and uniform without any macroscopic defects. These growth conditions and parameters were set as optimum growth conditions for preparing

ZnSe thin films and for preparation of Schottky barriers and heterojunctions with ZnSe to study their electrical and optical properties in the present case.

Before making junctions of thermally deposited ZnSe films, the electrical properties like ohmic contact, electrical conductivity etc. of the prepared films along with their photoconductivity were studied. Al was found to make good ohmic contact to intrinsic ZnSe films and to n-type ZnSe films. The electrical conductivity of the thermally deposited ZnSe films was found to depend on the substrate temperature during deposition. It was found to increase on increase of substrate temperature and post deposition annealing. The undoped ZnSe films possess high resistivity (of the order of 10^6 Ohm-cm). To improve the conductivity, this semiconductor was doped with Al by co-evaporation method. The conductivity of the doped films was found to increase upto 11×10^{-6} $Ohm^{-1}cm^{-1}$ with maximum attainable doping concentration 9.7×10^{14} cm^{-3}. The Al doped ZnSe films were found to be n-type. From the slopes of the ln σ vs 1000/T plots, the band gap of the films were calculated and found to be in the range of 2.58 eV to 2.63 eV. From the low temperature range of ln σ vs 1000/T plot, the activation energies of the films were calculated. The activation energy of undoped film was found to be 0.63 eV and that of the doped films with doping concentrations 1.4×10^{14} cm^{-3}, 4.8×10^{14} cm^{-3} and 9.7×10^{14} cm^{-3} were found to be 0.57 eV, 0.55 eV and 0.55 eV respectively. Al doped ZnSe films were found photosensitive and the photocurrent was found to be a function of intensity of illumination. The photoconductive rise and decay processes of ZnSe films were studied. The trap depth was found to be about 0.72 eV which was found to be less dependent on the intensity of illumination.

The optical constants of the films are required for correct design of optoelectronic devices and to determine the losses in detectors and optical coatings. From the results of optical study in the present case, it is found that the ZnSe films thermally deposited on glass substrate were highly transparent. In the investigated spectral range, the values of refractive index (n) were found to be in the range between 2.3 to 3.2, which is nearly similar to the value of bulk ZnSe. The ZnSe films exhibit normal dispersion in the studied spectral range (300nm to 900nm). The straight line fitting of the square of absorption coefficient versus photon energy ($h\nu$) plots indicate that the transition was direct and from these plots the optical band gap of the ZnSe films were found to be about 2.62 eV. As the transition is direct, these films are suitable for optoelectronic

devices. Also higher band gap of the films makes it possible to use it as a window layer for solar cells and optoelectronic devices working in the blue region. The values of the imaginary part of refractive index or the extinction coefficient (*k)* for all the films were found to be very small (10^{-2}). It was observed, the extinction coefficient (*k*) and so the imaginary part of dielectric constant ($\varepsilon''=2nk$) to decrease slowly up to the wave length 500nm and then remain nearly constant. This means that the static conductivity of ZnSe is low towards the IR region than in the blue region.

Chapter 6: Studies of Indium Tin Oxide (ITO) films

The results of studies of the structural, electrical and optical properties of thermally deposited ITO films have been presented in this chapter.

From X-ray diffractograms, it was found that, the films deposited at about 573K and above were polycrystalline in nature. From the XRD data, lattice constants and grain size of the films were calculated. Both the parameters were found to increase with increase of substrate temperature during deposition and on annealing thereafter.

The electrical conductivity of ITO films thermally deposited in the present case was found to be dependent on the deposition condition. Substrate temperature 593K during deposition and annealing 1 hour at the same temperature was found to be suitable for attaining higher conducting ITO films. The maximum conductivity attained in our thermally deposited film after annealing was 6.25×10^{-3}ohm^{-1}-cm^{-1}.

From the optical study, it was seen that the transmittance could be obtained upto 86% by air annealing the films at 593K. The optical band gap calculated from the absorption coefficients for unannealed film was about 3.0 eV and that for annealed films was about 3.55 eV. The refractive index calculated from the interference pattern of the transmission spectra was found to be 1.9. The lower values of extinction coefficient and dielectric constants of these films are the essential requirements for transparent conducting purposes.

Chapter 7: Studies on Au-(n)ZnSe and Ni-(n)ZnSe Schottky Barrier Junctions

Two types of metal-semiconductor junctions viz. Au-(n)ZnSe and Ni-(n)ZnSe were studied for their various junction properties. In this chapter the details of the current-voltage characteristics at different temperatures, junction parameters, photo-voltaic performance etc. of thin film Au-(n)ZnSe and Ni-(n)ZnSe structures have been presented.

Capacitance of both the junctions was measured under reverse bias condition. Three sets of Al-doped ZnSe films with doping concentration 1.4×10^{14}cm^{-3}, 4.8×10^{14}

cm^{-3} and 9.7×10^{14} cm^{-3} were used to prepare the Schottky barrier junctions. The barrier heights of Au-(n)ZnSe and Ni-(n)ZnSe Schottky barrier junctions with doping concentration 9.7×10^{14} cm^{-3} obtained from C^{-2}-V plots have been observed to be 0.865 eV and 0.785 eV respectively. Both Au-(n)ZnSe and Ni-(n)ZnSe Schottky barrier junctions showed rectification behaviour with soft reverse current. The diode ideality factors of both the junctions were found to be greater than unity. The diode ideality factor was found to decrease and reverse saturation current density was found to increase with doping concentration of the ZnSe films of the junctions. The diode quality was found to improve after annealing the junctions in vacuum at 373K for 10 minutes. The barrier height measured from *J-V* characteristics of Au-(n)ZnSe junction with doping concentration 9.7×10^{14} cm^{-3} was found to be 0.817 eV while that of Ni-(n)ZnSe junction of same doping concentration was found to be 0.724eV. The diode quality was found to improve with doping concentration of the ZnSe film of the junctions. This means that by increasing the doping concentration of ZnSe film, diode of good quality can be achieved. But in the present case, by the process of co-evaporation, the doping concentration could not be achieved beyond 9.7×10^{14} cm^{-3}.

The series resistances of both Au-(n)ZnSe and Ni-(n)ZnSe junctions (for doping concentration 9.7×10^{14} cm^{-3}) were found to be 1.7 MΩ and 3.5 MΩ respectively. Series resistance of the devices was found to be lowered on heat treatment of the devices.

Photovoltaic characteristics of Au-(n)ZnSe and Ni-(n)ZnSe Schottky barrier junctions have also been studied. Both types of junction exhibited photovoltaic effect. Very low photovoltages with low value of fill-factors have been observed for these junctions. Nearly linear nature of the *J-V* curves of these junctions under illumination showed the existence of very high series resistance in the junctions, which caused poor photovoltaic effect. The short-circuit current, open-circuit voltage and fill-factor for Au-(n)ZnSe junction of doping concentration 9.7×10^{14} cm^{-3} were found to be 0.42 $\mu A/cm^2$, 300mV and 0.40 respectively and those for Ni-(n)ZnSe junction with same doping concentration were found to be 0.46 $\mu A/cm^2$, 410mV and 0.42 respectively. Improvement of photovoltaic performance was also observed in heat treated devices.

Under illumination, the diode ideality factors of both Au-(n)ZnSe and Ni-(n)ZnSe Schottky barier junctions have been found to decrease, while the saturation

current density for both the junctions was observed to increase, which was due to the generation of more carriers under illumination.

Chapter 8: Studies on ITO/(p)Si, (n)ZnSe/(p)CdTe and (n)ZnSe/(p)Si Heterojunctions

Results of the studies on electrical properties and photovoltaic effect of three types of heterojuctions viz, ITO/(p)Si, (n)ZnSe/(p)CdTe and (n)ZnSe/(p)Si prepared by thermal evaporation have been presented in this chapter. All the compound semiconductors of these junctions except Si were vacuum deposited thin films. In case of Si, p-type single crystal wafers were used. All the junctions prepared in the present case exhibited rectifying characteristics.

Diode ideality factor of a typical (n)ITO-(p)Si junction of area 0.038 cm^2 has been found to be 4.7 with reverse saturation current density 7 nA/cm^2 and barrier height 0.525 eV. The current-voltage curves of ITO/(p)Si junctions were characterised by high series resistance of the order of KΩ (156 KΩ to 177 KΩ). All the ITO/(p)Si structures exhibited photovoltaic effect with very low photovoltaic conversion efficiency and low value of fill-factor. The linear nature of the photovoltaic characteristics with low fill-factor (0.32) was due to the presence of high series resistance. Very low values of short-circuit current (0.61 to 0.73 $\mu A/cm^2$) and open-circuit voltage (435 to 475 mV) have been observed.

The ideality factor of vacuum deposited (n)ZnSe-(p)CdTe heterojunction was also found to be more than unity (6.88). The saturation current density and the built-in potential of the junction at room temperature measured from current-voltage characteristics were found to be 6 $nAcm^{-2}$ and 0.77 eV respectively. The series resistance contributed by the resistive CdTe and ZnSe layers of the junction was found to be very high (16 MΩ). The junction exhibited low photovoltaic performance. The open-circuit voltage of the junction was found to be 470 mV and short-circuit current density 2.1 $\mu A/cm^2$ and maximum power output 3.64×10^{-4} mW/cm^2 with fill factor 0.38. The efficiency of the cell was found very low, 0.2%. The spectral response short-circuit current of the (n)ZnSe/(p)CdTe junction was also investigated. The maximum short-circuit current was obtained corresponding to the wavelength 840 nm (photon energy=1.47eV), which implies that the absorption was mostly within CdTe layer of the structure. The diode ideality factor of the junction under illumination was observed to decrease, while the saturation current density J_o was found to increase under illumination.

From the rectifying current-voltage characteristics of the (n)ZnSe-(p)Si heterojunction, the diode ideality factor was found to be 4.87 with built-in potential 0.744 eV. The series resistance of this junction was also found to be very high (2.2 MΩ). The high series resistance of this junction was due to the low conducting ZnSe film. The *J-V* curve of the (n)ZnSe/(p)Si junction was studied for its photovoltaic performance under illumination. Nearly linear nature of this plot implies the existence of a large series resistance in the junction. Very low photovoltage (about 125 mV) with low short-circuit current density (9.05 $\mu A/cm^2$) has been observed in the junction.

Chapter 9: Overall conclusions from the present study

In this last chapter of the thesis, the overall conclusion of the present studies has been summarized. The structural, electrical and optical properties of ZnSe and ITO films prepared by thermal evaporation method under different conditions have been studied. From the studies, the growth conditions of both the films suitable for preparation of Schottky barrier junctions and heterojunctions have been obtained. Two types of metal-semiconductor Schottky barrier junction viz. (Au-(n)ZnSe and Ni-(n)ZnSe) and three types of heterojunction viz. (ITO/(p)Si, (n)ZnSe/(p)CdTe, and (n)ZnSe/(p)Si) were prepared by thermal evaporation and they were studied for their junction properties. Both the Schottky barrier junctions and heterojunctions under investigation showed rectifying characteristics with diode ideality factor more than unity. All the junctions have high series resistance. The junctions under illumination showed poor photovoltaic effect with low value of fill-factor. From the present studies it is seen that there are great potentiality to prepare Schottky barrier junctions and heterojunctions with ZnSe and ITO by thermal evaporation method by improving their diode quality after proper doping, annealing, reduction of interfacial layer and passivation of surface states etc. There are future scopes of research in this respect.

CONTENTS

Page

CHAPTER 1

General Introduction 21

1 .1 Thin film technology 21

1.2 Metal-semiconductor (Schottky barrier) junctions and Heterojunctions 22

1.3 Aims and objectives of the present work 24

1.4 An overview of materials 26

1.4.1 ZnSe and its importance for optoelectronic devices 26

1.4.2 A brief review of research works on ZnSe 27

1.4.3 Brief review of research works on Schottky barriers and heterojunctions with ZnSe 30

1.4.4 ITO and its importance for optoelectronic devices 32

1.4.5 Physical properties of ITO and review of literature 32

CHAPTER 2

Preparation methods and growth process of thin films

2.1 Brief outline of different methods of thin film preparation 36

2.1.1 Physical vapour deposition 36

2.1.2 Sputtering 37

2.1.3 Chemical Vapour deposition 37

2.1.4 Chemical deposition 37

2.2 Choice of deposition process 38

2.3 Mechanism of thermal evaporation process 38

2.4 Processes of formation of thin film 40

2.4.1 Condensation 41

2.4.2 Nucleation and growth 41

2.5 Factors affecting the growth, structure and film properties 45

CHAPTER 3

Theoretical Backgound

3.1	Structural properties	46
3.1.1	Lattice constant	47
3.1.2	The grain sizes	47
3.1.3	Average stress and strain	48
3.1.4	Average grain size and strain from Williamson and Hall relation	49
3.1.5	Dislocation density	49
3.2	Semiconductor Theory	51
3.2.1	Conductivity of Intrinsic Semiconductor	51
3.2.2	Extrinsic Semiconductor	52
3.2.3	Temperature dependence conductivity of semiconductor	53
3.3	Optical properties of semiconductor	55
3.3.1	Optical absorption	55
3.3.2	Optical constants of thin films	58
3.3.3	Determination of optical constants of thin films	58
3.4	Photoconduction in Semiconductor	61
3.5	Metal-semiconductor junction	65
3.5.1	Ohmic contact to semiconductor	65
3.5.2	Schottky Barrier junction	65
3.5.3	Capacitance of a Schottky barrier	68
3.5.4	Influence of surface states	69
3.5.5	Lowering of the Schottky barrier by Image force	61
3.5.6	Schottky barrier with an Interfacial layer	72
3.5.7	General expression for Barrier Height	73
3.5.8	Electronic transport mechanisms of metal-semiconductor Junction	74
3.5.9	Thermoionic emission theory of *I-V* characteristics	76
3.6	Heterojuctions	78
3.6.1	Energy band diagram of abrupt anisotype heterojunction	78
3.6.2	Transport mechanisms of abrupt anisotype heterojunction Thermoionic emission model	79
3.7	Photovoltaic Effect and Solar Cells	80

3.7.1 Working of Photovoltaic cell 80
3.7.2 Current-voltage characteristics and Parameters of a Solar cell 82
3.7.3 Equivalent circuit of a Solar Cell 85
3.7.4 Effect of Diode Ideality factor 86

CHAPTER 4

Measuring Equipments and Experimental Techniques

4.1 Introduction 87
4.2 Materials used for sample preparation 87
4.3 Vacuum Coating unit 87
4.4 Selection of substrate 90
4.5 Cleaning of Substrates 91
4.6 Masks for generation of pattern in the deposited films 92
4.7 Substrate heating 92
4.8 Preparation of Semiconductor films 92
4.9 Preparation of junctions 95
4.9.1 Preparation of Au/(n)ZnSe and Ni/(n)ZnSe junctions (Schottky Barrier junctions) 95
4.9.2 Preparation of Heterojunctions 95
4.10 Measurement of Film thickness 98
4.11 Measurement of Optical transmission, absorbance and reflectance UV-visible spectrophotometer 99
4.12. Microstructural, morphological and compositional analysis 102
4.13 Determination of type of doping and doping concentration 103
4.14 Electrical and Optical measurements 104
(a) Sample Holder 104
(b) The main unit for mounting the sample 104
(c) Light source 105
(d) Arrangement for electrical measurement 107
(e) Photoconductive rise and decay measurement 108
(f) Measurement of photovoltaic effect 108
(g) Capacitance-Voltage measurement 109
Photographs 110-111

CHAPTER 5

Studies of ZnSe Films

5.1 Structural and Morphological studies of ZnSe thin films 112
5.1.1 X-ray diffractogram of ZnSe films 112
5.1.2 Microstructural parameters 117
5.1.3 Morphological study of ZnSe thin films by SEM 125
5.1.4 Compositional Analysis of ZnSe films 102
5.2 Electrical and Photoconductiveity of thermally deposited ZnSe films 134
5.2.1 Ohmic contact 134
5.2.2 The effect of substrate temperature on electrical conductivity 135
5.2.3 Variation of conductivity with temperature 136
5.2.4 Photoelectrical properties 139
5.3 Optical properties of ZnSe thin films 143
5.3.1 Transmittance 143
5.3.2 Refractive index 145
5.3.3 Absorption coefficient and extinction coefficient 147
5.3.4 Dielectric constants 147
5.3.5 Optical band gap 148
5.4 Discussions and conclusions 151

CHAPTER 6

Studies of Indium Tin Oxide (ITO) Films

6.1 Structural properties 154
6.1.1 X-ray diffractogram of ITO thin films 154
6.2 Morphological study of ITO thin films by SEM 158
6.3 Electrical studies of ITO films 159
6.3.1 Ohmic contact 159
6.3.2 Temperature Variation of conductivity 160
6.4 Optical studies of ITO films 162
6.5 Discussions and conclusions 164

CHAPTER 7

Studies on Au/(n)ZnSe and Ni/(n)ZnSe Schottky Barrier Junctions

7.1 Introduction 166

7.2 Capacitance-voltage measurements of the junctions 166
7.3 Studies of Current-voltage characteristics of Au-(n)ZnSe Schottky barrier junctions 169
7.3.1 *J-V* characteristics of of Au-(n)ZnSe Schottky barrier junctions in dark at room temperature 169
7.3.2 Effect of series resistance on *I-V* characteristics of the junction 172
7.3.3 Temperature dependence of *J-V* characteristics of Au-(n)ZnSe junctions 174
7.4 Studies of Current-voltage characteristics of Ni-(n)ZnSe Schottky barrier junctions 178
7.4.1 *J-V* characteristics of of Ni-(n)ZnSe Schottky barrier junctions in dark at room temperature 178
7.4.2 Series resistance of Ni-(n)ZnSe junction 180
7.4.3 Temperature dependence of *J-V* characteristics of Ni-(n)ZnSe junctions 181
7.5 Discussions and Conclusions 185
7.6 Studies of Current-voltage characteristics of Au-(n)ZnSe and Ni-(n)ZnSe junctions under illumination 187
7.6.1 Photovoltaic measurements 187
7.6.2 Studies of Photovoltaic Effect in Au-(n)ZnSe junctions 187
7.6.3 Diode parameters of Au-(n)ZnSe Schottky barriers under illumination 188
7.6.4 Studies of Photovoltaic Effect in Ni-(n)ZnSe junctions 190
7.6.5 Diode parameters of Ni-(n)ZnSe Schottky barriers under illumination 191
7.6.6 Discussions on Photovoltaic Effect 193

CHAPTER 8

Studies on ITO/(p)Si, (n)ZnSe/(p)CdTe and (n)ZnSe/(p)Si heterojunctions
8.1 Studies of ITO/(p)Si heterojunctions 195
8.1.1 Current-voltage characteristics 196
8.1.2 Effect of series resistance 197
8.1.3 Temperature dependence of *J-V* characteristics of ITO-(p)Si junctions 198
8.1.4 Capacitance-voltage characteristics 201
8.1.5 Photovoltaic effect 203
8.1.6 Summary on the studies of (n)ITO-(p)Si heterojunctions 204
8.2 Studies on (n)ZnSe-(p)CdTe heterojunctions 205
8.2.1 Current-voltage characteristics 205

8.2.2 Effect of Series Resistance 208
8.2.3 Capacitance-voltage characteristics 210
8.2.4 Photovoltaic effect 210
8.2.5 Spectral response 213
8.2.6 Summary on the studies of (n)ZnSe-(p)CdTe heterojunctions 214
8.3 Studies of (n)ZnSe/(p)Si heterojunctions 215
8.3.1 Current-voltage characteristics 215
8.3.2 Effect of series resistance 218
8.3.3 Capacitance- Voltage Measurement 219
8.3.4 Photovoltaic Effect 220
8.3.5 Summary on the studies of (n)ZnSe-(p)Si heterojunctions 221
8.4 Comparative study and discussions of ITO/(p)Si, (n)ZnSe/(p)CdTe and (n)ZnSe/(p)Si Heterojunctions 222

CHAPTER 9

Overall conclusions from the present studies 225-230

REFERENCES 231-258

LIST OF PAPER PUBLISHED

CHAPTER-1

General Introduction

1.1 Thin film technology

Thin film and devices play an important role in the development of modern science. The thin film is a two dimensional form of solid material, whose one dimension, called the thickness, is much smaller than the other two dimensions. The thin film is formed by atom to atom or molecule to molecule condensation process. In technical terms, the thickness of the films must be limited to the order of mean free path of the carriers participating in the particular electronic transport process for which the film has been fabricated. The limit of thickness may vary from a nanometer to a few micrometer depending upon the field of application [1].

At the initial stages, investigations on the thin films were made out of scientific curiosity, particularly for their significantly different properties from those of the same material in bulk form. However the acquired capability of controlling properties of the thin films in subsequent years, helps immensely the use of thin films in electronic, opto-electronic and other devices and as a result, the electronic industry has become the greatest beneficiary of thin film technology. On the other hand, the thin film technology contributes to the development of microelectronics, by reducing the sizes of semiconductor devices to two dimensions.

The use of thin films in making active and passive electronic components made it possible to produce VLSI and microcomputer. Due to use of thin film technology, now the three dimensional bulk display units become flat. Because of compactness, better performance and reliability and low production cost thin film devices and components are preferred over their bulk counterparts.

The development of thin film technology has led to its application in diverse fields from microelectronics to optics, space science to aircrafts, superconductivity to photovoltaics. One of the most important applications of thin films is in the photovoltaic devices and other solar cells [2, 3]. In the photovoltaic devices, the use of thin films, or rather thick films (2-3 μm thickness) enables not only material costs saving but also the fabrication of large area devices at a comparatively low cost. The

investigations on thin films have led to the development of new kind of active devices and passive components, different types of sensors [4], storage of solar energy and conversion to other forms [5], magnetic memories [6], superconducting films [7], optical image storing devices [8, 9], electromechanical device like strain gauge [10], gas detecting transducer [11], interference filter [12], reflecting and antireflecting coating [13] and many others [2, 3, 14]. Hence in addition to major contribution to variety of new and future scientifically based technology, the thin films studies have directly or indirectly caused the advancement of many new areas of research in solid state physics and chemistry and will continue to play increasingly important roles in the study of a variety of problems of basic and technological importance.

1.2 Metal-semiconductor (Schottky Barrier) junctions and Heterojunctions:

A metal-semiconductor junction exhibiting rectifying behaviour is commonly known as the Schottky barrier junction. The metal-semiconductor rectifying junction was the oldest solid state device used in electronics. More than hundred thirty years back, in 1874, Braun first reported the asymmetric nature of electrical conduction between metal-semiconductor contacts [15]. In 1938, Schottky suggested a model to understand the rectifying action of metal-semiconductor contact, according to which a potential barrier is developed when a metal makes intimate contact with a semiconductor [16], which is later named as Schottky-barrier contact. In the same year Mott also devised an appropriate theoretical model for swept-out metal-semiconductor contact [17] that is known as the Mott barrier. Schottky barrier junction or Schottky diode has a rectification capability, with a large current in forward bias and very low leakage current in reverse bias. Because of their importance in direct current and microwave applications and as tools in the analysis of other fundamental physical parameters, metal-semiconductor contacts have been studied extensively. The basic theory and historical development of rectifying metal-semiconductor contacts have been summarized by Henisch [18] and the properties and applications of Schottky barriers have been reviewed by Atalla [19]. The practical metal-semiconductor contacts are now made by evaporation of metal in vacuum to let it deposit onto the semiconductor. Today, the metal-semiconductor junctions are much used as rectifiers, microwave diodes, UV detectors, switching diodes, photo

sensors and solar cells [20-26]. Due to its fast switching effect, it is widely used in digital circuits and communications and radar applications [24-27].

A heterojunction is formed when two semiconductors, of different band gap energies are brought together. The study of semiconductor heterojunctions is a most desired field of research for advancement of semiconductor devices and technology. In 1951, Shockley first proposed the abrupt heterojunction to be used as an efficient emitter based junction in bipolar transistor [28]. In the same year, Gubanov published theoretical papers on heterojunctions [29]. Kroemer later analysed a similar, although graded, heterojunction as a wide gap emitter [30]. Since then, heterojunctions have been extensively studied, and many important applications such as room temperature injection laser, light emitter diode, photodiode and solar cell etc have been made. In addition, by forming periodic layered heterojunctions with layer thickness of the order of 100Å, the so-called super lattice structures are obtained [31]. The heterojunctions have been reviewed by Milnes and Feucht [32] and Sharma and Purohit [33].

Though bulk heterojunction diodes and Schottky barrier diodes are widely used in most of the electronic circuits for different applications, the research activities and development of various thin film heterojunctions and Schottky barrier junctions have also been in progress since last forty years. R. S. Muller and R. Zuleeg investigated the thin-film heterojunction diodes of vapor-deposited CdS and other semi-insulators viz, CdTe, Al_2O_3 and SiO_x [34]. W. A. Gutierrez reported a CdSe-ZnSe thin film heterojunction as rectifier [35]. F. A. Shallcross reported a photoconductor diode array made by CdS-CdSe thin films [36]. C. J. Moore and D. E. Brodie fabricated a ZnSe-ZnTe amorphorus thin film heterojunction by thermal evaporation method [37]. F. Pfisterer and others investigated ZnTe-CdS thin film solar cell prepared by vacuum deposition [38]. I. Gunal and M. E. Ozsan prepared Te/CdS thin film Schottky barrier diodes and studied their electrical properties [39]. J. Touskova et al investigated the fundamental properties of CdS-CdTe thin film heterojunctions prepared by electrochemically depositing CdTe layer over the CdS film prepared by spray pyrolysis method [40]. P. C. Sarmah studied Ag-(n)CdTe and Al-(n)CdTe thin film Schottky barrier junctions prepared by rf sputtering technique [41]. Some workers have investigated the Schottky barrier devices of organic semiconductors with different metals [42]. Venugopal et al have grown CdTe/$ZnSe_xCdS_{1-x}$ heterojunctions on glass substrates by vacuum evaporation [43]. N. I. Aly et al fabricated a heterojuction of amorphorus GaAs thin film and n-type Si

and studied the carrier transport mechanism [44]. M. Rami et al investigated the heating effect and $CdCl_2$ treatment on the electrodeposited CdTe/CdS heterojunction [45]. Mridha and Basak have investigated the p-CuO/n-ZnO thin film heterojunction prepared by sol-gel technique for H_2 gas sensor applications [46]. Adieovich et al studied the SnO_2-CdS-CdTe-Me thin film heterojunction and investigated the structure as photodiode arrays [47]. Hema Chanda et al fabricated the p-$AgGa_{0.25}In_{0.75}Se_2$/n-$Zn_{0.35}Cd_{0.65}S$ polycrystalline thin film heterojunctions and characterized it [48]. Weichsel studied the electrical and hydrogen sensing characteristics of Pd/ZnO Schottky diodes grown on GaAs [49]. G. C. Wary et al studied the optical and electrical properties of (n)ZnO/(p)CdTe heterojunction [50]. It is seen that in the study of thin film junctions, besides the electroluminescence cell and photodiode, more emphasis is given on the photovoltaic performance of the junctions. W. D. Gill and R. H. Bube studied the photovoltaic properties of Cu_2S-CdS heterojunctions [51]. Alan L. Fahrenbruch et al reported some II-VI heterojunctions for solar energy conversion [52]. Fredrik Buch et al studied the photovoltaic properties of n-CdSe/p-ZnTe heterojunctions by depositing epitaxial film of n-CdSe on p-ZnTe crystal [53]. T. L. Chu et al obtained 13.45% efficient thin film CdS/CdTe solar cells [54]. S. N. Alamri and A. W. Brinkman studied the effect of the transparent conductive oxide on the performance of thin film CdS/CdTe solar cells [55]. H. Bayhan investigated the current transport mechanism of CdS/CdTe thin film heterojunction solar cell prepared by thermal evaporation technique [56]. M. Purica et al studied the electrical properties of CdS/InP heterostructure for photovoltaic applications [57].

1.3 Aims and objectives of the present work:

The studies of semiconductor thin films and their junctions such as metal-semiconductor junctions (Schottky Barriers) and heterojunctions have received much attention due to their applications in various electronic and optoelectronic devices including solar cells. In the present work, studies were carried out on electrical and optical properties of (n)ZnSe and ITO based thin film Schottky barriers and heterojunctions with an aim for their possible use in optoelectronic devices.

The compound semiconductors of the second and sixth (II-VI) groups of the periodic table possess suitable energy gap and at present these compounds are being widely investigated for their possible uses in different fields. Among the compounds,

Zinc Selenide (ZnSe) is one of the most interesting semiconductors due to its wide band gap. Another important intermatellic compound semiconductor is CdTe. It possesses suitable energy gap and has high absorption coefficient suitable for using in a junction for photo-voltaic conversion.

The transparent conducting oxides have become one of the revolutionary areas in recent years due to their high optical transparency and high conductivity. One of the oxide semiconductors Indium Tin Oxide (ITO) is the most demanding because of its wide band gap, high transparency and high electrical conductivity. Considering their availability and easy of preparation, it was proposed in the present case to study these materials in the forms of thin films and their junctions.

The films and their junctions were proposed to be prepared by vacuum evaporation and the properties proposed to be studied were electrical and optical properties of these samples under different conditions.

The proposed vacuum evaporated thin films are ZnSe, CdTe and ITO and the thin film junctions proposed for study are Schottky barrier junctions: Au-(n)ZnSe and Ni-(n)ZnSe and Heterojunctions: ITO-(p)Si, (n)ZnSe-(p)CdTe and (n)ZnSe-(p)Si. Silicon has been selected to be as one of the candidates for making Schottky Barrier junction because of its most suitable band gap for photovoltaic effect and because of its abundance in nature.

In brief, following are the aims and objectives of the present works:

(i) To prepare the thin films of ZnSe and ITO by thermal evaporation method and to study: (a) Structural properties, (b) Electrical properties, and (c) Optical properties of these films;

(ii) To fabricate thin film Schottky Barrier junctions: Au-(n)ZnSe and Ni-(n)ZnSe,

(iii) To fabricate thin film heterojunctions: ITO-(p)Si, (n)ZnSe-(p)CdTe and (n)ZnSe-(p)Si.

(iv) To study the current-voltage characteristics, photovoltaic performance of all these thin film junctions and to determine junction parameters from the current-voltage characteristics.

1.4 An overview of materials

1.4.1 Zinc Selenide(ZnSe) and its importance for optoelectronic devices

The Zinc selenide (ZnSe) is a light yellow binary compound (II-VI) semiconductor with a wide bandgap of 2.7 eV [58]. The properties such as large bandgap, low resistivity and high photosensitivity make this semiconducting material highly attractive. ZnSe exists in two crystalline forms: wurtzite (hexagonal) and zincblende (cubic), of which the cubic phase is believed to be stable. The ZnSe has the electron affinity of 4.09 eV and electron mobility of about 530 $cm^2V^{-1}s^{-1}$at room temperature [59]. Like most II-VI compounds ZnSe is generally produced as an n-type semiconductor, but is difficult to produce as a p-type. Using nitrogen as the dopant, some degree of success has been achieved in making p-type ZnSe [60-63].

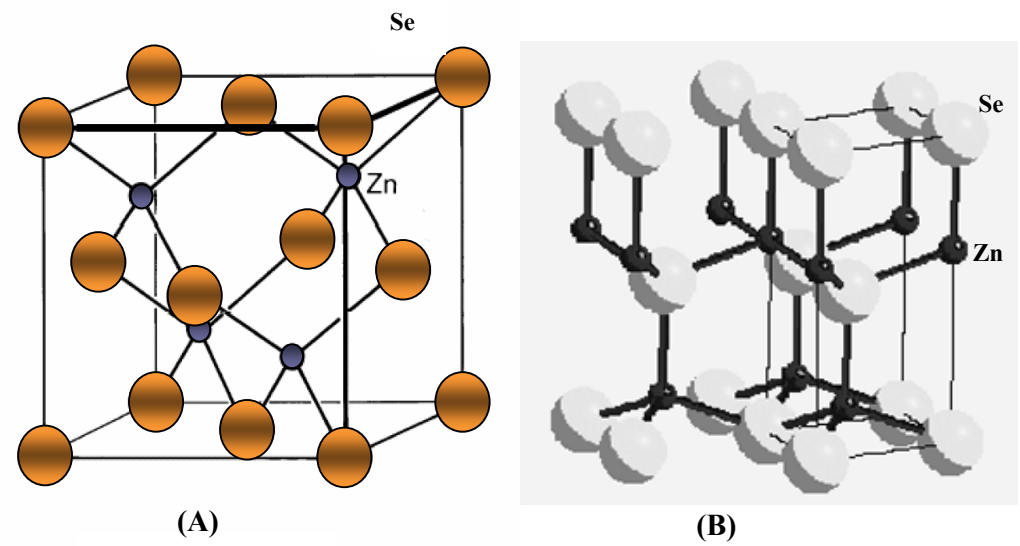

Figure 1.01: (A) Zincblende Structure and (B) Wurtzite structure of ZnSe crystal (small filled circles are Zn atoms and large circles are Se atoms)

Among different II-VI compound semiconductors, ZnSe has drawn considerable interest because of its direct and large band gap, which makes it appropriate for use in optoelectronics as detectors as well as emitters. It is useful for optical components in high power laser window and multispectral applications, providing good imaging characteristics [64, 65]. It is also used as an infrared optical material because of its wide transmission wave length range (600 nm to 2000 nm) [66]. It is commonly used as transmission window in IR spectroscopy, night vision applications and ATR prisms. ZnSe is also useful in high resolution thermal imaging systems, where it is used to correct for colour distortion which is often inherent in other lenses used in system.

The band gap of ZnSe (2.7eV at room temperature) corresponds to an optical absorption threshold at 460 nm. Thus, the material is useful to serve as the active region in blue-green emission light emitting diodes (LED) [67] and blue diode lasers [68-72]. Due to high transmission coefficient ZnSe is used as window layer in solar cells. It can substitute CdS in photovoltaic solar cell devices, aiming at higher cell efficiency by means of admission of more photons to the absorber layer, because of its larger band gap [73, 74]. ZnSe doped with tellurium can act as a scintillator with emission peak at 640 nm, stable for matching with photodiodes. It is used in X-ray and gamma ray detectors. ZnSe is widely used as optical switches [75] and photo detectors [76-81]. It is also used in ultrasonic transducers. Doped ZnSe is used as host layer of thin film electroluminescent devices [82, 83]. These various application potentialities of ZnSe have given considerable impetus to the investigation of its thin films in recent years.

1.4.2 A brief review of research works on ZnSe

The optoelectronic semiconducting material ZnSe, has been extensively studied as single crystals and also as epitaxial and polycrystalline thin films prepared by different techniques because of its unique optoelectronic and other properties with a hope of exploring potentialities for fabrication of new scientific and technological devices.

Many workers prepared single crystal as well as polycrystalline ZnSe in bulk form and also in thin film form and characterized their structural, electrical, optical properties etc. Aven, Marple and Segall investigated the electrical and optical properties of single crystal bulk ZnSe prepared by vapor growth technique [84]. Stringfellow and Bube studied the luminescence and photoelectronic properties of Cu-doped and self activated ZnSe single crystals [85, 86]. The inter band electronic property of zincblende ZnSe was theoretically and experimentally investigated by Markowski et al [87]. Marple reported the effective mass of ZnSe obtained by optical method [88]. Electrical properties of single crystal ZnSe was studied by Jones and Woods [89] and Cutter and Woods observed anomalous photovoltaic effect of it [90]. Strzalkowski et al measured dielectric constant of bulk ZnSe [91]. Some workers reported the blue electroluminescence from ZnSe crystals [92-94]. The photoconductivity of bulk ZnSe crystals were reported by many workers [95-97].

Different workers studied the photoluminescence of bulk and single crystal ZnSe [98-105].

Although studies of bulk crystals are useful and essential for understanding some of the more fundamental material properties, the preparation of high quality thin films is desirable for device applications. A variety of methods were employed for the growth of high quality ZnSe thin films. Single crystal ZnSe thin films have usually been grown by molecular beam epitaxy (MBE) [106-109] and chemical vapor deposition (CVD) [110-115]. The growth of monocrystalline ZnSe films by another method named atomic layer epitaxy, were also reported by some workers [116, 117]. Several reports on the electrodeposition polycrystalline ZnSe films from aqueous solutions have been published [118-122]. Many workers reported the studies of ZnSe films grown by chemical deposition method [123-127]. Kumarsen et al reported the deposition of ZnSe polycrystalline thin films by a novel method named photochemical deposition (PCD) [128]. Spray pyrolysis techniques were also used by different workers to prepare the polycrystalline ZnSe thin films [67, 129]. Kale and Lokhande deposited polycrystalline ZnSe films by successive ionic layer adsorption and reaction (SILAR) method [130]. Close space vapor transport (CSVT) technique is also used by some workers to prepare the polycrystalline thin films of ZnSe [131, 132]. Polycrystalline ZnSe films have been widely grown by various physical vapor deposition procedures. ZnSe films prepared by sputtering method have been reported by many workers [133, 134]. Perna et al studied the structural and optical properties of ZnSe films deposited by laser ablation technique [135, 136]. The studies of optical properties of ZnSe films grown by electron beam evaporation are also found in literature [137, 138].

In recent years, different properties of ZnSe polycrystalline thin films prepared by thermal evaporation methods were widely investigated by different workers. Thermally deposited polycrystalline ZnSe thin films prepared at different conditions were investigated by many workers for their structural, electrical and optical properties [139-144]. The bulk stoichiometry and the density of thin vapour-deposited films of ZnSe were determined by Khawaja et al [145]. The optical properties like refractive index, extinction coefficient and band gap of thermally evaporated ZnSe thin films were investigated by Thutupalli and Tomlin [146], Dawar et al [147], Sheirif et al [148], Sigh et al [149] at different laboratories. Lakshmikumar and Rastogi have prepared the polycrystalline ZnSe films by selenising vacuum

evaporated Zn films in a reactor having selenium vapor [150]. Gogoi and Barua studied the DC conduction mechanism and dielectric properties of thermally deposited ZnSe films [151]. Rusu et al studied the electronic transport properties of ZnSe films prepared by quasi closed volume technique under vacuum [152]. The anomalous photovoltaic effect in obliquely vacuum deposited ZnSe film was observed by El-Shazly et al [153]. Verma et al studied the thermally evaporated ZnSe films under solar illumination [154]. Antcliffet studied the electroluminescence of evaporated ZnSe films [155].

For the preparation of optoelectronic devices, the electrical conductivity of the semiconductor is one of the most important factors. ZnSe has been prepared in both n-type and p-type form. Although low resistivity bulk ZnSe has been prepared by high temperature annealing in molten Zinc [89] or implanting Al ion [156], it is extremely difficult to prepare low resistivity films of ZnSe. There are only a few reports of high conductivity as-grown thin films [157, 158] till 1980 which were prepared by MBE without intentional doping. D M Chiu prepared n-type ZnSe single crystals by the double impurity doping (iodine during growth and indium by diffusion) and found that though doping reduced resistivity, did not make the zinc selenide strongly degenerate [159]. The reason for the difficulty in preparing high conductivity ZnSe film is not well understood and is the subject of considerable controversy. Two proposed theories are that high resistivity occurs either as a result of self compensation by native defects or by compensation by residual impurities. Many approaches to grow high conducting n-type ZnSe thin films have been used. Aranovich et al reported high conductivity films of ZnSe produced by annealing, vacuum deposited with coevaporated Ga and Zn, in Zn vapor at 500^0C [160]. Kitagawa et al obtained ZnSe thin films on GaAs substrates with resistivities as low as 0.07 Ωcm by MBE method using Ga as dopant [161, 162]. Using CSVT method, Pawlikowski prepared polycrystalline thin films of ZnSe of resitivity about 800 Ωcm by introducing Al or Zn dopant followed by post deposition annealing [132]. Choudhury et al reported n-type Al-doped-ZnSe films prepared by laser assisted evaporation [163]. Oh et al reported highly conducting Al-doped n-type ZnSe film of carrier concentration up to $4x10^{18}$ cm^{-3} grown by MBE [164]. Chu et al prepared low resistive polycrystalline thin film of ZnSe doped with Al by Metal organic chemical vapor deposition (MOCVD) method [110]. Zulfiqar Ali et al reported low resistive Cu-doped ZnSe films deposited by two-source-evaporation method [165].

Although low-resistivity n-type ZnSe is easily prepared, p- type material is much more difficult to achieve. One of the main reasons for the difficulty in preparing a low-resistivity p-type ZnSe single crystal is the amphoteric behaviour of the incorporated acceptor impurities. It is known that acceptor-type impurities occupy both interstitial and substitutional sites. When group I elements are incorporated, impurities in the interstitial and substitutional sites behave as donors and acceptors, respectively, and compensate each other [99]. Robinson and Kun [166] claimed to have solved the problem by introducing group III elements such as indium, gallium and thallium in high concentrations, but unfortunately their work has never been reproduced. A A Qidwai and J Woods by studying Photocapacitance and defect levels in gallium-doped zinc selenide, concluded that although gallium in low concentration in ZnSe acts as a shallow donor, complex compensation effects occur if its concentration is increased, so the resistivity begins to increase with increasing impurity content [167]. It was already established that nitrogen is the best dopant for producing p-type ZnSe material with the highest carrier concentration so far approximately 10^{18} cm^{-3} [60-63]. In recent years, the investigation is going on to enhance the p-type doping of ZnSe films by using different dopants and techniques [168-171].

1.4.3 Brief review of research works on Schottky barriers and heterojunctions with ZnSe:

The growth of good quality ZnSe thin films led to preparation of different kinds of devices. Brinkman and Kirk studied the role of high temperature thermal annealing in changing the interfacial microstructure of Ge-ZnSe heterojunctions prepared by depositing ZnSe layer on Ge substrate [172]. High quality GaAs is widely used as a substrate for growth of ZnSe thin films because of its matching lattice constant with ZnSe (lattice mismatch 0.27%). The metal Au was used by different workers to form Schottky barrier with epitaxial n-type ZnSe layer [106, 173, 174]. Schull et al studied the ohmic contact of n-ZnSe with ITO [175] and Saidane studied the chemical reaction occurred in the interface of the ZnSe/ITO heterostructure [176]. Many workers investigated the ZnSe/GaAs heterojunctions and solar cells [113, 114,177]. Blieske et al studied n-ZnSe/p-GaAs heterojunction Solar Cells [178]. Seghier and Gislason [179], Kim et al [180, 181] studied the p-ZnSe/n-GaAs

heterojunction diode by growing N-doped *p*-type ZnSe thin films by MBE on n-GaAs substrates. Nurnberger et al studied the ZnSe p-n diodes on n-GaAs substrate [182]. High detectivity ZnSe-based Schottky barrier photodetectors were reported by different workers [65, 77-79, 183-184]. Dreifus et al studied ZnSe field effect transistor fabricated on GaAs substrate by MBE [185]. Thin film electroluminescent cell of n-Ge-ZnSe:Mn^{2+}-indium-tin oxide structure, with the low-threshold voltage, was investigated by Ohnishi et al [186]. Rubini et al have successfully fabricated epitaxial ZnSe/CdTe/ZnSe heterostructures by MBE on GaAs (001) [187]. By evaporating ZnSe polycrystalline films on Si wafers, different workers prepared ZnSe/Si junctions and studied their optoelectronic properties [188-190]. Rectifying heterojunctons and PIN photo diodes of ZnSe/Si were also studied by different workers [191-193]. A CdSe-ZnSe thin film rectifier was reported by Gutierrez and Wilson [35]. The photovoltaic properties of ZnSe heterojunctions with other II-VI compounds were studied by Fahrenbruch et al [52], Fredrik Buch et al [194], Chu et al and other workers [110]. Nelson investigated the ZnSe/CdTe heterojunction to understand the interface between them [195]. The performance of solar cell using ZnSe as a window layer was studied by different workers [74, 196-199]. Dharmadasa et al studied p-n junctions and multi-layer solar cell using electrodeposited p-type and n-type ZnSe layer [122]. Samantilleke et al developed optoelectronic devices using electrochemically grown thin ZnSe layers [68]. Chang et al fabricated ultraviolet/blue sensors by preparing ITO/ZnSe/ITO structure on the homoepitaxial ZnSe substrates [200].

1.4.4 Indium Tin Oxide (ITO) and its importance for optoelectronic devices

Although partial transparency, with acceptable reduction in conductivity, can be obtained for very thin metallic films, high transparency and simultaneously high conductivity cannot be attained in intrinsic stoichiometric materials. The only way this can be achieved is by creating electron degeneracy in a wide bandgap (E_g > 3eV or more for visible radiation) material by controllably introducing non-stoichiometry and/or appropriate dopants [201]. These conditions can be conveniently met for Indium Tin Oxide (ITO) as well as a number of other materials like Zinc Oxide, Tin Oxide doped with antimony or fluorine etc [202, 203]. ITO having bandgap of about

3.6 eV shows high transmittance as high as 95% and low resistivity as low as 10^2 μΩcm [201, 204]. This high conducting material with high transparency can be used as a window material in photovoltaic devices.

The properties, high transmittance and low resistivity of ITO are useful for a wide range of technological applications in electro-optical devices [205]. Uses of ITO have traditionally ranged from transparent heating elements of aircraft and car windows, antistatic coatings over electronic instrument display panels, heat reflecting mirrors, antireflection coatings and even in high temperature gas sensors. Early electro-optic devices using ITO include CCD arrays, liquid crystal displays and as transparent electrodes for various display devices. More recently, ITO has been used as a transparent contact in advanced optoelectronic devices such as imaging devices, solar cells, light emitting [206] and photo diodes, photo transistors and electrochromic display. Thus it is soon becoming an integral part of modern electronic technology wherever there is a potential for improving optical sensitivity of light detecting devices or quantum efficiency of light emitting devices.

1.4.5 Physical Properties of ITO and review of literature:

Indium Tin Oxide is essentially formed by substitutional doping of In_2O_3 with Sn which replaces the In^{3+} atoms from the cubic bixbyte structure of indium oxide [207]. Sn thus forms an interstitial bond with oxygen and exists either as SnO or SnO_2 - accordingly it has a valency of +2 or +4 respectively. This valency state has a direct bearing on the ultimate conductivity of ITO. The lower valence state results in a net reduction in carrier concentration since a hole is created which acts as a trap and reduces conductivity. On the other hand, predominance of the SnO_2 state means Sn^{4+} acts as an n-type donor releasing electrons to the conduction band. However, in ITO, both substitutional tin and oxygen vacancies contribute to the high conductivity and the material can be represented as $In_{2-x}Sn_xO_{3-2x}$. Indium Tin Oxide films have lattice parameters close to that of In_2O_3 and lie in the range 10.12Å to 10.31Å [208].

Extensive studies on Indium Tin Oxide (ITO) thin films as transparent conductors have been reported and the works are reviewed by Chopra et al [201, 202], Jain [204], Dhere et al [209] and Minami [203]. ITO thin films of varying quality were prepared by variety of methods, which include r.f. sputtering [210-215], magnetron sputtering [216- 218], d.c. sputtering [219], electron beam sputtering [220-

224], spray pyrolysis [225-230], reactive evaporation [231-236], thermal evaporation [237-239], pulsed laser deposition [240], chemical deposition method [241-243] etc. Each method has its advantages and disadvantages, but whichever technique is used it must be optimized so that the produced ITO film is highly conducting and highly transparent since growth conditions strongly affect the microstructure and chemical compositions of the films, which in turn modify the electrical and optical properties of it. Salehi [237] studied the effect of deposition rate and substrate temperature on electrical and optical properties of ITO films prepared by thermal evaporation method without introduction of oxygen into the chamber and observed that the deposited rate rather than the substrate temperature is the dominant factor in controlling the transmittance of ITO films. Yao et al produced ITO film (160Å) of transparency more than 90% and resistivity 4×10^{-5} Ωcm by sequentially evaporating indium and tin by introducing oxygen to the vacuum chamber followed by air annealing [238]. Balasubramanian and Subrahmanyam studied the effect of substrate temperature on reactively evaporated indium tin oxide films [236]. Krokoszinski and Oesterlein [223], Higuchi [244], Wang et al [221], Neubert et al [220] investigated the post deposition annealing effect and influence of heat treatment on oxygen atmosphere on evaporated ITO films. Tahar et al have reviewed the electrical properties of tin doped indium oxide thin films [245]. The electrical and optical properties of typical ITO films deposited using various techniques are summarized in Table 1.1. Variations in film properties can be easily noted; these are attributable to both pre- and post-deposition treatments as well as the techniques involved.

Table 1.1: Typical electrical and optical properties of ITO deposited by various techniques

Deposition Technique	Thickness [Å]	Hall Mobility [$cm^2V^{-1}s^{-1}$]	Carrier concentrations 10^{20}, [cm^{-3}]	Resistivity 10^{-4}, [Ωcm]	Transmittance [%]	Reference
r.f. Sputtering	7000	35	6	3	90	[208]
r.f. Sputtering	5000	12	12	4	95	[213]
r.f. Sputtering	4000	25	3	8	-	[215]
magnetron Sputtering	800	26	6	4	85	[246]
d.c. Sputtering	1000	35	9	2	85	[247]
Reactive evaporation	2500	30	5	4	91	[236]
Ion beam sputtering	600	26	2	12	-	[248]
Spray pyrolysis	3000	45	5	3	85	[230]
Thermal evaporation	-	30	10	2	85	[239]

Recently there are a number of reports available on Indium Tin Oxide films in conjunction with semiconductor like Si to form solar cells [204]. Dubow et al reported an efficient photovoltaic heterojunctions of ITO deposited on p-type Si [249]. Mizrah and Adler have studied the operation of ITO/Si heterojunction solar cells [212]. Manifacier and Szepessy [250] and Feng et al [224] also reported efficient ITO/Si solar cells. Sree Harsha et al reported n-indium tin oxide/p-indium phosphide solar cells [251]. Kobayashi et al studied the current transport mechanism of ITO/Si heterojunctions [227].

The high conductivity, σ, of ITO films is said to be due to high carrier concentration, N, rather than high Hall mobility, μ_H [202] bearing in mind that resistivity, $\rho = 1/\sigma = 1/(qN\mu_H)$ according to Ohm's law. The observed low mobility of ITO, compared to bulk In_2O_3, and its dependence on carrier concentration and substrate temperature has been explained in terms of scattering mechanisms due to ionized impurities or grain boundaries. Mobility is said to increase due to enhanced crystallinity of films deposited at higher substrate temperatures [248]. TEM and electron diffraction studies of r.f. sputtered ITO films on glass substrates by Sreenivas

et al suggest that films grown at room temperature have large stacking faults and represent an amorphous structure [213]; increasing this temperature to 473K leads to a polycrystalline structure and finally annealing results in near single crystallinity with uniform grain size which leads to increased conductivity. The authors further suggest that deposition of ITO on single crystal substrates, rather than amorphous glass, can enhance the grain growth process. The direct optical bandgap of ITO films is generally greater than 3.75 eV although a range of values from 3.5 to 4.06 eV have also been reported in the literature [207, 252]. The high optical transmittance, of these films is a direct consequence of their being a wide bandgap semiconductor. The fundamental absorption edge generally lies in the ultraviolet region of the spectrum and shifts to shorter wavelengths with increasing carrier concentration, N. This is because the bandgap exhibits an $N^{2/3}$ dependence due to the Moss-Burstein shift [238]. The conduction band is curved upwards, the valence band is curved downwards and the Fermi level is located at mid bandgap for the undoped material; addition of Sn dopants results in the formation of donor states just below the conduction band. As the doping density is increased, these eventually merge with the conduction band at a critical density, n_c, which was calculated to be 2.3×10^{19} cm^{-3} by Gupta *et al* [252]. Free electron properties are exhibited by the material when the density of electrons from the donor atoms exceeds this value. As Table 1.1 shows, all reported values of carrier concentration are greater than n_c. Hence all ITO films are expected to be degenerate in nature. Once the material becomes degenerate, the mutual exchange and coulombic interactions shift the conduction band downwards and the valence band upwards effectively narrowing the band gap. The bandgap increase by the Moss-Burstein shift is partially compensated by this effect. The reported value for the refractive index of ITO is 1.96 [246]. The transmittance of ITO films is also influenced by a number of minor effects which include surface roughness and optical inhomogeneity in the direction normal to the film surface. Inadvertently grown dark brown (effectively translucent) metallic films of ITO have also been reported. This opaqueness has been attributed to unoxidised Sn metal grains on the ITO surface as a result of instability due to absence of sufficient oxygen during deposition [207, 215].

CHAPTER 2

Preparation methods and growth process of thin films

2.1 Brief outline of different methods of thin film Preparation:

A large number of techniques have been successfully utilized to prepare solid thin films. However the methods of preparation of thin films may be divided essentially into four groups viz,

(i) Physical vapour deposition(PVD)

(ii) Sputtering

(iii) Chemical vapuor deposition(CVD)

(iv) Chemical deposition

2.1.1 Physical vapour deposition

Physical vapour deposition is the most common technique used for deposition of metal, alloy and many compound films. The primary requirement for the method is to achieve a vacuum of 10^{-5} torr or better. In this method the material evaporates or sublimates in vacuum due to thermal energy (resistive heating) and then the vapor steam of atoms or molecules condenses on a cooler substrate so as to form a continuous and adherent deposits of desired thickness [253]. Physical vapour deposition can be achieved by a variety of methods like thermal evaporation, electron beam evaporation, radio frequency induction heating, laser beam evaporation, molecular beam epitaxy (MBE), activated reactive evaporation (ARE), electron gun heating etc [254-256].

Multicomponent alloys or compounds which tend to distill fractionally may be evaporated by flash evaporation [257-259], in which fine particles or powder of the material is dropped continuously onto a hot boat or surface so that numerous discrete evaporations may occur to form the film on a substrate.

2.1.2 Sputtering:

Sputtering is a process of ejection of atoms from the surface of a material by bombardment with energetic particles. In this process the substance to be deposited (target) is kept in the form of an electrode (whose surface atoms (or molecules) are ejected by momentum transfer from the bombarding ions. The ejected or sputtered atoms are allowed to condense on a substrate to from a thin film. If the ejection is due to bombardment by positive ion, the process is known as cathodic sputtering. The ions required for bombardment is usually obtained by maintaining a glow discharge due to an applied electric field within the vacuum chamber. Over the years various sputtering techniques have been developed. The techniques are reactive sputtering, R-F sputtering, triode sputtering, ion plating, magnetron (direct and reactive) sputtering, ion beam sputtering etc [260-262].

2.1.3 Chemical Vapour Deposition (CVD):

The deposition of thin film from gaseous phases by thermal decomposition or chemical reactions on substrates at high temperature is known as the CVD process. The basic principle involves decomposition or partial dissociation of the vapour phase species and their subsequent deposition on substrates or reactions amongst the vapour species in a neutral atmosphere or otherwise and the deposition of the products. Sometimes a carrier gas is also introduced either to control the rate of reaction or to prevent undesired reactions at the prevailing elevated temperature. Again the CVD process is achieved by a variety of techniques viz thermal decomposition, vapour phase reaction, vapour transportation method etc [263-265].

2.1.4 Chemical deposition:

In chemical deposition method, thin films are deposited on the substrate from aqueous solution either by passing a current or by chemical reaction under appropriate conditions. Large or small and even or uneven surfaces of all types – conducting or insulating can be coated with relative ease by this cost effective method. The electrodeposition, spray pyrolysis, closed space sublimation (CSS), anodization, solution growth, screen printing etc. are different chemical deposition techniques normally used for the deposition of thin films [263-265].

2.2. Choice of deposition process

The ideal deposition process of thin film should meet the following functional criteria: (i) capability of deposition of any material, metal, alloy, simple or complex chemical compounds, (ii) ability to form crystalline or amorphous deposits, (iii) retention of the stoichiometry in compounds, (iv) good growing power, (v) reliable adhesion to different substrates, (vi) variability of residual stress and concentration of defects (line, point, area or volume), (vii) ability to deposit over a wide range of deposition parameters, (viii) ability to control the structural parameters like residual stress, dislocation density, and (ix) ability to control deposition parameters such as deposition temperature, deposition rate, thickness etc.

All the deposition methods have their inherent advantages and limitations. Hence the choice of certain deposition technique for some application is to be made very carefully.

The most of the above criteria can be met in the method of thermal evaporation in vacuum. The simplicity and versatility of vacuum evaporation to obtain materials of desired qualities particularly for the fabrication of devices on insulating substrates are some advantageous attributes of thermal evaporation method. The thermal evaporation technique has been most extensively used for the preparation of thin layers of photoconductors.

For preparation of compounds and alloys of widely different vapour pressure, co-evaporation i.e., simultaneous evaporation of their components from different sources are carried out. For preparation of semiconductor films and in particular II-VI semiconductors, vacuum methods utilizing evaporation and sputtering, continue to receive acceptance from workers interested in exploring the physical properties and fabricating various devices for different needs of science and technology. In the present investigation, considering all these factors, the thermal evaporation technique was adopted to prepare samples of semiconducting films and junctions.

2.3 Mechanism of thermal evaporation process

In the thermal evaporation process, the material to be evaporated is heated by means of resistive or RF induction heating to transform it into vapour. During heating when some surface atoms acquire thermal energy sufficient to break bonds with other surface atoms then they leave the surface as vapour. The heat of vapourization (ΔH_θ) is the energy that removes the atoms from the bulk substance. Atoms after leaving the

parent material, posses only kinetic energy, which on average is 3/2 kT per atom, where T is the ambient temperature inside the vacuum chamber.

Since vapour obeys ideal gas law at low pressures and ΔH_θ varies only slightly with temperature (i.e. approximately constant) the vapour pressure P_θ can be expressed from Clapeyron-Clausuis equation as

$$\ln P_\theta = Const - \frac{\Delta H_\theta}{RT} \qquad (2.01)$$

where, R = gas constant. When the evaporating molecules are immediately removed so that none returns to the parent material, the rate of evaporation is given by Langmuir expression [266]

$$G = CP_\theta \sqrt{M / T} \qquad (2.02)$$

where M = molecular weight, C = Constant.

The evaporation rate is lowered by the contaminants present on the evaporant. Estimation of vapour pressure of materials at high temperature is usually made from evaporation rate. To achieve reasonable evaporation rate, the evaporation is to be typically carried out by heating the material to be evaporated until its vapour pressure is 10^{-2} torr. Combining equations (2.01) and (2.02), the rate of change of evaporation rate with temperature change can be estimated by

$$\frac{dG}{G} = \left(2.303 \frac{B}{T} - \frac{1}{2} \right) \frac{dT}{T} \qquad (2.03)$$

where $B = \Delta H_\theta / 2.303R$. In case of metals $2.303B/T$ is in the range of 20 to 30 which indicates large change in evaporation rate for small change in temperature. Thus to achieve desired evaporation rate, accurate temperature control is necessary.

In conventional vapour deposition, the vapourised atoms obey Boltzmann distribution of thermal energies (0.01eV – 1eV) with most atoms reaching the substrate with less than 0.2eV. The structure and properties of vacuum deposited films are mainly governed by the available energy per condensing atom.

In case of thermal evaporation of multicomponent alloys or compounds the compounds may evaporate at different rates with different vapour pressures. Assuming Rault's law of dilute solutions to be applicable, Holland applied equation (2.01) to derive the ratio of evaporation rates of components A and B in the binary alloys [267].

$$\frac{G_A}{G_B} = \frac{W_A P_A}{W_B P_B}\sqrt{M_A / M_B} \qquad (2.04)$$

where W_A and W_B are the weight concentrations of the compounds and P_A and P_B are their respective vapour pressures in the pure state. As the vapourised atoms move from the source to the substrate, they collide with each other and with the residual gas molecules of the chamber. A fraction, N_1/N_0 (say) of the initial number of vapourised atoms, N_0, will collide at distances less than a path length, d, such that

$$\frac{N_1}{N_0} = 1 - \exp\left(-\frac{d}{L}\right) \qquad (2.05)$$

where, N_1 is the number colliding atoms and L is the mean free path. Applying this equation W.L Bond showed that when L is equal to the source to substrate distance d, 63 percent of the atoms will collide and when $L = 10d$, only 9 percent of the atoms will collide [268]. Therefore, the mean free path must be considerably greater than source to substrate distance in order to ensure a straight line path for most of the emitted vapour atoms. The mean free path L, of the air molecules can be expressed as

$$L = \frac{(5.985 \times 10^{-3})}{P} meter \qquad (2.06)$$

where P is the pressure in Pascal. If the residual medium is air and residual pressure, $P = 6.65 \times 10^{-3}$ Pa ($= 5 \times 10^{-5}$ torr), the value of L from (2.06) is equal to 90 cm. For such a value of mean free path to ensure the rectilinear motion of vapourized atoms, the source to substrate distance should be 6 to 9 cm. Due to rectilinear motion of vapourized atoms or molecules it is possible to put a mask between the source and the substrate to obtain a sharp pattern of the thin films.

2.4 Processes of formation of thin film:

The important processes involved in the formation of thin film are condensation, nucleation and growth on the substrate. Transformation of a substance from its vapour phase to the liquid or solid phase is called condensation, which in this case is initiated by the formation of small clusters or nuclei through combination of several incident atoms adsorbed on the substrate to form finally a coherent film is termed as growth.

2.4.1 Condensation:

Thermodynamically, for condensation to occur on a substrate, the partial vapour pressure in the gaseous phase should be equal to or greater than its vapour pressure in the condensed phase at the same temperature. If the substrate material is different from the vapour material, the impinging vapour atoms are first adsorbed on the surface of the substrate and condensation is initiated by the formation of small clusters of the adsorbed atoms. These small clusters then act as the initial centers of condensation. The process can be visualized as follows:

The impinging vapour atoms on approaching the substrate surface within a few atomic diameters come under the influence of the field of force of the surface atoms of the substrate and then several interactions may follow. They are: (1) an impinging atom may be reflected almost instantly retaining most of its kinetic energy, (2) there may be physical adsorption of vapour atoms under influence of Van der Waals force of the substrate atoms, (3) there may be chemical adsorption due to force of the type forming chemical bond between a vapour atom and a substrate atom, (4) impinging atom may form immediate association with other atom or atoms already adsorbed after finite stay time, or it may strike to the surface of the substrate and then migrate literally to join a cluster of adsorbed atoms. Adsorption of incident vapour atom is possible only when there is thermal accommodation with the substrate atoms. If the kinetic energy of an incident atom is less than the energy of desorption, the thermal accommodation takes place by giving up its excess kinetic energy through lattice vibration of the substrate and the atom is adsorbed. Under appropriate conditions, when the rate of adsorption becomes greater than the rate of desorption, the small clusters (consisting of monomers) begin to enlarge, leading to stable nucleation and growth. Several workers [269-271] have studied condensation phenomena experimentally.

2.4.2 Nucleation and Growth:

In the process of depositing thin film on a substrate the first stage is the formation of adsorbed monomers of one or more atoms which in the second phase, under the action force similar to surface tension, or capillarity combine to form small clusters. These clusters like the monomers are not stable and likely to be desorbed unless they attain a certain critical size corresponding to a particular temperature of

the substrate. On reaching a critical size, they continue to grow forming stable condensates.

Several theories are proposed to explain the formation of critical clusters leading to the growth of stable condensates. Out of all these, the two principal theories are the capillarity model and the atomistic model [272].

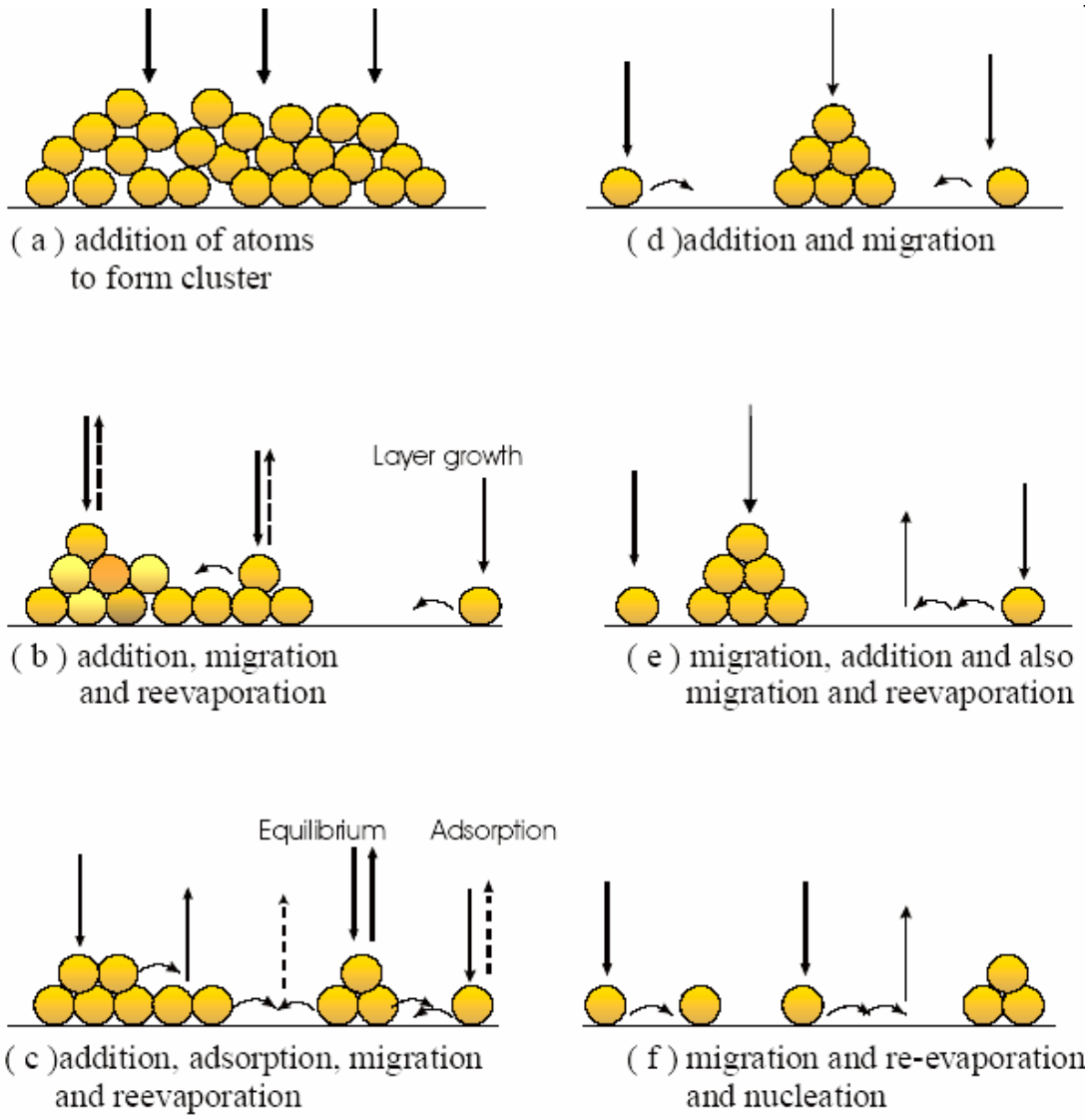

Figure 2.01: A Schematic diagram of growth process from vapour phase by different steps

Capillarity model [273] predicts that the free energy of a cluster passes through a maximum as it increases in size, and this maximum of free energy corresponds to the critical size of the cluster, which becomes stable above this critical

size, but may re-evaporate below this critical size. This is similar to the process of formation of liquid droplets from vapours as explained by classical capillarity theory. Thus in order to condense a permanent deposit, aggregates of critical size or larger have to be created first. Critical nuclei can grow to super critical size either by direct incorporation of impinging atoms from the gaseous phase or by incorporation of the adsorbed monomers diffusing over the surface of the substrate. In the latter process, the rate at which the critical nuclei grow is given by the initial number of nuclei per unit area of the substrate and the rate at which the adsorbed monomers diffuse to join them. Capillarity model of the theories of nucleation enables one to evaluate free energy of formation of cluster of critical size and shows as to how the critical size and nucleation rate depend on the substrate temperature, impingement flux and the nature of the substrate.

The atomistic or small cluster model of the theories of nucleation [274] is most identical with the capillarity model. In this case emphasis is given not on the free energy but on the dissociation energy of a critical cluster under specific condition of super saturation, and then the rate of nucleation corresponding to such a critical cluster is computed, leading to an expression involving parameters like number of monomers in the critical cluster, activation energy for desorption, activation energy for diffusion, substrate temperature, etc. The important prediction to be noted in this theory is that if the size of the critical nucleus changes by even one atom with super saturation, a discontinuity will occur in the nucleation rate versus temperature curve, and this may be verified experimentally.

Lewis [275], comparing the results of nucleation process derived from capillarity and small cluster models, shows that the fundamental concepts underlying the two models are identical. The essential difference between them is that the small cluster model uses discrete arrangement of atoms where as the capillarity model uses simple geometrical shapes of the clusters.

Experimental tests as to the validity of the nucleation theories have been made by several workers [276] by different techniques. The best of among them were the direct observations of the cluster formation and their growth in the electron microscope [277, 278]. The prediction of the nucleation theories, in general have been found to be true even through relatively crude experimentations. However, the observations have revealed distinct stages of film growth leading to a continuous film.

These stages are: (1) nucleation and island formation, (2) coalescence of islands, (3) channel formation and (4) formation of continuous film.

The existence of nuclear barriers as predicted by nucleation theories favours the formation of islands in the initial stage of film growth. When the nucleation barrier is large, a few large islands are formed initially, which persist up to relatively high average film thickness, resulting in the formation of a coarse grained film. Under the small nucleation barrier, large number of islands is formed, which becomes continuous at relatively low average film thickness and finer grained film is obtained.

As the deposition is continued, the islands grow in their sizes and come to each other. The large islands appear to grow by coalescence of smaller islands and the island density decreases monotonically. Surface diffusion is predominant for mass transfer between the islands during coalescence. Shape and area of an island, which has just been formed by coalescence, change during and after coalescence. According to Pashley et al. [279] the driving force for the coalescence process is provided by the change in the surface energy.

As the islands continue to grow by coalescence, change of shape still occurs particularly in the vicinity of the junction of islands and consequently islands become elongated and flatten to increase surface coverage. They join to form a network in which the deposited material is separated by long, irregular and narrow channels. Occasionally, the channels are uniformly wide, homogeneously distributed and possess approximately matching curvature over small area.

The channels are the uncovered area of substrate. The final stage of the growth is to fill these empty channels by considerable deposition and as such this is a slow process. If the uncovered surface area of the channels is large, secondary nuclei are formed in the channels with the progress of deposition and they grow coalescence and fill in as before and the film becomes continuous.

The growth sequence discussed above was first deduced by Andrade [280] and was found in remarkable agreement with electron microscopic observations [281]. In the case of polycrystalline layers, the coalescing pairs of islands have randomly distributed relative orientations.

2.5 Factors affecting the growth, structure and film properties:

Various factors affect the growth, structure and properties of a deposited film. They are: (i) nature of the substrate, (ii) substrate temperature, (iii) source temperature, (iv) presence of gas inside the chamber, (v) annealing, (vi) contamination by impurities and presence of defects on the substrate surface, (vii) presence of electrostatic charges etc.

The temperature of the substrate and thickness of the film are two very important parameters affecting its properties. The mobility of the just deposited adatoms on the substrate surface can be enhanced by increasing the temperature of the substrates during the deposition process. Higher mobility of the adatoms give the adatoms more chance to grow together in ordered manner leading to formation of thin films with large crystallites. Low mobility on the other hand leads to the formation of a film of amorphous nature. If the substrate is the face of a single crystal, periodic forces of cohesion induce an oriented growth called the epitaxial growth. Thus a thin film can be deposited in crystalline, polycrystalline and amorphous form.

CHAPTER 3

Theoretical Background

In this chapter, theoretical background related to the present work and required relations for calculating different parameters of the samples studied have been briefly discussed. Theories used for the studies of structural properties, electrical and optical properties of semiconducting films, and junctions are described.

3.1 STRUCTURAL PROPERTIES

In crystalline solids, atoms can be imagined to be orderly arranged in different set of equidistant parallel planes denoted by indices ($h\ k\ l$). When a beam of X-ray is allowed to pass through this solid, diffraction takes place when they satisfy the Bragg's law, given by

$$2d\sin\theta = n\lambda \qquad (3.01)$$

where, n is an integer, d is the inter-planar spacing of a particular set crystal plane, λ is the wave length of the incident X-ray and θ is the angle makes by the incident ray with the plane called angle of diffraction. It is obvious that the direction X-ray diffraction by a particular set of crystal planes and hence the X-ray diffraction pattern is determined by the inter planner distance. On the other hand intensities of the beams diffracted by the properly set planes are determined by the way in which the atoms are distributed in the unit cell. Thus structural information of the crystal is derived from knowing diffraction direction and information regarding arrangement of atoms is derived from intensity measurement.

From X-ray diffraction (XRD) study, information about lattice parameters, orientations of crystal planes, grain size, structure (i.e. epitaxial, polycrystalline, amorphous etc), composition (with the help of standards), defects and stress and strain in thin films can be studied [140-142].

3.1.1 Lattice constant

The lattice constant or lattice parameters are the crystallographic characteristics of a crystal lattice, which refer the distances of the neighboring unit cells in three dimensions. The inter-planar spacing '*d*' of a set of crystal planes is dependent on lattice parameters and the miller indices (*h*, *k*, *l*) of that plane. For cubic lattice, the lattice parameter '*a*' can be evaluated from the relation [282]

$$a = d\left(h^2 + k^2 + l^2\right)^{1/2} \qquad (3.02)$$

Accurate measurement of lattice parameter is necessary for the crystallographic characterization of thin films. There are several possible sources of error as described by many workers like divergence of the X-ray beams, refraction and absorption of X-rays by the specimens etc in the measurement of θ hence the *d* values. So the accuracy of determination of lattice constant is dependent upon the accuracy in measurement of *d*. Since from Bragg's law (for 1st order diffraction, *n*=1),

$$d = \frac{\lambda}{2}\operatorname{cosec}\theta$$

$$\delta d = -\frac{\lambda}{2}\left(\operatorname{cosec}\theta\cot\theta\right)\delta\theta$$

therefore for $\theta = \pi/2$, $\delta d/d = 0$.

Hence, the most accurate value of lattice parameters can be estimated from the Nelson-Riley plots when $\theta = \pi/2$. The Nelson-Riley curve is plotted between calculated lattice constant "*a*" for different planes and the error function [283],

$$f(\theta) = \frac{1}{2}\left(\cos^2\theta/\sin\theta + \cos^2\theta/\theta\right) \qquad (3.03)$$

The intercept of this plot with x-axis gives the corrected value of lattice constant.

3.1.2 The grain sizes

A very important structural parameter of a thin film is the size of the crystallites. It is found that crystallite size of thin film has some dependence on deposition parameters, particularly rate of deposition and substrate temperature. If $\beta_{2\theta}$ is the width of the diffraction line at the half of the maximum peak intensity (FWHM) for the diffraction angle θ, then according to Scherrer's formula, the average grain size D_{hkl} of the films for most preferred plane (*hkl*) [prominent diffraction peak] will be[284],

$$D_{hkl} = \frac{K\lambda}{\beta_{2\theta}\cos\theta} \qquad (3.04)$$

where, λ is the wavelength of X-ray used, K is the proportionality constant which is taken as 0.99.

3.1.3 Average stress and strain

Thin films are almost invariably in a state of stress. The lattice strain and stress are developed in the films due to some factors like substrate temperature, change of state from bulk to film etc. The total stress is composed of a thermal stress and intrinsic stress. The thermal stress is due to the difference in the thermal expansion coefficient of the film and the substrate material. The intrinsic stress is due to lattice mismatch between the film and the substrate and also due to the accumulating effect of the crystallographic flaws that are built in the film during deposition. The stress is also considered to be related to the film deposition conditions, compositions and structures of the films. It is difficult to avoid thermal stress for films deposited at any substrate temperature (T_s). Even at room temperature some heating of the substrate takes place during evaporation and condensation process at the time of film deposition. Again the crystal lattice is not perfect in thin film and intrinsic stress develops as it relaxes. The average internal stress developed in the films is calculate by using the relation [285],

$$S = \frac{E}{2\nu}\left[\frac{(a_0 - a)}{a_0}\right] \qquad (3.05)$$

where, a_0 and a are the lattice parameters of the material in bulk and in thin film form. E and ν are the Young's modulus and Poisson's ratio of bulk sample. Here 'a' refers to the lattice parameter perpendicular to the film plane. The origin of the strain is also related to lattice misfit, which in turn depends upon the growing conditions. The micro strain (ε) developed in thin film along different preferred orientations are calculated from the relation [286, 287]

$$\varepsilon_{hkl} = \frac{\beta_{2\theta}\cot\theta}{4} \qquad (3.06)$$

3.1.4 Average grain size and strain from Williamson and Hall relation:

The strains are always present in the thin film samples due to various reasons and they contribute to the broadening of the X-ray diffraction peaks. Considering the entire broadening of a diffraction profile to be due to simultaneous contributions from both particle size and strain, Williamson and Hall developed the following relation for the corrected value of full width at half of the maximum (β) of a broadened profile (for Cauchy nature) [288, 289],

$$\beta = \frac{\lambda}{D\cos\theta} + 4\varepsilon\tan\theta$$

$$\text{or, } \frac{\beta\cos\theta}{\lambda} = \frac{1}{D} + 4\varepsilon\frac{\sin\theta}{\lambda} \qquad (3.07)$$

where, D is the average grain size and ε is the average strain developed in the film.

For the multiple ordered diffraction pattern of a sample, for each peak found at different 2θ, β values are different. Now, when $\frac{\beta\cos\theta}{\lambda}$ versus $\frac{2\sin\theta}{\lambda}$ is plotted, according to above relation (3.07), it will be a straight line (called Williamson and Hall plot). Therefore, the y-intercept of the linear plot will give the average grain size (D) and the slope of this plot will give the average strain (ε) of the sample [290].

3.1.5 Dislocation density

The imperfection of crystallographic structure or lattice defects called dislocation occurs when the periodicity of atomic lattice array is interrupted along certain directions in the crystal. In polycrystalline thin films, on coalescence, dislocations are incorporated at the boundary of the two islands. Dislocations may be formed because of point defect aggregation during growth and an interface misfit-dislocation network may be set up to relieve strain at the film-substrate interface. The density of dislocations is the number of dislocation lines that intersect a unit area in the crystal. The average dislocation density ρ_{hkl} of a thin film can be evaluated making use of the values of grain size, average microstrain and lattice constants in to the relation [291]

$$\rho_{hkl} = \left(\frac{3nk\varepsilon^2}{D^2 b_{hkl}^2 F} \right)^{1/2} \qquad (3.08)$$

where n is the number of dislocations in a pile up, k is a constant depending upon strain contribution function, b_{hkl} is the Burgers vector of dislocation along different preferred orientations and F is the interaction parameter. De et al [142] modified the above formula for vacuum evaporated II-VI thin films, considering $n = F$, k = 18.8, 24 and16.1(for Gaussian, Cauchy and intermediate parabolic case respectively) [142] and $b \approx d_{hkl} = a/\sqrt{h^2 + k^2 + l^2}$, for cubic zincblende structure of II-VI thin films, the dislocation density along the most preferred directions are given by

$$\rho_{hkl} = \frac{m\varepsilon}{aD} \qquad (3.09)$$

where m is any constant and a is the lattice parameters of semiconductor thin films along different preferred orientations. The value of m is 15, 24 and 28 for (111), (220) and (311) planes respectively.

3.2 SEMICONDUCTOR THEORY

3.2.1Conductivity of Intrinsic Semiconductor

Due to thermal agitation and lattice vibration, some of the covalent bonds in a semiconductor are broken and some electrons become free. In the energy band theory concept, electrons in the valence band (bound electrons) on receiving appropriate energy get excited to the conduction band and become free. The two energy bands are separated by an energy gap E_g. When an electric field is applied, the free electrons in the conduction band drift towards the positive electrode and hence constitute the current. Similarly, the absence of an electron from a bond in the valence band, known as hole, constitutes a net positive charge. This hole moves towards the negative electrode constituting the current.

The total conductivity in intrinsic semiconductor due to the combined effect of free electrons and holes is

$$\sigma=e(n_e\mu_n+ n_h\mu_h)=en(\mu_n+ \mu_h) \qquad (3.10)$$

where, μ_n is the mobility of electron, μ_h is the mobility of hole, n_h is the density of holes in valence band and n_e the density of electrons in conduction band, and for intrinsic semiconductor $n_e=n_h=n$.

The density of electrons in conduction band is given by [292]

$$n_e = 2\left(\frac{2\pi m_e^* k_B T}{h^2}\right)^{3/2} \exp\left[\frac{(E_F - E_c)}{k_B T}\right] \qquad (3.11)$$

The density of hole in valence band is [292]

$$n_h = 2\left(\frac{2\pi m_h^* k_B T}{h^2}\right)^{3/2} \exp\left[\frac{(E_v - E_F)}{k_B T}\right] \qquad (3.12)$$

where, m_e^* and m_h^* are the effective mass of electron and hole respectively, E_F, E_v and E_c are the energy of Fermi level, top of the valence band and bottom of the conduction band respectively and k_B is the Boltzmann constant and T is the absolute temperature .

The Fermi level is given by,

$$E_F = \frac{E_c + E_v}{2} + \frac{3}{4}kT \ln \frac{m_h^*}{m_e^*}$$

This means that for intrinsic semiconductor if $m_e^*=m_h^*$, the Fermi level lies exactly half way between the top of valence band and bottom of conduction band at T=0K.

In terms of band gap energy, the density of carriers ($n=n_e=n_h$) in a band is given by,

$$n = 2\left(\frac{2\pi k_B T}{h^2}\right)^{3/2}\left(m_h^* m_e^*\right)^{3/4}\exp\left(\frac{-E_g}{2k_B T}\right) \qquad (3.13)$$

and the conductivity of an intrinsic semiconductor is given by [293]

$$\sigma = 2\left(\frac{2\pi k_B T}{h^2}\right)^{3/2}\left(m_h^* m_e^*\right)^{3/4}\exp\left(\frac{-E_g}{2k_B T}\right)e\left(\mu_h + \mu_e\right) \qquad (3.14)$$

The mobilities of electrons and holes are influenced by scattering. The main sources of scattering in semiconductor are phonons and ionized atoms (mainly donors and acceptors). Other defects such as dislocations also contribute towards scattering but to lesser degree. If we consider electrons and holes to behave in a similar way and scattering from the charged defects is negligible. Then major scattering is due to phonon only. In that case, mobility $\mu \propto T^{-3/2}$ [294] and the relation (3.14) becomes,

$$\sigma = \sigma_0 \exp\left(\frac{-E_g}{2k_B T}\right) \qquad (3.15)$$

where, σ_0 is a constant.

3.2.2 Extrinsic Semiconductor

n-type Dopant or donor impurity

In the case of Si, n-type doping involves doping by a pentavalent impurity (Si is tetravalent) like P or As. They are also called donor atoms as they donate a free electron to the semiconductor. The majority carriers in this type of doping are electrons. II-VI semiconductors like ZnSe, CdTe, CdS can be doped n-type by adding any element of group III or VII to these semiconductors. In an n-type semiconductor, the Fermi level lies closer to the conduction band because of higher concentration of electrons than that of holes.

p-type Dopant or acceptor impurity

In the case of Si, p-type doping involves doping by a trivalent impurity like B (boron) or Al. They are called acceptor atoms as they accept electrons. The majority carriers in this type of doping are holes. II-VI semiconductors like CdTe, CdS can be doped p-type by adding any elements of group I or V to the semiconductor. In a p-type semiconductor, as there is a low concentration of electrons than that of holes, the Fermi level lies closer to the valence band.

In n-type semiconductor of donor concentration N_d, the density of electrons in the conduction band is [294]

$$n_e = (2N_d)^{1/2}\left(\frac{2\pi m_e^* k_B T}{h^2}\right)^{3/4} \exp\left[\frac{\Delta E}{2k_B T}\right] \qquad (3.16)$$

where, $\Delta E = E_c - E_i$ is the ionization energy also called activation energy.
Similarly, for p-type semiconductor, the density of holes is [294]

$$n_e = (2N_a)^{1/2}\left(\frac{2\pi m_h^* k_B T}{h^2}\right)^{3/4} \exp\left[\frac{\Delta E}{2k_B T}\right] \qquad (3.17)$$

here, $\Delta E = E_i - E_v$ and N_a is the acceptor concentration.

3.2.3 Temperature dependence conductivity of semiconductors

In a high purity semiconductor in which no donor or acceptor level occurs at 0^0K, the valence band is full and conduction band is empty. The Fermi level lies midway between the two i.e., $\frac{1}{2}E_g$ [295, 296]. As temperature is raised the electrons are excited into the conduction band, and then if the density of states at the bottom of the conduction band is equal to that at the top of the valence, E_F will remain in the middle of the gap. If however, density of states is not same for two bands then E_F will move to higher or lower energies as T is raised.

For an n-type semiconductor, if donor states be at an energy E_d above the valence band, then at 0^0K all the states up to E_d are filled and all states above E_d are vacant. Thus E_F will lie midway between the donor level and bottom of the conduction band i.e., at $\frac{1}{2}(E_d + E_c)$. In this case, however since density of states will not remain same for the donor level as well as for conduction band, when temperature is increased, the Fermi level will not remain constant.

As temperature is increased E_F shifts slowly downwards and cross the donor level. At sufficiently high temperature all the donors will be ionized and most of the electrons in the conduction band are excited from the valence band just as in intrinsic semiconductor. An analogous situation occurs for p-type semiconductor also.

At low temperature, the majority carrier concentration in an n-type semiconductor is a strong function of temperature, determined essentially by the ionization of the dopant impurities i.e. by the position of E_F.

The expression (3.15) is generally utilized to obtain the activation energy of impurity semiconductor [294] from its logarithm of conductivity versus $1/T$ curve. At

higher temperature the donor levels may be exhausted or acceptor levels saturated, since these levels generally contain fewer state than either in conduction or valence band. The carrier concentration then becomes insensitive to temperature. At sufficiently high temperatures electrons are excited from valence to conduction band in large numbers since sufficient energy is available for that. The equal quantities of electrons and holes are liberated and exceed by far the limited number of extrinsic carriers. The conduction therefore becomes intrinsic. At this range the slope of $\ln\sigma$ vs$1/T$ curve as per relation (3.15) will give the value of forbidden energy gap.

3.3 OPTICAL PROPERTIES OF SEMICONDUCTOR

3.3.1 Optical absorption

An Important technique for measuring the band gap energy of a semiconductor is the measurement of transmission (or absorption) of incident photons by the material. In this case photons of selected wave length are directed at the sample, and relative transmission of the various photons is observed. Since photons with energies greater than the band gap energy ($h\nu \geq E_g$) are absorbed while photons with energies less than the band gap are transmitted, the measurement of transmitted (or absorbed) photon can give the band gap energy of the semiconductor.

In semiconductor optical radiation is absorbed by inducing excitation from one level to higher one provided that the frequency of radiation ν is such that $h\nu$ is equal to or greater than the energy difference between the two concerned levels. The dependence of , the intensity of radiation *I,* transmitted through the semiconductor of thickness '*d*' is of the form [297]

$$I = I_0 \exp(-\alpha d) \qquad (3.18)$$

where I_0 is the initial intensity of radiation and α is the absorption coefficient.

There are four main types of transition which can be induced by radiation: (a) Intrinsic absorption, (b) free carrier absorption, (c) Localized states absorption and (d) Lattice absorption.

Out of all above processes of absorption, the excitation of electron from valence to conduction band contributes directly to intrinsic absorption. The carrier absorption occurs from the excitation of free carriers in the valence or conduction band into vacant states of higher energy within the energy band. The localized state occurs due to presence of impurity levels within the energy gap. Electrons and holes bound to the localized states (impurity levels) can be excited to the conduction and valence bands as well as to higher bound states by radiation of smaller energy than that needed to create free carriers intrinsically. The interaction of optical radiation with lattice vibration results in lattice absorption and is ascribed to phonon interaction.

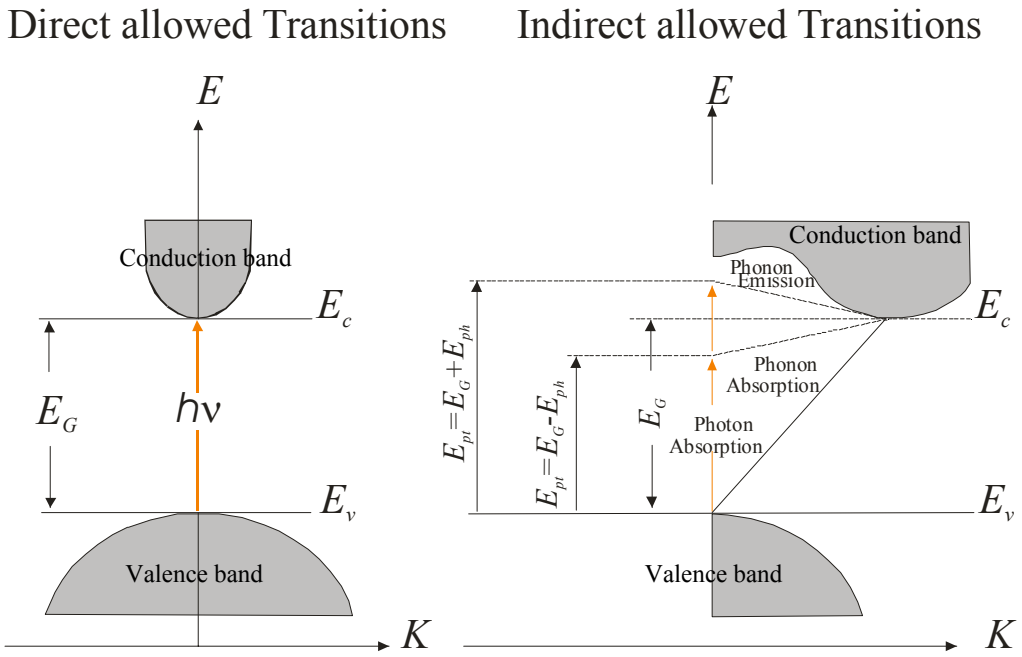

Figure 3.01 Schematic diagrams of energy levels of semiconductor illustrating (a) direct and (b) indirect transitions

frequency of electromagnetic radiation, n is the index of refraction and c is the velocity of light. When only photon of frequency ν takes part in the two transitions, say at k and k', then for momentum conservation,

$$\Delta k = k' - k = \frac{2\pi n \nu}{c} \qquad (3.19)$$

Comparing Δk with the value of $k_{max}=\pi/a$ and assuming that the energy is conserved approximately for both the transitions, the energy difference involved being just $\Delta E=h\nu$, we get,

$$\frac{\Delta k}{k_{\max}} = \frac{2\nu n a}{c} = \frac{2na\Delta E}{hc} \qquad (3.20)$$

For a typical value of n, a and E, it can be shown that the momentum of a photon can be effectively neglected and the allowed transition involving photon only is represented by a vertical line between the valence and conduction band (Fig 3.1(a)). In the direct band gap semiconductor where the maximum of valence band and minimum of conduction band occur at the same point (at k=0), the vertical transition takes place at this point.

In some cases conduction band minimum and valence band maximum occur at different k values. In such cases there is not only the possibility of direct transition (Δk=0) but also of an indirect transition ($\Delta k \neq 0$). Indirect transition involves the interaction of lattice with photon and is accompanied by absorption or emission of a phonon. Since both energy and momentum conservation laws must hold in indirect transition, we must have for the conservation of momentum,

$$k_{ph} = k_f - k_i$$

where, k_{ph} is the momentum vector of the phonon and k_f and k_i are the k vectors for final and initial states of the transition, respectively. For conservation of energy,

$$E_g = E_{pt} \pm E_{ph} \qquad (3.21)$$

where, E_{pt} and E_{ph} are the energy of photon and phonon respectively and E_g is the energy band gap. The plus sign is for phonon absorption and minus sign for emission.

The absorption coefficient for direct transition usually reaches values from 10^4 cm^{-1} to 10^5 cm^{-1}, whereas the absorption coefficient for indirect transition is usually from 10 cm^{-1} to 10^{-3} cm^{-1}.

For allowed transitions the following dependencies are expected,
For direct transition,

$$\alpha \propto (h\nu - E_g)^{1/2} \qquad (3.22)$$

For indirect transition, omitting phonon energy,

$$\alpha \propto (h\nu - E_g)^2 \qquad (3.23)$$

In actual practice, for allowed transition for example if α^2 is plotted against photon energy, a straight line for direct transition will be obtained. The intercept on the energy axis gives the band gap of direct band gap semiconductor. Again if $\alpha^{1/2}$ is plotted against photon energy, a straight line for indirect transition will be obtained. As phonon has to be accounted for, two straight lines are usually obtained for indirect transition. Thus two intercepts can be drawn; one corresponding to (E_g+P_{ph}) and other corresponding to (E_g-P_{ph}) [298].

3.3.2 Optical Constants of thin films

The optical behaviour of thin films deals primarily with optical reflection, transmission and absorption properties and their relations to the optical constants of

the films. Optical constants describe how light propagates through a film. In simple terms, the electromagnetic field that describes light traveling in x-direction through a material of refractive index '*n*' is given by [299]

$$E_x = E_{0x}\exp[i\omega\{nx/(c-t)\}]\exp(-\omega kx/c) \qquad (3.24)$$

where, *k* is the extinction coefficient also known as the imaginary part of the complex refractive index of the medium. The optical behaviour of a material is generally utilized to determine its optical constants such as complex refractive index ($n^*=n-ik$), real part of complex refractive index(*n*), imaginary part of complex refractive index (*k*), absorption coefficient(α) and dielectric constant(ε) of the films. Real part of refractive index '*n*' is related to important physical properties of the semiconductor, for example the reflectance spectrum, which in turn is connected with the band structure [300]. Also the knowledge of this parameter is important for thin film semiconductors such as multilayer structures and antireflection coatings. From equation 3.24, it is seen that the wave is attenuated by $exp(-\omega kx/c)$. The attenuation of the intensity is thus given by $exp(-2\omega kx/c)$. The absorption coefficient 'α', defined by relative decrease of intensity per unit distance in the propagation direction through $I=I_0exp(-\alpha x)$ is then given by

$$\alpha = \frac{2\omega k}{c} = \frac{4\pi k}{\lambda} \qquad (3.25)$$

where λ is the wave length of the incident light.

3.3.3 Determination of the optical constants of thin films

Different methods were developed by different workers to determine the optical constants *n*, *k* and α for weakly absorbing thin films, from the measurement of transmittance spectrum. A simple straightforward method was developed by Swanepoel [301, 302] on the basis of the method developed by Manifacier et al. [303] which is described below.

For a homogeneous film of uniform thickness '*d*', prepared on a transparent substrate of refractive index '*s*', the transmission for normal incidence, taking into account interference due to multiple reflections at the film-substrate interface, is given by [304],

$$T = \frac{Ax}{B - Cx\cos\phi + Dx^2} \qquad (3.26)$$

where, $A=16n^2s$ $B=(n+1)^3(n+s^2)$

$C=2(n^2-1)(n^2-s^2)$ $D=(n-1)^3(n-s^2)$

$\phi=4\pi nd/\lambda$ $x=exp(-\alpha d)$

The envelopes around the interference maxima (T_M) and minima (T_m) are considered to be continuous function of λ. For the region of weak and medium absorption, the real part of the refractive index 'n' can be calculated at any wave length using the formula,

$$n = \left[N + (N^2 - s^2)^{1/2} \right]^{1/2} \qquad (3.27)$$

where, $$N = 2s\frac{T_M - T_m}{T_M T_m} + \frac{s^2 + 1}{2} \qquad (3.28)$$

and T_M and T_m are the transmission maximum and minimum at the same wave length, one being measured from the spectrum and the other found from the envelope.

With this value of refractive index of the film the 'order' m of the different extremes of the transmission curve is determined with the equation for interference fringes,

$$2nd=m\lambda$$

The values of 'm' are then approximated to the close integer or half integer. These values of m are used to determine the corrected value of refractive index for that wave length, from the same relation.

In the region of strong absorption the interference fringes disappear. The value of n can be estimated by extrapolating the values calculated in the other part of the spectrum.

The absorption coefficient and thereby the extinction coefficient k for the weak and medium absorption region are calculated by using the relation (3.26) $\alpha = \frac{1}{d}\ln\left(\frac{1}{x}\right)$ knowing the value of x from the following relation,

$$x = \frac{\left[G - \left[G^2 - (n^2-1)^6 (n^2 - s^4)^2 \right]^{1/2} \right]^{1/2}}{(n-1)^3 (n - s^2)} \qquad (3.29)$$

where,

$$G = \frac{128n^4 s^2}{T_\alpha^2} + n^2(n^2-1)^2(s^2-1)^2 + (n^2-1)^2(n^2-s^2)^2 \qquad (3.30)$$

and T_α is the interference free transmittance which is the geometric mean of T_M and T_m ie, $T_\alpha = \sqrt{T_M T_m}$

Nearly at the absorption edge, the absorption coefficient (α) is measured by the expression [305],

$$\frac{T_1}{T_2} \approx \exp^{\alpha(d_1 - d_2)} \qquad (3.31)$$

where, T_1 and T_2 are the transmittance for the samples of thickness d_1 and d_2 respectively.

Once the refractive index in the interference region is known, by extrapolation of *n,* the refractive index in the interference-free region can also be calculated using Cauchy's dispersion relation [306],

$$n = A + \frac{B}{\lambda^2} \qquad (3.32)$$

where A and B are constants and can be obtained from the n versus $1/\lambda^2$ plots.

Absorption is a phenomenon of fundamental interest because of its relation to the dynamics of the electrons and ions of the medium under the electromagnetic radiation. An absorbing medium is characterized by a complex dielectric constant followed by relation [307],

$$\varepsilon = \left(\varepsilon' - i\varepsilon''\right) \qquad (3.33)$$

The real and imaginary parts of the dielectric constants of the films ε' and ε'' respectively can be determined from [308],

$$\varepsilon' = n^2 - k^2 \qquad (3.34)$$

and

$$\varepsilon'' = 2nk = 4\pi\sigma/\omega \qquad (3.35)$$

where, ω is the angular frequency of the incident light and σ is the static (dc) electrical conductivity.

3.4 Photoconduction in Semiconductor:

The use of photoconductivity is a powerful tool in understanding the behavior of solid, specially the semiconducting solids. Photoconductivity processes involve the absorption of energy from light quanta, the excitation of charge carriers from a nonconducting ground state to a higher state where they are free to contribute to the electrical conductivity and return of charge carriers from the conducting state to their ground state. When a semiconductor is illuminated, the absorption of light quanta occurs if the photon energy is large enough to raise an electron from the valence band (E_v) into an empty conduction band state (E_c), thereby generating one electron-hole pair. The photon energy needs to be larger than the band gap energy (E_g) to satisfy this condition. The photon is absorbed in this process and the excess energy, E_{ph} - E_g, is added to the electron and the hole in the form of kinetic energy. This leads to the rise of conductivity in the semiconductor. The process disappears as soon as illumination ceases to fall on it. The rise and decay processes in a semiconductor can be explained on the basis of release of new electrons under the illumination with light accompanied by their recombination.

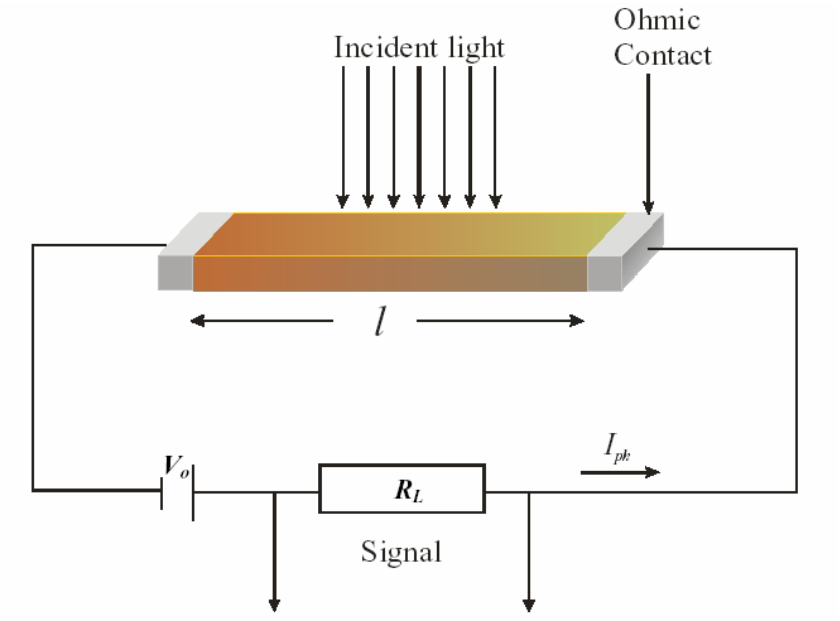

Figure 3.02: Schematic representation of a photo-resistor and the circuit diagram for measurement of photoconductivity.

The internal liberation of electrons under light is known as the intrinsic photoeffect. An additional conductivity acquired by a semiconductor under irradiation is called photoconductivity. The conductivity caused by the thermal excitation of charge carriers is termed as dark conductivity. The devices intended for the detection of radiation by photoconductivity are known as photoresistors. Fig.3.02 shows the schematic arrangement for photoconductivity measurement. The sensitive elements of a photoresistor is a bar or film from a single crystal or polycrystalline semiconductor with two ohmic contacts. The element is connected to a bias source V via a load resistance R_L. The element thickness must be sufficiently large so that the element can absorb the entire power of light. If the requirement is met, the number of carriers (or pairs of carriers in band gap absorption) generated by light per unit time in the sensitive element at $\lambda < \lambda_{max}$ (λ_{max} is maximum wave length of light upto which light is absorbed) is equal to [309],

$$G = W(1-r)\eta/(\hbar\omega) \qquad (3.36)$$

where, W is the incident power of light, r is the surface reflection coefficient, and η is the quantum yield of the intrinsic photo-effect, which determines the average number of electron-hole pairs generated by each absorbed photon. It can be larger than unity if the absorption of one high energy photon gives birth to two or more electron-hole pairs or it can be smaller than unity if a fraction of photons are absorbed by free carriers.

The voltage V applied to the photo-resistor causes the light generated carriers to drift, thereby producing in the circuit a current called photocurrent I_{ph}. This current is easy to determine from the following reasoning. During its life time τ, every charge carrier passes τ/t_{dr} times through the resistor, where t_{dr} is the transit time or more accurately, the drift time of the carrier. It is equal to the length l of the sensitive element divided by the drift velocity v_{dr}:

$$t_{dr} = l/v_{dr} = l/\mu E = l^2/\mu V \qquad (3.37)$$

where μ is known as carrier mobility. The photo current I_{ph} is equal to the number G of carriers generated every second in the semiconductor under the action of light multiplied by τ/t_{dr} and electron charge q:

$$I_{ph} = (qG\tau)/t_{dr} = (qG\tau\mu V)/l^2 = (q\Delta N\mu V)/l^2 \qquad (3.38)$$

where $\Delta N = G\tau$. is the number of excess carriers in the photoresistor. If the light generates a pair of carriers, we should replace μ by the sum of mobilities, (μ_e +

μ_h).Where, μ_e and μ_h are electron and hole mobility respectively. Putting G from (3.36) into (3.38) and using $\hbar\omega = hc/\lambda$ we get

$$I = [W(1-r)q]\eta\tau\mu\lambda V/(hcl^2) \qquad (3.39)$$

The ratio

$$(I_{ph})/W = \{q(1-r)/(hcl^2)\}\eta\tau\mu\lambda V \qquad (3.40)$$

defines the response (responsivity) of a photo-resistor. It is directly proportional to the wavelength of incident light (up to λ_{max}), applied voltage V, carrier lifetime τ, and carrier mobility μ and inversely proportional to the square of length of the photo-resistor's sensitive element.

Rise and Decay of photoconductivity:

The carrier lifetime determines not only the response of a photo-resistor but also its time lag: the response rises with τ, but then the lag also grows. Excess carriers recombine after switching off the light source and their concentration decays by the law [309]

$$\Delta n = \Delta n_0 \exp(-t/\tau) \qquad (3.41)$$

The decay of the semiconductor photoconductivity will proceed by the same law (curve BC of Fig 3.3) [309]:

$$\sigma_{ph} = \sigma_{ph_0} \exp(-t/\tau) \qquad (3.42)$$

where σ_{pho} is the stationary (steady-state) photoconductivity in the conditions of steady illumination of the photo-resistor.

From (3.42) it is apparent that the photoconductivity drop is slower with a longer lifetime of excess carriers, so the time lag of the radiation detector becomes greater.

It is easy to show that the tangent drawn to the photoconductivity decay curve $\sigma_{ph}(t)$ at point t_0 cuts off on the time axis a portion that is numerically equal to the excess carrier lifetime τ. This is a common method for determining decay time, τ_{decay}.

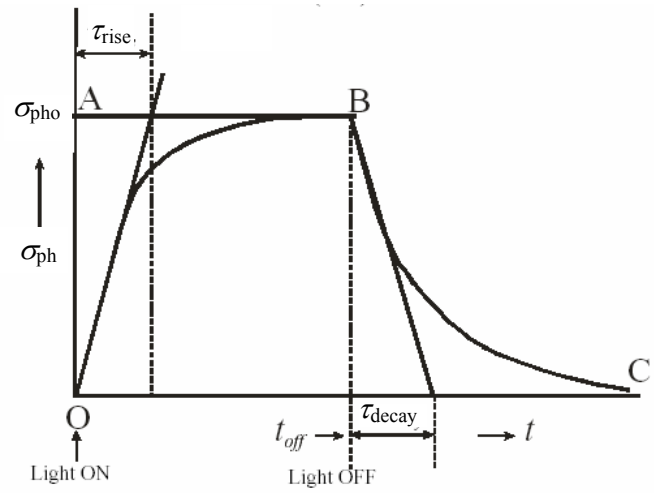

Figure 3.03: The curve of the growth of photoconductivity of a semiconductor under illumination and the decay of photoconductivity

Fig 3.03 also illustrates the character of growth of the semiconductor photoconductivity on applying a light pulse (curve OB) in accordance with the following relation:

$$\sigma_{ph} = \sigma_{ph_0}[1-\exp(-t/\tau)] \qquad (3.43)$$

The tangent to $\sigma_{ph}(t)$ curve at the origin intercepts the straight line $\sigma_{ph} = \sigma_{pho}$, at $t = \tau_{rise}$ which corresponds to the photoconductivity growth or rise time.

The instantaneous life time can be evaluated from the initial stage of photoconductive decay curve using the relation [310]:

$$\tau = \Delta\sigma_{st} / [\frac{d}{dt}(\Delta\sigma)]_{t=0} \qquad (3.44)$$

where $\Delta\sigma_{st}$ is the conductivity at steady state (just at $t = t_{0ff}$).

In actual practice, to determine decay constant the decay curve is fitted most often by an expression of the form [310]:

$$I_t = I_0(1+at)^{-b} = I_0 t^{-b} \qquad (3.45)$$

(considering $1+at \approx t$, a being a constant).

Where, I_0 is the initial photocurrent at $t = t_{0ff}$ and I_t is the photocurrent after time t from t_{0ff} and b is the decay constant. The decay constant is dependent on light intensity and temperature.

3.5 METAL-SEMICONDUCTOR JUNCTIONS

When a metal makes an intimate contact with a semiconductor and a thermal equilibrium is established, a metal-semiconductor junction is formed. Metal-semiconductor junctions are of great importance since they are present in every semiconductor device. They can behave either as an ohmic contact or as a rectifying contact called Schottky barrier depending on the characteristics of the interface.

3.5.1 Ohmic contact to semiconductor

An ohmic contact is defined as metal-semiconductor junction that has negligible contact resistance relative to the bulk or series resistance of the semiconductor. This is the most important factor in measurement of semiconductor parameters. The important feature of such contact is that voltage drop across the junction must be negligible compared with the voltage drop across the device or specimen, so that contact does not effect the *I-V* characteristics [311]. This happens when there is no effective barrier for electrons at the metal-semiconductor junction.

In general, for n-type semiconductors ohmic contact can be made by using a metal of work function (Φ_m) less than the work function of the semiconductor (Φ_s). In p-type semiconductors the work function of the metal should be greater than the semiconductor work function i.e., $\Phi_m > \Phi_s$. However, there are a few metal-semiconductor combinations which satisfy this condition. In vast majority of cases for ohmic contact, a thin layer of heavily doped semiconductor immediately adjacent to the metal is made such that, the carrier can readily tunnel through the thin depletion layer.

3.5.2 Schottky Barrier junction

If there is a barrier at the metal-semiconductor junction affecting the flow of carriers, allowing easier flow in one direction and hard flow in the opposite direction, the the barrier is called Schottky Barrier. A metal can make Schottky Barrier junction with both n-type and p-type semiconductor if the work function of the connecting materials meets the required criteria. For Schottky barrier with n-type semiconductor Φ_m should be greater than Φ_s, and with p-type semiconductor Φ_m should be less than

Φ_s. The energy band diagram of a metal and an n-type semiconductor is as shown in figure 3.04(a), the zero of energy being the energy of an electron at rest outside of either solid. If the metal and semiconductor are connected electrically by means of a wire, electrons pass from the semiconductor to the metal and the Fermi levels are forced into coincidence. In the process, there must be excess negative charge on the surface of the metal, balanced by a positive charge on the semiconductor. Since the semiconductor is n-type, this positive charge is provided by conduction electrons receding from the surface, leaving uncompensated donor ions. There is thus an electric field in the gap. Because the concentration of these donors is many orders of magnitude less than the concentration of electrons in the metal, the balancing positive charges occupy a layer of appreciable thickness W, and the bands in the semiconductor are bent upwards as shown in Fig 3.04(b). The work-function of the metal (Φ_m) and the electron affinity of the semiconductor (χ_s) remain unaltered as shown. As the metal and semiconductor approach each other, the drop in electrostatic potential (Δ) associated with the field in the gap tends to zero if the field is to remain finite, as shown in figure 3.04(c). Finally, if the gap becomes truly zero (corresponding to perfectly intimate contact between metal and semiconductor), the thin potential barrier separating them disappears altogether, as in Fig 3.04(d) and we are left with a barrier arising from the band-bending. If the contact is not perfect, a very thin high barrier separating metal and semiconductor still remains as shown in Fig 3.4(c). This barrier is usually so thin (~ 10 Å) that electrons can easily pass through it by tunneling, and the situation shown in figure 3.2(c) is then essentially equivalent to 3.04(d). Clearly, in the limit of perfect contact, the limiting value of the barrier height is $\phi_{bo}=\Phi_m - \chi_s$**.** This relationship was first derived by Schottky [312]. This is the potential barrier seen by electrons in the metal trying to move into the semiconductor. On the other hand the barrier seen by electrons in the conduction band of the semiconductor trying to move into the metal is given by $qV_{bi}= \phi_{bo} - \xi$. This built-in potential V_{bi} is a slight function of the semiconductor doping.

To make Schottky barrier with a metal and p-type semiconductor, the metal work function should be less than the semiconductor work function (Φ_s). For an ideal contact between a metal and p-type semiconductor of energy band gap E_g, the barrier height is $\phi_{bo} = E_g - (\Phi_m - \chi_s)$.

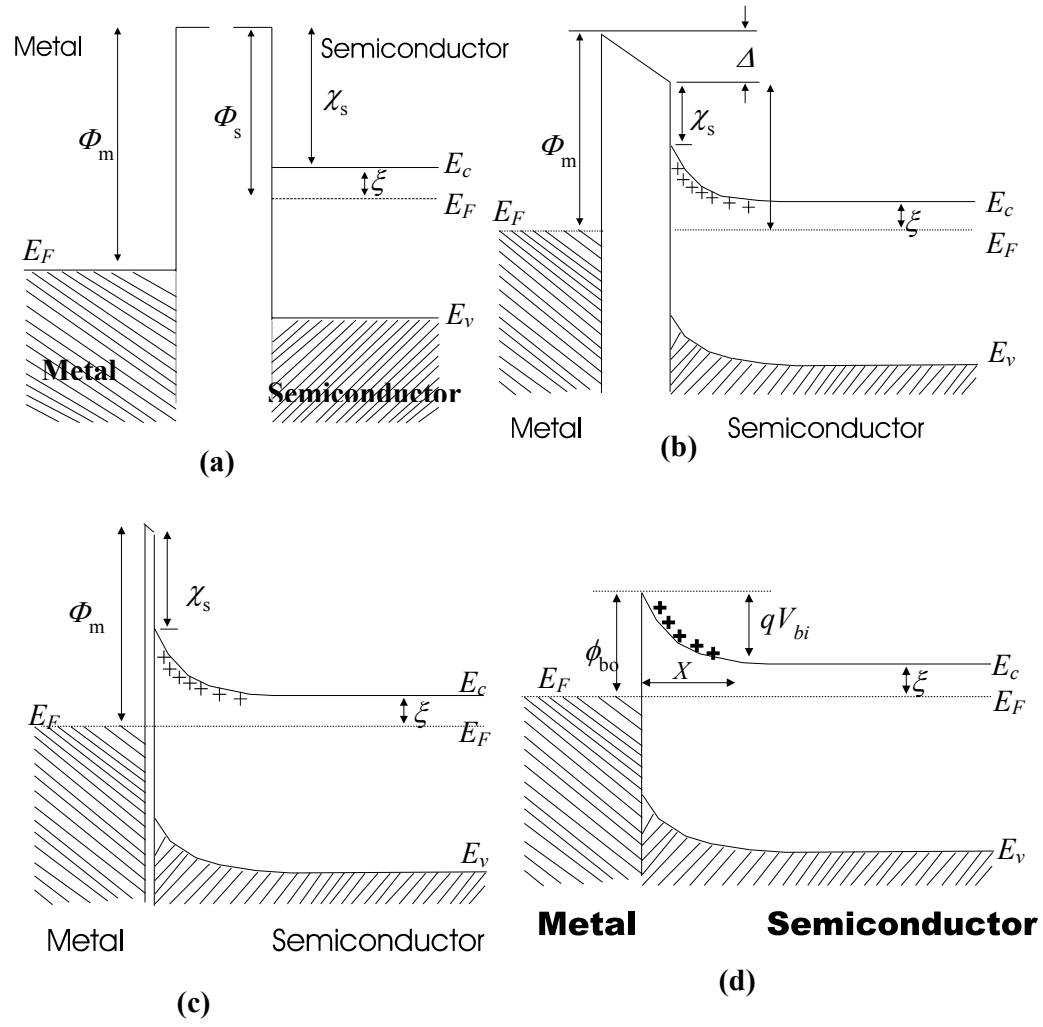

Figure 3.04 Formation of Schottky barrier from metal and semiconductor(n-type): (a) neutral and isolated, (b) electrically connected, (c) separated by narrow gap, (d) perfect contact.

In actual practice, the ideal condition for metal-semiconductor intimate contact is never reached because there is usually a thin insulating layer of oxide called interfacial layer on the surface of the semiconductor. The barrier presented by this layer is thin enough such that electrons can easily tunnel through it.

3.5.3 Capacitance of a Schottky barrier

The depletion region of a Schottky barrier behaves generally like a parallel plate capacitor. Measurement of capacitance under reverse bias can be used to gather information about the barrier parameters. For an ideal Schottky barrier with an n-type non-degenerate semiconductor with uniform doping concentration, the capacitance under reverse bias per unit area can be expressed in terms of the diffusion potential (V_{bi}) and donor density (N_d), if the effect of the holes can be neglected, by the relation [313],

$$C^{-2} = \left(\frac{2}{q\varepsilon_s N_d}\right)\left(V_{bi} + V_r - \frac{kT}{q}\right) \qquad (3.46)$$

where, ε_s is the permittivity of semiconductor, N_d is the donor density, V_{bi} is the diffusion voltage at zero bias and V_r is the applied reverse bias.

This relation shows that a graph of C^{-2} as a function of V_r should be a straight line with a slope of $2/(q\varepsilon_s N_d)$ and a negative intercept on the V_r axis equal to $-V_i = -V_{bi} + kT/q$, from which V_{bi} can be calculated. N_d can be known from the slope of the line if the permittivity of the semiconductor is known. Since barrier height $\phi_{bo} = qV_{bi} + \xi$, where ξ is the distance of the Fermi level from the conduction band, relation (3.46) becomes

$$C^{-2} = \left(\frac{2}{q\varepsilon_s N_d}\right)\left(\phi_{b0} - \xi + V_r - \frac{kT}{q}\right) \qquad (3.47)$$

If the built in potential V_{bi} is independent of V_r (i.e. if there is no appreciable interfacial layer) a plot of C^{-2} against V_r should give a straight line with an intercept $-V_i$ on the horizontal axis equal to $-(\phi_{bo} - \xi - kT/q)$.

The barrier height is then given by

$$\phi_{bo} = V_i + \xi + kT/q \qquad (3.48)$$

ξ is known from [314],

$$\xi = \left(\frac{kT}{q}\right)\ln\left(\frac{N_c}{N_d}\right) \qquad (3.49)$$

The capacitance C in the above relation (3.47) represents the response of the depletion region to a change in the reverse bias. Hence the effect of minority carrier has been assumed to be negligible. The capacitance can be known experimentally by superpositioning an a.c. voltage on the steady d.c. bias V_r and measuring the

capacitance in the normal way by means of a bridge which responds only to the a.c. component of the current.

The effect of hole is appreciable, if the barrier height is greater than (E_g- ξ), in which case, the hole density adjacent to the metal exceeds the donor density and the electric field at the interface is due partly to the holes and partly to the uncompensated donors, C^{-2} vs V_r plot will not be linear and the intercept on V_r axis will give less V_i and hence ϕ_{bo}.

If the Schottky barrier has an insulating interfacial layer, its capacitance is altered because the layer modifies the charge in the depletion region on the bias voltage. The capacitance of the interfacial layer is effectively in series with the capacitance of the depletion region but because the layer is non-linear, the overall capacitance is a rather complicated function of the parameter involved. The details of the Schottky barrier with interfacial layer will be discussed in the section 3.5.6.

3.5.4 Influence of surface states

It was soon found that in the case of point contact rectifiers the barrier is often independent of the work function of metal. On the basis of the theoretical model of surface states by Shockley [315], Bardeen [316] was the first to point out the importance of surface states in the semiconductor in determining the barrier height. The surface states are normally unsaturated (or 'dangling') bonds on the surface of the semiconductor. The surface states are usually continuously distributed in energy within the forbidden gap, and are characterized by a 'neutral level' ϕ_o such that if the surface states are occupied up to ϕ_o and empty above ϕ_o the surface is electrically neutral. If we approximate the Fermi-Dirac distribution by a step function, it follows that when the Fermi level E_F lies above ϕ_o the surface states possess a net negative charge, while if E_F lies below ϕ_o they possess a net positive charge. In other words, the states below ϕ_o are 'donor-like' (positive when empty) and the states above ϕ_o are 'acceptor-like' (negative when occupied). In the case shown in figure 3.5, for which $\phi_o > E_F$, there is a net positive charge in the surface states, and some of the lines of force terminating on the metal emanate from surface charges rather than from ionized donors; in this case the space charge region is not as thick as when surface states are

absent, and the barrier height is reduced. In the same way, if $\phi_o < E_F$, there is a net negative charge in the surface states and the barrier height is increased. Thus the charge in the surface states has a 'negative feed-back' effect which always tends to reduce the deviation of ϕ_o from E_F. If the density of surface states is very high, the gain in the feedback loop is very large, and ϕ_o tends to be locked to E_F so that the barrier height is virtually independent of the metal. Cowley and Sze [317] have shown that, in the case of an n-type semiconductor, Bardeen's theory can be approximately expressed in the form [318]

$$\phi_b=\gamma(\Phi_m-\chi_s)+(1-\gamma)(E_g-\phi_o) \quad (3.50)$$

where E_g is the energy gap of the semiconductor and the neutral level ϕ_o is measured from the top of the valence band. The approximations leading to (3.50) are strictly justified only if the charge in the surface states is very much greater than the charge in the space-charge layer. However, in practice it seems to be a reasonable approximation in all cases. This equation assumes that the metal and semiconductor do not make perfect contact as in figure 3.04(d) but remain separated by a thin oxide film of thickness δ as in figure 3.04(c). γ is given by [318]

$$\gamma = \varepsilon_i\varepsilon_o/(\varepsilon_i\varepsilon_o + e\delta D_s) \quad (3.51)$$

where ε_i is the relative permittivity of the oxide film, ε_o is the permittivity of free space, δ is the thickness of the oxide film and D_s is the density of surface states per electron-volt per unit area of semiconductor surface. If there are no surface states, $\gamma =$ l and the relation (3.50) reduces to the simple Schottky relationship $\phi_{bo} = \Phi_m - \chi_s$. On the other hand, if D_s is very large, γ tends towards zero and ϕ_b, approximates to $E_g-\phi_o$, i.e. the barrier becomes stabilized so that the Fermi level coincides with ϕ_o independently of the value of ϕ_m.

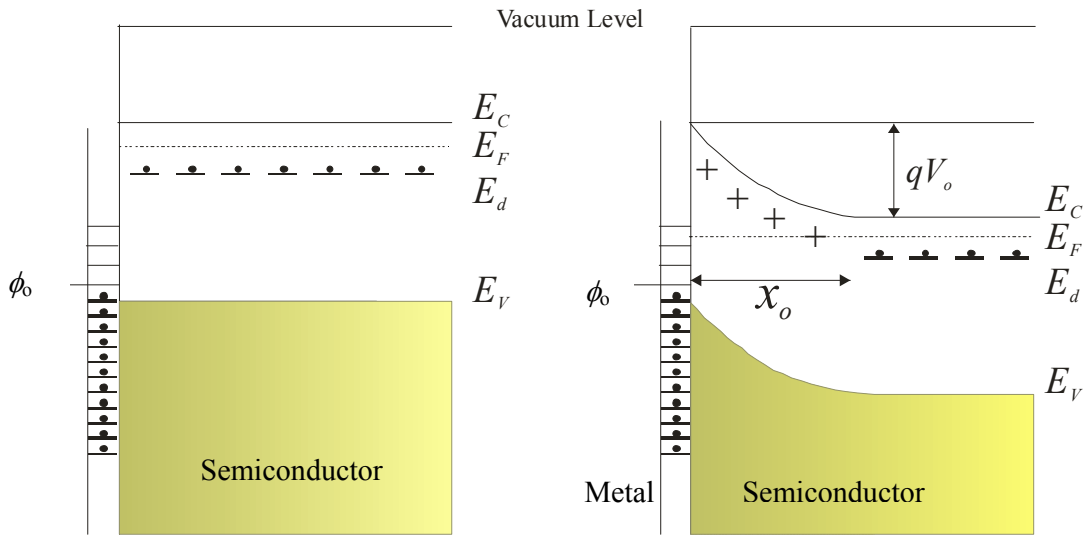

Figure 3.05 (a) Semiconductor surfacewith surface states and (b) Metal-semiconductor contact with surface states.

3.5.5 Lowering of the Schottky barrier by Image force

Image charges of opposite nature are induced in the metal electrode of a metal-semiconductor junction as carriers approach the metal-semiconductor interface. This image charge, being of opposite sign, lowers the potential energy. The effect on a Schottky barrier is shown in figure 3.06, and causes a lowering of the barrier by an amount $\Delta\phi_b$ at the location x_{max}, given by [319],

$$\Delta\phi_b = \sqrt{\frac{qE_{max}}{4\pi\varepsilon_0}} = 2E_{max}x_{max} \qquad (3.52)$$

where, E_{max} is the maximum external electric field applied.

Since the barrier lowering $\Delta\phi_b$ depends on the maximum electric field across the barrier and is therefore a function of the applied bias. This has two fold effects: (i) The barrier increases with increasing forward bias so the forward current increases less rapidly with V than it would otherwise do, and hence, the diode ideality factor will be more than unity; (ii) under reverse bias condition, the barrier decreases with increasing reverse bias, so that the current does not saturate, instead the reverse

current increases gradually with the increase of reverse voltage. This barrier reduction is small compared to the barrier height itself.

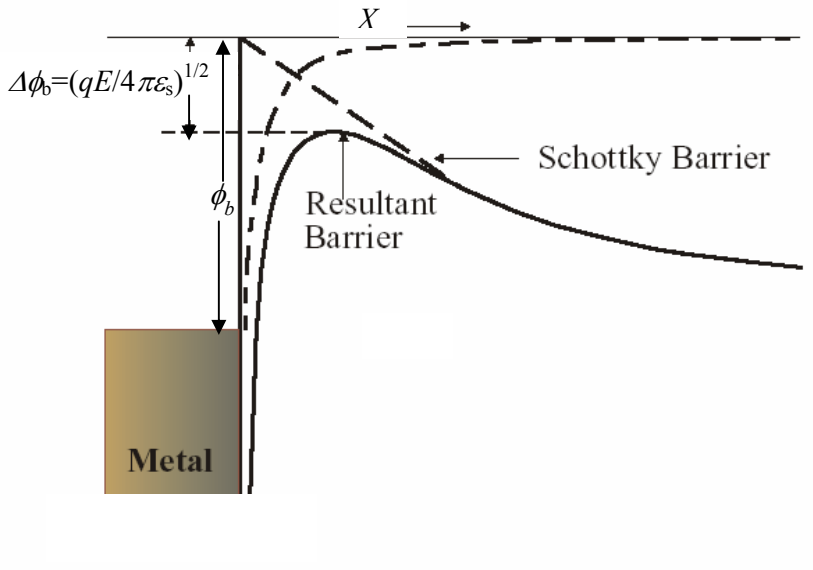

Figure 3.06 Image force lowering of Schottky barrier

3.5.6 Schottky barrier with an interfacial layer

In practice, a metal-semiconductor junction, unless it is made by cleavage in ultra-high vacuum, will inevitably include a thin insulating layer between metal and semiconductor. Typically this layer is a thin oxide layer, which naturally forms on the surface of a semiconductor when exposed to air. This film is normally so thin (~ 10Å) that electrons can tunnel though it quite freely.

The capacitance of a Schottky barrier containing an interfacial layer between the semiconductor and the metal can be considered as the series connection of the oxide and semiconductor capacitance. Hence, the interfacial layer reduces the capacitance of the Schottky barrier diode, although a capacitance measurement will have the same characteristics as an ideal Schottky barrier diode except that the built-in voltage is increased. However the potential across the semiconductor is decreased due to the voltage drop across the oxide layer, so that at low voltage the barrier for electrons flowing into the semiconductor is reduced yielding a higher current. It has been assumed that the interfacial layer forms a very thin tunnel barrier which at low voltages does not restrict the current. As the voltage applied to the Schottky barrier is more positive, the depletion layer width reduces, so that the field in the oxide also

reduces and with it the voltage drops across the oxide. The current under forward bias conditions therefore approaches that of the ideal Schottky diode until the tunnel barrier restricts the current flow. This results in a higher ideality factor for Schottky barrier with an interfacial layer [320, 321].

If an appreciable interfacial layer is present, the barrier height depends on the bias voltage (V_r). If the interfacial layer is so thin that the occupation of the surface states is determined by the Fermi level in the metal, then according to Cowley [322], the barrier height found from the intercept ($-V_i$) of the C^{-2} vs V_r plot will be

$$\phi_b = \phi_{bo} + \phi_1 / 4$$

where ϕ_{bo} is the flat band barrier height and, $\phi_1 = 2\alpha_2 q N_d / \varepsilon_s$

and $\alpha = \delta\varepsilon_s / \varepsilon_i + q\delta D_s$

δ and ε_i being thickness and permittivity of the interfacial layer respectively and D_s is the density of states.

For most practical cases ϕ_1 is less than ϕ_{bo} by about two orders of magnitude, the *C-V* method essentially gives the flat band barrier height.

If the interfacial layer is thick enough so that the interface states are partially or fully in equilibrium with the semiconductor, the situation is much more complicated, because the interface states are indeed filled from the semiconductor. The case is similar to that of an MOS capacitor and the graph of C^{-2} against V_r is generally non linear.

3.5.7 General Expression of Barrier Height

In general, in the metal-semiconductor contact there is always an interfacial oxide layer of atomic layer dimensions and the semiconductor surface has surface states. A more general energy band diagram of a metal-n-type semiconductor contact is shown in Fig 3.07. The surface of the semiconductor is characterized by the neutral energy level ϕ_0 which coincides with the Fermi level of the semiconductor before the metal-semiconductor contact is formed. Cowley and Sze had developed a general expression for barrier height of metal-semiconductor with an interfacial layer and surface states [323] as,

$$\phi_{bn} = c(\Phi_m - \chi) + (1-c)\left(\frac{E_g}{q} - \phi_0\right) - \Delta\phi_b \qquad (3.53)$$

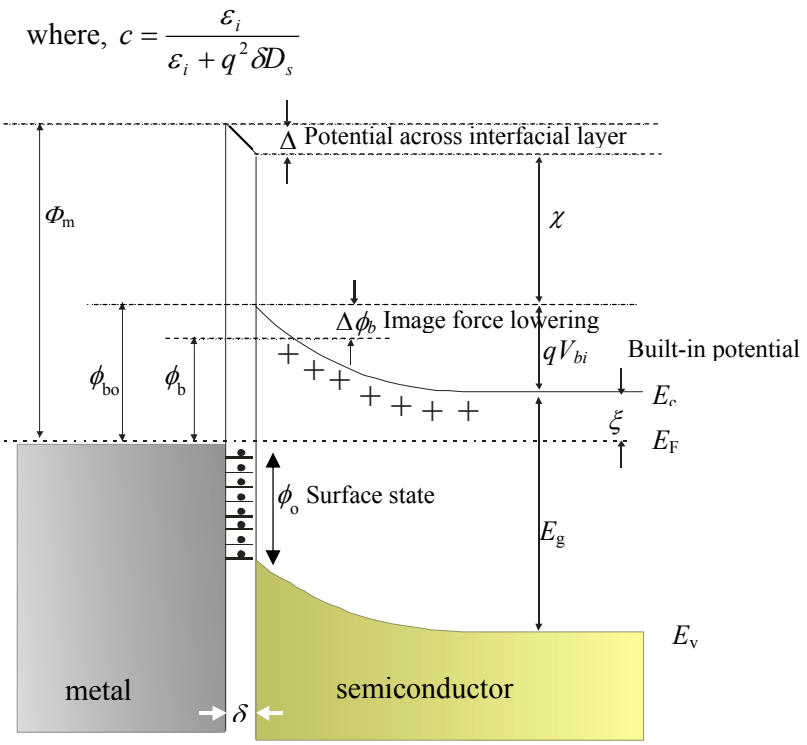

Figure 3.07 Energy band diagram of Schottky barrier with an interfacial layer

3.5.8 Electronic transport mechanisms of metal-semiconductor Schottky Barrier Junction

Under the forward bias voltage (V), the Fermi level in the semiconductor region will rise by qV and lowers the barrier from the side of the semiconductor, while the barrier from the side of the metal will remain same and the thickness of the depletion layer increases. The current transport in a metal-semiconductor junction is mainly due to majority carriers in contrast to p-n junction where minority carriers are responsible. The main transport processes under forward bias condition are: diffusion of carriers from the semiconductor over the potential barrier into the metal, thermionic emission of carriers across the Schottky barrier and quantum mechanical tunneling through the barrier. The diffusion theory assumes that the driving force is distributed over the length of the depletion layer. The thermoionic emission theory on the other hand postulates that only energetic carriers, which have energy equal to or larger than the conduction band energy at the metal-semiconductor interface, contribute to the current flow. Quantum-mechanical tunneling through the barrier takes into account the wave-nature of the electrons allowing them to penetrate through

thin barriers. In a given junction one finds that a combination of all three mechanisms could exist. However, typically one finds only one to limit the current, making it the dominant current mechanism. The various ways in which electrons can be transported across a metal-(n) semiconductor junction under forward bias are shown in Fig 3.08. In the reverse bias condition band bending will increase and the thickness of depletion layer decrease.

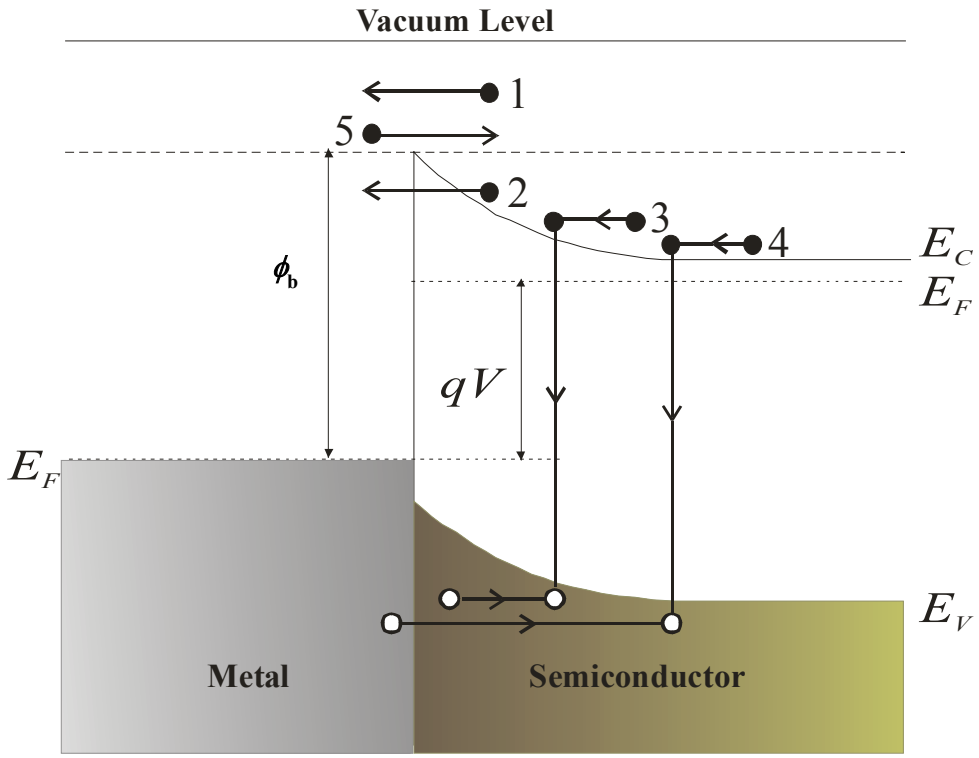

Figure 3.08 Transport processes in a forward-biased Schottky barrier: (1) emmission over barrier, (2) quantum mechanical tunneling through the barrier, (3) recombination in the space charge region, (4) recombination in neutral region (5) flow of electron from metal to semiconductor

If the height of a Schottky barrier on n-type semiconductor is greater than half of the band gap, a region of the semiconductor adjacent to the metal becomes p-type and a high concentration of hole occurs. There are possibilities of these holes to diffuse into the neutral region of the semiconductor under forward bias. This gives rise to the injection of holes. Early works on hole injection of metal-semiconductor contact has been summarized by Henisch [324].

The recombination process in metal-semiconductor junction normally takes place via localized centers and most effective centers are those with energies lying near the centre of the gap. Recombination current is the common cause of departure from ideal behaviour in Schottky diode.

3.5.9 Thermoionic emission theory of *I-V* characteristics

For a Schottky barrier junction with moderate doping at room temperature the transport mechanism namely emission of electron over barrier can be adequately described by thermoionic emission theory [325]. The current flow mechanism in metal-semiconductor junction where n-type semiconductor is in depletion near the surface is shown in Fig.3.08. J_{sm} is the current density of electrons flowing from the semiconductor to the metal and J_{ms} is the current density of electrons flowing from metal to semiconductor. At thermal equilibrium the current density is balanced by two equal and opposite flow of carriers, thus there is zero net current. These current components are proportional to the density of electrons at the boundary. When bias is applied the balance is upset and net current flows through the device.

The current-voltage relation according to thermoionic emission theory is given by

$$J = J_0\left[\exp\left(\frac{qV}{kT}\right) - 1\right] \qquad (3.54)$$

where, $J_0 = A^* T^2 \exp\left(\frac{-q\phi_b}{kT}\right)$ and A^* is called the Richardson constant

The equation (3.54) is similar to *J-V* expression for p-n junction and correct barrier height is independent of bias. However, in the presence of interfacial layer, the barrier height ϕ_b depends on the bias voltage. Even in a perfect contact with no interfacial layer, the barrier height is reduced as a result of an image force by an amount $\Delta\phi_{bi}$ which depends on the bias voltage. Thus we can write the effective barrier

$$\phi_{ef} = \phi_{b0} - (\Delta\phi_b)_0 + \beta V \qquad (3.55)$$

where, ϕ_{bo} is the barrier height at zero bias and $(\Delta\phi_b)_0$ is the image force lowering at zero bias. The coefficient β is a positive quantity.

The current density now becomes [326] (replacing ϕ_b by ϕ_{ef} in (3.54)),

$$J = A^* T^2 \exp\left[-q\{\phi_{bo} - (\Delta\phi_b) + \beta V\}/kT\right]\left[\exp(qV/kT) - 1\right]$$

$$J = J_0 \exp\left(\frac{qV}{nkT}\right)\{1 - \exp(-qV/kT)\} \qquad (3.56)$$

where, $J_0 = A^* T^2 \exp\left(\frac{-q(\phi_{bo} - (\Delta\phi_b)_o}{kT}\right)$

and $\frac{1}{n} = 1 - \beta = 1 - (\delta\phi_{ef}/\delta V)$

n is called "ideality factor". It is constant if $\delta\phi_{ef}/\delta V$ is constant.

For $V>3kT/q$, equation (3.56) can be written as,

$$J = J_0 \exp\left(\frac{qV}{nKT}\right) \qquad (3.57)$$

The value of 'n' can be found experimentally by plotting $\ln(J/\{1-\exp(-qV/kT)\})$ against V. This graph should be straight line of slope q/nkT, if n is constant even for $V<3kT/q$. Usually $\delta\phi_{ef}/\delta V$ is not constant and n becomes a function of bias and in that case the $\ln(J/\{1-\exp(-qV/kT)\})$ vs V plot is not linear. But still n is a useful concept and can be obtained from the plot through the relation,

$$\frac{1}{n} = \frac{kT}{q}\frac{d}{dV}\left[\ln(J/\{1-\exp(-qV/kT)\})\right] \qquad (3.58)$$

$$\frac{1}{n} = \frac{kT}{q}\frac{d}{dV}(\ln J) \text{ for } V>3kT/q \qquad (3.59)$$

The parameter 'n' is generally a function of V, and can be specified for a particular operating point on the characteristics.

The value of J_0 is obtained directly from the intersection of $\ln(J/\{1-\exp(-qV/kT)\})$ vs V plot with the vertical axis. As J_0 is a function of temperature T, it can be measured from the forward J-V characteristics over a range of temperature. A plot of $ln(J_0T^{-2})$ against T^{-1} should give a straight line with intercept on the vertical axis equal to A^* and slope $-q\phi_{efo}/k$, where ϕ_{efo} is the effective barrier height for zero bias.

Therefore the value of effective Richardson constant (A^*) and the effective barrier height can be calculated from $ln(J_0T^{-2})$ against T^{-1}, the Richardson plot.

3.6 HETEROJUNCTIONS

A heterojunction is a junction formed between two semiconductors of different band gaps. When the two semiconductors have the same type of conductivity, the junction is called isotype hetrojunction. When the conductivity type differs, the junction is called anisotype heterojunction. Out of the various heterojunction models, abrupt heterojunction models are found to be a good approximation for many heterojunctions.

3.6.1 Energy band diagram of abrupt anisotype heterojunction:

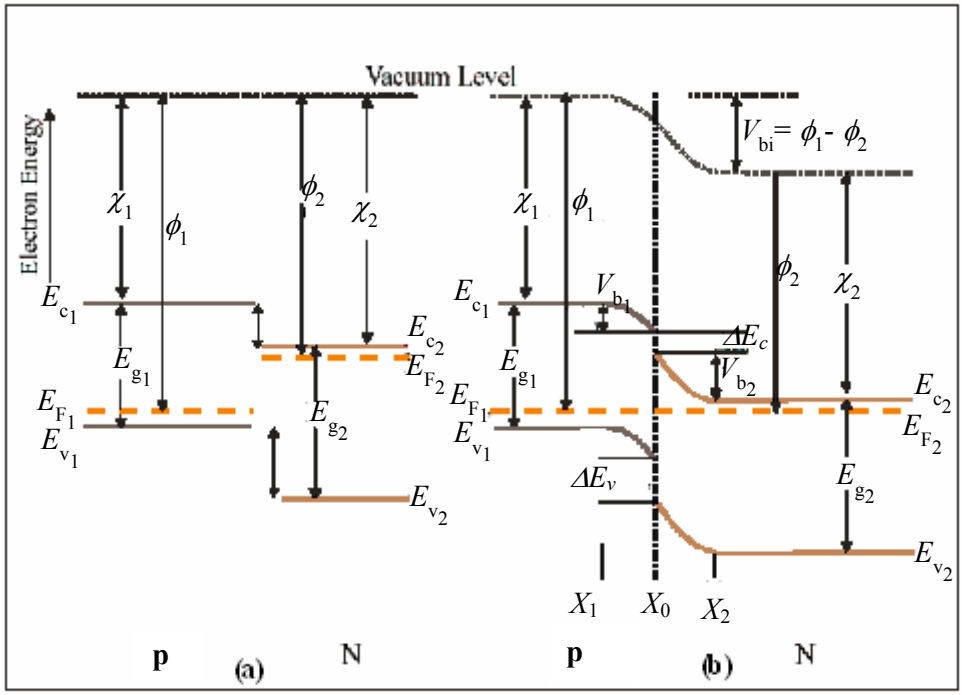

Figure 3.09 Energy Band Diagram (a) before the formation and (b) after the formation of p-N heterojunction

This model was first developed by Anderson and generally known as Diffusion model. Energy band diagram of a heterojunction before and after equilibrium have been shown in Fig. 3.09(a) and (b) respectively.

Here two semiconductors are assumed to have different energy gaps (E_g), different dielectric constants (ε), different work functions (Φ) and different electron

affinities (χ). In writing hetero-junctions (such as p-N junction), semiconductor of small energy band gap is written in small letter and that of large energy band gap in capital letter. The discontinuity in the conduction band edges (ΔE_c) is equal to the different in electron affinities ($\Delta E_c = \chi_1 - \chi_2$) of the two semiconductors. The subscripts 1 and 2 refer to p- and n-type semiconductors respectively. In-this type of hetero-junction a depletion layer is formed on the either side of the interface and since the interface states are absent on this model, the space charges of these layers are opposite and equal in magnitude. The built-in potential (V_{bi}) due to difference in work function ($\Phi_1 - \Phi_2$) is equal to the sum of built-in potential on both sides ($V_{bi} = V_{b1} + V_{b2}$).

3.6.2 Transport mechanisms of abrupt anisotype heterojunction: Thermoionic emission model:

Thermoionic emission model combines a classical kinetic model for the evaluation of emission currents with a diffusion model for determination of extent of minority carrier built up at the edge of the depletion region. Assuming thermoionic emission over the heterojunction barrier to be dominant mechanism, similar to that in a Schottky diode, current-voltage relation can be expressed as [327],

$$J = A^* T^2 \exp\left(-\frac{qV_{b2}}{kT}\right)\left(\exp\left(\frac{qV_2}{kT}\right) - \exp\left(\frac{-qV_1}{kT}\right)\right)$$

where, V_1 and V_2 are the voltage distribution in p and N side of the junction respectively. Putting these values of $V_{bi}=V_{b1}+V_{b2}$ and $V=V_1+V_2$ in the above expression, it can be shown that,

$$J = A^* T^2 q V_{bi} \exp(-qV_{bi}/kT)(1 - V/V_{bi})[\exp(qV/kT) - 1]$$

$$= J_0(1 - V/V_{bi})[\exp(qV/kT) - 1]$$

where, $J_0 = (qA^* TV_{bi}/k)\exp(-qV_{bi}/kT)$ (3.60)

and $V_{bi} = \Phi_1 - \Phi_2$

It is seen that, the value of J_0 is temperature dependent. The reverse current never saturates but increases linearly with voltage at large bias voltage.

3.7 PHOTOVOLTAIC EFFECT AND SOLAR CELLS

A photovoltaic device or a solar cell is a metal-semiconductor or p-n junction which works on the principle of photovoltaic effect i.e., by converting sunlight directly into electricity when the light is shone on the solar cell. The sun is the only natural source of light for the earth that radiates an essentially continuous black body spectrum of electromagnetic radiation at 6000K. A quantity called air mass or solar constant is normally used to quantify the amount of energy received on the earth's surface. Air mass is defined as the degree to which the atmosphere affects the sunlight received at the earth's surface. The atmosphere effect is mainly attributed to attenuation of sunlight due to water vapor absorption, ozone absorption and scattering by airborne dust particles. The secant of the angle between the sun and the zenith (sec θ) is called the air mass and it measures the atmospheric path length relative to the minimum path length when the sun is directly overhead. Air mass 1.5 (sun at 45^{o} above the horizon) has been proven to be the optimum value for terrestrial applications.

3.7.1 Working of photovoltaic cell

The working principle of a p-n junction solar cell has been shown schematically in Fig 3.10. The layer (p or n) facing the light should be thinner so that light can be absorbed near the junction. When light (photons) of energy $h\nu$ is incident on a semiconductor of bandgap energy E_g, part of it is reflected and the rest is transmitted or absorbed. A photon with energy less than the bandgap energy ($h\nu < E_g$) is not absorbed and simply passes. A photon with energy equal to or greater than the bandgap energy ($h\nu \geq E_g$) is absorbed by the semiconductor and in turn leads to the formation of Electron-Hole Pairs (EHP) by optical excitation and the excess energy generated is released as heat. The photogenerated electrons and holes, before they recombine are separated by the electric field provided by the junction, causing flow of current through an external load [328].

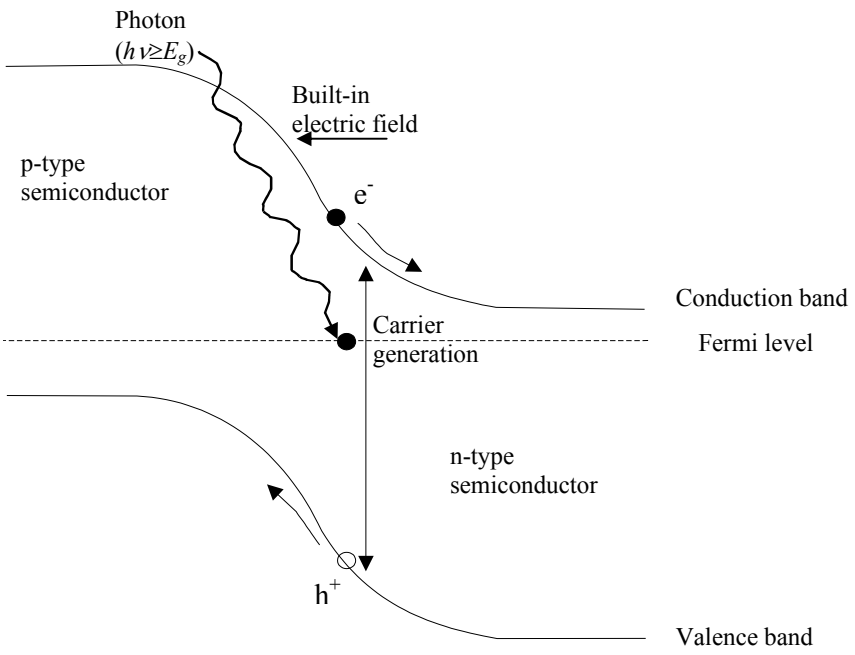

Figure 3.10 The energy band diagram of a p-n junction solar cell under illumination

Schottky barrier diode similar to p-n photodiode, can be operated in photovoltaic mode of operation. A schematic energy diagram of a Schottky barrier solar cell under illumination is shown in Fig 3.11 [329]. The metal must be thin enough to allow a substantial amount of the light to reach the semiconductor. When light of energy ($h\nu \geq E_g$) falls on the Schottky barrier, a part of light is absorbed in the metal and excite electrons over the barrier into the semiconductor, remaining part of the light entering semiconductor is mainly absorbed in the depletion region. If white light is used, light of shorter wavelengths will be absorbed first and light of longer wavelength will travel into the neutral region to create EHP, just as in a p-n junction.

The absorber layers may be polycrystalline or amorphous films. In both cases due to development of potential barrier, the generated electron-hole pairs are separated and a photocurrent is obtained without any external voltage source.

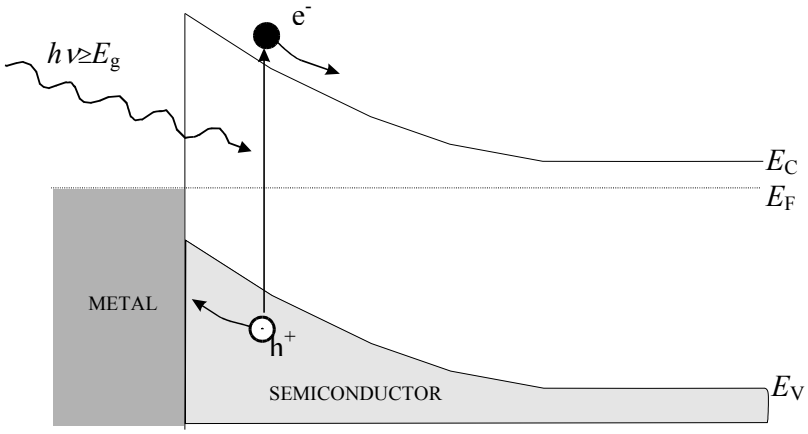

Figure 3.11 Energy band diagram of a Schottky barrier solar cell under illumination

3.7.2 Current-voltage characteristics and Parameters of a Solar Cell

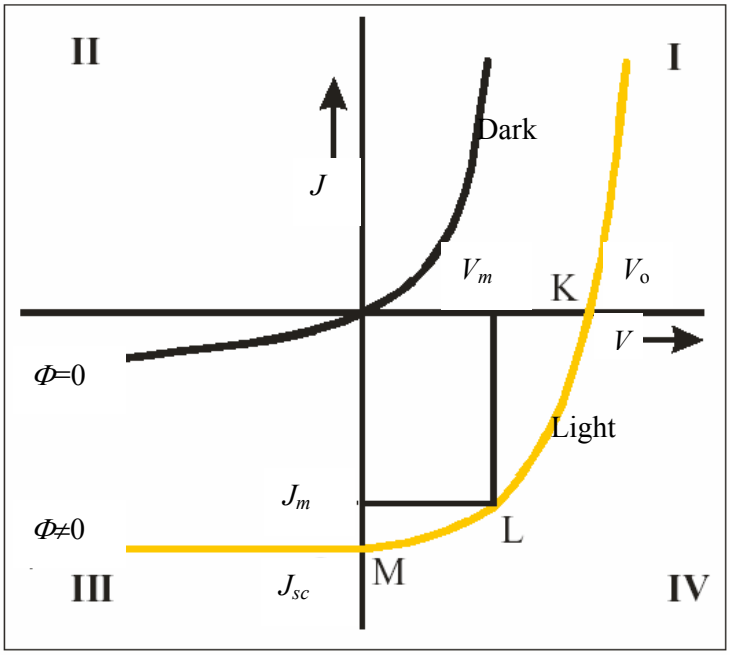

Figure 3.12 *J-V* characteristics under dark and illumination conditions

The dark current density through a Schottky barrier under forward bias is given by (3.56),

$$J_d = J_0 \exp\left(qV \big/ nkT\right)\{1 - \exp(-qV/kT)\}$$

When the diode is illuminated by light of flux Φ, the junction becomes forward bias by photo generated voltage and the expression for current can be written as [330]:

$$J = J_0\left[\exp\left(\frac{qV}{nkT}\right) - 1\right] - J_{ph}(\Phi) \qquad (3.61)$$

where $J_{ph}(\Phi)$ is the current due to photocarriers (photocurrent). The Fig 3.12 illustrates *J-V* characteristics of a photodiode in dark and under illumination.

Short-circuit current and Open-circuit voltage (V_{oc}):

The current-voltage characteristics of a photodiode lie in quadrants I, III and IV. Quadrant IV of the *J-V* characteristics describes the operation of the photodiode in photovoltaic mode. The point of intersection K of curve with the voltage axis corresponds to value of photo-e.m.f or open-circuit voltage (V_{oc}). When there is no load, the cell is short-circuited, current equation reduces to $J_{sc} = -J_{ph}$. That means short circuit current is the same as the photogenerated current. In the Fig 3.12, the point of intersection M of the *J-V* curve with the current axis corresponds to the value of the short-circuit current density (J_{sc}). Under short-circuit condition the current will be given by $J_{sc} = J_{ph}$ which is the flow of photo carriers generated by light in the diode.

Under open-circuit condition, no current flows in the external circuit and the open-circuit voltage V_{oc} is obtained by setting $J_D = 0$ and $V = V_{oc}$, Thus, from (3.61)

$$V_{oc} = \frac{nkT}{q}\ln\left(\frac{J_{sc}}{J_o} + 1\right) \qquad (3.62)$$

Diode ideality factor and Reverse saturation current density under illumination:

Under open-circuit condition, setting $V = V_{oc}$, $J=0$ and $J_{ph}=J_{sc}$, we get,

opening circuit voltage, $$V_{oc} = \frac{nkT}{q}\ln\left(\frac{J_{sc}}{J_o}+1\right) \qquad (3.62)$$

Short-circuit current, $$J_{sc} = J_0\left[\exp\left(\frac{qV_{oc}}{nkT}\right)-1\right] \qquad (3.63)$$

The equation (3.63) can be written as,

$$\ln J_{sc} = \ln J_0 + \frac{qV_{oc}}{nkT} \qquad (3.64)$$

When, $\ln J_{sc}$ is plotted against V_{oc} developed under different intensity of illumination, a straight line will be obtained as per relation (3.64). Therefore the intercept and slope of this linear plot will give the reverse saturation current density J_0 and diode ideality factor n, of the solar cell under illumination respectively.

Fill factor and Efficiency of a solar cell:

The power dissipation of the device in the fourth quadrant i.e. J and V product is negative and hence the power is generated. The maximum power P_m will therefore be obtained when the area of the rectangle is maximum.

Thus,

$$P_m = J_m V_m \qquad (3.65)$$

The fill factor (FF) or curve factor defined to be the ratio of the peak output ($V_m J_m$) to the variable output ($V_{oc} J_{sc}$) is given by,

$$FF = \frac{J_m \times V_m}{V_{oc} \times J_{sc}} \qquad (3.66)$$

The efficiency of a solar cell defined to be the ratio of the photovoltaically generated output to the incident power falling on it. It is a measure of the light energy successfully converted to the electrical energy. The efficiency, η (%) of a solar cell is written as,

$$\eta = \frac{P_m}{P_{in}} = \frac{J_m V_m}{P_{in}} = \frac{(FF)V_{oc}J_{sc}}{P_{in}} \times 100\% \qquad (3.67)$$

where, P_i is the input power.

For maximum conversion efficiency, the solar cell must be designed so as get maximum values of J_{sc}, V_{oc} and FF for a given point.

3.7.3 Equivalent circuit of a Solar Cell:

To explain the *J-V* characteristic of a practical solar cell, the resistance due to semiconductor material and metallic contacts cannot be neglected. Therefore, an actual solar cell is represented by an equivalent circuit shown in figure 3.13. In this equivalent circuit, R_s represents the series resistance of the solar cell, which is dependant on the material properties and process technology. The major part of the series resistance mainly arises from the contact resistance of the front and back contacts of the solar cell. Some of the other components include the contact resistance between the metal and semiconductor and the ohmic resistance in the semiconductor material.

The relation (3.61) is modified as,

$$J = J_o\left(e^{q(V-JR_s)/nkT} - 1\right) - J_{ph} \qquad (3.68)$$

where, R_s is the series resistance. Therefore the series resistance, which affects the short circuit current, is responsible for decreasing V_{oc} as per relation (3.62). Higher R_s values lead to a decrease in the *FF* of the solar cell which in turn affects the efficiency.

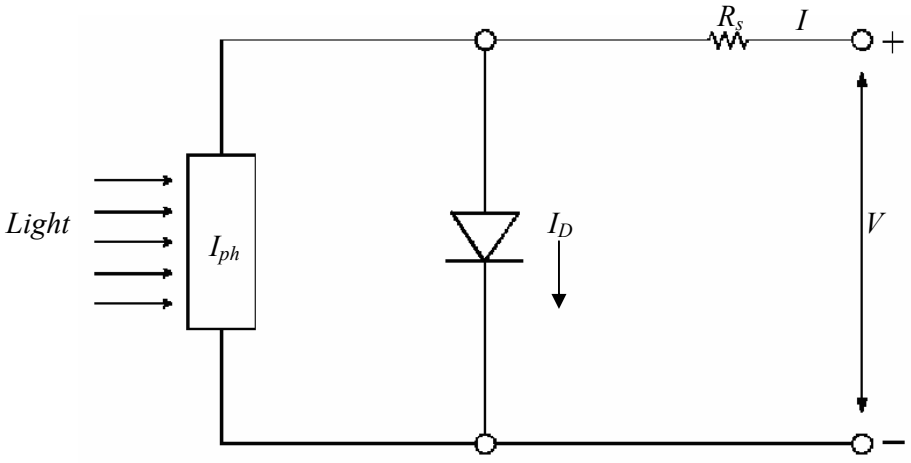

Figure 3.13 Equivalent Circuit of a Solar Cell with series resistance

3.7.4 Effect of Diode Ideality Factor (*n*)

The diode quality factor is used to determine the perfectness of the junction and it varies for every diode due to physical phenomena such as surface effect, recombination and tunneling. It is a measure of how close the measured *J-V* characteristics match the ideal characteristics. For an ideal diode, diode quality factor is normally 1. High values of diode quality factor can lead to excess forward voltage, heating and a loss in the efficiency. The value of n more than unity leads to deterioration in the *FF*.

The low value of shunt resistance and a high value of series resistance significantly degrade the performance of a solar cell. For an ideal solar cell, R_{sh} is equal to infinity and R_s equal to zero. Similarly, incorporating the effects of R_s, R_{sh} and n, the total current I, flowing through the circuit is given by [331],

$$I = I_0\left[\exp\left(\frac{q(V - IR_s}{nkT}\right) - 1\right] + \frac{V - IR_s}{R_{sh}} - I_{ph} \qquad (3.69)$$

where, I_L is the light generated current, I_0 is the diode saturation current, R_s is the series resistance, R_{sh} is the shunt resistance and n is the diode quality factor.

CHAPTER 4

Measuring Equipments and Experimental Techniques

4.1 Introduction

In this chapter details of sample preparation, vacuum evaporation techniques, characterization of samples, experimental techniques to study different electrical and optical properties have been discussed.

4.2 Materials used for sample preparation

Pure (99.99%) bulk ZnSe and CdTe in the form of powder procured from M/S Aldrich Chemical Co., U.S.A., were used as the source materials for the preparation of thin films of ZnSe and CdTe by vacuum evaporation. Indium Tin Oxide (ITO) powder was obtained from a 99.99% pure sputtering target which was procured from M/S Testbourne, UK. For electrode and doping purposes highly pure (99.99%) Aluminium, Gold, Silver, Nickel rods obtained from M/S Johnson and Matthey Co. London, were used for thermal evaporation. Good quality molybdenum boats procured from M/S Hind High Vacuum Co (Pvt) Ltd., Bangalore, were used for ZnSe and ITO evaporations. For evaporation of different metals, coils of tungsten of helix form were used.

4.3 Vacuum coating Unit

The most important factor in thermal evaporation technique is the high vacuum, which can minimize the interaction between the residual gases and the sensitive surface of growing films.

For preparation of thin films and electrodes a conventional coating unit (Vacuum Coater, Vacuum Instruments Company, New Delhi, India model VC-12) was used (Photograph 1). The schematic layout of the vacuum unit used for thermal evaporation has been shown in Fig. 4.01. The evacuation of the chamber was made by an oil diffusion pump (model A-105SS) of 4 inch diameter having speed of about 500 lit/sec backed by a double stage ballast rotary pump which has a suction capacity of 300 lit/min. The rotary pump was double stage pump fitted with a magnetic air

admittance cum isolation valve. Silicon fluid was used in the diffusion pump which is capable of producing vacuum in the range of 10^{-5} to 10^{-7} torr. The rough and high vacuums were measured by a Pirani gauge and Penning ionization gauge respectively. The diffusion pump is connected to the chamber through a water cooler isolation valve known as the baffle valve, which can adequately baffle the diffusion pump against the direct entry of oil vapour molecules in to the chamber.

The coating chamber consists of a 30 cm diameter bell jar made of corning glass fitted with a L shaped neoprene gasket at its base. The system was provided with air admittance valve for admitting air and needle valve for introducing any gas if needed be. The bell jar with the gasket is placed on a stainless steel base plate. The base plate is firmly joined by welding to the top of the baffle valve and is fitted with number of electrodes to facilitate external electrode connections for heater, thermocouples, thickness monitor unit, power supply etc. A source to shutter swinging over the source position can be operated by means by an external level attached to a Wilson seal arrangement, which is fixed to the base plate. Before every deposition run, the glass bell jar, neoprene gasket, base plate and all other components inside the bell jar were thoroughly cleaned.

For holding the masks and substrates, a circular holder was specially designed from aluminium plate. This plate had seven numbers of square slits of desired size on which mask and the substrates could be placed. The mask holder was supported by three metallic rods within the bell jar, the distance of which from source heater could be adjusted. Placement of substrates and filament inside the vacuum chamber is shown in Fig. 4.02.

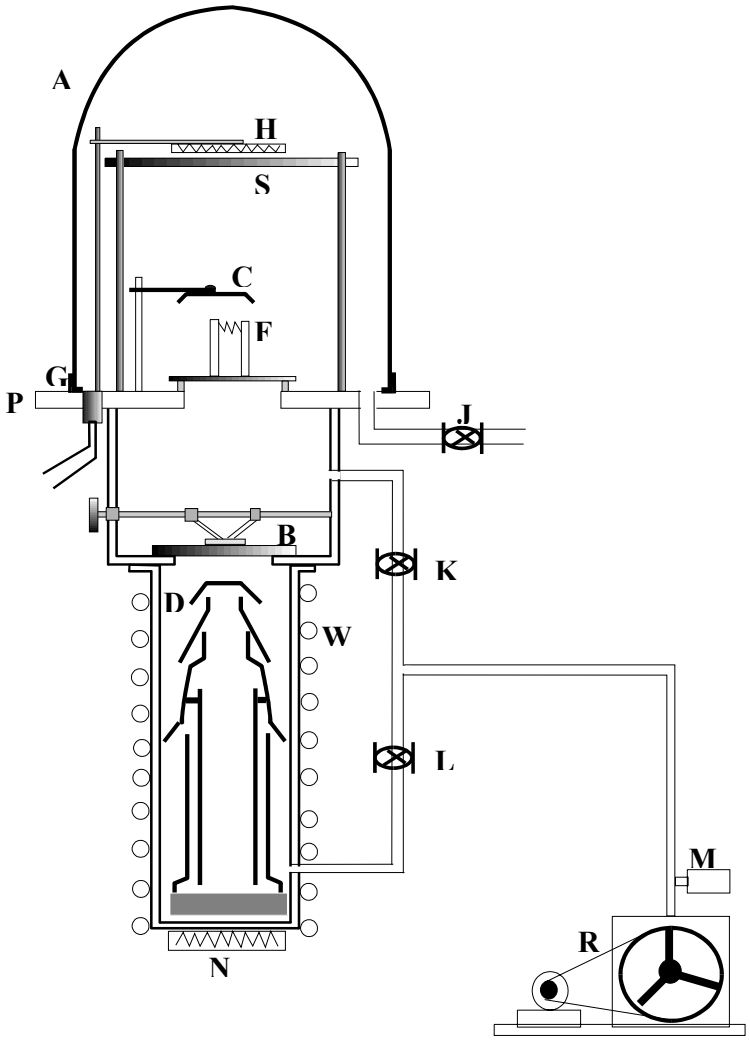

Figure 4.01: A schematic diagram of the vacuum deposition unit used: A- Bell jar, G-Neoprene rubber gasket, P- Base plate, H-substrate heater, S-Substrate holder, C-Shutter, F-Filament, D-Diffusion pump, R-Rotary pump, B-Baffle valve, M-Magnetic air admittance valve, J-air admittance valve, K-Roughing valve, L-Baking valve, N-Diffusion pump heater, W-Water cooling coils

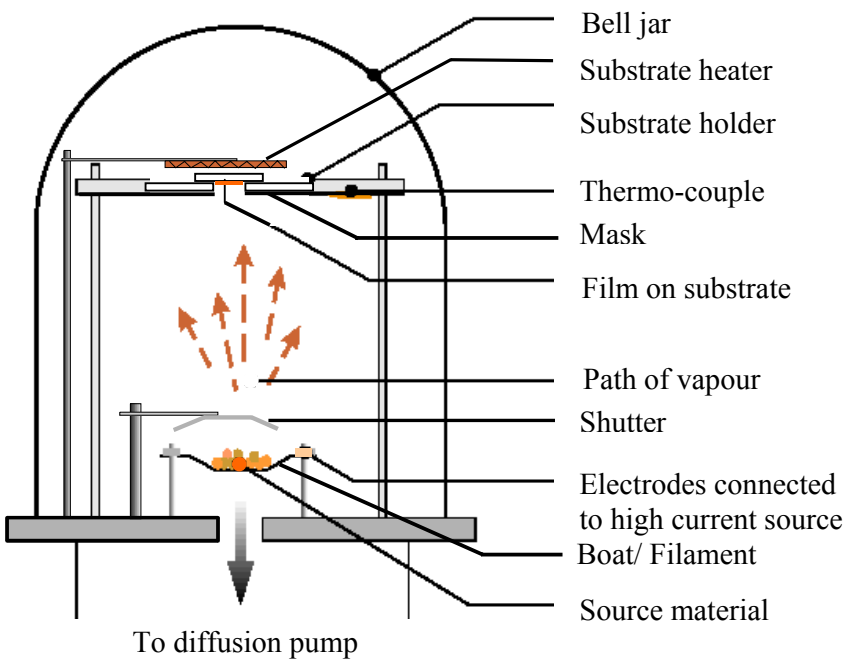

Figure 4.02: Schematic diagram of the thermal evaporation chamber

4.4 Selection of substrate

For deposition of thin films of a material suitable supporting material known as substrate is required. The surface of the substrate plays a major role in the nucleation and growth process of the film and thereby influences the thin film properties considerably. An ideal substrate should have the following requirements [332, 333]

(a) The surface should be flat and smooth.

(b) High mechanical strength to enable the substrate to withstand strain during processing and monitoring

(c) High resistivity

(d) High thermal conductivity.

(e) Nearly same coefficient of thermal expansion with that of the film to minimize thermal stress.

(f) Zero porosity to minimize out gassing and to ensure film uniformity, and

(g) Low cost.

It has been observed that there is no material that would satisfy all these requirements. Glass is most widely used as substrate material for deposition of polycrystalline films. In the present study microscopic glass slides of thickness 1.35mm (Upen Instruments, Nashik, India) were used as substrate material due to their fulfillment of most of the requirements as good substrates. Substrates of appropriate sizes (2.5×2.5 cm^2 and 1.8×2.5 cm^2) were then cut out from the glass slides for use.

4.5 Cleaning of substrates

The substrates should be highly cleaned and uncontaminated for proper adhesion of the films and for producing reproducible film properties. Usually the fine dust particles due to packaging, fingerprints and sticking of different impurity atoms are the common contaminants. The removal of these contaminants by different cleaning techniques depends upon the nature of the substrate and the type of contaminants. The chemical reagents, such as acids, alcohol or alkalis with proper concentrations remove the contaminants by breaking the bonds between the contaminants molecules as well as between the contaminants and substrate. Acid converts oxide layer if any and greases into water-soluble compounds. The ultrasonic cleaning is another recommended process for removing gross contaminants such as greasy particles and fingerprints. This procedure enhances the dissolution of residues sticking on the substrate by the intense local stirring action by the shock waves created in the solvent.

The substrates of appropriate sizes 2.5×2.5 cm^2 and 2.5×1.8 cm^2 cut from the glass slides were first washed with ordinary detergent solution and then these were treated in a mixture of nitric acid and Isopropyl alcohol. Taking out from this solution the substrates were washed by freshly prepared distilled water and then immersed in isopropyl alcohol and after wards these are again rinsed with de-ionised water. The drying of cleaned wet substrates is also critical because of probable recontamination due to adsorption of gaseous particles and dust. So, necessary precautions were taken in drying the substrate in an atmosphere free from any air borne contaminants. Taking out the substrates from the deionised water, the substrates were put vertically in a clean pettry dish so that there is no water stick mark on the substrate. These were then put inside a cleaned closed stainless still oven for drying for an hour at 373K.

4.6 Masks for generation of pattern in the deposited films

The desired shapes or patterns of films are generally obtained by masking substrates during deposition so that only desired areas receive the vapour atoms. A mask should be stable over the temperature range encountered during deposition and chemically inactive with the vapour atoms. In the present case, freshly cleaved good quality mica sheets were used for making different masks according to requirement. They were cut to different geometrical shapes by shaving blades and micro punch. In some cases aluminium and molybdenum foils were also used. The masks were thoroughly cleaned by detergent and finally washed in acetone. They were dried properly by hot air blower.

4.7 Substrate heating

The radiation heater fitted above the substrate holder assembly was used to raise the temperature of the substrate during deposition to any desired value (called substrate temperature). The power to the radiation heater was supplied and controlled from outside through an autotransformer and a thermostat. The temperature was measured with the help of a copper-constantan thermocouple which was connected to a digital micro voltmeter (Agronic112, M/S scientific equipments & service, Roorkee, India). By this method the substrate temperature could be raised up to 673K.

4.8 Preparation of semiconductor films

Molybdenum boats were used for evaporation of both ZnSe and ITO. ZnSe powder attains sufficient high vapour pressure before reaching the melting point and subsequently sublimates to form a film on the substrates. The sublimation temperature of ZnSe is achieved nicely by adjusting the heating current in the range 3 – 4.5 amperes keeping the voltage at 25-35 volt. The source to substrate distance was kept at about 8 cm for deposition of films. The rate of deposition of ZnSe sample was 1.5Å/sec to 5Å/sec. The deposition parameters were adjusted to produce films of different requirements. For preparation of doped ZnSe films, the dopant material (Al) of suitable amount was evaporated from a tungsten filament at the time of evaporation of ZnSe from the molybdenum boat. The films after deposition were kept in the

vacuum chamber overnight and then they were annealed in vacuum with a radiation heater at temperature 473K for 1 hour.

ITO films were deposited on the chemically cleaned glass substrates from molybdenum boat from ITO powder at a deposition rate 1.5Å/sec to 3Å/sec. The substrates were kept at 10 cm away from the source. After deposition, the films were annealed in air at 523K for 1 hour.

For optical and structural studies square shaped films of ZnSe and ITO were prepared on cleaned glass substrates.

For the studies of electrical conductivity and photoconductivity of undoped and doped ZnSe and ITO films, two types of samples were prepared: (a) gap type and (b) sandwich type. For the present experimental work aluminium was selected as electrode material because, (i) it makes ohmic contact to ZnSe and ITO films, (ii) it has high conductivity and good adhesion with glass substrates and also has mechanical stability along with low stress [334].

For a gap type structure rectangular shaped (3mm×5mm) semiconductor film was first deposited over the glass substrate with a suitable musk (Fig 4.03(g)). Over these films a rectangular electrode of aluminium with a spacing 3mm was vacuum deposited on the two ends of the film with the help of a suitable mask (Fig. 4.03(a)).

For sandwich type structure, first the aluminium electrode was deposited on glass substrate before deposition of ZnSe. Finally rectangular or circular shaped aluminium electrodes were again deposited on the ZnSe and ITO films. Thus the semiconductor film was sandwiched between the lower and upper electrodes.

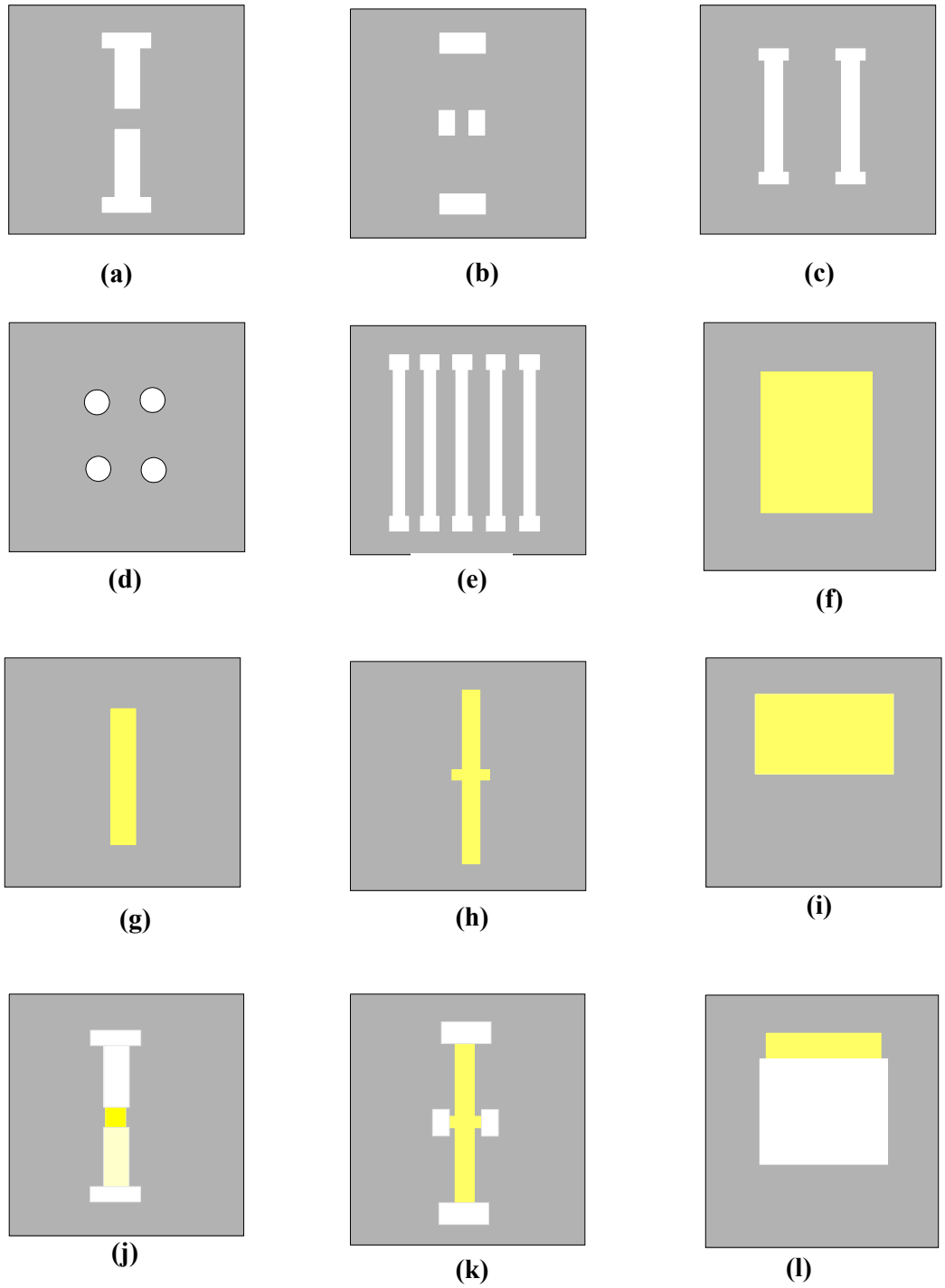

Figure 4.03: Schematic diagrams of different types of films deposited on glass substrates: (a) Electrodes for resistivity measurement, (b) Electrodes for Hall effect measurement, (c) Double electrodes, (d) Dot type electrodes, (e) Electrodes for junction preparation, (f) film for optical/ structural studies, (g) semiconductor film for electrical measurement, (h) semiconductor film for Hall effect measurement, (i) semiconductor film for thickness measurements and schematic representation of different types of samples after preparation: (j) for conductivity measurements (gap type), (k) for Hall effect measurements, (l) for thickness measurements (side view).

4.9 Preparation of junctions

Two classes of junctions were prepared for studying the junctions properties: (a) Metal-semiconductor junction (Schottky barrier junction) and (b) Heterojunction.

4.9.1 Preparation of Au/(n)ZnSe and Ni/(n)ZnSe junctions (Schottky barrier junction):

For studying metal-(n)ZnSe junction, the sandwich type samples are prepared on glass substrates by sequential thermal evaporation process at a base pressure of $5x10^{-5}$ Torr. First for ohmic contacts, three parallel strips of aluminum each of width 0.1cm and length 2 cm were thermally deposited over glass slides from an electrically heated tungsten spiral. Above these Al-doped ZnSe films of area 1.5×1.5 cm^2 were thermally deposited by co-evaporation of ZnSe powder from electrically heated molybdenum boat and Al metal from tungsten spiral filament. Al made ZnSe films n-type. At the time of deposition, the substrate temperature was maintained at 453K. After deposition the films were annealed in vacuum at 473K for 60 minutes. Finally, for the barrier metal, three Au electrodes (each of width 0.1 cm) were vacuum deposited over the Al-doped ZnSe films using suitable masks to form Au-(n)ZnSe-Al structures of junction area 0.01 cm^2 each. Thus, 9 junctions of equal area (10^{-2} cm^2) were obtained on the same substrate. Exactly in the same manner, Ni-(n)ZnSe-Al structure was made. The Schottky barriers were formed between Au or Ni and (n)ZnSe films, Al is for ohmic contact. A schematic diagram of a device structure having 9 Au-(n)ZnSe Schottky barrier junctions on a single substrate has been shown in Fig.4.04 (a).

4.9.2 Preparation of Heterojunctions:

For the preparation of (n)ITO/(p)Si and (n)ZnSe/(p)Si heterojunctios Si wafers were used. The specifications of Si wafers used were: boron-doped (p-type), orientation (100), resistivity 10-20 ohm cm, thickness 500-550 μm and area 1.5×1.5 cm^2. Before preparation of the junctions, the Silicon wafers were etched chemically by hydrofluoric acid. Initially, ITO films of area 1.2×1.2 cm^2 were vacuum deposited on the other side at a substrate temperature 593K to make the

(n)ITO/(p)Si junctions. Before deposition of electrodes, the junction structures were annealed in vacuum for one hour at 593K temperature. After annealing the (n)ITO/(p)Si structures Al was vacuum deposited on the free surface of Si for ohmic contact. Finally three counter-electrodes of Al (width 0.2 cm and length 1.2 cm) were vacuum deposited over ITO films and thus three Al-(n)ITO/(p)Si-Al structures each of area 0.04 cm^2 were obtained.

To make the (n)ZnSe/(p)Si heterojunctions, similar steps were taken. But for these junctions (n)ZnSe films of area 1.2×1.2 cm^2 were vacuum deposited on Si wafer by co-evaporating Al with ZnSe at substrate temperature 453K. After deposition of (n)-ZnSe films whole structures were annealed in vacuum at 473K for one hour. Al electrodes were used as ohmic contacts for both the semiconductor (p)Si and (n)ZnSe. Thus three structures of the type Al-(n)ZnSe/(p)Si-Al were obtained each with junction area 0.04 cm^2 in a single substrate (Fig. 4.04(b)).

For preparation of (n)ZnSe/(p)CdTe heterojunctions, first three parallel Au electrodes each of width 0.2 cm and length 2.2 cm, were vacuum deposited on glass substrates at a pressure of 10^{-5} Torr. Above these, a square shaped (1.8×1.8cm^2) p-type Sb-doped CdTe was deposited by coevapoating CdTe and Sb from a molybdenum boat keeping the substrate temperature 350K. The films were then annealed for 1 hour at a temperature 373K in vacuum. Above them three strips of Al-doped ZnSe films of width 0.4 cm and length 1.8 cm, were deposited at substrate temperature 453K so that they made crosses with the Au strips. Then the samples were again annealed in vacuum at 473K for 1 hour. Finally a strip of Al of width 0.2 cm and length 2.2 cm was deposited over each (n)ZnSe films thus making nine Al-(n)ZnSe/(p)CdTe-Au junctions each of area (0.04 cm^2) as shown in Fig. 4.04 (c). Changing the number of lower and upper electrodes number of junctions could be varied. In a typical two lower and two upper electrodes system four junctions were obtained and in some cases, for five lower and five upper electrodes system of twenty five junctions at a time were obtained on the same substrate.

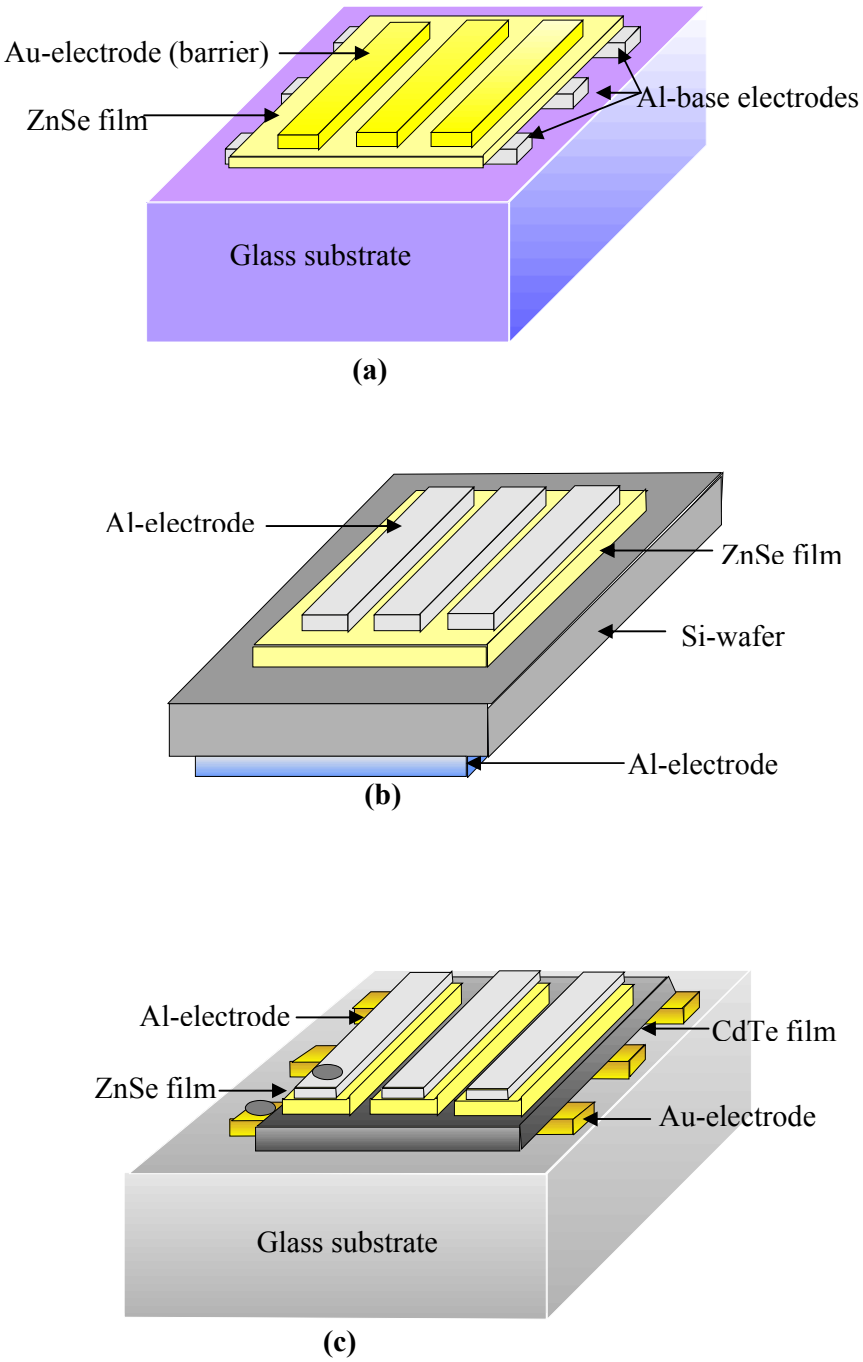

Figure 4.04: Schematic diagrams of different junction structures: (a) Au-(n)ZnSe-Al structures, (b) Al-(n)ZnSe-(p)Si-Al sections, (c) Al-(n)ZnSe-(p)CdTe-Au structures.

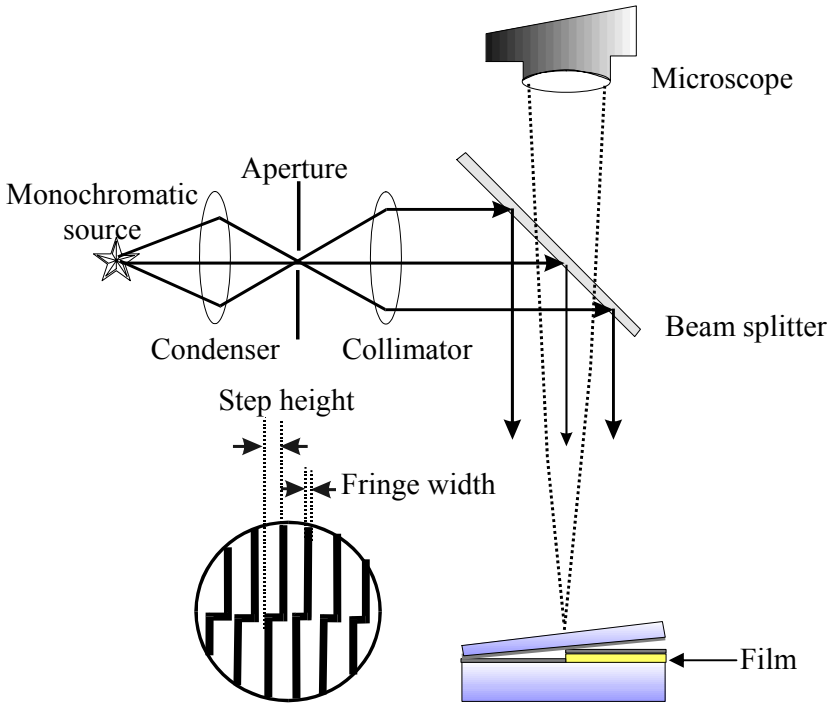

Figure 4.05: Schematic arrangement of multiple interferometic technique for thickness measurement of thin films

4.10 Measurement of film thickness

Thickness of different films was measured outside the vacuum chamber by the multiple beam interferometric method developed by Tolansky [335-339]. For this purpose, the thin film whose thickness is to be measured is deposited on an optically flat glass substrate so as to leave a sharp edge between film and uncoated surface of the substrate. A highly reflecting coating of silver is deposited covering the film and the bare surface of the substrate so as to form a sharp step on the film edge. The height of the step is the thickness of the film. A flat and thin glass slide coated with partially transparent silver film (called Fizeau plate) is then placed over the step in such a way that thin wedge of air film is formed at the step as shown in the Fig 4.05. When parallel monochromatic light is allowed to fall normally, dark fringes with displacement or stepper can be observed with a low power microscope. Thus the film thickness is calculated from equation [339],

$$d = \frac{D}{b}\frac{\lambda}{2} \text{ Å} \qquad (4.01)$$

where, b is the fringe width, D is the displacement of the fringes at the step and λ is the wavelength of the light used.

The experimental arrangement for observing the fringes and measurement has been shown in Fig 4.05. A Philips sodium vapour lamp (55 watt) was used as the source for monochromatic light (λ=5893Å). The light from the sodium lamp was rendered parallel by using a collimating lens. The lens systems were coaxially placed inside a metallic cylinder. The incoming beam was split by putting a glass plate on the way at 45^0 to incident light and allowed to fall normally on the Fizeau plate placed at an edge over the silver coated films. A sample holder is suitably designed so as to accommodate the Fizeau plate and silver coated film assembly and to adjust the air gap with a fine micrometer screw. The holder was made of brass with a hinge on one side and micrometer screw placed on the other side of the upper plate. The microscope is placed normally above the film assembly.

4.11 Measurement of Optical transmission, absorbance and reflectance

UV-visible spectrophotometer:

For the optical transmittance, absorbance and reflectance measurements of the films a UV-Visible spectrophotometer ***CARY 300*** (Varian, Australia) was used. The range of the spectrophotometer is 200nm to 900nm. The Schematic diagram of this spectrophotometer is shown in Fig 4.06. It is a double beam Instrument, in which the incident light is split into two beams before it reaches the sample. One beam is used as the reference; the other beam passes through the sample. The two beams pass through a beam chopper, which blocks one beam at a time and the detector alternates between measuring the sample beam and the reference beam. The diffraction gratings are used to separate different wave length of the incident light. The detector is a photomultiplier tube (R928). The transmission, absorbance and reflectance spectra are recorded by *Cary Win UV (Scan Application) Software Version: 3.00(182)*. The spectra were collected by an Integrating Sphere (Labsphere DRA-CA-30I) which is equipped with the spectrophotometer. The advantage of use of the integrating sphere is that in case of diffused (solid) sample including thin film, more accurate spectra can be observed by using integrating sphere.

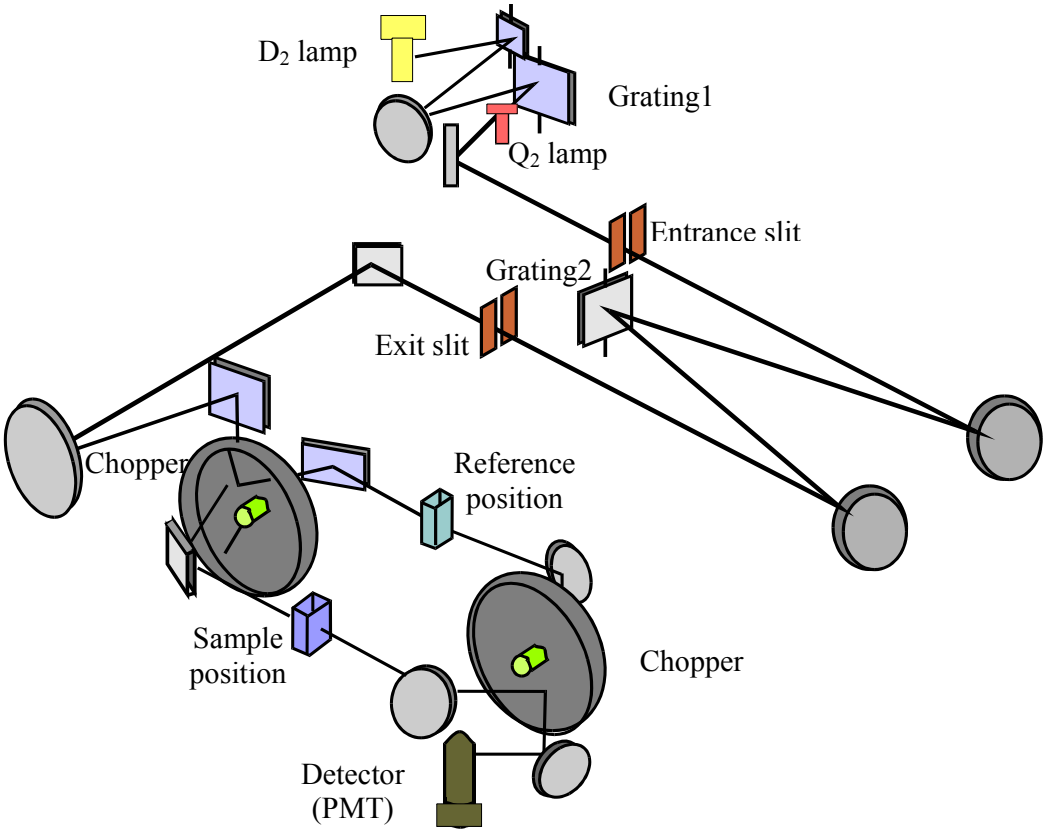

Figure 4.06: Optical arrangement of the Spectrophotometer (Cary 300)

Integrating sphere and its working principle

The integrating sphere (model DRA-CA-30I) of 70 mm diameter has been machined from a special material (Labsphere's proprietary Spectralon material). It is designed to perform reflectance and transmission of various materials. The schematic top view of the accessory is shown in Fig. 4.07.

The integrating sphere measures reflectance and transmittance factor, commonly called reflectance and transmittance. The relative spectral reflectance (transmittance) is defined as the ratio of the flux reflected (transmitted) by the specimen to that of a standard surface under identical geometrical and spectral conditions. For transmittance the standard surface is air, and for reflectance the standard surface is a secondary white standard calibrated relative to the perfectly reflecting diffuser.

Because of the geometry of the integrating sphere, it has the ability to collect most reflected or transmitted radiation, remove any directional preferences and present an integrated signal to the detector.

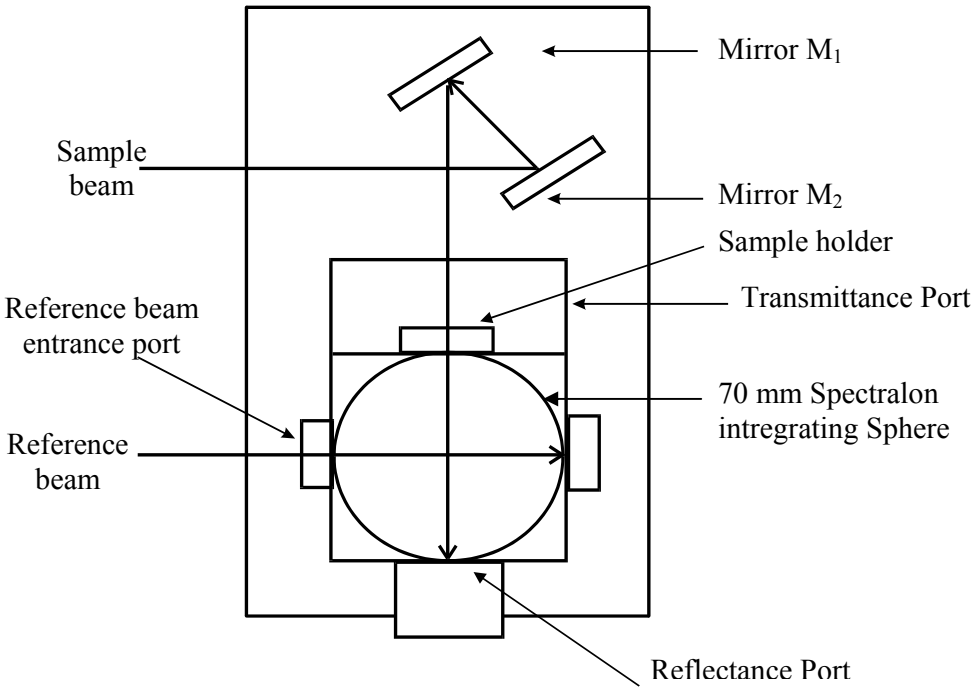

Figure 4.07: Top view of the Integrating sphere (DRA-CA-30I) and accessories

4.12 Microstructural, morphological and compositional analysis

The behaviour of the as-deposited and annealed ZnSe and ITO thin films under different growing conditions in vacuum are also very important and can be characterized structurally, physically and chemically with the help of sophisticated analytical instrumentations viz. X-ray diffractometer (XRD), Scanning Electron Microscope (SEM) based on the established principles. The reports of such various properties of the films are discussed in detail in the corresponding chapters, and brief descriptions of the methods used for structural and compositional analyses are discussed here.

4.12.1 X-ray diffraction studies of the samples:

X-ray diffractometer is a very useful analytical instrument for determination of the whole range of detail information viz. crystal structure, orientation, crystalline sizes, lattice constants, defects, stresses and strains developed in the samples. Philips X-ray diffractometer (Philips X'Pert Pro) with CuK_{α} radiation of wavelength 1.54056Å was used to take X-ray diffraction spectra. The diffractometer operated at 40KeV and 30mA. X-ray diffractogram analysis including the peak search was done by computer programming Philips X'pert software. XRD patterns of all the films as well as bulk samples were taken from 20 to 70 (2θ) degree. The detail analytical reports of the films have been discussed at appropriate sections in chapter 5.

4.12.2 Scanning of Electron Microscope [SEM] studies of the samples:

In order to understand the behavior of the surface morphology of the thermally deposited ZnSe thin films, the Scanning Electron Micrographs of the films were taken with the help of a Scanning Electron Microscope (LEO 1430VP) with an operational voltage of 15 KV at IIT, Guwahati. A separate film along with each batch of films having substrate size $7 \times 7 \times 1.30$ mm^3 was prepared for these analyses.

Compositional Analysis:

The quantitative compositional analysis was done on different prepared samples by the Energy Dispersive X-ray Analysis (EDAX) attached to the SEM system.

The composition of the prepared films was also studied from the X-ray Fluorescence (XRF) spectra recorded by XRF spectrometer (AXIOS PANlalytical) at the Sophisticated Analytical Instrument Facility (SAIF) of Gauhati University.

4.13 Determination of type of doping and doping concentration

The type of doping was determined by simple hot probe method [340]. It consists of a millivoltmeter with two measuring probes as shown in Fig. 4.08. The two probes were placed on the film and the voltage developed was monitored in the millivoltmeter. On heating one probe, positive thermo-emf is developed indicating the semiconductor to be n-type. Reverse is observed for p-type semiconductor.

The carrier concentration was measured from the Hall effect study for the lower resistive samples. In case of the high resistive films, the current through the sample is very low, so the doping concentration could not be measured by the Hall effect method. The doping concentration of the highly resistive ZnSe films were calculated from the C^{-2} versus V plots of the Schottky barrier junction with the semiconductor film under reverse bias condition which is discussed in detail in chapter 7.

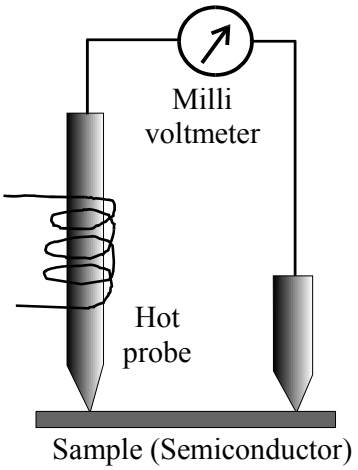

Figure 4.08: Schematic diagram of hot probe method

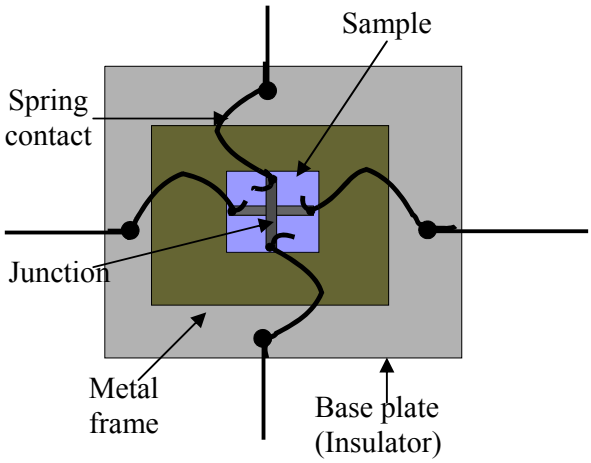

Figure 4.09: Sample holder for measurements of *I-V* characteristics

4.14 Electrical and Optical measurements:

(a) Sample holder

The sample holder used was specially designed to suit the apparatus. This was a thick rectangular aluminium plate. The plate was fixed inside a rectangular frame of perspex by four screws. The four sides of the Perspex block contained four metallic strips as electrodes, which were fixed properly by screws. These strips were properly bent to get spring action on the contacting points and flexible conducting wires for electrical measurements were connected at the other ends. The schematic diagram of this holder has been shown in Fig 4.09.

(b) The main unit for mounting the samples:

The main experimental arrangement for measuring electrical and optical properties has been shown schematically in Fig 4.10. The specially designed arrangement consists of two coaxial metallic cylinders. The inner cylinder was supported by the outer cylinder and the annular space was used to put the sample for study. The outer cylinder was provided with a side tube fitted with an air tight glass window. The window was fitted with a shutter so that the annular space can be made completely dark by closing the shutter.

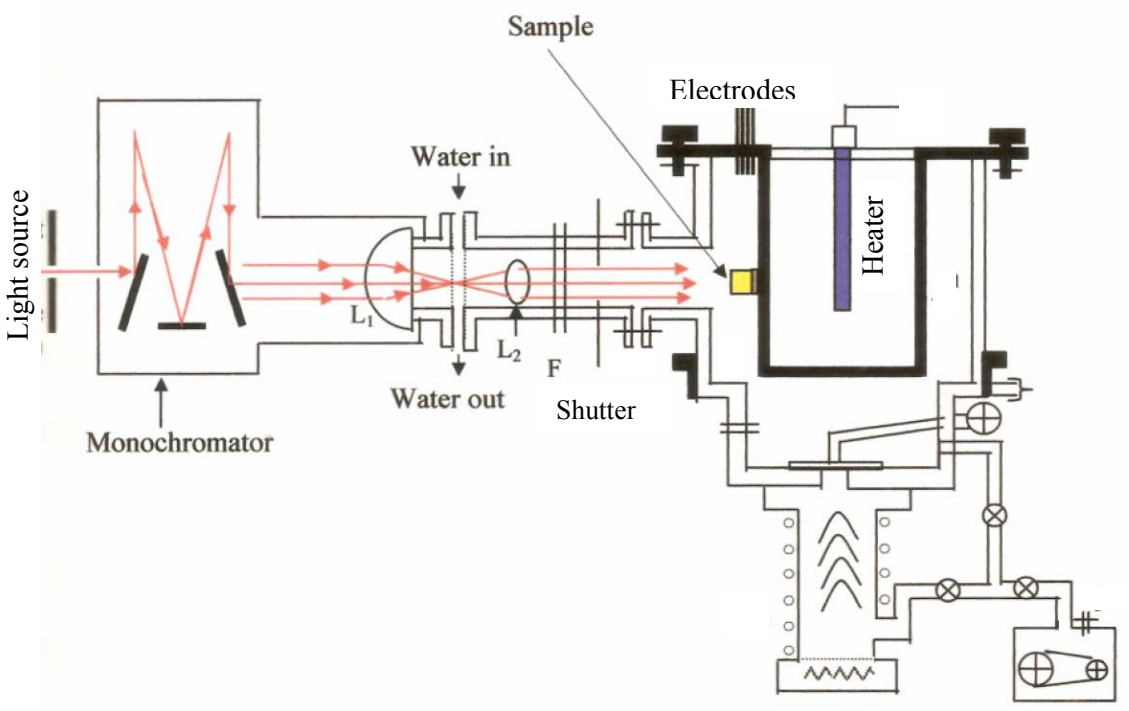

Figure 4.10: Experimental arrangement for *I-V* characteristics in dark and under illumination, temperature dependence of resistivity and photovoltaic measurements

The upper ends of the coaxial cylinders were joined together and made airtight by an "O" ring and screw arrangements. The bottom of the outer cylinder was connected to a pumping system for evacuation of the annular space. The sample holder was vertically clamped to the outer surface of the inner cylinder so that the sample, when mounted on it, faces the glass window. The insulating frame of the sample holder was fixed by screws to provide necessary electrical connections. Four conducting strips were fixed on the insulating frame to make pressure contacts to the electrodes. A chromel-alumel thermocouple was fitted inside the assembly to measure the temperature. Shielded wires from the sample holder and thermocouple wires were brought out from the chamber through air tight feedthroughs fitted at the top of the assembly.

The temperature of the annular space could be uniformly raised with the help of an immersion heater immersed in silicon oil (boiling point 523K) kept inside the inner cylinder. The temperature was controlled by a specially designed electronic temperature controller. The thermo e. m. f. of the thermocouple was measured with the help of a digital micro voltmeter (Agronic112, M/S Scientific Equipments & Service, Roorkee, India).

(c) Light source :

For studying effects of light on sample properties a special light source was designed. The light source is a Quartz Tungsten Halogen (QTH) lamp mounted on a ceramic base. The lamp, housed in a rectangular wooden box fitted with a cooling fan (Fig. 4.11) gives high visible and near infrared output with little ultraviolet. It has a smooth spectral curve and stable output in the wave length range 250 nm to 2500 nm (Fig 4.12). The power of the OTH can be adjusted varying the input voltage of the lamp from zero to 12 V.

For measuring sample properties under white light, intense light from the QTH source was concentrated at the focus of a planoconvex lens where IR part of the ray was filtered out by using a cold water filter. The parallel rays from it were allowed to fall on the sample through the glass window with the help of a shutter.

For getting monochromatic light or for studying spectral response of the sample properties, the QTH was used for the monochromator (Model 77200, Oriel Instruments, USA) as light source and the monochromatic light output from the monochromator was allowed to fall on the sample through the glass window of the specially designed vacuum chamber (Fig. 4.10).

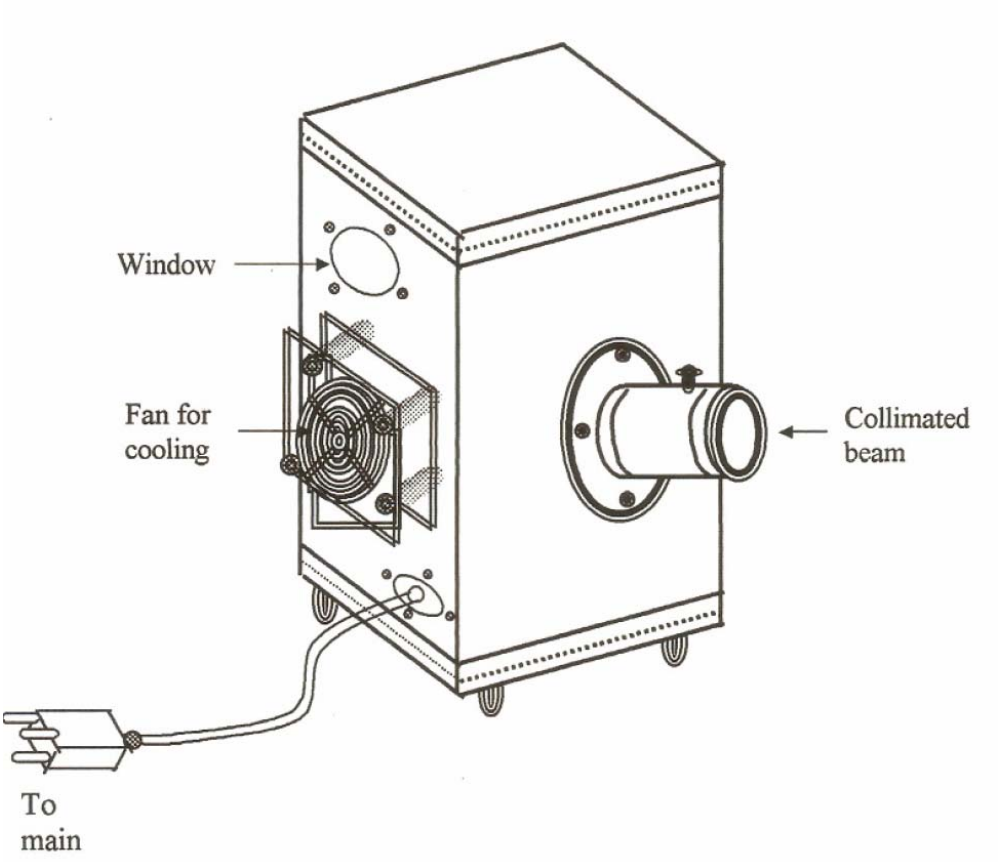

Figure 4.11: Dimensional diagram of Quartz Tungsten Halogen Lamp Housing.

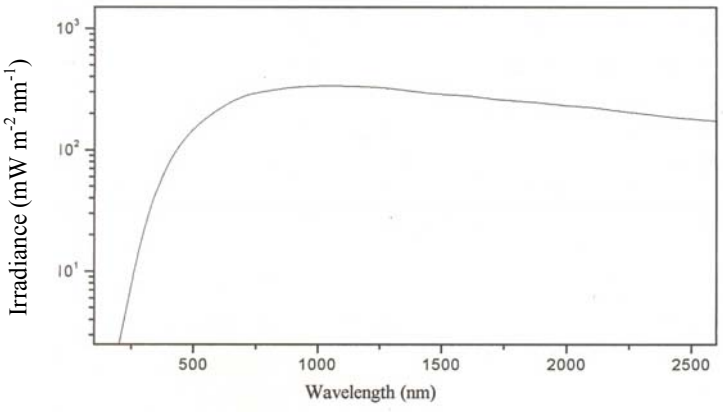

Figure 4.12: Spectral irradiance curve of a 1000W QTH lamp (6315).

(d) Arrangement for electrical measurements:

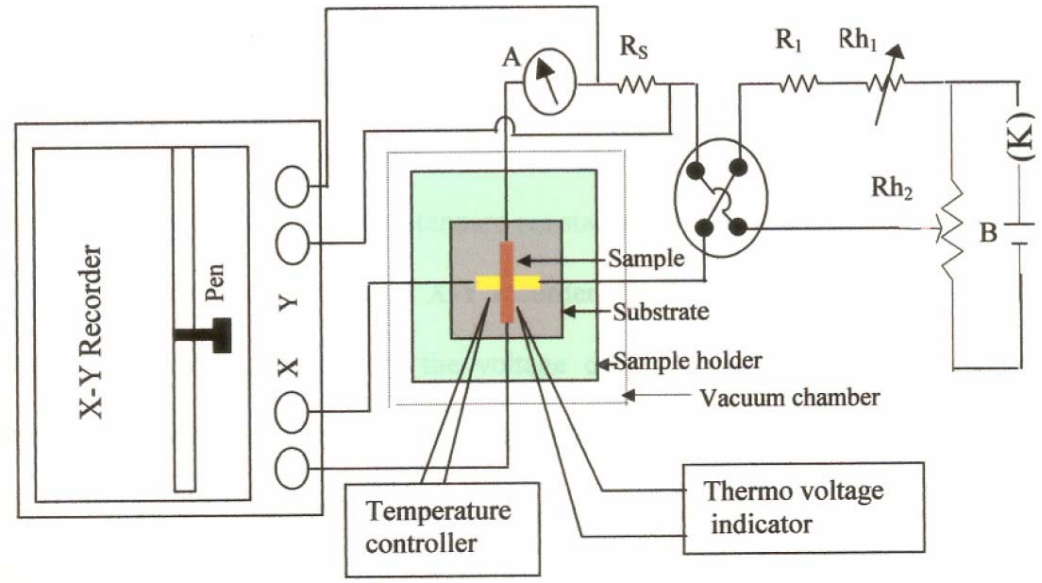

Figure 4.13: Arrangement of X-Y/t Recorder for measurement of *I-V* characteristics, photoconductive rise and decay and photovoltaic effect

The experimental arrangement for taking *I-V* characteristics of Schottky barrier junctions as well as heterojunctions in dark and under illumination is shown in Fig. 4.13. The sample holder with the sample in it was mounted on the unit as shown in Fig 4.10 and all electrical leads taken out from the chamber were used for *I-V* measurements as shown in Fig 4.13. An X-Y/t recorder (M/S Digital Electronics Ltd, Mumbai, India Model: Omnigraphic 2000) was used for this purpose. The bias voltage source was either a variable ramp (Systronics, Model: 1014) or a source meter (Scientific Electronics PS-25). The voltage across the junction was recorded along the X-axis and the current was obtained by recording voltage drop across a standard resistance along Y-axis of the recorder. Before measurement, the chamber was evacuated by a rotary pump to a pressure of about 10^{-2} Torr.

In some cases instead of X-Y recorder, direct measurements of the junction voltage was recorded with the help of digital voltmeter and the current was recorded with the help a digital picoammeter (M/S Scientific, DPM111) or an Electrometer (Keithley, USA, Model 6514).

The electrical measurements could be performed at different temperature of the sample by changing the input voltage of the immersion heater and controlling the temperature with the help of a temperature controller.

(e) Photoconductive rise and decay measurement:

For photoconductive rise and decay, either gap-type or sandwich type sample was mounted on the sample holder. A constant voltage was applied to the sample through a standard resistance and was connected to the X-Y/t recorder. The voltage applied to the sample was recorded along the X-axis of the recorder and the potential drop across the standard resistance due to the current flowing through the sample was recorded along the Y-axis of the recorder. The experimental arrangement for this has been shown in Fig 4.13 which was associated with Fig.4.10.

The chamber was evacuated before the experiment. First, the recorder was switch on and kept in a Y-t mode, and then high intensity white light from QTH lamp was allowed to fall on the sample for a short period of time. The change in Y-axis due to light 'on' and 'off' was recorded. The intensity of light was measured by a Luxmeter (LUSOMET 300 ED).

(f) Measurement of photovoltaic effect:

For measuring photovoltaic effect on the junctions, the same arrangement made for *I-V* characteristics (Fig.12.13) was used. The junction was mounted on the sample holder and the chamber was evacuated to about 10^{-2} torr. The bias source was either a continuously variable (-5V to+5V) power supply or a ramp (Systronics 1014). For *I-V* measurement under illumination, the junction in the chamber was illuminated through glass window using the white light from a tungsten halogen lamp (250W). The intensity of the light could be varied using a variac for the input power of the lamp. *I-V* characteristics under illumination were recorded by X-Y recorder. In some cases a picoammeter or a Keithley Electrometer was connected directly to measure the current at various intensities of illumination. Light intensity was measured by a Luxmeter and converted it to power by laser power meter (LPM-20). The power meter was standardized using a PIN Silicon photodetector.

(g) Capacitance-Voltage Measurement:

Capacitance of Schottky junctions and heterojunctions at different bias voltages was measured by using an autocompute LCR-Q meter (Aplab 4910). The measuring frequency was 1KHz. The samples were placed in a shielded box to avoid any noise during measurement. A variable d.c. power supply (Scientific Electronics model: PS 25) was used to apply different bias voltages. The experimental arrangement is shown in Fig 4.14.

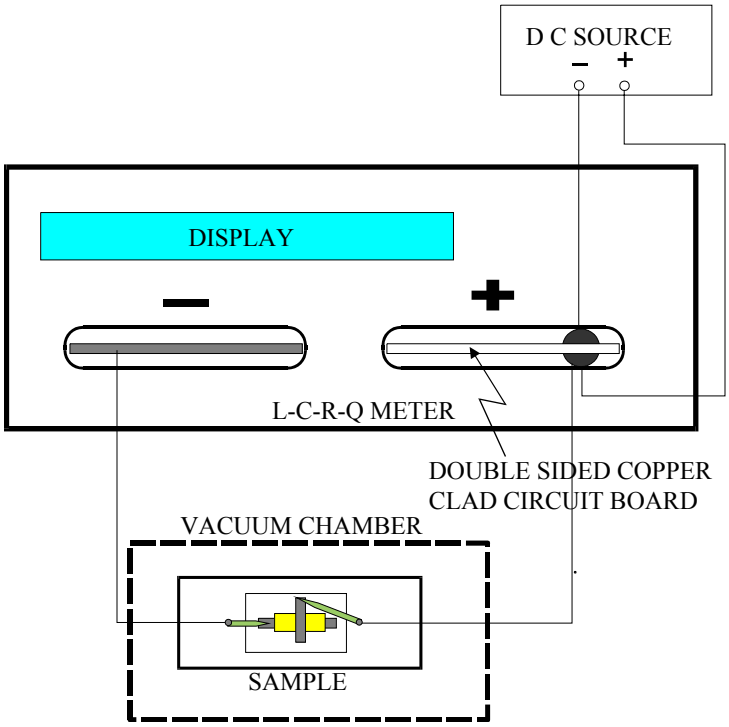

Figure 4.14: Circuit arrangement for Capacitance –Voltage measurements

Photograph 1: Vacuum coating unit

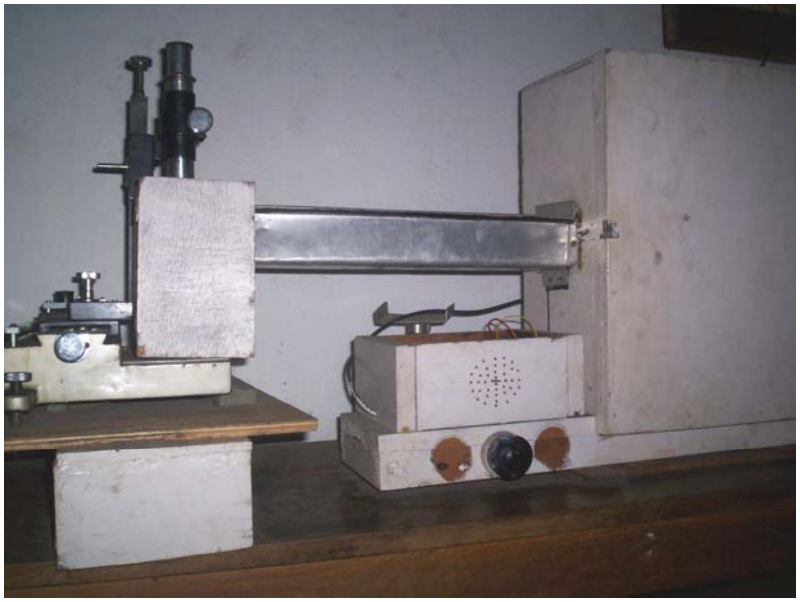

Photograph 2: Instrumental arrangement for thickness measurement

Photograph 3: Cary-300 UV-Visible spectrophotometer

Photograph 4: Instrumental arrangement for measuring *I-V* characteristics in dark and under illumination, at different temperature and photovoltaic measurements

CHAPTER 5

Studies of ZnSe Films

The electrical and optical properties of ZnSe films are very sensitive to the structural properties of the films. Again the structural properties depend on the methods of preparation and deposition conditions. In this chapter, the structural, optical and electrical properties of vacuum evaporated ZnSe thin films prepared at different substrate temperatures are described in details. An attempt has also been made to obtain the optimum growth condition for these ZnSe films, so as to prepare Schottky barrier and heterojunctions with these films.

5.1 Structural and Morphological studies of ZnSe thin films

5.1.1 X-ray diffractogram of ZnSe thin films

The structural properties of ZnSe samples both powder (as-supplied) and prepared films (as-deposited) were studied by X-ray diffraction method. The X-ray diffractogram of pure powder of ZnSe (99.99%) procured from Aldrich Chem. Co. USA, is shown in fig 5.01. The spectrum exhibits polycrystalline nature of ZnSe powder with sharp peaks at 2θ values corresponding to diffraction from different planes. The different 2θ values and corresponding d values (inter planar distance) along with the relative intensities are tabulated in Table 5.01.The diffraction planes (hkl) were obtained by comparing the experimental values of d and relative intensities with those obtained from JCPDS (Joint Committee on Powder Diffraction Standard) X-ray Powder diffraction data file No. 37-1463 for the cubic (Zinc-blende) structure of ZnSe with lattice constant a=5.667 Å.

Table 5.01: d_{hkl} values of as-supplied powder and JCPD Standard data

	From JCPDS data		For powder ZnSe (source)		
Plane	*d* Å	I/I_0	2θ (degree)	*d* Å	I/I_0
111	3.273	1.00	27.175	3.378	1.00
220	2.003	0.70	45.185	2.005	0.825
311	1.707	0.44	53.546	1.710	0.306
400	1.416	0.09	65.829	1.417	0.061
331	1.299	0.13	-	-	-
422	1.156	0.15	-	-	-
511	1.090	0.08	-	-	-

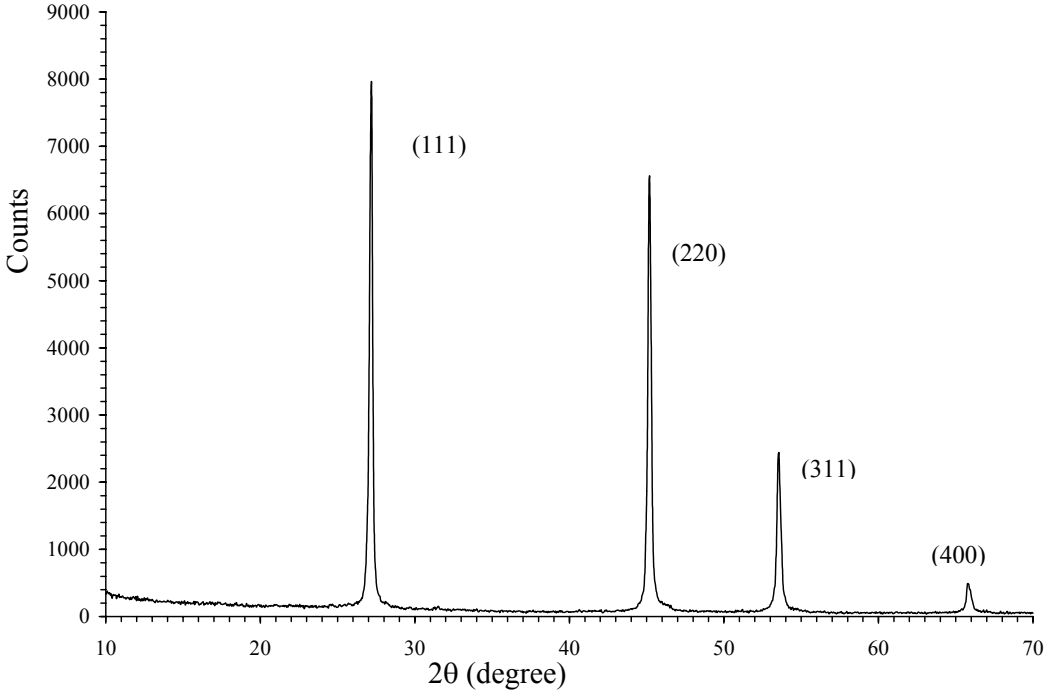

Figure 5.01 XRD of source material ZnSe (powder)

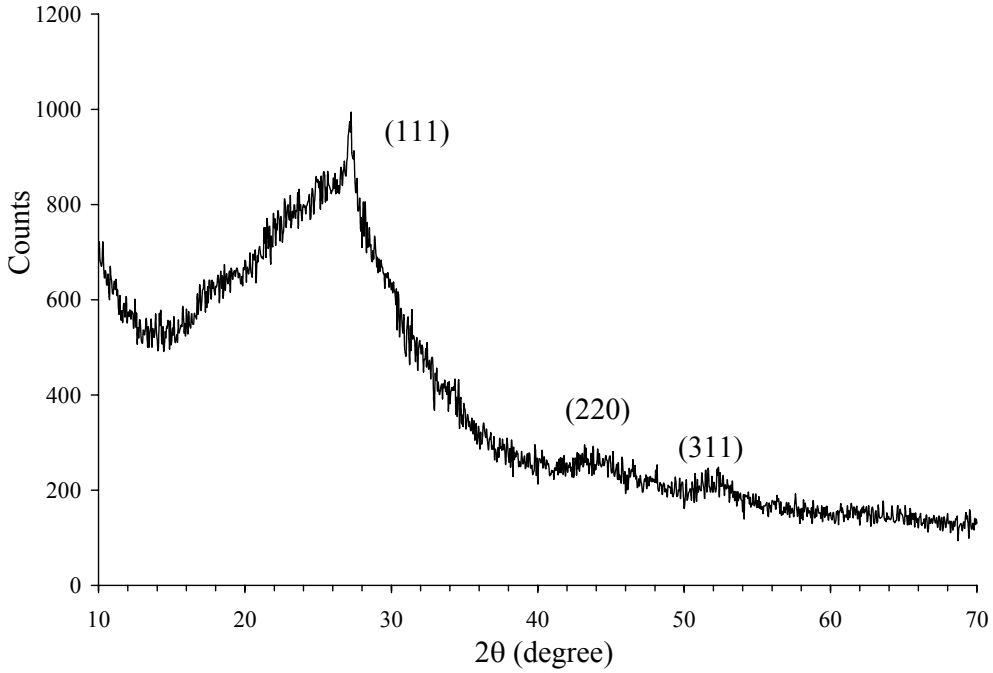

Figure 5.02: XRD spectra of a ZnSe film (annealed at 373K for 1 hour) of thickness 2150Å, thermally prepared at substrate temperature 303K (room temperature)

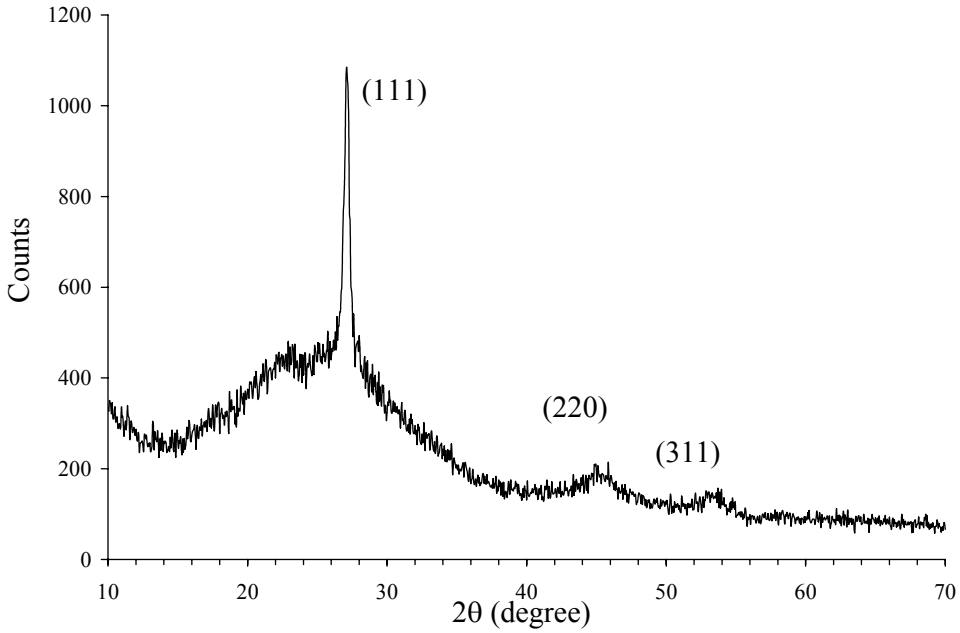

Figure 5.03: XRD spectra of a ZnSe film (annealed at 373K for 1 hour) of thickness 2800 Å, thermally deposited at substrate temperature 373K

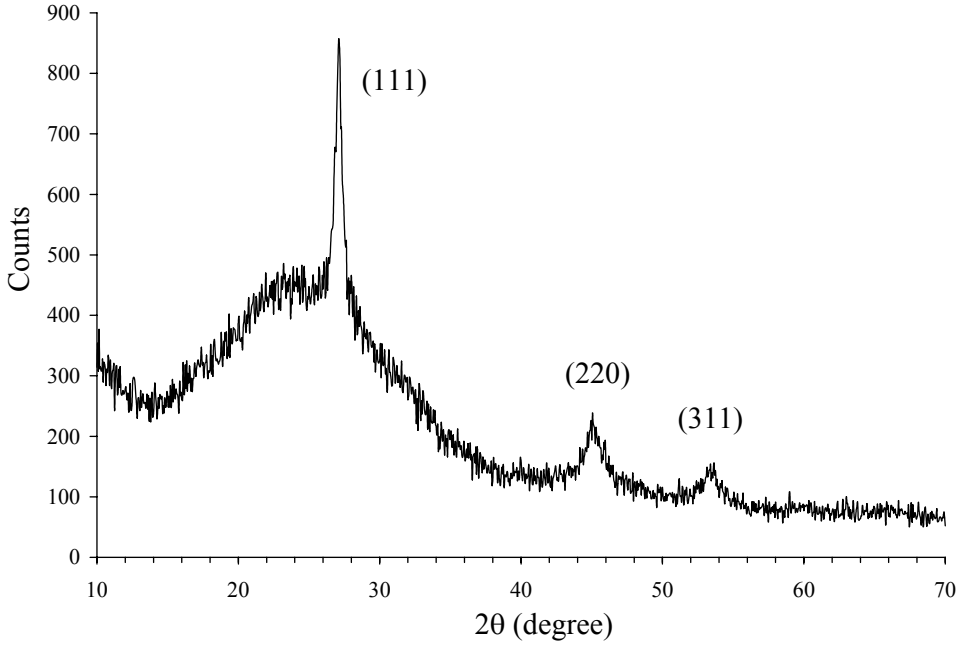

Figure 5.04: XRD spectra of a ZnSe film (annealed at 423K for 1 hour) of thickness 3100 Å thermally deposited at substrate temperature 423K

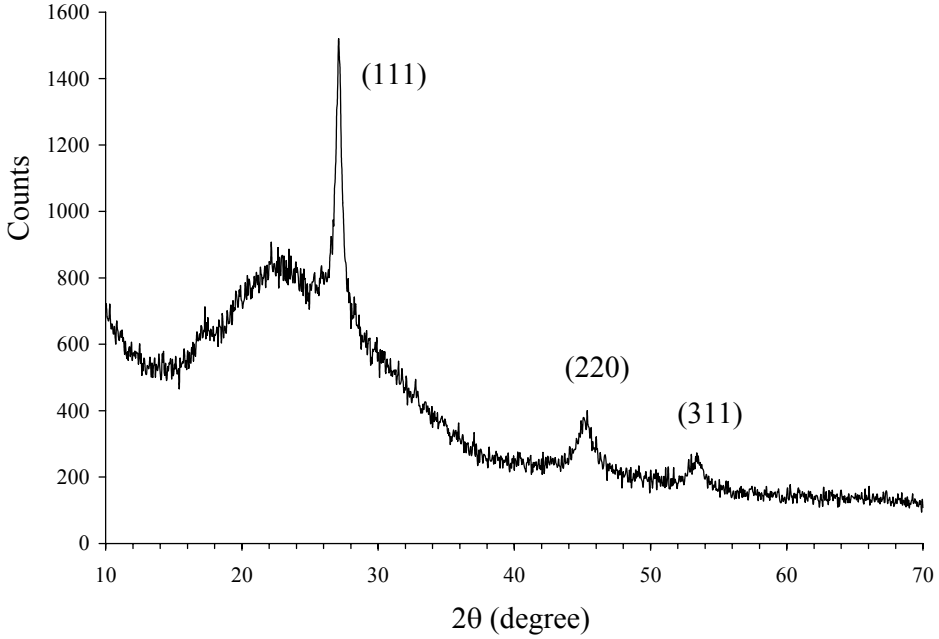

Figure 5.05: XRD spectra of a ZnSe film (annealed at 473K for 1 hour) of thickness 3200 Å, thermally deposited at substrate temperature 473K

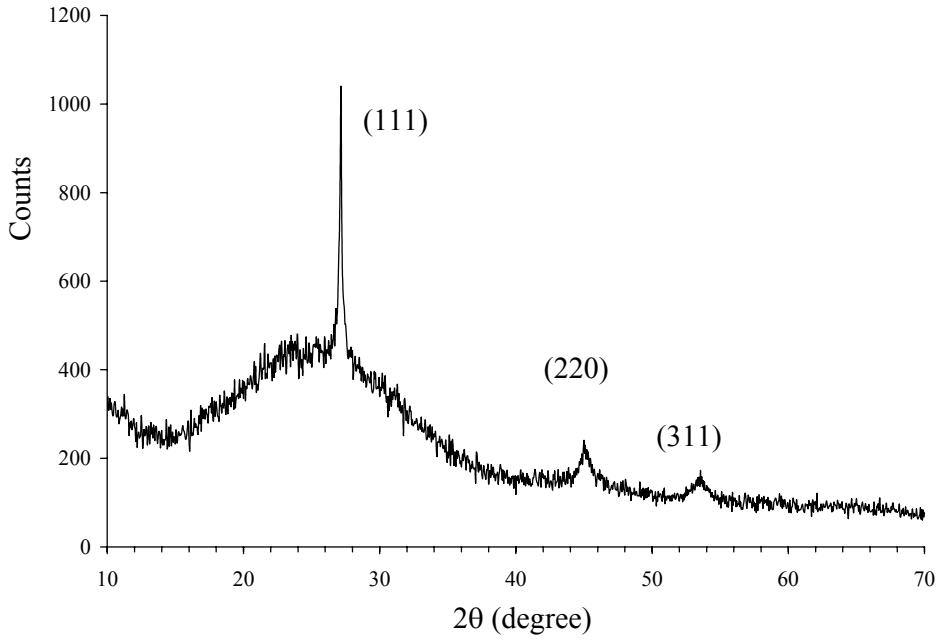

Figure 5.06: XRD spectra of a ZnSe film (annealed at 523K for 1 hour) of thickness 2900 Å, thermally deposited at substrate temperature 523K

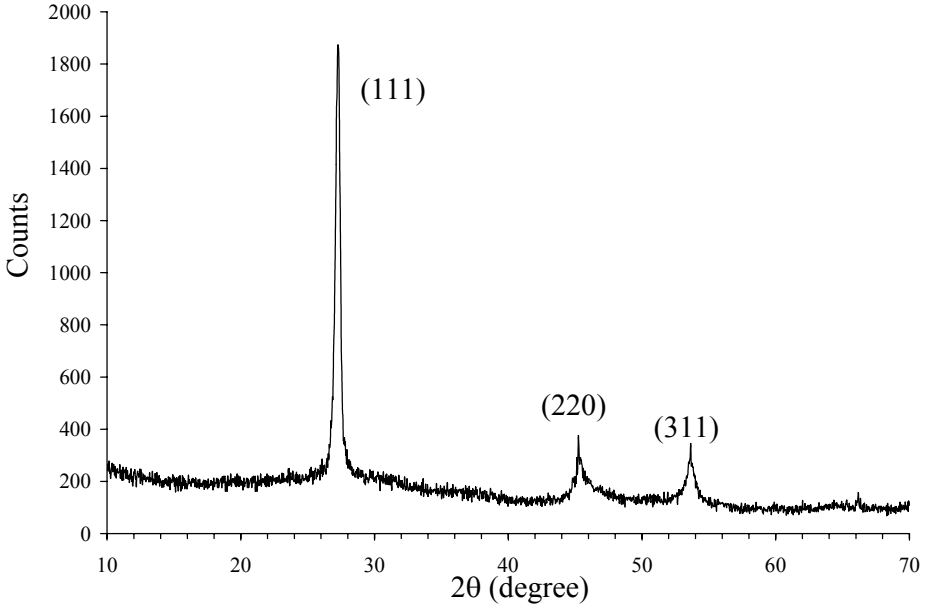

Figure 5.07: XRD spectra of a ZnSe film (annealed at 573K for 1 hour) of thickness 3000 Å, thermally deposited at substrate temperature 573K

The X-ray diffractograms of ZnSe films deposited on glass substrate at different substrate temperatures have been shown in figures from Fig 5.02 to Fig 5.07. Fig. 5.02 shows the X-ray diffraction pattern of an annealed ZnSe thin film of thickness 2150Å deposited at substrate temperature 303K. This film is found to be polycrystalline with a little broad peak corresponding to 2θ values at 27.2^0. Fig. 5.03 to Fig. 5.07 show the X-ray diffraction patterns of annealed ZnSe films of thickness in between 2700Å to 3200Å deposited at different substrate temperatures (T_s) i.e, 373K, 423K 473K 523K and 573K respectively. The as-deposited ZnSe thin films deposited at room temperature are found to be amorphous in nature, while it becomes polycrystalline (Fig. 5.02) on annealing it at 373K for one hour. The X-ray diffraction patterns show that the films prepared at elevated substrate temperatures and annealed at the temperature same as the substrate temperature for 1 hour are polycrystalline in nature. More numbers of diffraction peaks with higher intensity are observed for the annealed films than the freshly prepared films. The main features of the diffraction patterns of the films prepared at different substrate temperatures are the same but only the peak intensity varies. The diffraction spectra display the characteristic diffraction peaks of the cubic phase of ZnSe with zincblende structure [341]. Three prominent diffraction peaks were observed at 2θ values nearer to 27.224, 45.23 and 53.649

degree corresponding to (111), (220) and (311) planes respectively of this phase and indicate random orientation of crystallites in these films [342]. However, in all cases the intensities of the (220) and (311) peaks are extremely low in comparison with the (111) one. This indicates a preferential orientation of the micro-crystallites along [111] direction perpendicular to the substrate. The [111] is the close packing direction of zincblende structure. It is also observed that with increasing T_s or annealing, the peak intensity (counts/sec) increases and the peaks become sharper indicating larger crystallite size D at elevated substrate temperature or on annealing.

5.1.2 Microstructural parameters

5.1.2.1 Lattice constant

The lattice constant, a of ZnSe thin films prepared on glass substrates at different substrate temperatures were calculated for each plane using the relation 3.02 (for cubic structure). The values are tabulated in table 5.02. The lattice constant is found to have slightly different values for different orientations of the same film. This is due to several sources of error in the measurement of 2θ. To determine the accurate value of lattice constant of a film, the lattice constant, a already found for each plane (i.e., for different θ) have been plotted against the error function $f(\theta) = \frac{1}{2}\left(\cos^2\theta/\sin\theta + \cos^2\theta/\theta\right)$ (Nelson–Riley plot) as discussed in chapter 3. The corrected value of lattice constant is estimated from the intercept of this plot at $f(\theta)=0$ i.e., where the error function is zero. The Fig. 5.08 (a) and (b) are the Nelson Riley plots of the films prepared at different substrate temperatures. The corrected values of lattice constants found for the film are tabulated in Table 5.03. Variation of lattice constant (corrected) with substrate temperature has been shown in Fig. 5.09. It is seen from the plot that the lattice constant first increases with substrate temperature and reaches nearer to the value of lattice constant of bulk ZnSe (5.667 Å) at substrate temperature in between 500K and 523K. Above this substrate temperature the lattice constant shows nearly a constant value. The deviation of lattice constants of these films from that of bulk sample indicates that the films are in stress. Further, the lattice constant of films of higher thickness (3000 Å) has been found to be lower than that of films of lower thickness (2100 Å).

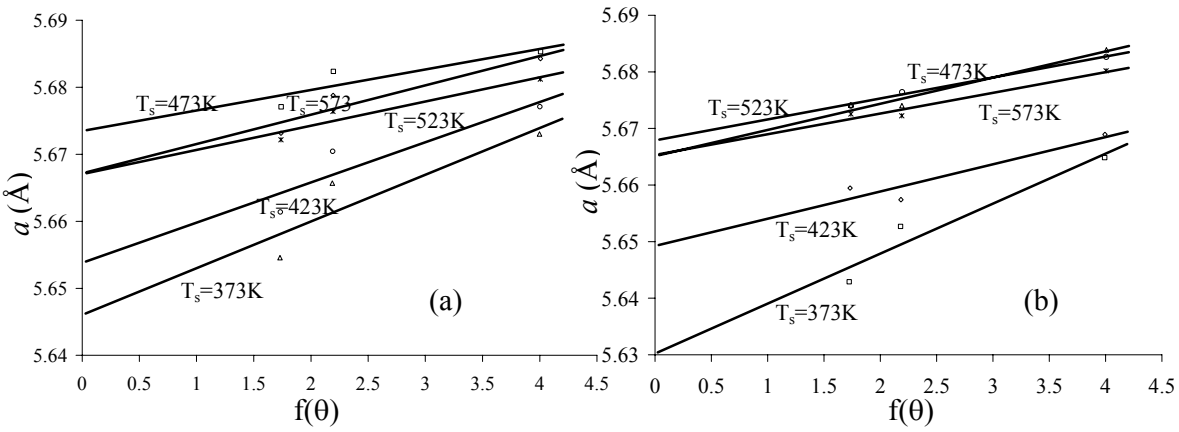

Figure 5.08: Nelson-Riley plots for calculation of corrected value of lattice constant of ZnSe films deposited at different substrate temperatures of thickness, (a) 2100Å and (b) 3000 Å

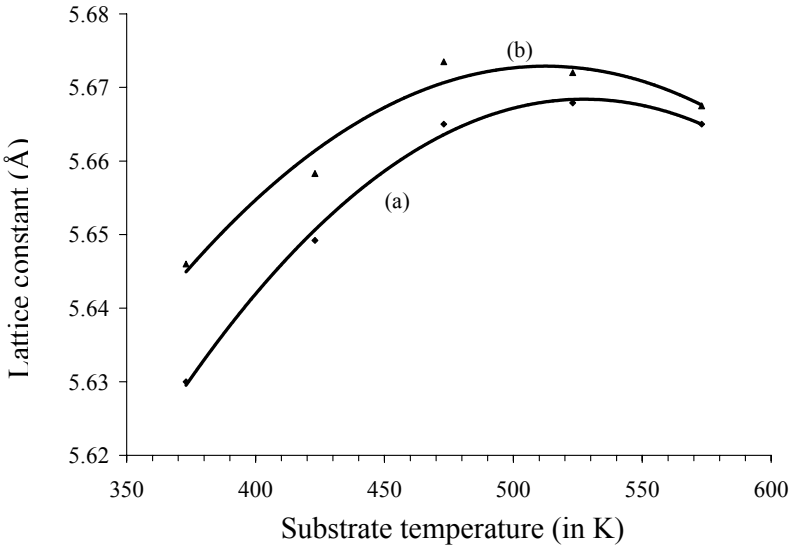

Figure 5.09. Variation of lattice constant (corrected) of ZnSe film with temperature of the substrate during deposition, films thickness: (a) 3000Å and (b) 2100 Å

5.1.2.2 Grain size measured

The FWHM (Full Width at Half Maximum) for most preferred [prominent diffraction peak] plane (111) of all the films prepared at different substrate temperatures were measured. FWHM has been found to decrease markedly with film thickness and substrate temperature. The average grain size (D) of ZnSe films was calculated from the value of FWHM of (111) peak using the Debye-Scherrer's relation, $D = k\lambda / \beta \cos\theta$. Table 5.02 shows a comparative look of grain size for different planes of the ZnSe thin films of different thicknesses prepared at different substrate temperatures on glass substrates. The grain size is found to increase with increase of substrate temperature.

5.1.2.3 Average Grain size and strain measured from W-H plot

The broadening of X-ray diffraction peaks arises due to the presence of stress and strain in the thin film samples. According to Williamson and Hall for Cauchy nature of broadened profile, we have the relation (3.07) as discussed in 3.1.4,

$$\frac{\beta \cos\theta}{\lambda} = 4\varepsilon \frac{\sin\theta}{\lambda} + \frac{1}{D} \qquad (3.07)$$

where β is the full width at half of the maximum, D is the average grain size and ε is the average strain developed in the film.

For the multiple ordered diffraction pattern of a sample, for each peak found at different 2θ, β values are different. Now, when $\frac{\beta \cos\theta}{\lambda}$ versus $\frac{2\sin\theta}{\lambda}$ is plotted, according to above relation (3.07), it will be a straight line (called Williamson and Hall plot). Therefore, the intercept and slope of this plot will give the average grain size (D) and average strain (ε) respectively. Fig. 5.10 and Fig. 5.11 are the Williamson and Hall (W-H) plots for the films prepared at different substrate temperatures. In this study, the corrected value of full width at half maximum (β) of each peak by subtracting instrumental broadening from the observed peak width is used. The average grain size (D) and average strain (ε) of the films were calculated from the intercept and slope of these linear plots respectively. The calculated average grain sizes and average strain of different films are tabulated in table 5.03. Figure 5.12 shows the variation of average grain size of the prepared films with substrate temperature for two ranges of thickness.

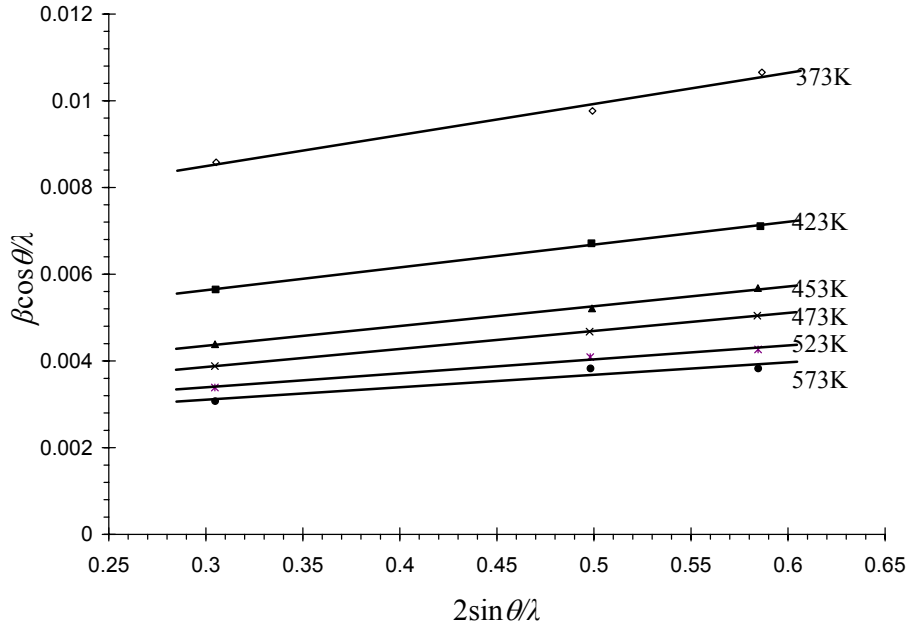

Figure 5.10: W-H plots of ZnSe films of thickness 2100 Å deposited at different substrate temperatures

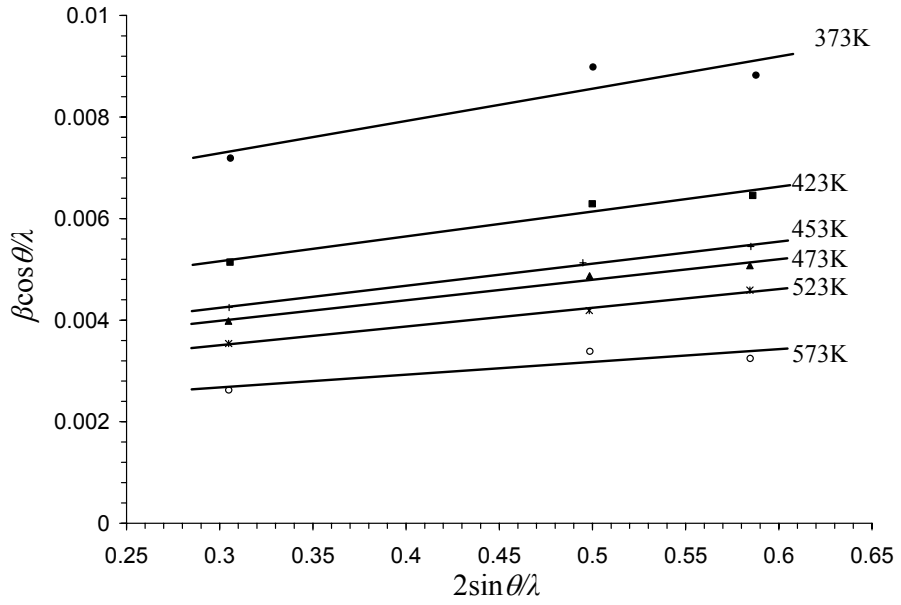

Figure 5.11: W-H plots of ZnSe films of thickness 3000 Å deposited at different substrate temperatures

The average internal strain of the film prepared at 373K is found to be 3.6×10^{-3} which is reduced to 1.25×10^{-3} for the film prepared at 573K. Figure 5.13 shows the variation of average micro strain of the films of different thicknesses with the substrate temperature. Comparison of Fig 5.12 with Fig 5.13 shows that with

increase of substrate temperature during deposition, the average grain size increases while average strain developed in the film decreases. Average grain size has been found to increase with thickness while average strain found to decrease.

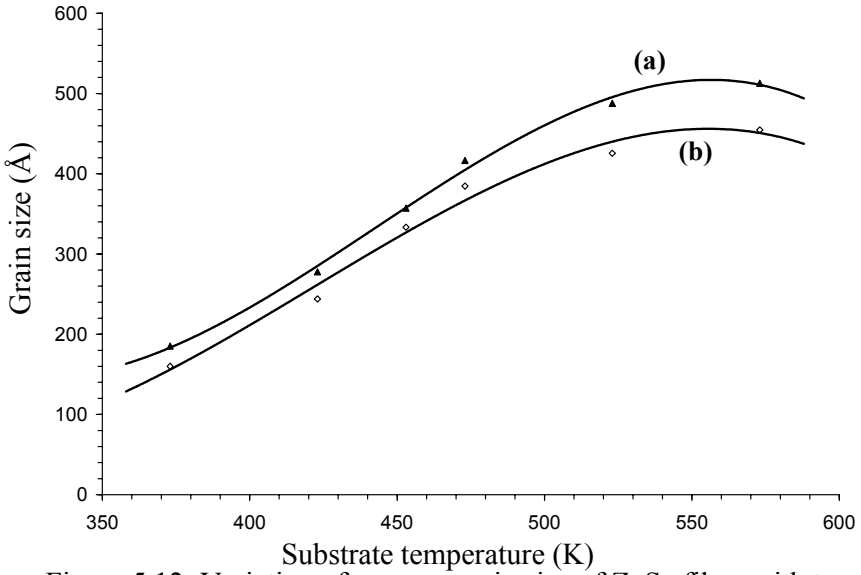

Figure 5.12: Variation of average grain size of ZnSe films with temperature of the substrate during deposition of thickness (a) 3000Å and (b) 2100 Å

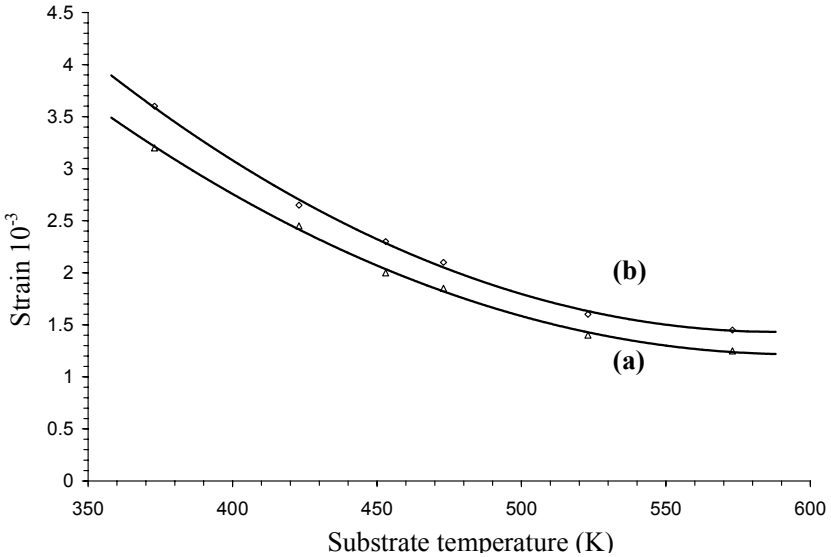

Figure 5.13: Variation of average internal strain of ZnSe films with temperature of the substrate during deposition of thickness (a) 3000Å and (b) 2100 Å

5.1.2.4 Average internal stress

A stress is always developed in all vacuum deposited films due to lattice misfit with the substrate. The average internal stress developed in the films is calculated by

using the relation (3.05) as discussed in chapter 3.1.3. In the calculation, standard value of lattice constant (a_0 =5.667 Å), Young's modulus (E =67.2×10^9 dyne/cm^2) and Poisson's ratio (γ=0.28) for bulk material [59] are used. The negative value of average stress indicates the compressive stress and the positive sign of the stress indicates the tensile stress [343]. From Fig. 5.14, it is seen that ZnSe films deposited at 373K possess compressional stress and as substrate temperature is raised it decreases. Above about 473K tensile stress is developed in the films of thickness 2100 Å. Similar behaviour was observed by other workers on physical vapour deposited ZnSe films [58, 140, 142, 344]. This behaviour indicates that tensile free ZnSe film of thickness about 3000 Å can be vacuum deposited on glass substrate maintaining the substrate temperature around 473K. This temperature however has been found to vary with film thickness.

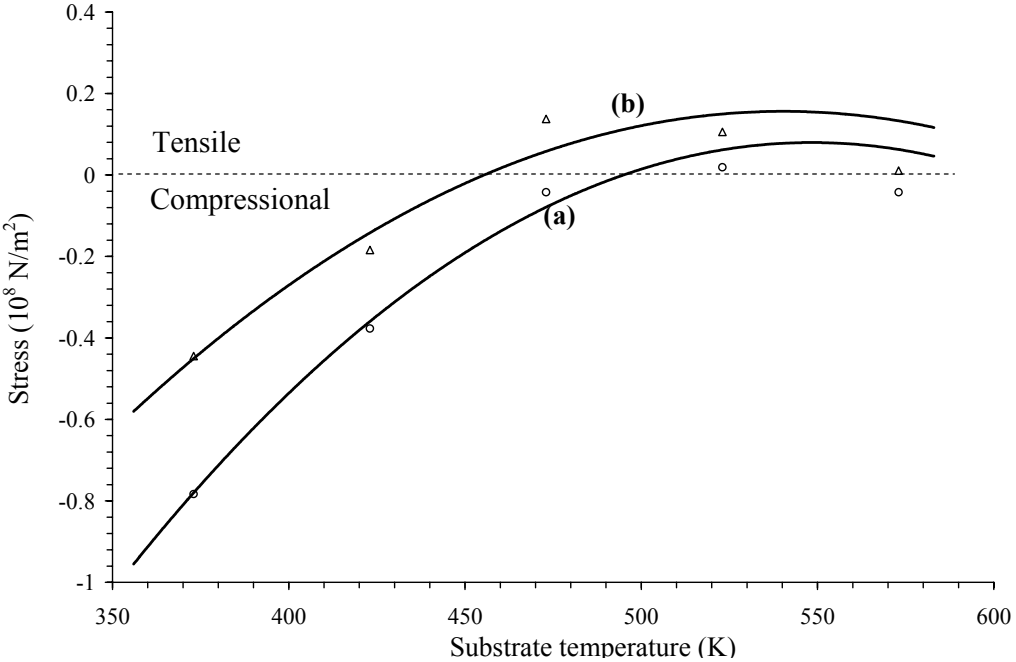

Figure 5.14: Variation of average stress of ZnSe films with temperature of the substrate during deposition of thickness (a) 3000Å and (b) 2100 Å

5.1.2.5 Dislocation density of ZnSe thin films

The average dislocation density of ZnSe thin films for the preferred orientation has been evaluated making use of the values of grain size, average microstrain and lattice constants in the relation (3.09), $\rho_{hkl} = m\varepsilon / aD$.

Here the value of the constant m=15 has been taken for (111) plane as discussed in chapter 3.1.5. The dislocation density (ρ) along preferred orientation [111] calculated for annealed ZnSe thin films of different thicknesses deposited at different substrate temperatures are tabulated in Table 5.02 and presented in figure 5.15. It is seen that the dislocation density decreases significantly with increase of substrate temperature up to 473K and then decreases slowly beyond this temperature.

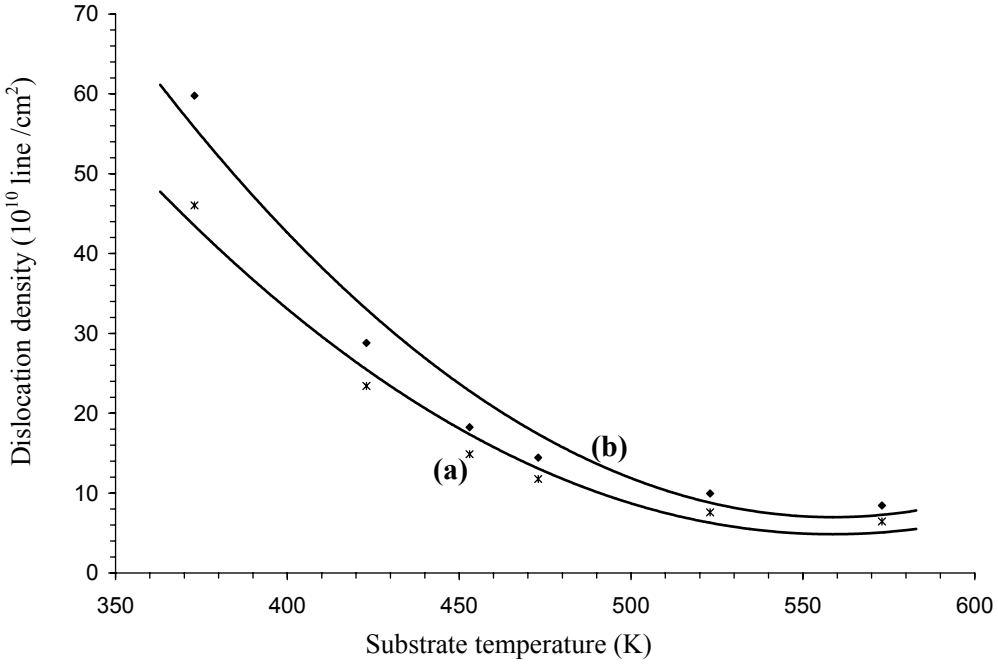

Figure 5.15: Variation of lattice dislocation density of ZnSe films with temperature of the substrate during deposition of thickness (a) 3000Å and (b) 2100 Å

Table 5.02: Structural parameters of ZnSe films deposited on glass substrate at different substrate temperatures

Substrate temperature (K)	Thickness in (Å)	Plane hkl	Interplanar spacing (*d*) (Å)	Lattice constant (Å)	FWHM (degree)	Grain Size (Å)
373	2000	111	3.27532	5.673	0.79	111
		220	2.00313	5.666	0.88	108
		311	1.70492	5.655	0.97	101
	2800	111	3.27060	5.665	0.71	127
		220	1.99852	5.653	0.83	114
		311	1.70140	5.643	0.93	105
423	2100	111	3.27768	5.677	0.56	168
		220	2.00481	5.670	0.73	134
		311	1.70697	5.661	0.80	112
	3100	111	3.27296	5.669	0.52	182
		220	2.00019	5.657	0.69	142
		311	1.70639	5.659	0.76	129
473	1900	111	3.28240	5.685	0.37	243
		220	2.00900	5.682	0.54	175
		311	1.71170	5.677	0.62	158
	3200	111	3.28159	5.684	0.33	272
		220	2.00607	5.674	0.51	186
		311	1.71081	5.674	0.57	172
523	1800	111	3.28182	5.684	0.32	281
		220	2.00775	5.678	0.48	197
		311	1.71052	5.673	0.52	188
	2900	111	3.28088	5.682	0.29	310
		220	2.00691	5.676	0.46	206
		311	1.71078	5.674	0.50	196
573	2200	111	3.28005	5.881	0.30	300
		220	2.00691	5.676	0.42	225
		311	1.71022	5.672	0.49	200
	3000	111	3.27945	5.680	0.27	333
		220	2.00544	5.672	0.37	256
		311	1.71034	5.672	0.43	228

Table 5.03: Micro-structural parameters of ZnSe films deposited on glass substrate at different substrate temperatures

Substrate temperature (K)	Thickness (Å)	Corrected Lattice Constant (Å)	Average Grain Size (Å)	Average Internal stress (10^8N/m^2)	Average Internal strain (10^{-3})	Dislocation density (10^{10}line/cm^2)
373	2000	5.646	160	-4.447	3.60	59.77
	2800	5.630	185	-7.835	3.2	46.04
423	2100	5.658	244	-1.842	2.65	28.80
	3100	5.650	278	-3.769	2.45	14.87
473	1900	5.674	385	+1.376	2.10	14.43
	3200	5.665	417	-0.423	1.85	11.75
523	1800	5.672	425	+1.058	1.60	9.94
	2900	5.668	488	+0.190	1.40	7.60
573	2200	5.668	454	+0.106	1.45	8.44
	3000	5.665	513	-0.423	1.25	6.45

5.1.3 Morphological study of ZnSe thin films by scanning electron microscope (SEM)

Surface morphology of thermally deposited ZnSe thin films were studied using the Scanning Electron Microscope (LEO 1430 VP) operating with an accelerating voltage 15-20kV. Figures 5.16, 5.17 and 5.18 show the scanning electron micrographs of a few typical as deposited and annealed ZnSe thin films deposited at different substrate temperatures. SEM micrographs show that the films are continuous on the glass substrates and the annealed films deposited at higher substrate temperatures are fairly uniform and polycrystalline. The grain sizes in the films are seen to be almost uniform. There are no macroscopic defects like void, pinhole, peeling or cracks. The SEM photographs of annealed films clearly show the improvement in crystallite size of ZnSe film. The grain size is observed to increase in annealed samples. It may be due to coalescing of smaller grains into effectively larger grains. It has been found that the grain sizes of the annealed films deposited at

substrate temperature of 473K is in the range of 410 Å to 490 Å. Therefore, it is observed that the average value of grain size measured from SEM is slightly higher than that of average crystallite size measured by XRD technique (385 Å to 417 Å, table 5.03).

From the featureless surface morphology of the annealed films thermally deposited at elevated temperature, we can anticipate that these films will exhibit very low optical scattering losses and should therefore be suitable for optoelectronic applications [345, 346].

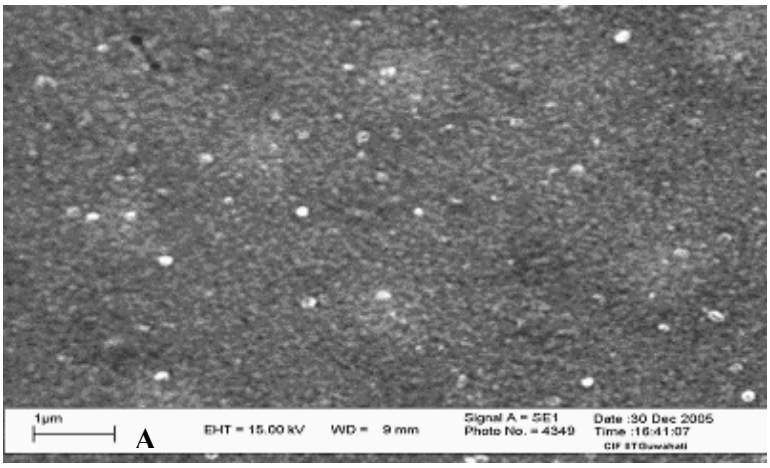

Figure 5.16(A): SEM photograph of a fresh unannealed ZnSe film of thickness 1500Å deposited at substrate temperature 373K

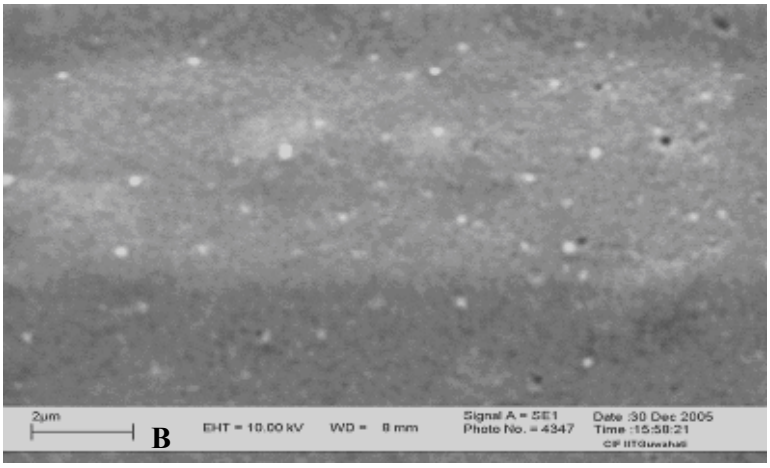

Figure 5.16(B): SEM photograph of ZnSe film of thickness 1500Å deposited at substrate temperature 373K annealed at 473K for 1 hour.

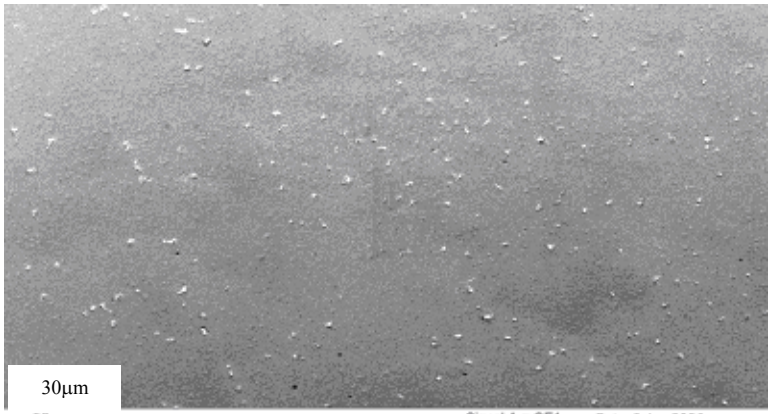

Figure 5.17(a): SEM photograph of a fresh unannealed ZnSe film of thickness 1400Å deposited at T_s=423K

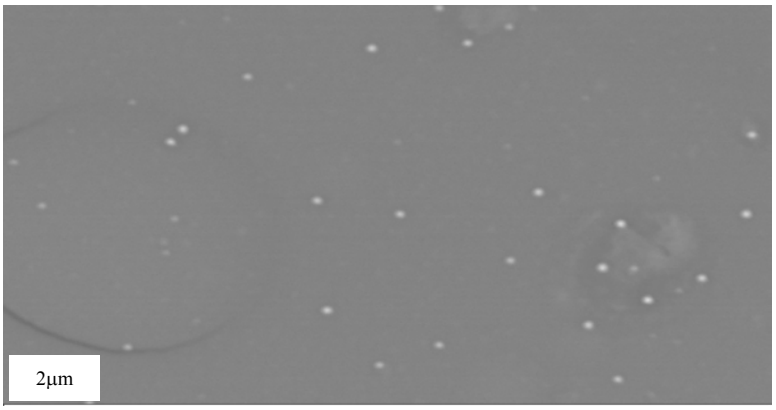

Figure 5.17(b): SEM photograph of a ZnSe thin film of thickness 1400Å deposited at T_s=423K and annealed at 473K for 1 hour

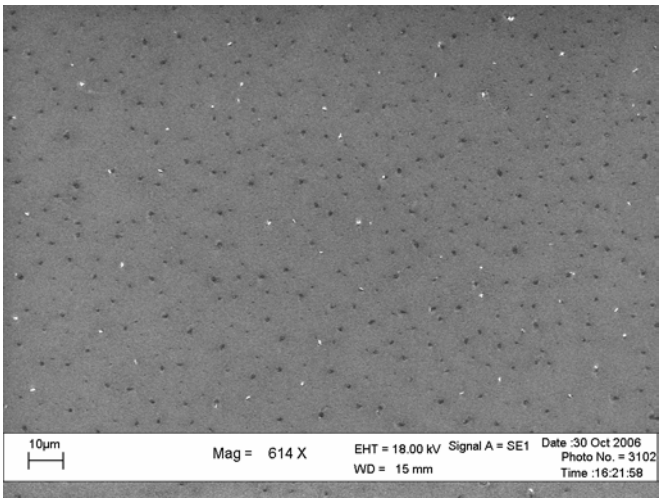

Figure 5.18(a): SEM photograph of a ZnSe film of thickness 1900Å deposited at T_s= 473K and annealed at 473K for 1 hour

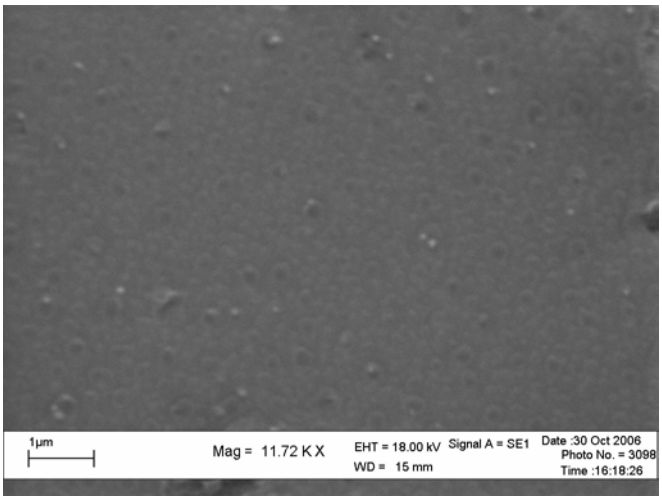

Figure 5.18(b): SEM photograph of a ZnSe film of thickness 1900Å deposited at T_s=473K and annealed at 473K for 1 hour

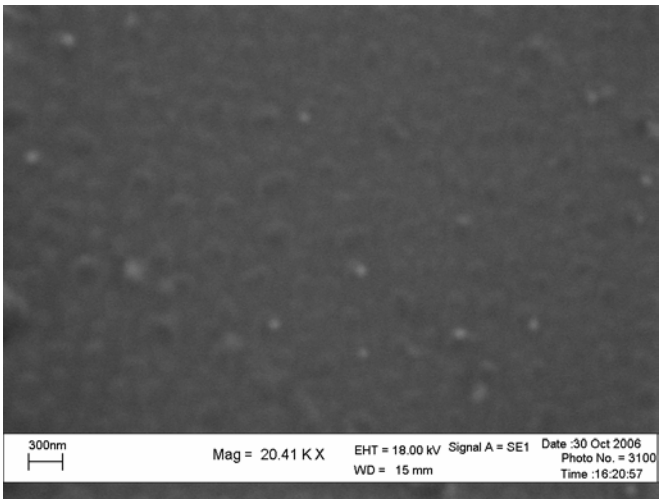

Figure 5.18(c): SEM photograph of a ZnSe film of thickness 1900Å deposited at T_s=473K and annealed at 473k for 1 hour

5.1.4 Compositional Analysis of ZnSe films

5.1.4.1 Energy dispersive X-ray Analysis (EDAX)

The quantitative compositional analyses of the ZnSe films prepared at different substrate temperatures were carried out by EDAX (Energy dispersive X-ray Analyzer) attached with the SEM. Typical EDAX results showing the atomic contents of elements present in some of the samples are presented in figure 5.19(a) and 5.19(b). The films prepared at lower substrate temperatures are found to be Zn deficient as reported by other workers [142]. This is because the vapour pressure of Se is greater than that of Zn and their sticking coefficients are also different. For the ZnSe film thermally deposited at substrate temperature 473K, the average atomic percentage of Zn and Se is found to be 49.2 and 50.8 respectively showing that the film is almost stoichiometric. The peaks of Si and Ca were also found which are due to the elements present in the glass substrate.

5.1.4.2. X-ray Fluorescence (XRF) studies

For elemental analysis ZnSe thin films were loaded into a perspex mask of Axios XRF spectrometer. The X-ray tube was operated at 40kV and 40mA. The characteristics of the X-rays originated from the sample were analyzed by LiF 200, LiF 220 and PX1 crystals using Flow and Scintillation tandem detectors. Software program was made using X40 software and recorded the scanning of ZnSe thin films. Fig. 5.20(a), 5.20(b) and 5.20(c) show the XRF spectra of ZnSe thin film deposited at substrate temperature 423K analyzed by the three detectors. The spectrum in Fig. 5.20(a) exhibits the prominent peaks of SeK_{β}, SeK_{α}, ZnK_{β} and ZnK_{α} lines showing the presence of Zn and Se in the prepared film. The spectrum shown in fig 5.20(b) shows peaks of SeL_{α}, SeL_{1}, ZnL_{α} and ZnL_{1} lines along with the lines of MgK_{A} and NaK_{A} lines. The spectrum in Fig 5.20(c) shows the spectra of SeK_{B} and ZrK_{A}. Peaks for Mg, Na and Zr appear from the target used in the XRF instrument and probable impurities present in glass substrate used. The figure also shows another line for presence of oxygen which is because of the absorption of atmospheric oxygen by the ZnSe film. Fig 5.21(a), (b), (c) and (d) show the XRF spectra of Al doped ZnSe films. The spectra shown in figure 5.21(a) and 5.21(b) are similar to the Figure 5.20(a) and

(b) which indicate the presence of Zn and Se in the films. The peak found at $2\theta=145.12^0$ in figure 5.21 (d) is due the presence of Al in the film.

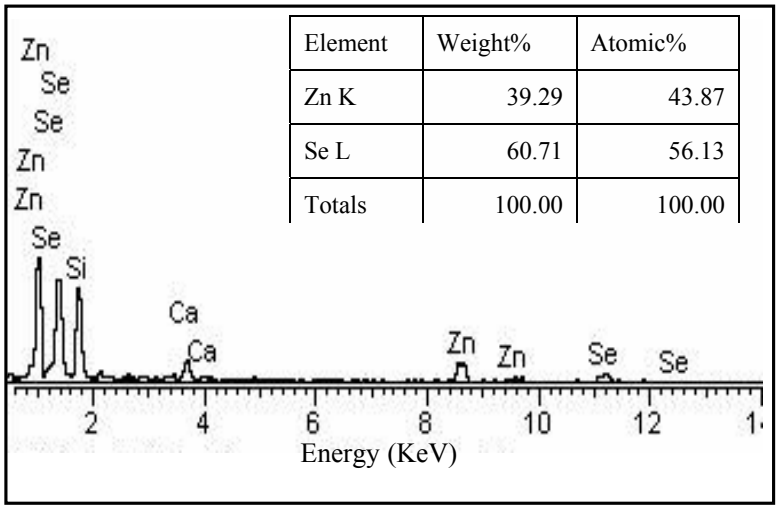

Element	Weight%	Atomic%
Zn K	39.29	43.87
Se L	60.71	56.13
Totals	100.00	100.00

Figure 5.19(a): The EDAX spectrum giving the compositional information of ZnSe film deposited at substrate temperature 373K.

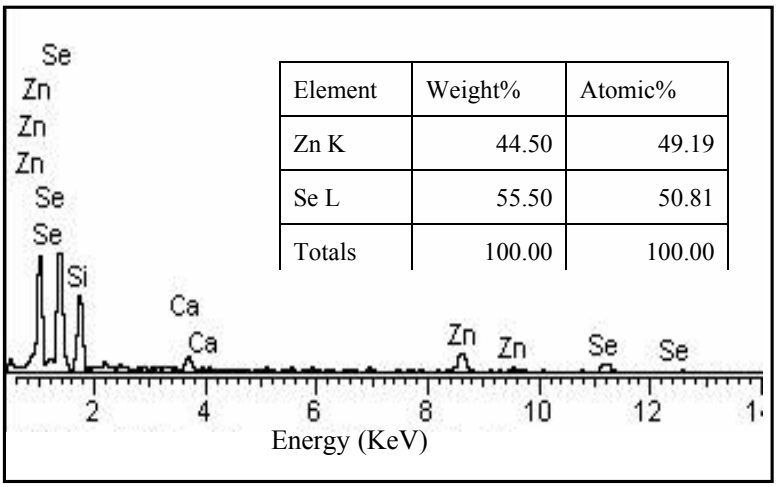

Element	Weight%	Atomic%
Zn K	44.50	49.19
Se L	55.50	50.81
Totals	100.00	100.00

Figure 5.19(b): The EDAX spectrum giving the compositional information of ZnSe film deposited at substrate temperature 473K.

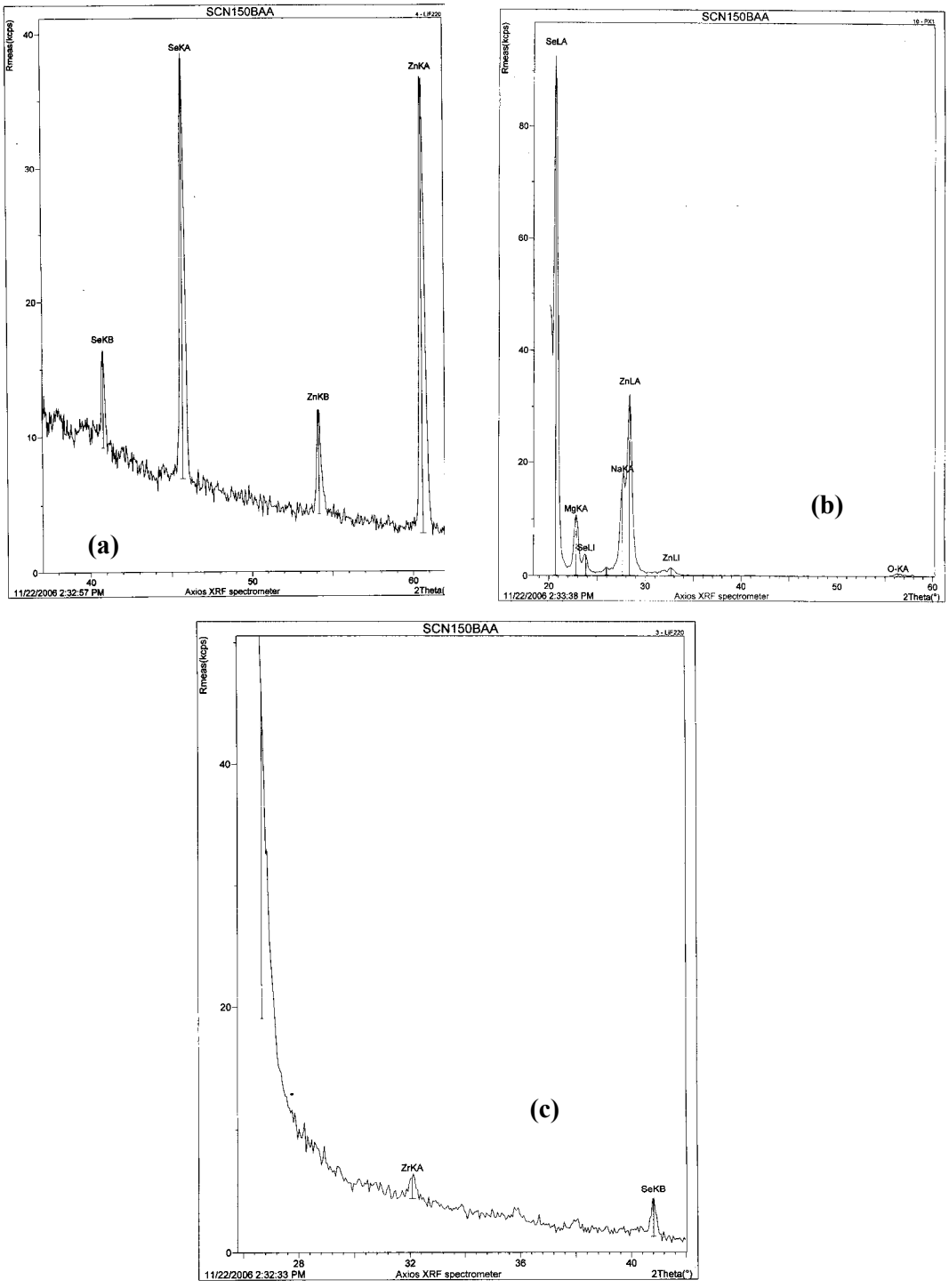

Figure 5.20 : XRF spectra of ZnSe films deposited at substrate temperature 423K analyzed by (a) LiF 220, (b) PX1 and (c)LiF 200 crystals respectively.

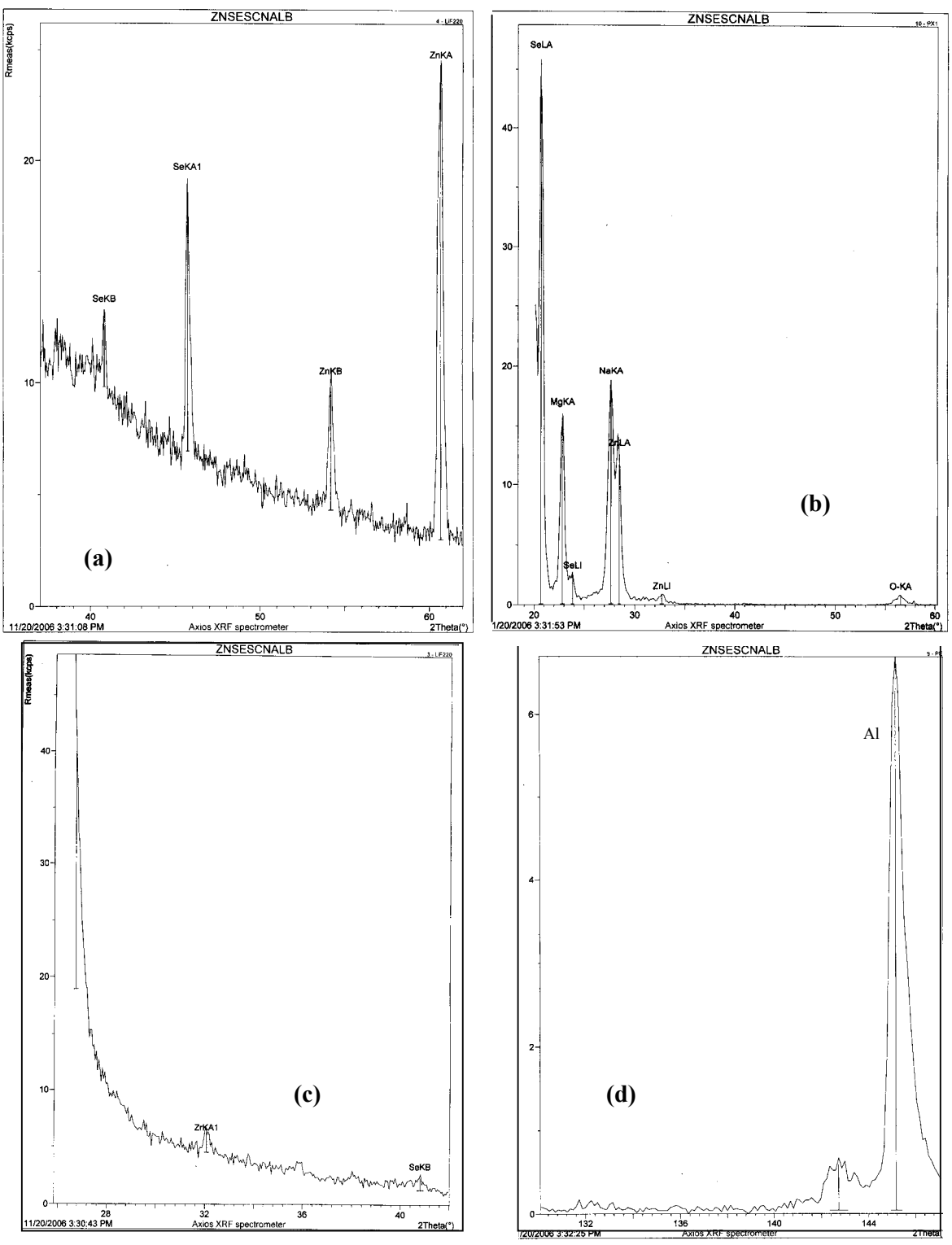

Figure 5.21 : XRF spectra of Al-doped ZnSe films deposited at substrate temperature 423K analyzed by (a) LiF 220, (b) PX1, (c)LiF 220 and (d) PE crystals respectively.

The structural properties of thermally deposited ZnSe films were studied from their X-ray diffractograms. It is found that, the films deposited at elevated

temperatures are in cubic phase of ZnSe with zincblende structure. The lattice constant of the films increases with substrate temperature during deposition and reaches nearer to its value of bulk ZnSe at substrate temperature in between 473K and 523K. The grain size of the films is found to increase with increase of substrate temperature. The average grain size measured from W-H plot of the ZnSe film of thickness 2900 Å deposited at substrate temperature of 523K is found to be 488Å. The stress and dislocation density of the deposited films have also been estimated from the XRD data. The average internal stress and dislocation density of the films deposited at 373K to 573K is found to be in the order of 10^8 N/m^2 and 10^{10} line/cm^2. The stress and dislocation density is found to decrease with increase of substrate temperature. In most of the films the stress is found to be compressional in nature. It is observed that the thermally deposited ZnSe films on glass substrates are in stress and the internal strain of the films decrease with increase of substrate temperature. Since the dislocation density and strain are the manifestation of dislocation network in the films, the decrease in the dislocation density and strain indicates the formation of higher quality films at higher substrate temperatures.

From the morphological and compositional studies of the thermally deposited ZnSe films it is seen that the films prepared at the substrate temperature in the range of 473K to 523K were nearly stoichiometric and uniform. Annealing of the films at 473K for 1 hour further enhances the quality and minimizes the macroscopic defects of the films.

5.2 Electrical and Photoconductivity of thermally deposited ZnSe films:

Before making junctions of thermally deposited ZnSe films, it is necessary to examine ohmic contact to ZnSe and to study the electrical conductivity and photoconductivity. For electrical measurements, the gap-type samples of ZnSe films of desired geometry were prepared. The details of sample preparation and experimental arrangements for measurement of electrical conductivity in dark and under illumination have been given in chapter 4.

5.2.1 Ohmic contact:

In the present study, metal Al (work function 4.1eV) [375] was used for making ohmic contacts to intrinsic as well as n-type ZnSe films (electron affinity= 4.09eV) [376]. The ohmic character of the contact was tested by taking *I-V* characteristics of a typical Al-ZnSe-Al and Al-(n)ZnSe-Al structures for both forward and reverse bias voltages. The doping concentration of n-ZnSe (Al-doping) was 4.8×10^{14} cm^{-3}. Electrode area of both samples was 0.04 cm^2. The *I-V* curves show linear dependence of current with voltage (Fig 5.22). This indicates that Al makes good ohmic contact to ZnSe as well as to (n)ZnSe.

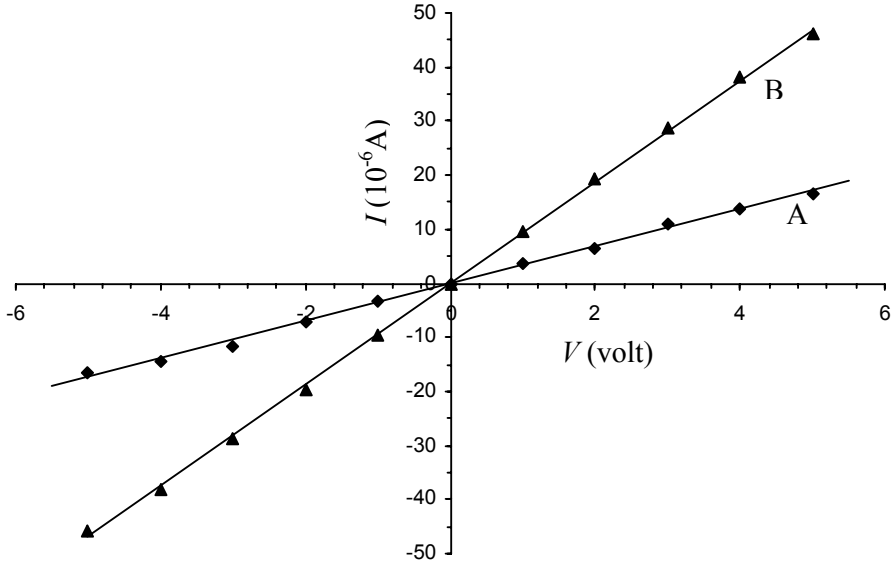

Figure 5.22: *I-V* plots showing ohmic contacts of Al with intrinsic ZnSe and (n)ZnSe films

5.2.2 The effect of substrate temperature on electrical conductivity:

The electrical conductivity of ZnSe films prepared at different substrate temperatures were measured in gap type structure and tabulated in Table 5.04. The as grown intrinsic ZnSe films were found to be highly resistive and at room temperature their conductivity was of the order of $10^{-7}ohm^{-1}cm^{-1}$. The electrical behaviour of as-deposited ZnSe films was found to be unstable. After deposition, the films were heated in vacuum upto 523K at a very slow rate (5K/min) and then allowed to cool slowly. The process was repeated three times and there after the resistivity of the films were found to be stable. The resistivity of the films also exhibited aging effect, decreasing slowly with time and became nearly stable after about 7 days when kept in dry air or in vacuum. Therefore electrical measurements were carried out after stabilization of the films. The room temperature electrical conductivity of ZnSe films deposited at different substrate temperatures have been tabulated in Table 5.04. The nature of change of room temperature electrical resistivity of a ZnSe film with substrate temperature maintained at the time of deposition is represented in Figure 5.23. It is found that electrical conductivity increases with increase of substrate temperature and becomes stable beyond about 453K. Thus in our study, the substrate temperature was maintained at 453K at the time of deposition of the films.

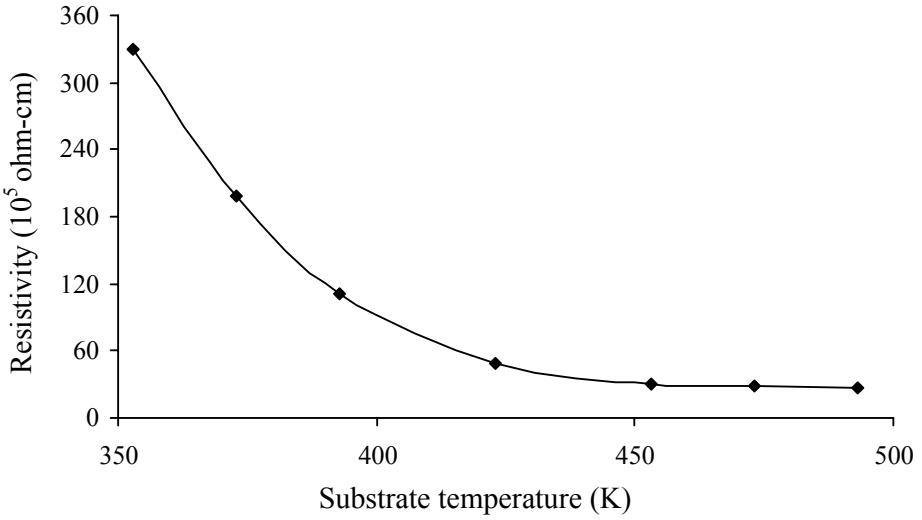

Figure 5.23: Variation of room temperature electrical resistivity of ZnSe films prepared at different substrate temperatures

When Al is coevaporated with ZnSe, the conductivity of the resulting films was increased considerably. Al doped ZnSe films were found to be n-type in nature. As the

ionization energy of donor Al in ZnSe is 0.021 to 0.023 eV [349], the room temperature thermal energy is sufficient to give conductivity at room temperature. The conductivity of Al doped ZnSe films for different doping concentrations are given table 5.05.

5.2.3 Variation of conductivity with Temperature:

The electrical conductivity of ZnSe films both intrinsic and doped, exhibited temperature dependence characteristics of a semiconductor. Temperature dependence of dark conductivity of some samples deposited at substrate temperature 453K have been shown in figure 5.24. The plots show three slopes in the entire temperature range of the experiment. From the intrinsic region, the value of band gap were calculated using the relation (3.15), $\sigma = \sigma_0 \exp\left(-E_g \big/ 2k_B T\right)$. The band gap so obtained at the high temperature range were 2.63 eV, 2.60 eV, 2.59 eV and 2.58 eV for undoped and Al-doped ZnSe films of doping concentration 1.4×10^{14} cm^{-3}, 4.8×10^{14} cm^{-3} and $9.7\times10^{14}cm^{-3}$ respectively (Table 5.05). The corresponding activation energies obtained from the slopes at the two low temperature regions have been tabulated in Table 5.05. Al doping causes a decrease in the band gap energy and the activation energy of the ZnSe film. Since the films were sufficiently thick, these parameters do not seem to be affected by thickness. Decrease of band gap energy and activation energy with increasing doping concentration indicates that there has been band tailing due to increase in doping concentration [350].

The value of activation energy at lower temperature corresponds to impurity conduction due to excess Al. As the temperature is raised the impurity levels are exhausted and the conduction becomes intrinsic in nature. The temperature was not lowered enough to see the phonon assisted conduction mechanism.

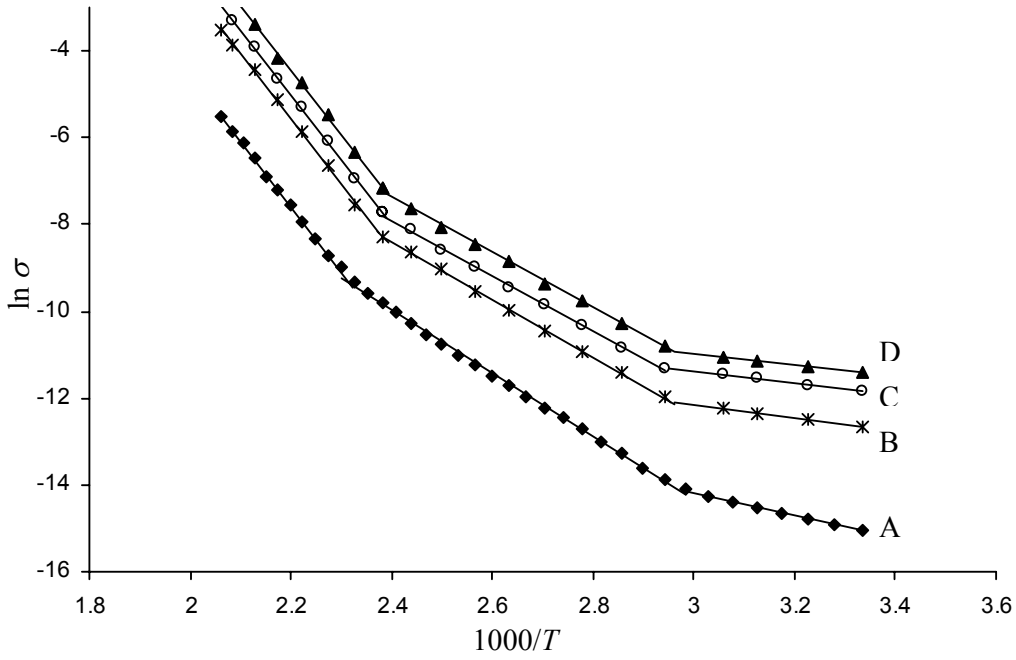

Figure 5.24: ln σ vs 1000/T plots of (A) undoped ZnSe film and Al-doped ZnSe film with doping concentrations: (B) 1.4×10^{14}cm^{-3}, (C) 4.8×10^{14} cm^{-3} and (D)9.7×10^{14} cm^{-3}

Table 5.04: The room temperature electrical conductivity of ZnSe films (undoped) deposited at different substrate temperatures

Temperature of the substrate during film deposition(K)	Electrical conductivity (10^{-8} ohm^{-1}cm^{-1})
353K	3.04
373K	5.04
393K	9.10
423K	20.5
453K	33.0
473K	35.3
493K	37.5

Table 5.05: The conductivity of a few undoped and Al doped ZnSe films for different doping concentration deposited at 453K and vacuum annealed at 453K for 1 hour

Doping Concentration (10^{14} cm^{-3})	Electrical conductivity (10^{-6} $Ohm^{-1}cm^{-1}$)	Band gap (eV)	Activation Energy E_a(eV)	
			Range I	Range II
Undoped	0.330	2.630	0.22	0.63
1.4	3.475	2.597	0.13	0.57
4.8	10.10	2.585	0.12	0.55
9.7	27.80	2.576	0.11	0.55

5.2.4 Photoelectrical Properties:

Thermally deposited Al-doped ZnSe films were found to be photosensitive. The photoconductivity was measured by exposing the gap type sample to different light intensities, from 3000 lux to 6500 lux. Fig. 5.325 shows the plot of photocurrent versus light intensity for a typical Al-doped n-type ZnSe film of doping concentration 4.8×10^{14} cm^{-3}. The plot indicates a gradual increase of photocurrent with light intensity and shows saturation beyond 5500 lux.

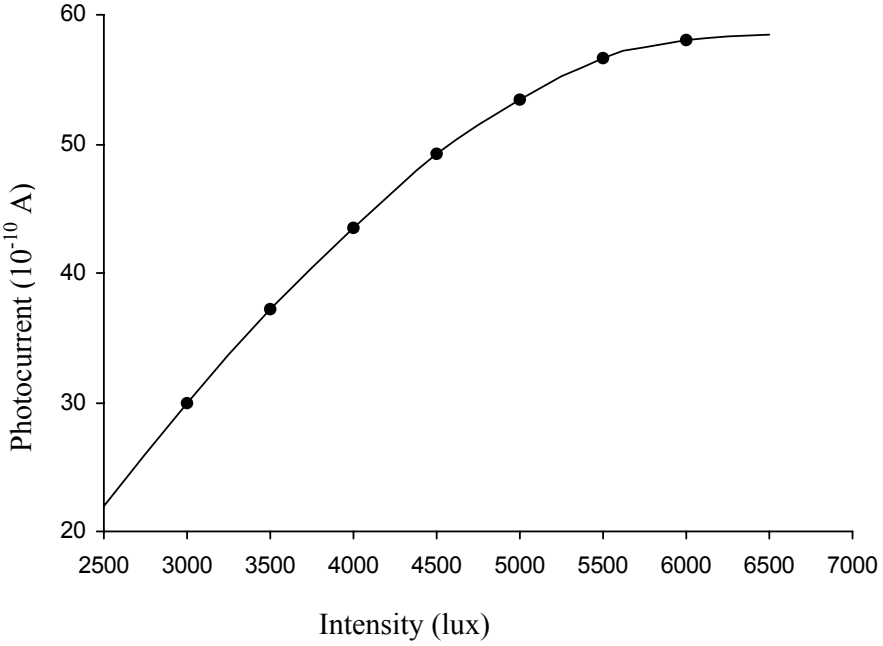

Figure 5.25: Variation of photocurrent with intensity of illumination for (n)ZnSe films

Photoconductive rise and decay:

For studying the photoconductive rise and decay characteristics of Al-doped ZnSe films, a gap-type samples with two Al electrodes deposited on the two ends of a rectangular Al-doped ZnSe films was prepared as discussed in chapter 4 (section 4.8). The rise and decay curves were recorded with an X-Y/t recorder. The measurements were carried out at room temperature and sample was exposed to light of intensity, 3000 lux, 4000 lux and 5000 lux. The details of measurement with arrangement for illumination have been discussed in chapter 4.

Figure 5.26 shows the rise and decay curves of a typical film for intensity of illumination 3000 lux. Both rise and decay have been observed to be slow as seen from the time scale. The rise is comparatively steeper than the decay.

Estimation of photoconductive rise time (t_r) and decay time (t_d) were determined from the tangents to the photoconductive rise and decay curves. The values are found to decrease with increase of illumination. The values of t_r and t_d for a typical sample are tabulated in Table 5.06.

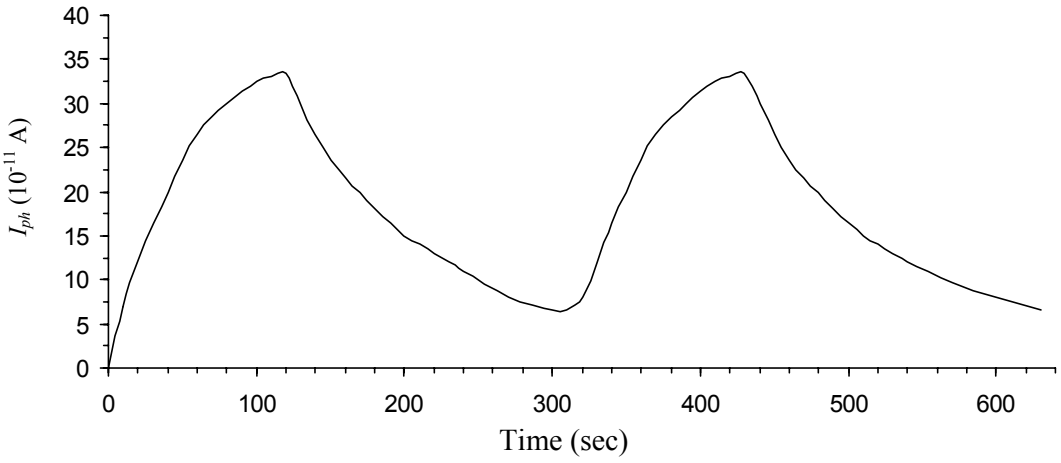

Figure 5.26: Rise and decay of photocurrent with time of a typical Al-doped ZnSe film for intensity of illumination 3000 lux,

Table 5.06: Value of Rise and Decay times and trap depth of a typical Al-doped ZnSe film for three different illuminations at room temperature (300K)

Intensity of illumination (Lux)	Rise time (sec)	Decay time (sec)	Trap depth (eV)
3000	40	95	0.718
4000	40	75	0.718
5000	37	66	0.719

Study of trap depths based on photocurrent decay:

Native defects such as traps can cause a considerable change in electrical and optical properties of the semiconductor thin films [351, 352]. These defects characterize the electronic properties of the material because they give rise to charged centers acting as donors or acceptors [353]. Actually trapping is a fundamental process for energy storage in almost all electronically active solids as well as thin films. This storage is accompanied by the spatial localization of an excited electron or hole, in such a way that the electron or hole is prohibited from moving freely through the crystal unless supplied with thermal or optical energy. When the trapped electron or hole is released, it is free to move until the captured electrons and holes are detained in a restricted volume, called traps [354, 355]. The trap depths can be calculated from the photoconductive decay current by using the decay law [356]

$$I_t = I_0 \exp(-pt_d) \qquad (5.01)$$

where I_0 is the photocurrent at the termination of illumination and I_{ph} is the photocurrent at any subsequent time t_d after termination of illumination and p is the probability of escape of an electron from the trap per second and is given by [357]

$$p = S \exp\left(-\frac{E_t}{kT}\right) \qquad (5.02)$$

Using these two relations we get the expression

$$E_t = kT\left[\ln S - \ln\left(\frac{\ln(I_0/I_t)}{t_d}\right)\right] \qquad (5.03)$$

where E_t is the trap depth for electrons below the bottom of the conduction band, S is the frequency factor (defined in terms of number per second that the quanta from the lattice vibrations (phonons) attempt to eject the electron from the trap), k the Boltzmann constant, T the ambient temperature in K. For ZnSe the frequency factor S is considered as 10^{10} sec^{-1}[139].

In Fig. 5.27 plots of $\ln(I_0/I_t)$ versus decay time (t_d) of a ZnSe film have been shown for three different illuminations. From the slope of these plots, using the relation (5.03) the trap depths of the film were calculated and tabulated in table 5.06. The trap depth of ZnSe film deposited at 473 K is found to be 0.718 eV, which is less dependent on intensity of incident light.

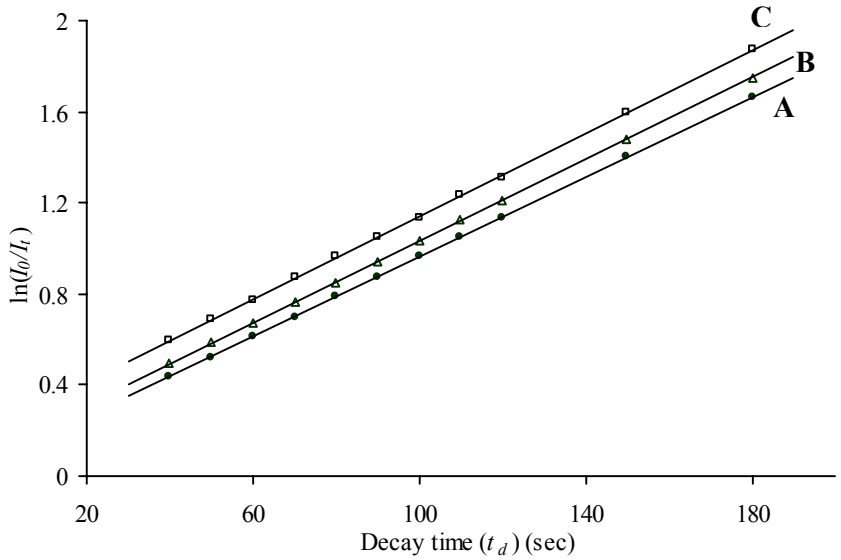

Figure 5.27: Plot of $\ln(I_0/I_t)$ versus decay time (t_d) of a typical ZnSe film for three different illuminations: (A) 3000 lux, (B) 4000 lux and (C) 5000 lux

From the above electrical studies it is found that Al makes good ohmic contact to both intrinsic and n-type ZnSe films. The electrical conductivity of the thermally deposited ZnSe films was found to depend on the substrate temperature during deposition. It was found to increase on increase of substrate temperature and annealing. The undoped ZnSe films deposited at substrate temperature 453K has conductivity 3.3×10^{-7} $Ohm^{-1}cm^{-1}$ while, the conductivity of the ZnSe film doped with Al by co-evaporation method was found to increase upto 27.8×10^{-6} $Ohm^{-1}cm^{-1}$ with maximum attainable doping concentration 9.7×10^{14} cm^{-3}. The Al doped ZnSe films were found n-type. From the slope of the higher temperature range of ln σ vs $1000/T$ plots, the band gap of the films were calculated and found to be in the range of 2.58 eV to 2.63 eV. From the another two slopes of low temperature range of ln σ vs $1000/T$ plots, two activation energies of each film were calculated. The activation energies of undoped film were found to be 0.22eV and 0.63 eV and that of the films of doping concentrations 1.4×10^{14} cm^{-3}, 4.8×10^{14} cm^{-3} and 9.7×10^{14} cm^{-3} have been found to be 0.13eV and 0.57eV; 0.12eV and 0.55eV; and 0.11eV and 0.55eV respectively. The Al-doped ZnSe films were found to be photosensitive and the photocurrent was found to be a function of intensity of illumination. The trap depth calculated from decay curve has been found to be about 0.72eV.

5.3 Optical properties of ZnSe thin films:

The optical constants of films are required for correct design of optoelectronic devices and to determine the losses in detectors and optical coatings. The optical absorbance and transmittance spectra of ZnSe films in the present studies were recorded using the UV-Visible spectrophotometer (Carry 300, Varian Australia) in the range 350nm to 900nm wavelength at room temperature. The details of measurements have been discussed in chapter 4.

5.3.1 Transmittance:

The transmission spectra of a few ZnSe films of different thicknesses are shown in Fig.5.28. Interference maxima (T_M) and minima (T_m) are observed in the transmission curves due to multiple reflections at the film-substrate interface. The number of the interference fringes formed in the transmission curves depend on the thickness of the film. For thick films producing interference pattern in the transmission spectra, the transmittance in the interference region is calculated for those wave lengths where the interference maxima (T_M) and minima (T_m) are observed. For this purpose, T_{M} and T_{m} for that particular wavelength were recorded from the envelopes created over the maxima and minima of the spectra (Fig 5.29) and the transmittance is calculated by taking geometrical mean of T_{M} and T_{m} for each wavelength ($T = \sqrt{T_M T_m}$) [301]. The transmittance maxima and minima of a film have been tabulated in Table5.07. The transmittance of film prepared at constant substrate temperature is found to decrease with increase of film thickness. Figure 5.29 shows transmission spectra of a typical ZnSe film deposited at substrate temperature 453K before and after annealing at 453K for one hour in vacuum. On heat treatment the transmittance is found to increase slightly.

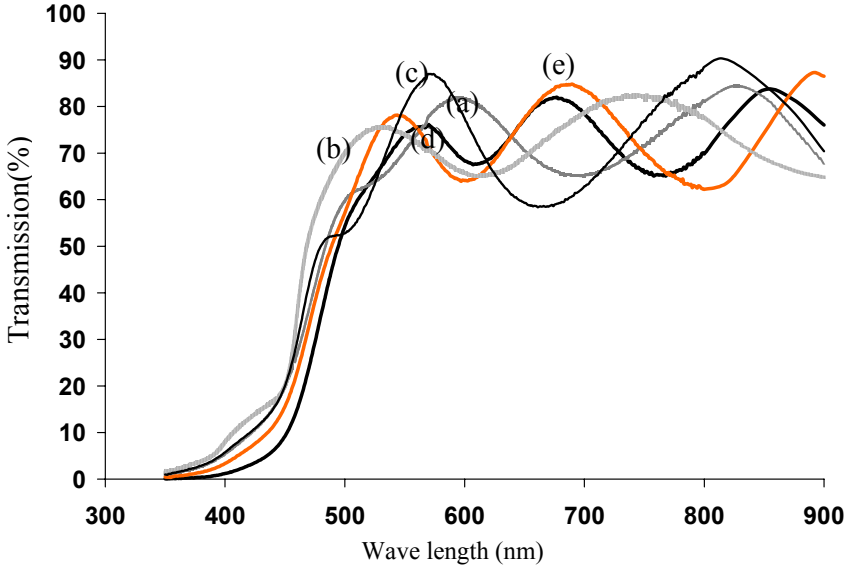

Figure 5.28. The transmission spectra of a few typical ZnSe films of thickness (a) 3200Å (b)3400 Å (c)3800 Å (d)3900 Å and (e)4350 Å ,thermally deposited on glass substrate

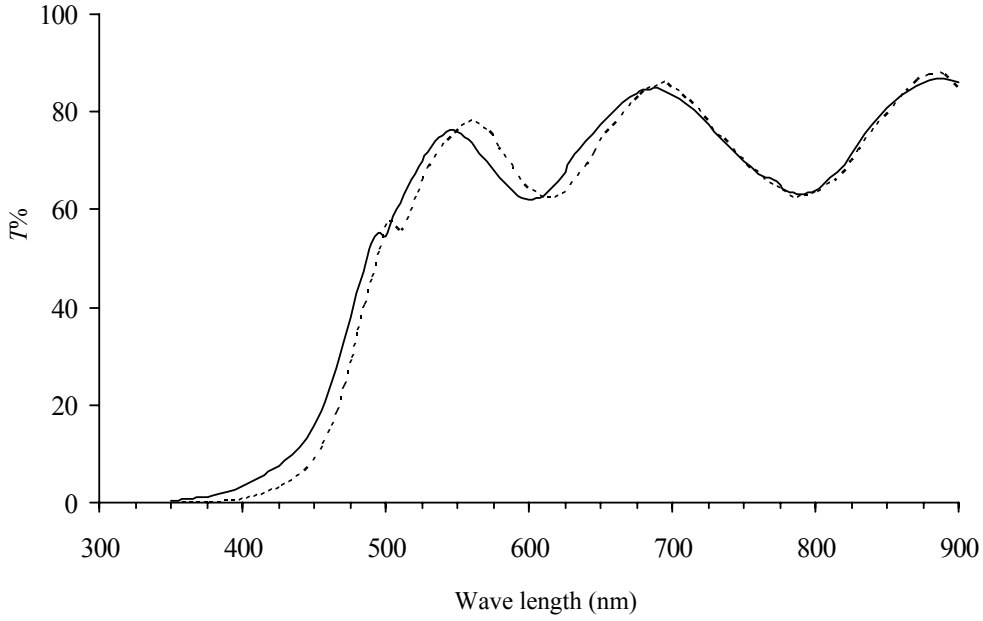

Figure 5.29. The transmission spectra of a typical unannealed (solid line) and annealed (dotted line) ZnSe film of thickness 4350Å thermally deposited at substrate temperature T_s=453K,

5.3.2 Refractive index:

The values of refractive index (n) of ZnSe films in the interference zone were calculated by creating envelopes over the interference maxima (T_M) and minima (T_m) in the transmission curves [301, 302, 358]. The refractive indices were calculated for those particular wave lengths where interference maxima(T_M) or minima (T_m) were formed by using the relation, $n = \left[N + (N^2 - s^2)^{1/2} \right]^{1/2}$,

where, $N = 2s\frac{T_M - T_m}{T_M T_m} + \frac{s^2 + 1}{2}$ and s is the refractive index of the glass substrate.

With this value of refractive index of the film the 'order' m of the different extremes of the transmission curve is determined with the equation for interference fringes,

$$2nd=m\lambda$$

The values of 'm' are then approximated to the close integer or half integer (m is an integer for maxima and a half integer for minima). These values of m are used to determine the corrected value of refractive index for that wave length, from the relation $2nd=m\lambda$.

The refractive indices measured in this way for a typical ZnSe film of thickness 4150Å deposited at 453K before and after annealing have been tabulated in Table 5.07. By extrapolating the values of refractive indices in the interference region calculated in the above way, the refractive indices in the interference free region were obtained using Cauchy's dispersion relation $n=A+B/\lambda^2$ (Fig 5.30). The values of refractive index calculated at 500nm; of some films prepared at different substrate temperatures are summarized in Table 5.08. In the visible region, the refractive index of the films is found to be in the range of 2.2 to 2.65, which is nearly similar value of bulk ZnSe. Fig 5.31 shows the variation refractive index for a particular wavelength with the substrate temperature during deposition of the films. It is seen clearly that the refractive index is more for the films deposited at higher substrate temperature. Similar behaviour has been observed in thin films of other II-VI semiconductors prepared by thermal evaporation method [359].

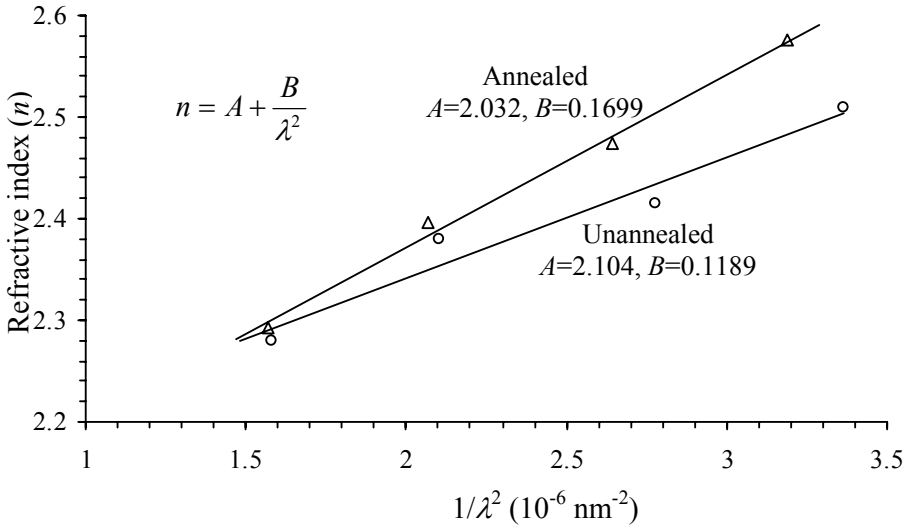

Figure 5.30. Linear nature of refractive index (n) vs $1/\lambda^2$ plot of a typical ZnSe film (as-deposited and annealed at 453K for 1 hour) of thickness 4350Å deposited at substrate temperature 453K.

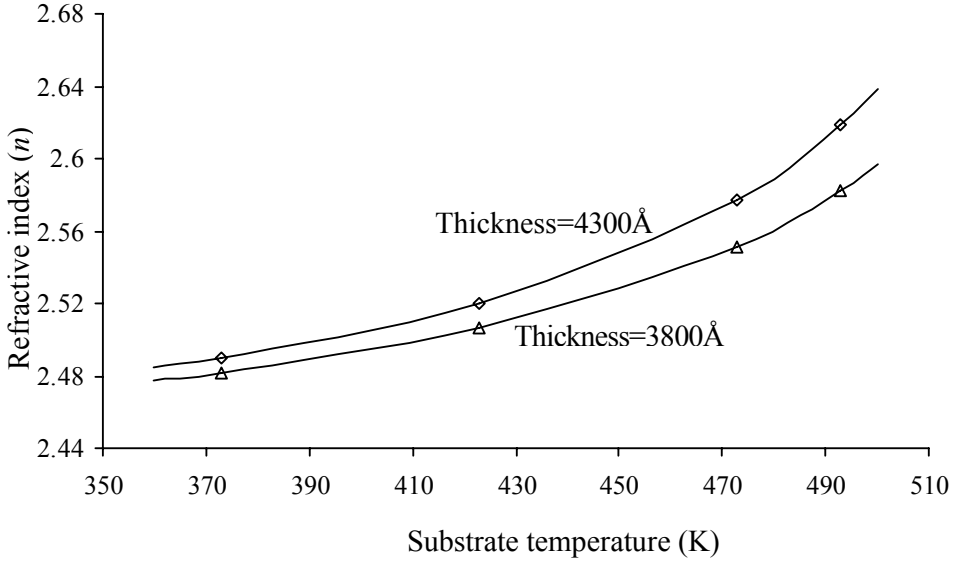

Figure 5.31**.** Variation of refractive index (n) at wave length 500 nm of ZnSe films of two thicknesses with substrate temperatures during deposition.

5.3.3 Absorption coefficient and Extinction coefficient:

Absorption coefficients (α) in the interference free region were calculated from transmittance value using the expression (3.31), $(T_1/T_2)\approx\exp[\alpha(d_1-d_2)]$. To calculate absorption coefficient in the interference region, the value of transmittance found from the envelopes as described in section 5.3.1 have been used. From the value of absorption coefficient, the extinction coefficient or the imaginary part of refractive index (k) of the films for different wavelengths were estimated with the help of the relation $k = \alpha\lambda/4\pi$. In the transmission region, the values of k for all the films are very small. The values of extinction coefficient estimated for a few ZnSe films are tabulated in Table 5.07 and 5.08. The extinction coefficient has been found to decrease with increase of wavelength as shown in Fig.5.32. The decrease is more sharp in the lower wave length region upto about 500nm followed by a slow decrease.

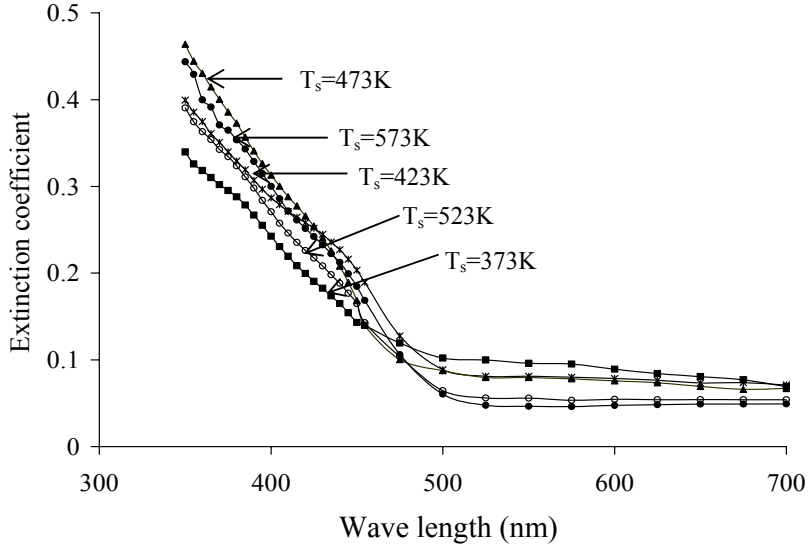

Figure 5.32. Variation of extinction coefficient (k) with wave length of a vacuum deposited ZnSe films prepared at different substrate temperatures.

5.3.4 Dielectric constants:

From the knowledge of n and k, the real and imaginary part of dielectric constants ε' and ε'' of the films were calculated using the relations $\varepsilon'=n^2-k^2$ and $\varepsilon''=2nk$ respectively and are tabulated in Table 5.07 and 5.08. From figure 5.32, it is observed that the extinction coefficient (k) i.e., the imaginary part of refractive index (and so, imaginary part of dielectric constant ε") decreases upto the wave length 500nm for all films and then remains nearly constant. That means, the static conductivity of ZnSe film is low towards the IR region than the blue region according to the relation (3.35), $\varepsilon'' = 4\pi\sigma/\omega$.

5.3.5 Optical band gap:

From the calculated values of α near the absorption edge, the $(\alpha h\nu)^2$ for all the films were plotted against the incident photon energy($h\nu$), considering the expression (3.23), $\alpha h\nu = A(h\nu - E_g)^{1/2}$ for direct transition. Figure 5.33(a) shows the $(\alpha h\nu)^2$ vs $h\nu$ plots of a typical film deposited at substrate temperature 453K, before and after heat treatment. For all the films as shown in Fig. 5.33 (a) and (b), the plots were found straight-line, which indicates band to band transition. The straight-line portion is extrapolated to cut the x-axis, which gives the energy gap (E_g). The optical band gaps of these films were found within the range 2.59 eV to 2.66 eV, which agree with the earlier reported values [67, 190, 360]. Optical band gaps of ZnSe thin films determined for various substrate temperatures are given in the Table 5.08. The value of band gap energy has been observed to depend on thickness, showing decrease on increase of film thickness, the films being deposited at the same substrate temperature. The band gap energy also shows dependence on the temperature of the substrate maintained at the time of deposition. It decreases as the temperature of the substrate during deposition increases. Similar observations have been reported for vacuum-evaporated ZnSe films [67, 190, 360].

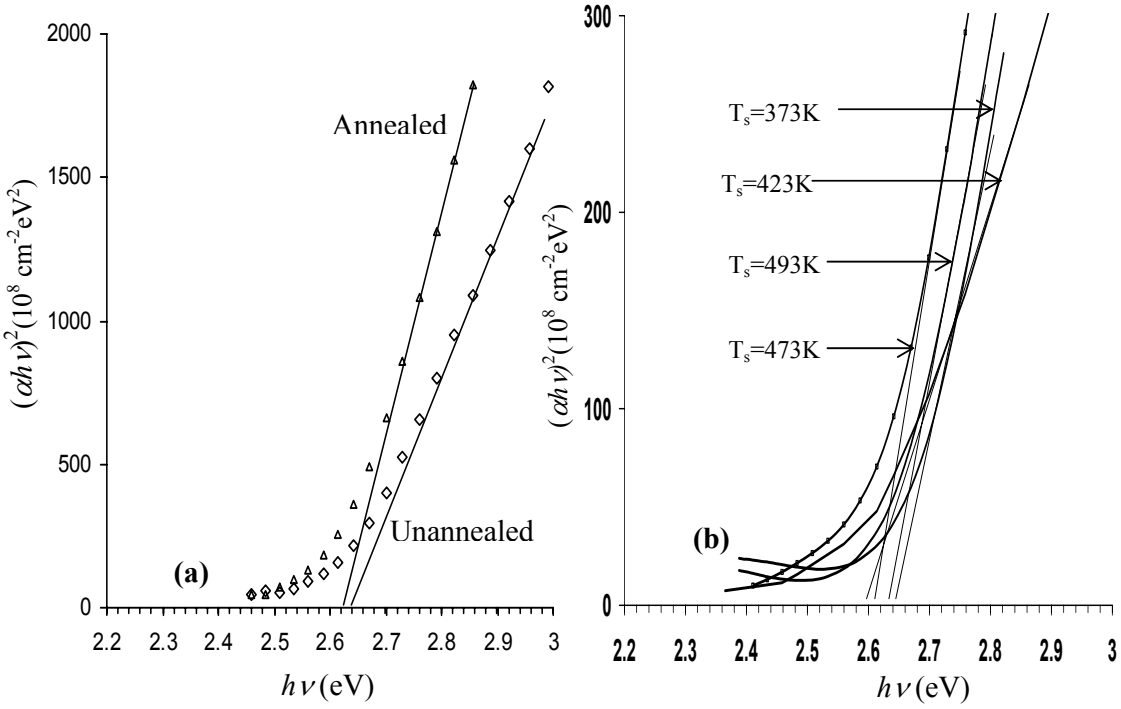

Figure 5.33. $(\alpha h\nu)^2$ vs photon energy ($h\nu$) of ZnSe films vacuum deposited at substrate temperature (a) 453K (thickness 4150Å) and (b) 373K, 423K, 473K and 493K (all films are annealed at 473K for 1 hr and have thickness 4300Å).

Table 5.07: Optical parameters of a typical ZnSe film (unannealed and annealed at 473K for 1 hour) of thickness 4150Å thermally deposited at substrate temperature T_s=453K.

Film	λ nm	T_{max}%	T_{min}%	T%	n	α (cm^{-1})	k	ε'	ε''	E_g (eV)
Unannealed	545	77	61	68.53	2.51	8687	0.0377	6.299	0.189	2.62
	600	83	62	71.74	2.414	7635	0.0365	5.826	0.176	
	690	84	63	72.74	2.38	7317	0.0402	5.662	0.191	
	795	86	63.5	73.9	2.28	6953	0.0440	5.196	0.200	
Annealed	560	79	61	67.4	2.575	8397	0.0374	6.629	0.193	2.615
	615	84	62.7	72.6	2.474	7361	0.036	6.12	0.178	
	695	86	63	73.6	2.396	7047	0.039	5.74	0.187	
	798	87.2	63.5	74.4	2.293	6798	0.0432	5.256	0.198	

Table 5.08: Some optical parameters of some annealed ZnSe films thermally deposited at different substrate temperatures.

Thickness (Å)	Substrate Temperature (T_s) K	Transmittance at λ=550 nm	Refractive index at λ=500 nm	Absorption coefficient at λ=500 nm (cm^{-1})	Extinction coefficient at λ=500 nm	Real dielectric constant (ε') at λ=500 nm	Imaginary dielectric constant (ε'') at λ=500	Band gap (E_g) eV
3800	373	64.5%	2.48	25624	0.102	6.17	0.507	2.67
	423	68.0%	2.51	22314	0.088	6.38	0.445	2.66
	473	68.5%	2.55	22002	0.087	6.45	0.442	2.64
	493	69.2%	2.58	16204	0.064	6.76	0.333	2.62
4300	373	63.0%	2.49	15745	0.063	6.20	0.312	2.65
	423	66.5%	2.52	12487	0.050	6.35	0.250	2.63
	473	67.5%	2.58	12140	0.048	6.65	0.249	2.615
	493	68.0%	2.62	10969	0.044	7.02	0.232	2.59

From the results of optical study presented above, it is found that ZnSe films thermally deposited on glass substrate are highly transparent. In the investigated spectral range, the values of refractive index *n* were found to be in the range between 2.3 to 3.2, which is nearly similar to the value of bulk ZnSe. The films prepared at higher substrate temperatures and film of higher thickness has higher refractive index. The band gap energy calculated from $(\alpha h\nu)^2$ vs $(h\nu)$ plots of these ZnSe films were found in between 2.59 eV to 2.67 eV. The extinction coefficient (*k*) was found in between 0.036 to 0.1 which was found to decrease with increase of wave length. The real part of the dielectric constant of the films was found in the range of 6.

5.4 Discussions and conclusions:

The structural, morphological and compositional properties of thermally deposited ZnSe films have been discussed in the first section. From X-ray diffractograms, it is found that, the films deposited at elevated temperatures are polycrystalline in nature. The crystallinity is improved on increase of substrate temperature during deposition and on annealing thereafter. As the film thickness increases, the diffraction intensity increases due to the growth of the materials incorporated in the diffraction process [346]. When the substrate temperature increases the line width becomes narrow due to the increase in crystallite size. FWHM has been found to decrease markedly with film thickness and substrate temperature. Such a decrease reflects the decrease in the concentration of lattice imperfections due to the decrease in the internal micro-strain within the films and an increase in the crystallite size [361].

From the XRD data, lattice constant and grain size of the films were calculated. It is found that both are increased with increase of substrate temperature during deposition. The lattice constant at lower substrate temperature has been found to be less than the value for bulk sample, which indicates that the films are in stress. This is due to the lattice misfit of the film with substrate and also due to the presence of defects in the film. The stress and dislocation density of the deposited films have been estimated from the XRD data. The stress and dislocation density are found to decrease with increase of substrate temperature. In most of the films the stress is found to be compressional in nature. The compressive stress is due to the grain boundary effect, which is predominant in polycrystalline film [362].

From the W-H plots of polycrystalline ZnSe thin films it has been observed that the X-ray line broadening is due to the presence of both size effect as well as strain effect. It is observed that the crystallite size increases but the internal strain of ZnSe films on glass substrates decreases with increase of substrate temperature. Since the dislocation density and strain are the manifestation of dislocation network in the films, the decrease in the dislocation density and strain indicates the formation of higher quality films at higher substrate temperatures. The adatom mobility also increases as the substrate temperature increases which also results in the increase of the crystallite size and crystallinity of the films [362].

From the studies of structural properties, it can be concluded that the substrate temperature 453K and annealing of the films at 473K for 1 hour are the suitable optimum growth conditions to thermally prepare good quality polycrystalline thin films of ZnSe. The films prepared at this temperature were found nearly stoichiometric and uniform without any macroscopic defects. These growth conditions and parameters were set as optimum growth conditions for preparing ZnSe thin films and for preparation of Schottky barriers and heterojunctions with ZnSe for studying their electrical and optical properties in the present case.

Electrical studies of doped and undoped ZnSe films show that Al makes good ohmic contact to intrinsic ZnSe films and also to n-type ZnSe film. The electrical conductivity of the thermally deposited ZnSe films was found to depend on the substrate temperature during deposition. It was found to increase on increase of substrate temperature and annealing. The undoped ZnSe films deposited at 453K and annealed at 473K for 1 hour, possess high resistivity (of the order of 3×10^{6} Ohm-cm). To improve the conductivity, this semiconductor was doped with Al by co-evaporation method. The conductivity of the doped films was increased upto 11×10^{-6} $Ohm^{-1}cm^{-1}$ with maximum attainable doping concentration 9.7×10^{14} cm^{-3}. The Al doped ZnSe films were found n-type. From the slope of the ln σ vs 1000/T plots, the band gaps of the films were calculated and found to be in the range of 2.58eV to 2.63 eV. The band gap measured from variation of conductivity with temperature was found to be slightly lower than the optical band gap measured from optical absorption coefficients. From the other two slopes of low temperature range of ln σ vs 1000/T plot, two activation energies of undoped and doped films were calculated and found in the range of 0.55 eV to 0.63eV and 0.11eV to 0.22 eV. The different activation energies are due to presence of some localized states or defect levels of the thermally deposited films. The Al-doped films are mostly disordered with a lower value of activation energy. Similar observation was also reported by earlier researchers in Al-doped films [163]. This is probably due to the increase of defect centers in the doped film and change of stoichiometry. The Al doped ZnSe films displays a reduction of the activation energy. This confirms the Al enclosure in the films. The doping increases free-carrier concentration, thus changing conductivity, and it simultaneously reduces the height of the potential barrier between the crystallites composing the films, thereby decreasing the activation energy.

Al doped ZnSe films were found photosensitive and the photocurrent was found to be a function of intensity of illumination. The photoconductive rise and decay processes of ZnSe films were found to be controlled by slow processes. From the plot of $\ln(I_0/I_t)$ versus decay time (t_d), trap depths were calculated. The trap depth has been found to be about 0.718 eV which is found nearly equal to the values of activation energy obtained from temperature dependence conductivity plots.

From the results of optical study presented above, it is found that the ZnSe films thermally deposited on glass substrate are highly transparent. The experiments show that transmission coefficient strongly depends on the film structure, which is determined by the film thickness and its deposition condition. It is observed that for the heat treated samples the transmission coefficient is greater than the value obtained before heat treatment. This fact is probably due to the increase in crystallite size and reduction of structural defects on heat treatment, because these factors influence the absorption process. The sharp fall of transmittance curve at the band edge also confirms that the deposited films are having the crystalline nature.

In the investigated spectral range, the values of refractive indices, n of ZnSe films were found to be in the range between 2.3 to 3.2, which is nearly similar to the value of bulk ZnSe. The films prepared at higher substrate temperatures have higher refractive index due to the compactness for larger grain size and lower strain as discussed in section 5.1.2. The ZnSe films exhibit normal dispersion in the studied spectral range. The straight line fitting of the plot $(\alpha h\nu)^2$ vs photon energy ($h\nu$) as per the relation (3.23) indicate that the transition is direct and from these plots the optical band gaps of these ZnSe films were found to be around 2.65 eV. As the transition is direct, these films will be suitable for optoelectronic devices. Also higher band gap of the films makes it possible to use it as a window layer for solar cell and optoelectronic devices working in the blue region.

The extinction coefficient (k) is also found to decrease with increase of wave length. In the transmission region, the values of k for all the films are very small (10^{-2}). It is observed that the imaginary part of refractive index (k) (and so, imaginary part of dielectric constant ε'') decreases slowly up to the wave length 500nm and then remains nearly constant. That means, the static conductivity of ZnSe is low towards the IR region than in the blue region.

CHAPTER 6

Studies of Indium Tin Oxide (ITO) Films

6.1 Structural studies of ITO thin films

6.1.1 X-ray diffractogram of ITO thin films

The structural properties of ITO (In_2O_3:SnO_2) samples both powder (as-supplied) and thermally deposited films were studied by X-ray diffraction method. The X-ray diffractogram of pure powder of ITO (99.99%) procured from Testbourne, UK, is shown in fig 6.01. The spectrum exhibits polycrystalline nature of ITO powder with sharp peaks at 2θ values corresponding to diffraction from different planes. The different 2θ values and corresponding d values along with the relative intensities are tabulated in Table 6.01. The diffraction planes (h k l) were obtained by comparing the experimental values of d values and relative intensities with those obtained from JCPDS (Joint Committee on Powder Diffraction Standard) X-ray Powder diffraction data file No. 06-0416 and 41-1445 for the modified cubic (bixbyite) structure of In_2O_3 (lattice constant a=10.118 Å) and SnO_2 respectively.

Table 6.01: Indexing of as-supplied ITO powder

JCPDS data			Source material (ITO powder)		
d (Å)	hkl	I/I_0	d (Å)	hkl	I/I_0
4.19	211	0.14	4.193	211	0.28
3.35(SnO_2)	110	-	3.34	110	0.14
2.921	222	1.00	2.937	222	1.00
2.529	400	0.30	2.544	400	0.42
2.385	411	0.08	-	-	-
2.157	332	0.06	2.167	332	0.18
2.12(SnO_2)	210	-	2.126	210	0.15
2.066	422	0.02	2.068	422	0.14
1.984	431	0.10	1.994	431	0.18
1.848	521	0.04	-	-	-
1.788	440	0.35	1.796	440	0.35
1.641	611	0.06	-	-	-
1.561	541	0.04	-	-	-
1.525	622	0.25	-	-	-

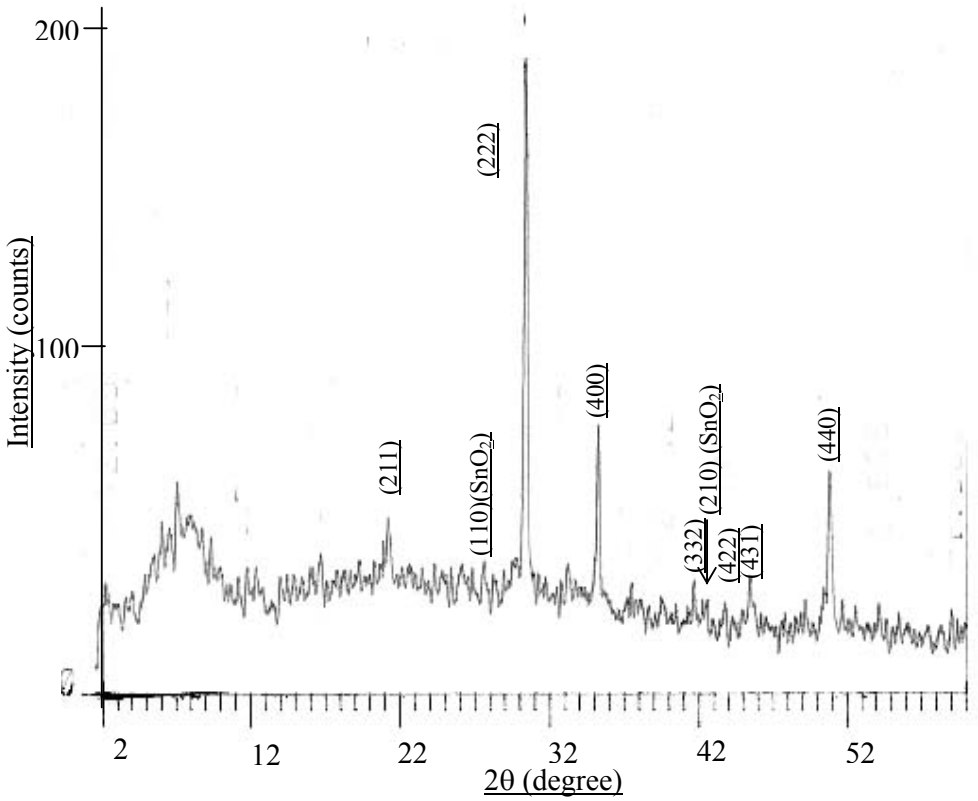

Figure 6.01: XRD spectra of as-supplied source material (ITO powder)

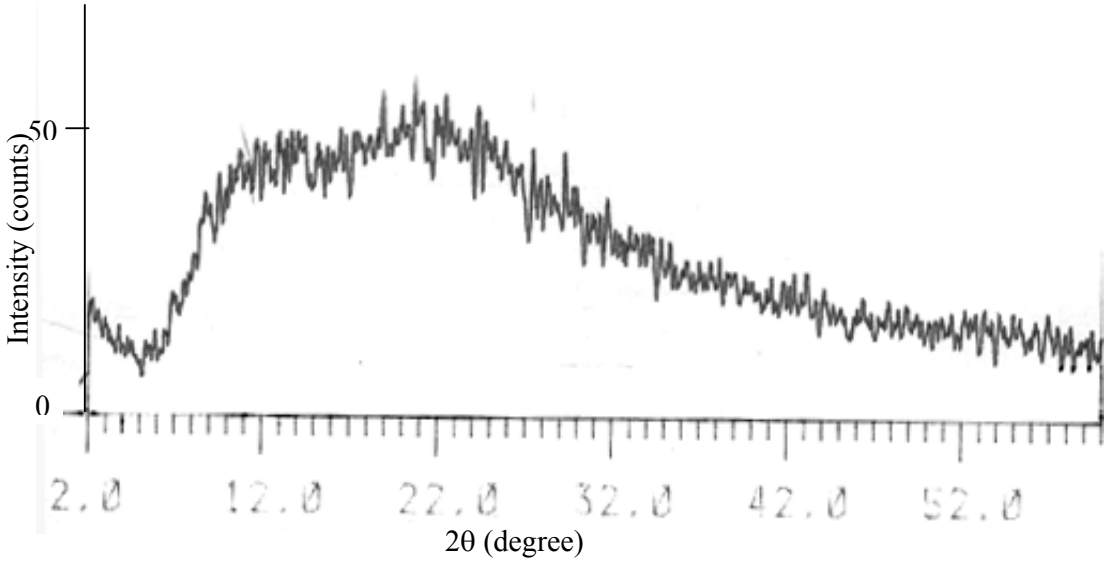

Figure 6.02: XRD spectra of ITO film deposited at substrate temperature 473K (unannealed) of thickness 2970 Å.

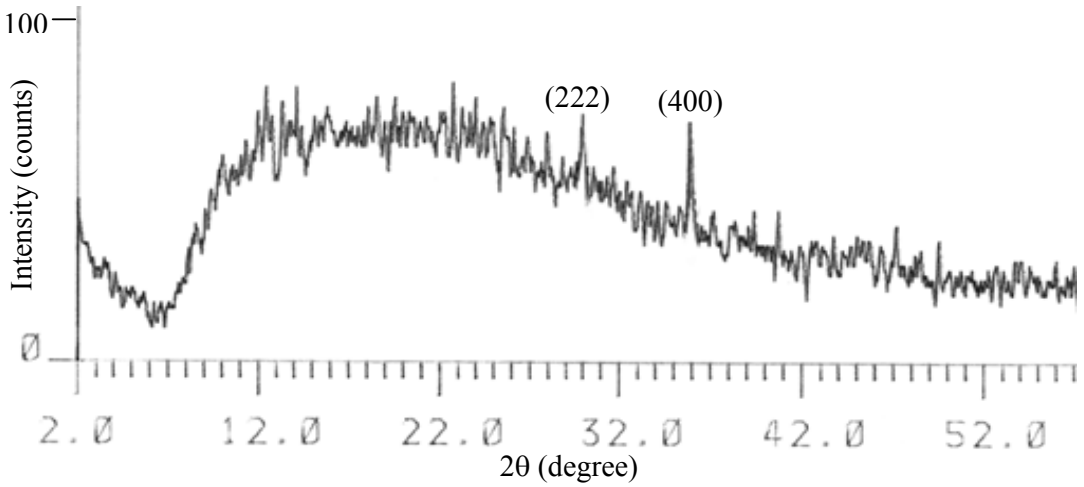

Figure 6.03: XRD spectra of ITO film deposited at substrate temperature 573K and annealed at 573K for 1 hour of thickness 3100 Å.

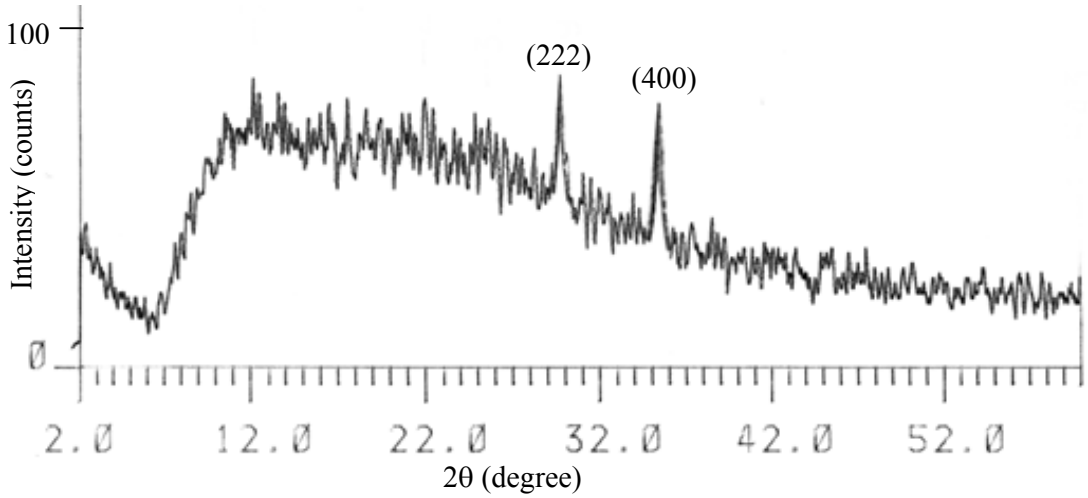

Figure 6.04: XRD spectra of ITO film deposited at substrate temperature 593K and annealed at 593K for 1 hour of thickness 3220 Å.

The X-ray diffractograms of ITO films thermally deposited on glass substrates at different substrate temperatures have been shown in Fig. 6.02 to Fig 6.04. The X-ray diffraction patterns show that the films prepared at lower substrate temperatures showed amorphous nature (Fig 6.02), whereas the annealed films deposited at higher substrate temperatures exhibited polycrystalline nature (Fig 6.03 , Fig 6.04). The peak intensities for the planes (222) and (400) are found to be nearly equal, while

according to JCPDS data the (222) plane shows maximum peak intensity. This indicates that the (400) plane of the deposited film has a partially preferred orientation. In case of thermally deposited ITO films, similar behaviour was also reported by other workers [220, 237]. From the value of inter-planar spacing (*d*), the lattice constants were calculated both for [222] and [400] directions. As substrate temperature during deposition was increased, the value of lattice constant was found to increase (Table 6.02). This could be due to the improvement of crystallinity of the films. The grain size calculated from FWHM of the diffraction peak in (222) and (400) planes using Debye-Scherre's relation (3.04) have been tabulated in table 6.02. The grain size is found to increase with increase of substrate temperature.

Table 6.02: Structural parameters of ITO films prepared on glass substrates at different substrate temperatures and annealed in air at 593K for 1 hour.

Substrate temperature (K)	2θ degree	d (Å)	Plane	Lattice constant (Å)	FWHM degree	Grain size (Å)
573	30.51	2.928	222	10.143	0.315	287
	35.61	2.52	400	10.080	0.339	273
593	30.45	2.933	222	10.163	0.303	298
	35.53	2.525	400	10.100	0.296	306

6.2 Morphological study of ITO thin films by SEM

Figures 6.05(A) and (B) show the scanning electron micrographs of two typical ITO thin films deposited at substrate temperatures 573K and 593K respectively. The surface morphology under SEM studies show that the films were continuous over the glass surface and were fairly uniform. The grains of the films have different shapes and sizes, but almost compact. There are no macroscopic defects like voids, pinholes, peeling or cracks.

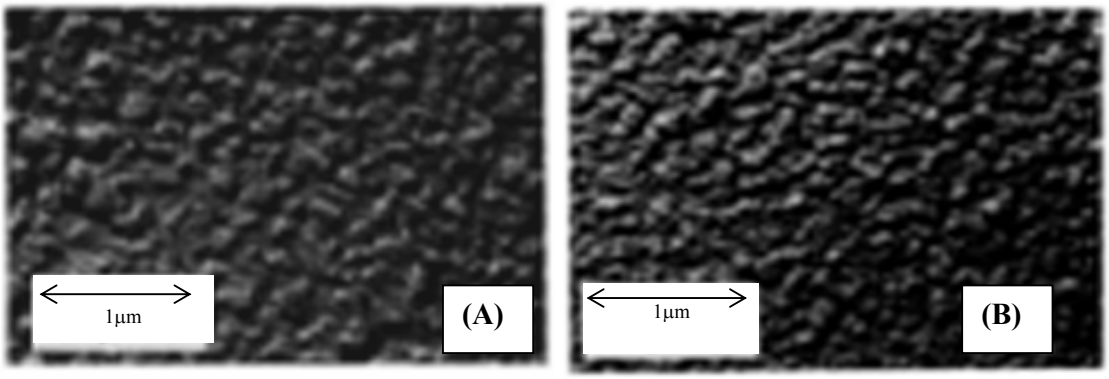

Figure 6.05: SEM photographs of two typical thermally deposited ITO thin films, thickness 3000Å, substrate temperature during deposition (A) 573K and (B) 593K.

6.3 Electrical studies of ITO films

6.3.1 Ohmic contact and electrical conductivity:

The study of *I-V* plots (Figure 6.06) for sandwich type structure of ITO with Ag and Al, indicated that both Ag (work function=4.44 eV) and Al (work function= 4.1eV) make good ohmic contact to ITO (electron affinity= 4.5eV). The conductivity of ITO films deposited at different substrate temperatures was measured from their *I-V* plots of gap type structures as discussed in chapter 4. Figure 6.07 shows the variation of the resistivity of thermally evaporated ITO films deposited at different substrate temperatures. From the study it is found that the resistivity of the film deposited at 373K is 15.8×10^3ohm-cm, which reduces to the value of 160 ohm-cm for the film deposited at substrate temperature 593K and subsequently annealed at 593K for one hour.

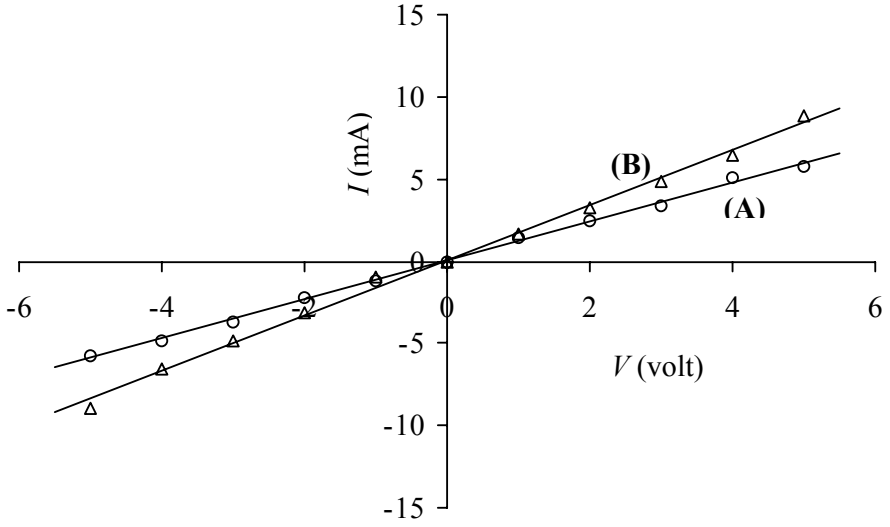

Figure 6.06: *I-V* plot of (a) Ag-ITO-Ag and (b) Al-ITO-Al (T_s=593K) structure of effective area=0.04 cm^3 and thickness 4550 Å in dark at room temperature

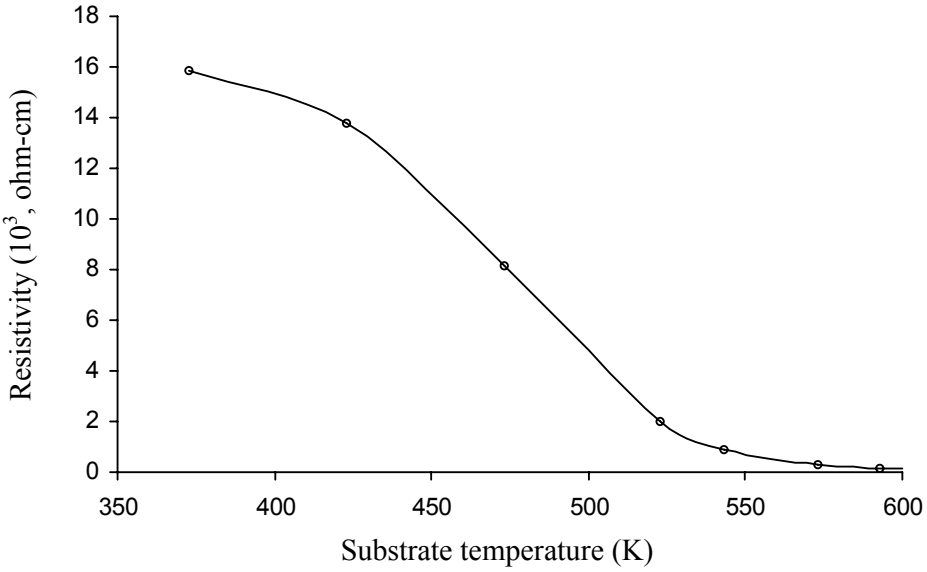

Figure 6.07: Variation of electrical conductivity of ITO films with substrate temperature

6.3.2 Temperature variation of conductivity:

For studying the variation of electrical conductivity with temperature, ITO films were deposited at substrate temperature 593K and subsequently annealed at 593K for one hour. Figure 6.08 shows the variation of conductivity of ITO films with inverse of temperature. The activation energies of these degenerate semiconducting ITO films calculated from the slopes of $\ln\sigma$ versus $1000/T$ plots are tabulated in table 6.03.

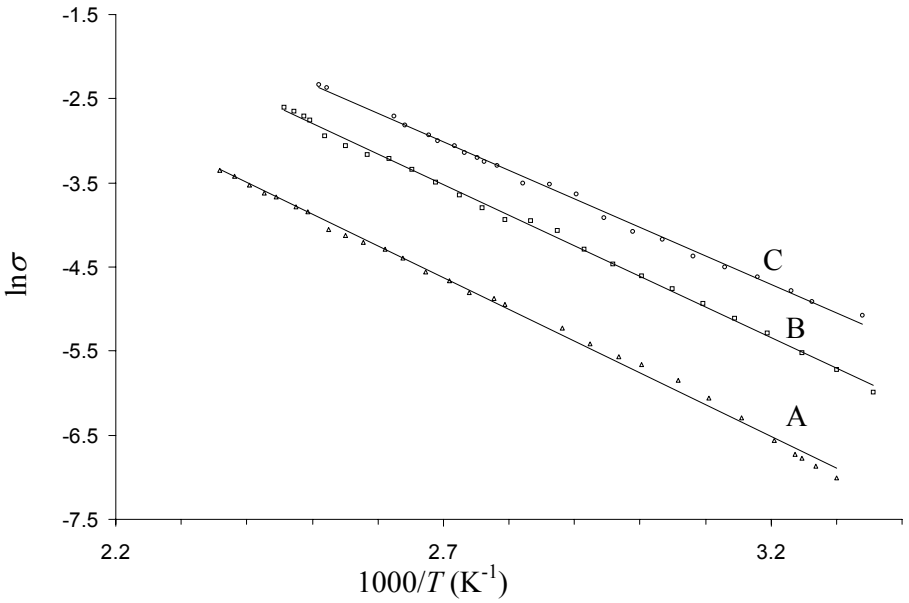

Figure 6.08: ln σ vs 1000/T plots of ITO films deposited at (A) 543K, (B) 573K and (C) 593K (films were annealed at their respective substrate temperature for one hour)

Table 6.03: The conductivity, sheet resistance and activation energy of a few ITO films deposited at different substrate temperatures and annealed at 593K for 1 hour

Substrate temperature (K)	Thickness (Å)	Conductivity (10^{-3}, ohm^{-1}cm^{-1})	Sheet resistance (10^{5}, ohm/sq)	Activation energy (eV)
543 K	2130	0.90	521	0.325
573 K	2200	2.51	181	0.313
593 K	1950	6.25	82	0.292

From the studies of electrical properties of ITO films, it has been found that 593K is the suitable substrate temperature to get low resistive ITO films by vacuum deposition method. Both Al and Ag electrodes are found to be ohmic contact with ITO films.

6.4 Optical Studies of ITO films

The optical properties of the thermally deposited ITO films were investigated from their transmittance spectra measured in the range between 300 to 800 nm. The optical transmittance was found to show considerably different results with substrate temperature and annealing. Freshly prepared ITO films were found to be partially transparent in the visible range. The transparency got improved after annealing at 573K in air for 1 hour. According to previous workers [363-365], the high absorbance of samples prepared at low substrate temperatures is caused by an incomplete oxidation of the ITO. By heat treatment in oxygen atmosphere (like air) the absorption edge is found to move towards the ultraviolet range and also the transmittance in the visible range increases. Figure 6.09 represents a few typical transmission spectra of ITO films before and after annealing in air. The refractive index (n) was calculated from the interference pattern of the transmission spectrum of thicker films by the method described in chapter 5. The absorption coefficient (α) was calculated from the transmission spectra near the absorption edge. $(\alpha h\nu)^2$ versus $(h\nu)$ plots were drawn for unannealed and annealed ITO films (Fig 6.10). For all the films as shown in Fig. 6.10, the plots were found straight-line as per relation $\alpha h\nu = A(h\nu - E_g)^{1/2}$ which indicates that the transition is direct band to band transition. The straight-line portion is extrapolated to cut the X-axis, which gives the band gap energy (E_g). The optical band gap of unannealed film is found to be about 3eV while band gap of annealed films is found to within 3.53 eV to 3.6 eV. These results agree with the earlier reported values [210, 222, 225]. The different optical parameters like refractive index (n), extinction coefficient (k), dielectric constants (ε' and ε'') and optical band gap (E_g) of some films are given in table 6.04.

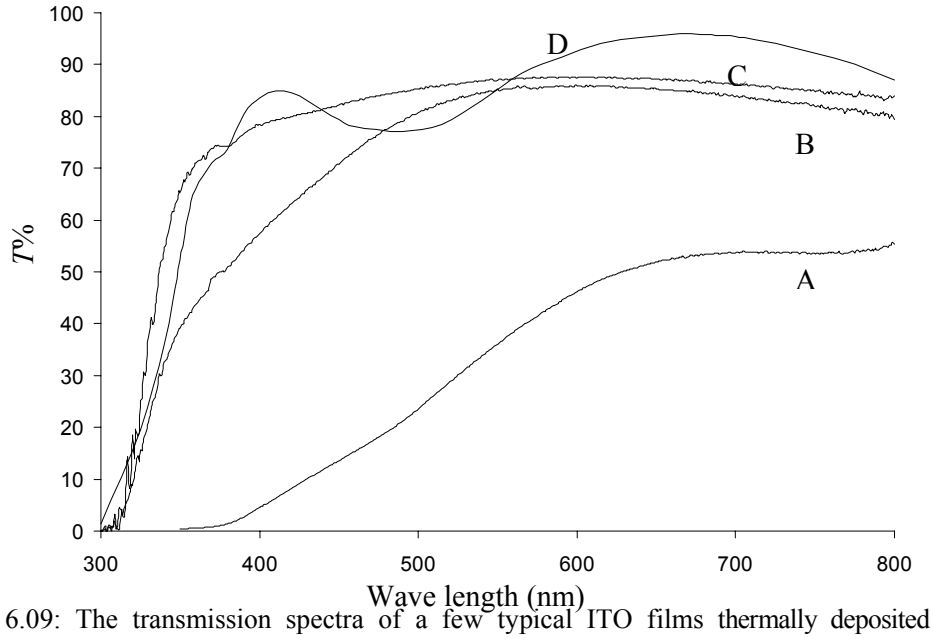

Figure 6.09: The transmission spectra of a few typical ITO films thermally deposited at substrate temperatures: (A) 543K (unannealed), (B) 543K (air-annealed at 543K for1 hour), (C) 573K (air-annealed at 573K for1 hour) and (D) 593K (air-annealed at 593K for1 hour)

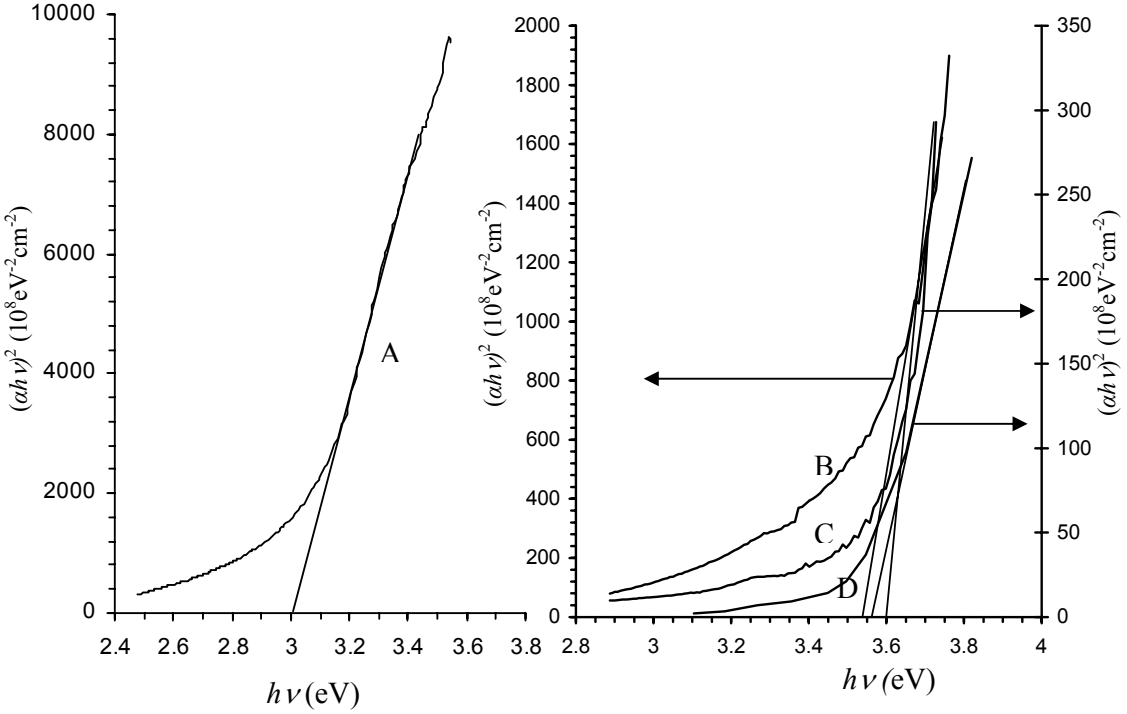

Figure 6.10: $(\alpha h\nu)^2$ vs photon energy ($h\nu$) of a few ITO films thermally deposited at substrate temperatures: (A) 543K (unannealed), (B) 543K (air-annealed at 543K for1 hour), (C) 573K (air-annealed at 573K for1 hour) and (D) 593K (air-annealed at 593K for1 hour)

Table 6.04: Optical parameters of a few typical ITO films (unannealed and air-annealed) thermally deposited at different substrate temperatures

Substrate temperature (K)	Thickness (Å)	T% at 550nm (%)	α (10^3 cm^{-1})	n	k (10^{-3})	ε'	ε'' (10^{-2})	E_g (eV)
543 (unannealed)	1800	36	62.85	-	-	-	-	3.0
543 (air-annealed)	1500	85	15	-	-	-	-	3.53
573 (air-annealed)	1350	87	12	-	-	-	-	3.60
593 (air-annealed)	3350	86	7.417	1.9	2.953	3.61	1.12	3.55

From the optical study, it is seen that the transmittance can be improved upto 85% by air annealing the films. The optical band gap calculated from the absorption coefficients for unannealed film was about 3eV and that for annealed films was about 3.6 eV. The band gap value for the annealed film agrees with the reported values [210, 222, 225]. The refractive index of comparatively thicker film was calculated from the interference pattern of the transmission spectra and was found about 1.9 for wave length 500 nm. The lower values of extinction coefficient and dielectric constants of the prepared film make the film suitable for transparent conducting purposes.

6.5 Discussions and conclusions:

The structural, electrical and optical properties of thermally deposited ITO films have been discussed in this chapter. From X-ray diffractograms, it is found that, the films deposited at about 573K and above are polycrystalline in nature. The crystallinity is improved on annealing and increase of substrate temperature. From the XRD data, lattice constants and grain size of the films were calculated. Both the parameters are found to be increased with increase of substrate temperature during deposition. The values of the lattice constant are found to be less than the value of bulk sample, which indicates that the films are in stress. This is due to the lattice misfit of the films with substrate and also due to the presence of defects. However the

lattice constant of thicker films (above 3220Å) deposited at substrate temperature 593K is found to be nearer the bulk value. For junction formation with ITO film, this condition was maintained.

The electrical conductivity of ITO films thermally deposited in the present case is found to be dependent on the deposition condition. Substrate temperature 593K during deposition and air annealing 1 hour thereafter at the same temperature is found to be suitable for attaining higher conducting ITO films. The maximum conductivity attained in our thermally deposited film after annealing is 6.25×10^{-3}ohm^{-1}-cm^{-1}. The thin film of ITO with high conductivity was thermally deposited by other workers also [237].

From the optical study, it is seen that the transmittance can be improved upto 85% by air annealing the films. The optical band gap calculated from the absorption coefficients for annealed films was about 3.6 eV. The increase of band gap after annealing is due to incorporation of oxygen. The refractive index of comparatively thicker film was calculated from the interference pattern of the transmission spectra and was found to be about 1.9 for wave length 500 nm. The lower values of extinction coefficient and dielectric constants of the prepared film make them suitable for transparent conducting purposes.

Thus from the study it is concluded that high conductivity with high transmittance ITO films can be prepared by thermal deposition by maintaining the substrate temperature at 593K and post deposition annealing of the film at 593K in air for one hour. These films are polycrystalline in nature and uniform. The films are transparent in the visible range. Therefore, for junction preparation with ITO films, substrate temperature was maintained at 593K during deposition and films were air annealed at the same temperature for one hour.

CHAPTER 7

Studies on Au-(n)ZnSe and Ni-(n)ZnSe Schottky Barrier Junctions

7.1 Introduction:

The electrical and photovoltaic properties of thin film Au-(n)ZnSe and Ni-(n)ZnSe structures have been studied in the present investigations. The details of preparation of these junctions have been discussed in chapter 4. Thermally deposited Al was used to make ohmic contact to ZnSe films. Al was also used to dope ZnSe films during deposition. Before junction preparation Al-doped ZnSe films were vacuum annealed at 473K for 1 hour. The barrier metal, Au and Ni were vacuum deposited separately over the annealed Al-doped ZnSe films as counter electrodes to form respectively Au-(n)ZnSe and Ni-(n)ZnSe structures. The structures were then annealed at 373K for 10 minutes in vacuum to improve the quality of the ZnSe films and to reduce interfacial layer between semiconductor and metal. The details of junction preparation have been discussed in chapter 4. In this chapter the details of the current-voltage characteristics at different temperatures, photo-voltaic performance etc. of the junctions have been reported.

7.2 Capacitance-Voltage measurement of the junctions:

The Au-(n)ZnSe and Ni-(n)ZnSe junctions have been observed to form Schottky barriers, which will be discussed in next sections. In a Schottky barrier there is a depletion region between the metal and the neutral region of the semiconductor forming a capacitor. The capacitance of the Au-(n)ZnSe and Ni-(n)ZnSe junctions were measured under reverse bias condition at room temperature. The details of measurements have been discussed in chapter 4. The reverse bias condition refers to a bias voltage across the junction with positive polarity connected to the n- type ZnSe film through Al electrode making ohmic contact at the back and negative polarity to the counter electrodes of barrier metal Au or Ni. The *C-V* measurements on the junctions were performed to determine the doping concentrations of the films and to measure the barrier heights of the junctions.

The C^{-2}-V plots of three junctions of Au-(n)ZnSe and three of Ni-(n)ZnSe structures have been shown in Figures 7.01 and 7.02 respectively. For lower bias the inverse of the square of the capacitance of the samples showed linear dependence with reverse voltage. The doping concentration N_d was calculated from the slope of C^{-2}-V plots of the junction under reverse bias condition using relation (3.46)

$$C^{-2} = \left(2/q\varepsilon_s N_d \right)\left(V_{bi} + V_r - kT/q \right)$$

here, V_{bi} is the diffusion voltage at zero bias (Fig. 3.4) which is equal to V_i+kT/q, where V_i is the negative intercept on the reverse voltage (V_r) axis and ε_s is the permittivity of ZnSe whose value is $9.1\varepsilon_o$ (ε_o permittivity of free space) [366]. The doping concentrations evaluated from slopes of C^{-2}-V plots of Au/Ni-(n)ZnSe Schottky barrier junctions for three sets of Al-doped ZnSe films were found to be 1.4×10^{14}cm^{-3}, 4.8×10^{14} cm^{-3} and 9.7×10^{14} cm^{-3} respectively.

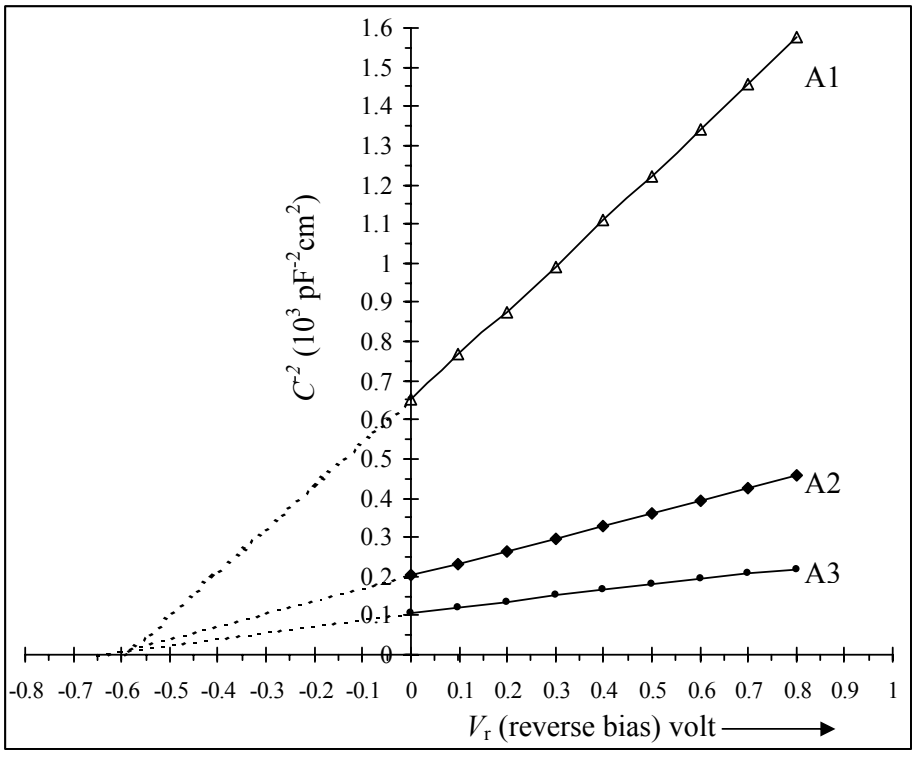

Figure 7.01: C^{-2}-V plots of Au-(n)ZnSe junctions (nos: A1, A2, A3) for three different doping concentrations (Effective junction area 0.01 cm^2).

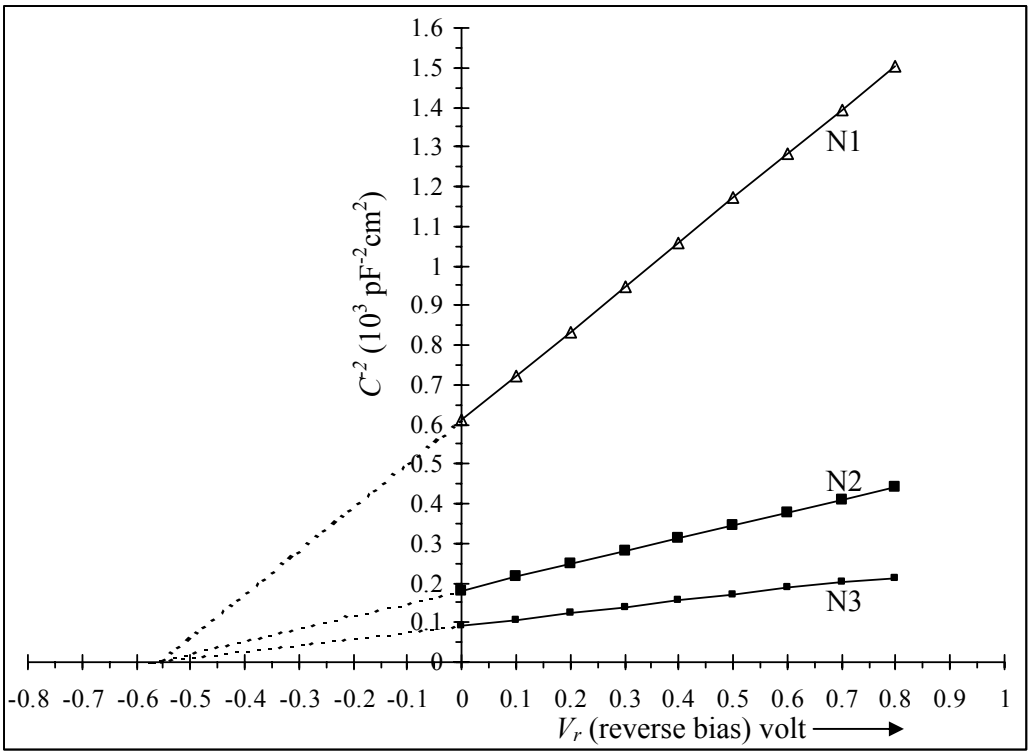

Figure 7.02: C^{-2}-V plots of Ni-(n)ZnSe junctions (nos: N1, N2 and N3) for three different doping concentrations (Effective junction area 0.01 cm^2).

The barrier heights were also calculated from the intercept (V_i) of the C^{-2}-V plots using the relation, $\phi_b = V_{bi} + \xi = V_i + \xi + kT/q$, where ξ is the energy difference between Fermi level and the bottom of the conduction band. The value of ξ is known from the relation $\xi = \left(kT/q\right)\ln\left(N_c/N_d\right)$ after finding the doping concentration (N_d) from the slopes of C^{-2}-V plots. Here the value of effective density of states in conduction band (N_c) at room temperature for ZnSe is 0.79175×10^{18} cm^{-3} [367].

The barrier heights obtained from these C^{-2}-V plots of Au-(n)ZnSe and Ni-(n)ZnSe junctions with different concentrations are tabulated in Table 7.01. The doping in the present case was done by co-evaporation of Al and ZnSe from two different heating sources. The maximum doping concentration possible to obtain in this way and determined from C^{-2}-V plots was found to be 9.7×10^{14} cm^{-3}. The barrier heights of Au-(n)ZnSe and Ni-(n)ZnSe junctions were found to be about 0.82 eV and

0.727 eV respectively. The barrier heights were observed to depend on the doping concentration, increasing with increase of doping concentration.

Table 7.01: The barrier height obtained from C^{-2}-V plots for Au-(n)ZnSe and Ni-(n)ZnSe junctions of different doping concentrations

Sample No	Thickness of ZnSe layer (Å)	Barrier metal	Doping concentration N_d (10^{14}, cm^{-3})	Diffusion potential V_{bi} (V)	Barrier height (eV)
A1	3250	Au	1.36	0.616	0.860
A2	3100	Au	4.82	0.653	0.865
A3	3500	Au	9.67	0.679	0.873
N1	3250	Ni	1.44	0.541	0.785
N2	3100	Ni	4.78	0.587	0.799
N3	3500	Ni	9.73	0.590	0.785

7.3 Studies of Current-Voltage characteristics of Au-(n)ZnSe Schottky Barrier Junctions

7.3.1 *J-V* characteristics of Au-(n)ZnSe junctions in dark at room temperature

The *J-V* characteristics of Au-(n)ZnSe-Al structures of different doping concentrations as-prepared and after heat treatment (for 10 minutes) have been shown in Fig. 7.03. The rectifying nature of *J-V* characteristics with soft reverse current of the fabricated structures indicated the existence of barrier between the films of Au and (n)ZnSe. Rectification is more pronounced at higher doping concentration of ZnSe film. The current density J of a diode of saturation current density J_0 and diode ideality factor n, are related by the relation (3.56),

$$J=J_0\exp(qV/nkT)[1-e^{-qV/kT}]$$

Figure 7.04 shows the plots of $\ln[J/(1-e^{-qV/kT})]$ vs V for three typical Au-(n)ZnSe Schottky barrier junctions at room temperature. The ideality factor(n) and the saturation current density (J_0) of different junctions, as-prepared and after heat treatment, were calculated from the slopes and intercepts of the respective $\ln[J/(1-e^{-qV/kT})]$ vs V plots of them and are tabulated in Table7.02. The diode ideality factor for all the junctions was found

much greater than unity and has been lowered on heat treatment of the structures. However, the structure with semiconductor of higher doping concentration showed improvement of diode quality with reduced diode ideality factor. The reverse current of the junctions as seen in Fig. 7.03 does not show saturation. The barrier heights calculated from the values of J_0 are also shown in Table 7.02 and they are found to be increased with doping concentration.

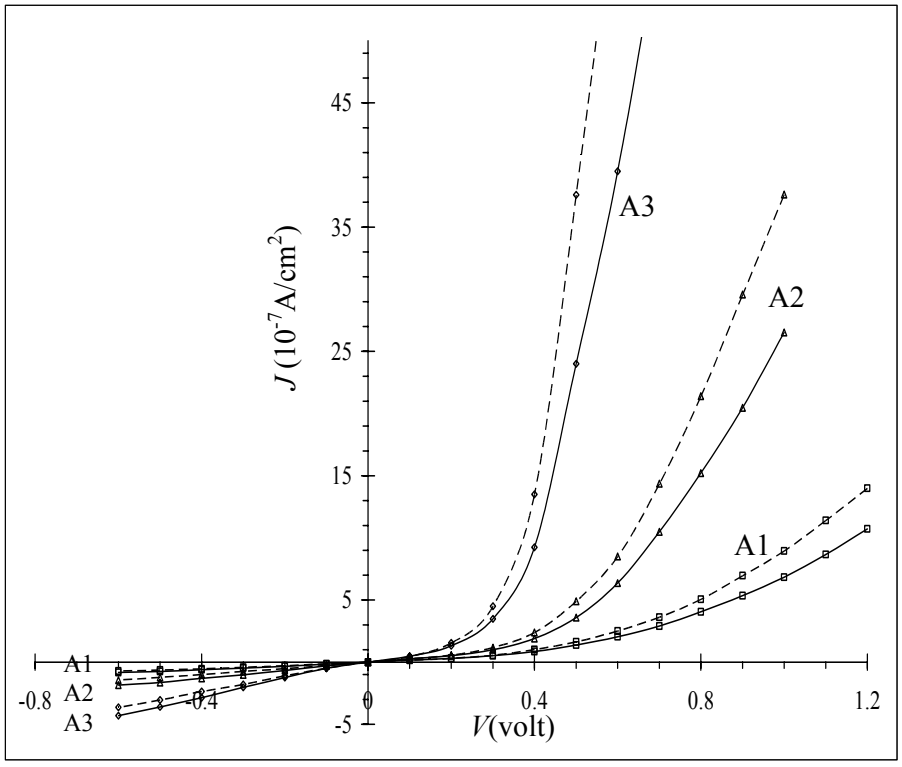

Figure 7.03: *J-V* characteristics at room temperature (300K) of three typical Au-(n)ZnSe Schottky barrier junctions in dark for doping concentrations: A1=1.4×10^{14} cm^{-3}, A2=4.8×10^{14} cm^{-3} and A3=9.7×10^{14} cm^{-3} as-prepared (solid line) and after heat treatment of the junctions for 10 minutes (dotted line)

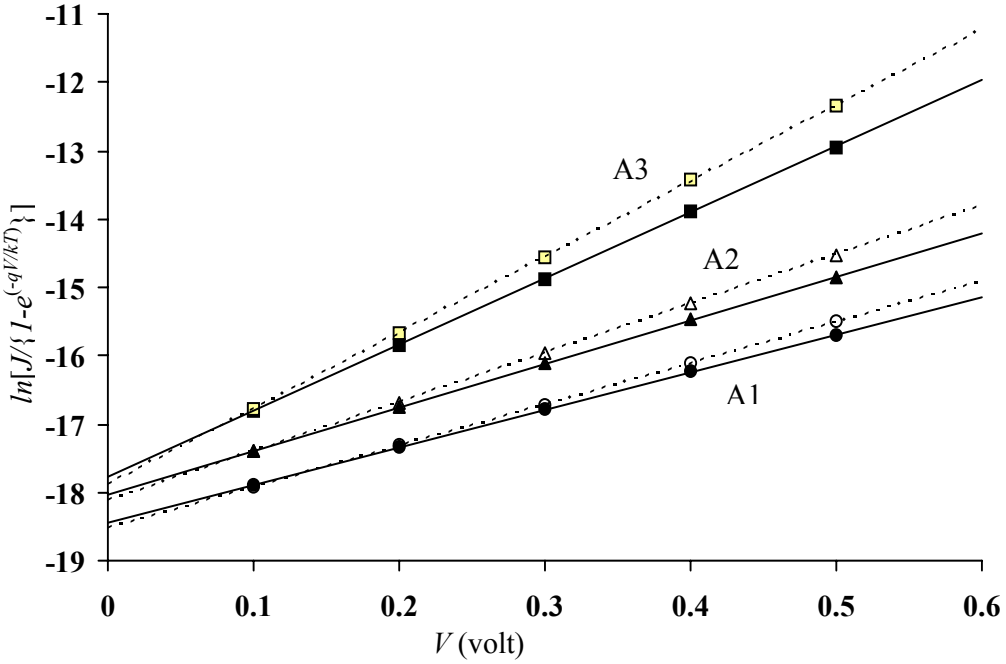

Figure 7.04: $ln[J/\{1-e^{(-qV/kT)}\}]$ vs V plots at room temperature (300K) of three typical Au-(n)ZnSe Schottky barrier junctions in dark for doping concentrations: A1=1.4×10^{14} cm^{-3}, A2=4.8×10^{14} cm^{-3} and A3=9.7×10^{14} cm^{-3} as-prepared (solid line) and after heat treatment of junctions for 10 minutes (dotted line)

Table 7.02: Junction parameters of a few Au-(n)ZnSe Schottky barrier junctions (Area=0.01cm^{-2}) from J-V plots at room temperature before and after heat treatment for 10 minutes

Junction number	Thickness of ZnSe layer (Å)	Doping concen-tration N_d (10^{14} cm^{-3})	Ideality factor n		Saturation current density J_0 ($nAcm^{-2}$)		Barrier height (eV)	
			As - prepared	Heat - treated	As-prepared	Heat - treated	As-prepared	Heat-treated
A1	3250	1.4	7.20	6.48	10	9	0.805	0.815
A2	3100	4.8	6.03	5.36	15	13	0.809	0.816
A3	3500	9.7	3.97	3.53	19	17	0.817	0.820

7.3.2 Effect of series resistance on *I-V* characteristics of the junction

From the ln*I* versus *V* plots (Fig. 7.05) of these Schottky barrier junctions it is observed that, at higher forward voltages, the curve is deviated from linearity. It is due to the effect of series resistance R_s associated with the neutral region of the semiconductor [368]. At large forward current (I) through the diode, the voltage drop across the series resistance causes the actual voltage drop across the barrier to be less than the voltage applied to the terminals of the junction. Hence, the current is proportional to $[e^{q(V-IR_s)/kT}-1]$, instead of obeying the ideal condition. The horizontal displacement between the actual ln*I*-*V* curve and extrapolation of the linear region (Fig. 7.05) gives the voltage drop $\Delta V = IR_s$ across the neutral region.

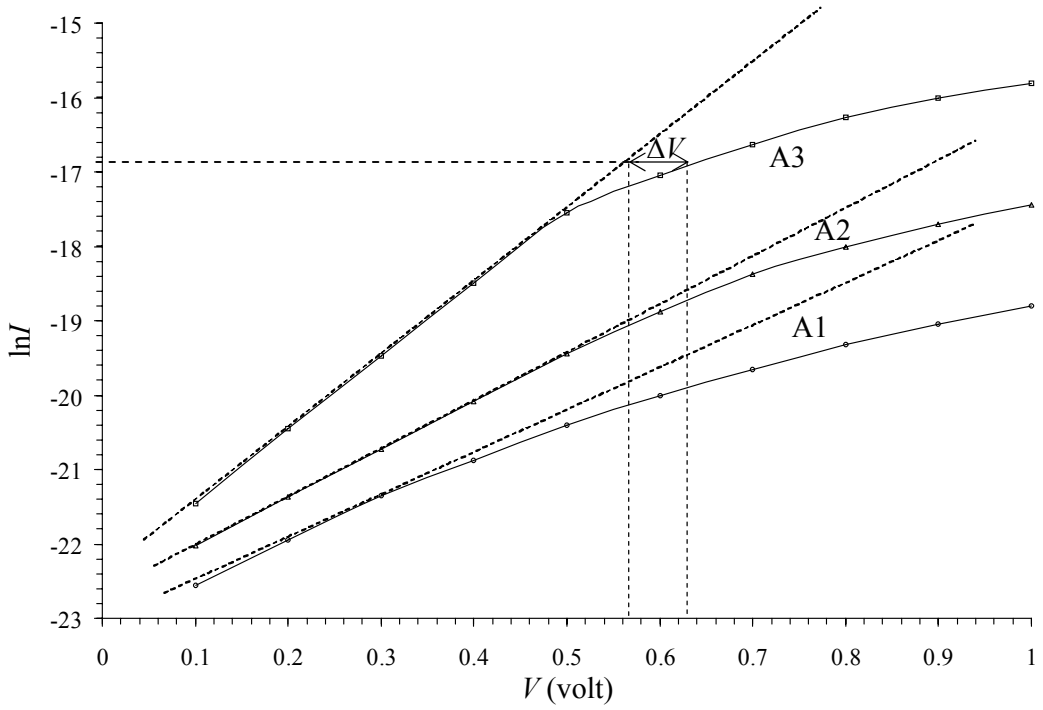

Figure 7.05: ln*I* vs *V* plots at room temperature of three typical Au-(n)ZnSe Schottky barrier junctions in dark for different doping concentrations: A1=1.4×10^{14} cm^{-3}, A2=4.8×10^{14} cm^{-3} and A3=9.7×10^{14} cm^{-3}

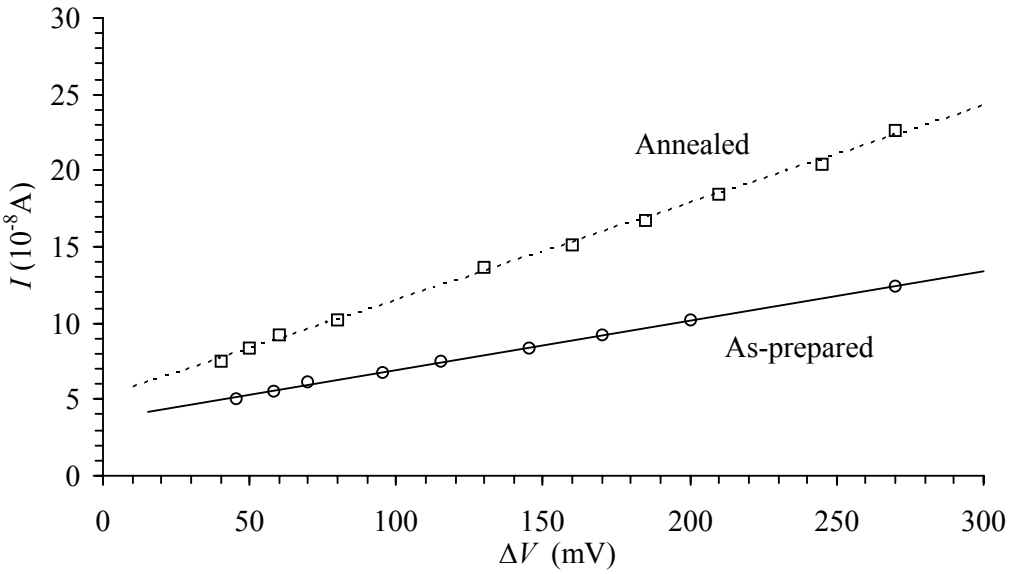

Figure 7.06: I vs ΔV plots at room temperature of a typical Au-(n)ZnSe Schottky barrier junction in dark (sample no: A3) of doping concentrations 9.7×10^{14} cm^{-3} before and after annealing

The series resistances of these typical Au -(n)ZnSe junctions calculated from the I vs ΔV plots (Fig. 7.06) are given in Table 7.03. The series resistance so obtained is found to be in the order of MΩ. The series resistance of the junction is found to depend on doping concentration, decreasing with increasing concentration and also found to decrease on heat treatment.

Table 7.03: Room temperature series resistance of a few Au-(n)ZnSe Schottky barrier junctions (Area=0.01 cm^{-2}) as-prepared and heat-treated for 10 minutes in dark

Junction number	Thickness of ZnSe layer (Å)	Doping concentration N_D (10^{14} cm^{-3})	Series Resistance	
			As-prepared (10^6 Ω)	Heat-treated (10^6 Ω)
A1	3250	1.4	14.5	12.0
A2	3100	4.8	4.7	3.8
A3	3500	9.7	1.7	1.0

7.3.3 Temperature dependence of *J-V* characteristics of Au-(n)ZnSe junctions (in dark)

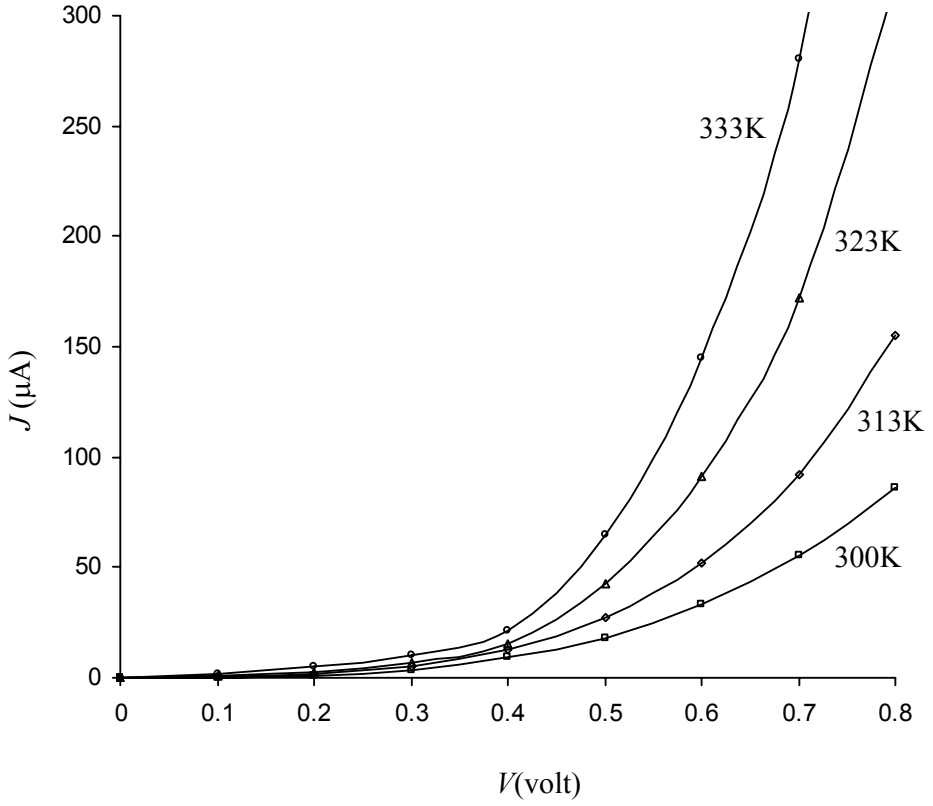

Figure 7.07: *J-V* characteristics of a typical Au-(n)ZnSe junction (A3) in dark at different temperatures (doping concentration 9.7×10^{14} cm^{-3} and junction area=0.01 cm^2)

The temperature dependence of *J-V* characteristics of a Au-(n)ZnSe junction have been studied within the temperature range 300K to 333K. Figure 7.07 shows *J-V* curves of a typical Au-(n)ZnSe junction in dark under forward bias at various temperatures. It has been observed that beyond room temperature (300K), the current increases abruptly with voltage.

The saturation current density at various temperatures of the junction were obtained from $\ln[J/(1-e^{-qV/kT})]$ vs V plots for each temperature. Figure 7.08 shows the linear portions of the $\ln[J/(1-e^{-qV/kT})]$ vs V plots of a typical Au-(n)ZnSe junction (A3) at different temperatures. The saturation current density and ideality factor at different temperatures of a typical junction calculated from these plots are given in Table 7.04. At all temperatures, the ideality factor (n) has been observed to be of nearly same value while the saturation current density J_0 is found to increase with increase of temperature.

The calculated values of J_0 at different temperatures were used to draw $\ln(J_0/T^2)$ vs T^{-1} plots. Figure 7.09 shows such a plot for a typical Au-(n)ZnSe junction. The linear nature of these plots indicates that the current transport is due to thermoionic emission process and it follows the relation (3.54),

$$J_0=A^*T^2e^{-q\phi_b/kT}$$

where, ϕ_b is the barrier height of the junction (Fig. 3.07), A^* is the effective Richardson constant.

The value of A^* was calculated from the intercept on the vertical axis of the plots and the barrier height of the junction was estimated from its slope. Table 7.04 shows the value of A^* and barrier heights of a typical as-prepared and annealed junctions. The barrier heights of the Au-(n)ZnSe junctions measured from this Richardson plots, were found in the range of 0.804 to 0.82 eV. The barrier heights have been observed to increase on increasing temperature as well as on annealing the junction.

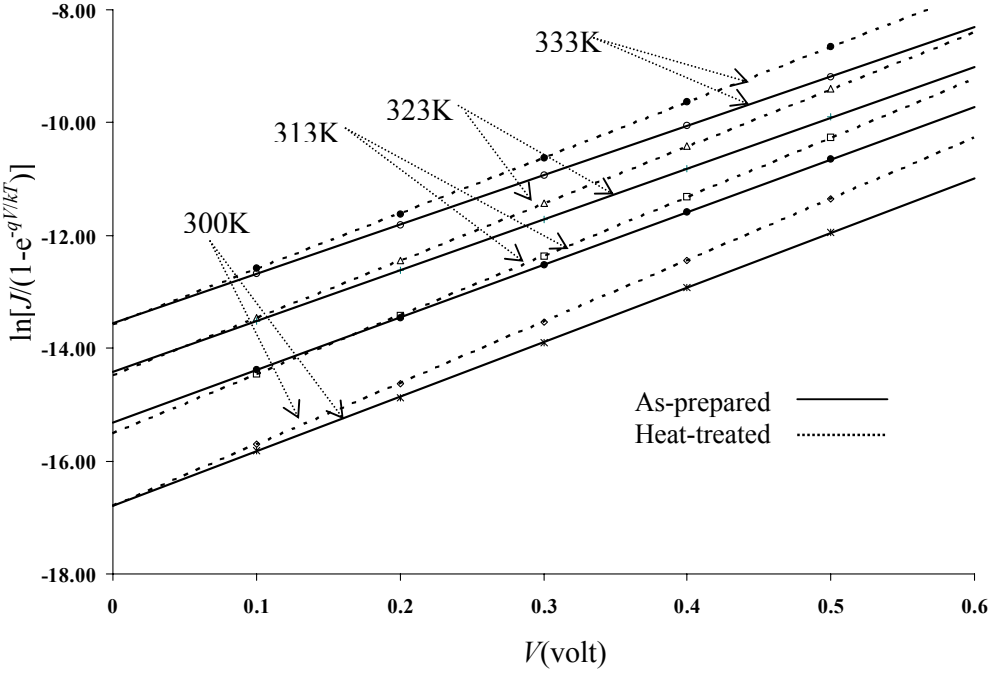

Figure7.08: $\ln[J/(1-e^{-qV/kT})]$ vs V plots of a typical Au-(n)ZnSe junction (A3) (N_D=9.7x10^{14} cm^{-3}) at different temperatures

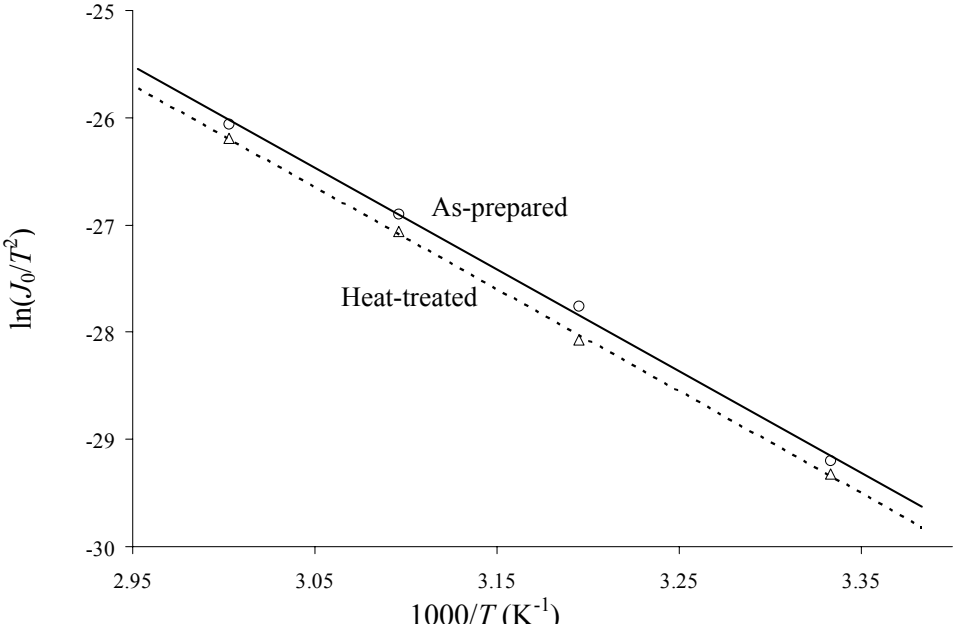

Figure7.09: $\ln(J_0/T^2)$ vs T^{-1} plots of a typical Au-(n)ZnSe junction (A3) (N_D=9.7x10^{14} cm^{-3})

Table 7.04: Some parameters of as-prepared and heat-treated Au-(n)ZnSe Schottky barrier junction (A3) of Area=0.01 cm^{-2} (N_D=9.7×10^{14} cm^{-3}) at different temperatures in dark

Temperature (K)	Ideality factor n		Saturation current density J_0 (nAcm^{-2})		Richardson constant A* (A cm^{-2}K^{-2})		Barrier height ϕ_b (eV)	
	As-prepared	Heat-treated	As-prepared	Heat-treated	As-prepared	Heat-treated	As-prepared	Heat-treated
300K	3.97	3.53	19	17	41	40.5	0.817	0.820
313K	3.90	3.58	87	63			0.818	0.820
323K	3.94	3.62	217	185			0.819	0.821
333K	3.98	3.54	535	465			0.820	0.821

From the study it is found that the *J-V* characteristics of Au-(n)ZnSe Schottky barrier junctions are of rectifying in nature. The *J-V* characteristics show linear relationship at low voltage and low temperature. The increase of doping concentration enhances the current with voltage as seen in the *J-V* characteristics. The diode ideality factors three as-prepared junctions of different doping concentrations have been found to be 3.97, 6.03 and 7.20 which were found to reduce to 3.53, 5.36 and 6.48 respectively on heat treatment of the device (Table 7.02).

The series resistance measured from the deviation of ln*I-V* plot was found to be 1.7 MΩ to 14.5 MΩ. The series resistance of the junctions of higher doping concentration was found less.

In the *J-V* characteristics at different temperatures it has been observed that the saturation reverse current density also found to increase from 19 $nAcm^{-2}$ to 535 $nAcm^{-2}$ (Table 7.04) with the increase of temperature from 300K to 333K. The barrier heights measured from the values of J_0 at different temperatures for three sets of Au-(n)ZnSe junctions of doping concentrations 1.4×10^{14} cm^{-3}, 4.8×10^{14} cm^{-3} and 9.7×10^{14} cm^{-3} are found to be 0.805eV, 0.809eV and 0.817eV respectively, while the barrier heights of the same junctions after heat treatment are found to be 0.815eV, 0.816eV and 0.820eV respectively.

Heat treatment of the devices lowers the diode ideality factor and increases the barrier heights. The reverse saturation current density of the annealed devices was found less than the unannealed devices.

7.4 Studies of Current-Voltage characteristics of Ni-(n)ZnSe Schottky Barrier Junctions

7.4.1 *J-V* characteristics of Ni-(n)ZnSe junctions in dark at room temperature

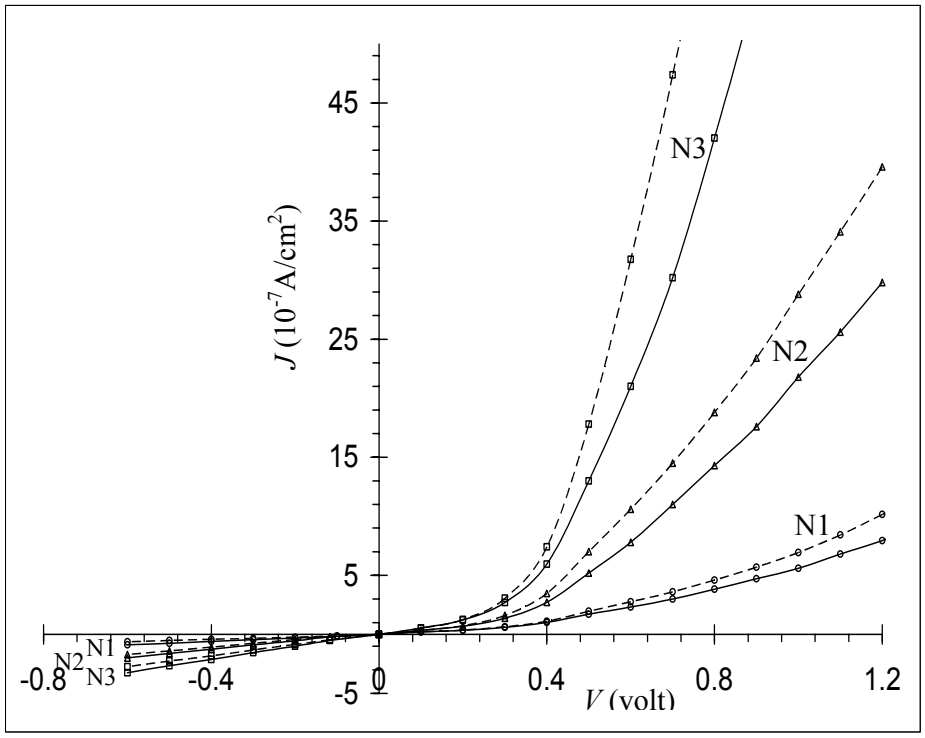

Figure 7.10: *J-V* curves at room temperature (300K) of three typical Ni-(n)ZnSe Schottky barrier junctions in dark for different doping concentrations: N1=1.4×10^{14} cm^{-3}, N2=4.8×10^{14} cm^{-3} and N3=9.7×10^{14} cm^{-3}; as-prepared (solid line) and heat-treated (dotted line)

The *J-V* characteristics of as-prepared and heat-treated three typical Ni-(n)ZnSe-Al structures of different doping concentrations are shown in Fig. 7.10. The rectifying nature of *J-V* characteristics with soft reverse current of the fabricated structures indicated the existence of barrier between thin films of Ni and (n)ZnSe. The reverse current does not saturate.

Figure 7.11 shows the plots of $\ln[J/(1-e^{-qV/kT})]$ vs V for three typical Ni-(n)ZnSe Schottky barrier junctions at room temperature. The ideality factor (n) and the saturation current density (J_0) of different junctions as-prepared and after heat treatment were calculated from the slopes and intercepts of the linear region of respective $\ln[J/(1-e^{-qV/kT})]$ vs V plots of them and are tabulated in Table7.05. The diode ideality factors of all the junctions were found to be greater than unity and have been lowered on heat treatment of the

structures. However, the structure with semiconductor of higher doping concentration showed improvement of diode quality with reduced diode ideality factor.

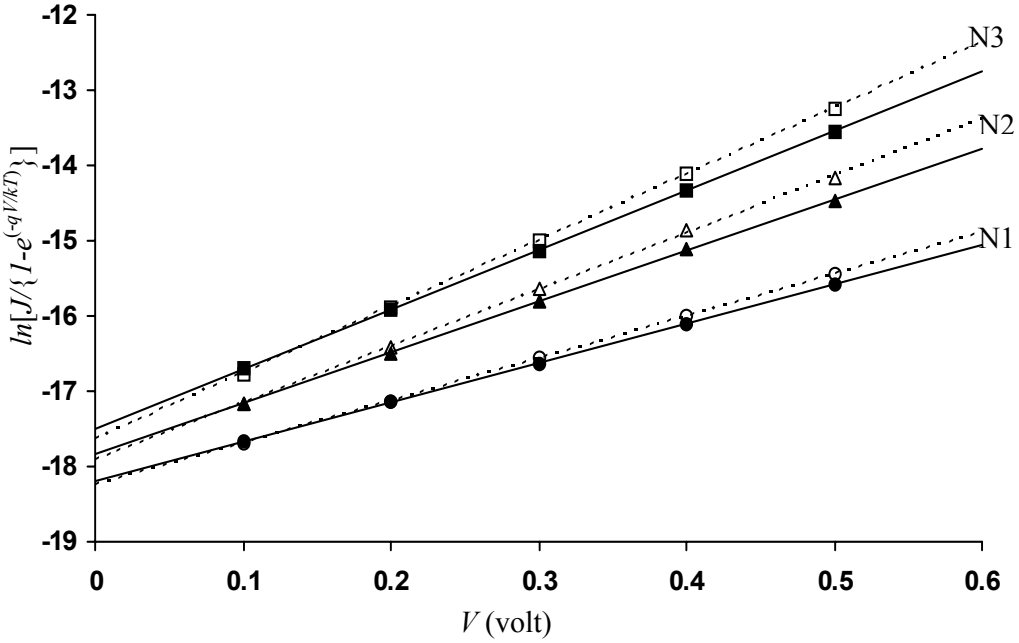

Figure 7.11: $ln[J/\{1-e^{(-qV/kT)}\}]$ vs V plots at room temperature (300K) of three typical Ni-(n)ZnSe Schottky barrier junctions in dark for different doping concentrations: N1=1.4×10^{14} cm^{-3}, N2=4.8×10^{14} cm^{-3} and N3=9.7×10^{14} cm^{-3}, as-prepared (solid line) and heat-treated (dotted line)

Table 7.05: Junction parameters of a few as-prepared and heat-treated Ni-(n)ZnSe Schottky barriers junctions in dark (Area=0.01 cm^{-2}) from *J-V* plots at room temperature (300K)

Junction number	Thickness of ZnSe layer (Å)	Doping concen-tration N_d (10^{14} cm^{-3})	Ideality factor *n*		Saturation current density J_0 ($nAcm^{-2}$)		Barrier height (eV)	
			As-prepared	Heat-treated	As-prepared	Heat-treated	As-prepared	Heat-treated
N1	3250	1.4	7.39	6.87	13	12	0.714	0.717
N2	3100	4.8	5.64	5.04	18	16	0.717	0.722
N3	3500	9.7	4.89	4.36	25	21	0.724	0.727

7.4.2 Series resistance of Ni-(n)ZnSe junctions

Due to the existence of series resistance, at higher forward voltages the ln*I* versus *V* plots (Fig. 7.12) of these Schottky barrier junctions are observed to deviate from linearity. The series resistances of these typical Ni -(n)ZnSe junctions calculated from the *I* vs ΔV plots (Fig. 7.13) are given in Table 7.06. The series resistance of the junctions is found to be of the order of MΩ. The series resistance found to depend on doping concentration, decreasing with increasing concentration and also found to decrease on heat treatment.

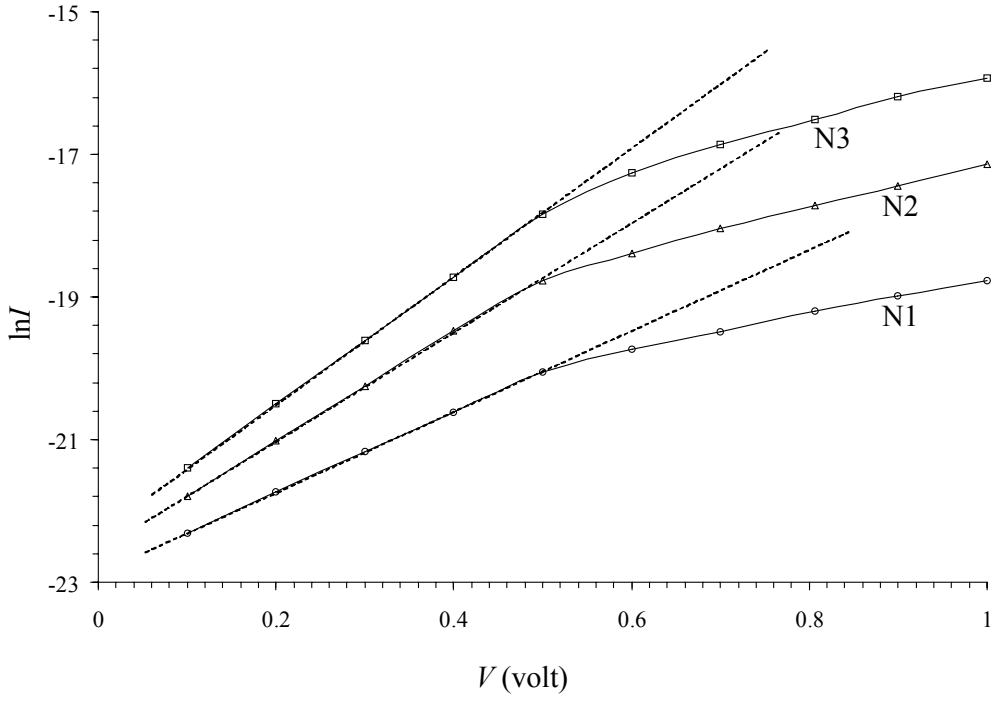

Figure 7.12: *lnI* vs *V* plots at room temperature of three typical Ni-(n)ZnSe Schottky barrier junctions in dark for different doping concentrations N1=1.4×10^{14} cm^{-3}, N2=4.8×10^{14} cm^{-3} and N3=9.7×10^{14} cm^{-3}

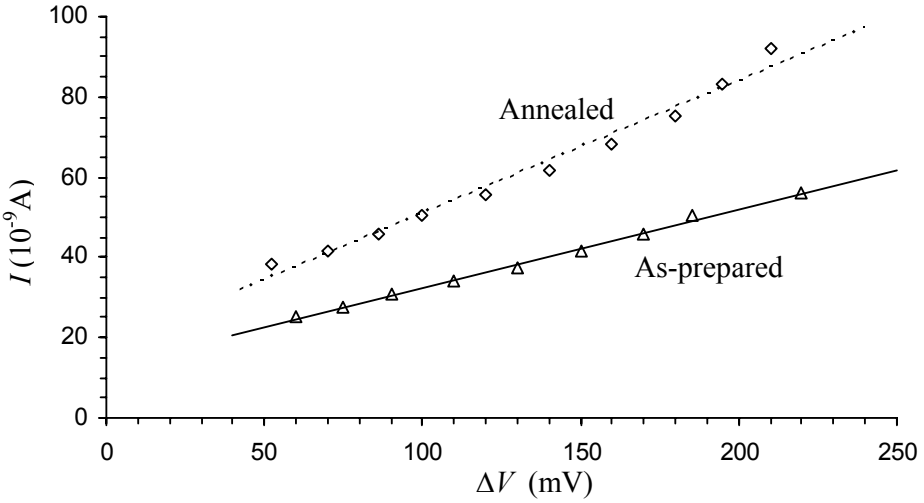

Figure 7.13: I vs ΔV plots at room temperature (300K) of a typical Ni-(n)ZnSe Schottky barrier junction in dark (sample no: N3) of doping concentration 9.7×10^{14} cm^{-3} before and after annealing the junction for 10 minutes

Table 7.06: Room temperature (300K) series resistance of a few Ni-(n)ZnSe Schottky barrier junctions (Area=0.01 cm^{-2}) as-prepared and heat-treated for 10 minutes in dark

Junction number	Thickness of ZnSe layer (Å)	Doping concentration N_D (10^{14} cm^{-3})	Series Resistance	
			As-prepared (10^6 Ω)	Heat-treated (10^6 Ω)
N1	3250	1.4	36.5	29.5
N2	3100	4.8	12.6	8.0
N3	3500	9.7	3.5	2.2

7.4.3 Temperature dependence of *J-V* characteristics of Ni-(n)ZnSe junctions (in dark)

The temperature dependence of *J-V* characteristics of the junction has been studied within the temperature range 300K to 333K. Figure 7.14 shows *J-V* curves of a typical Ni-(n)ZnSe junction in dark under forward bias at various temperatures. It has been observed that beyond room temperature (300K), the current increases abruptly with voltage.

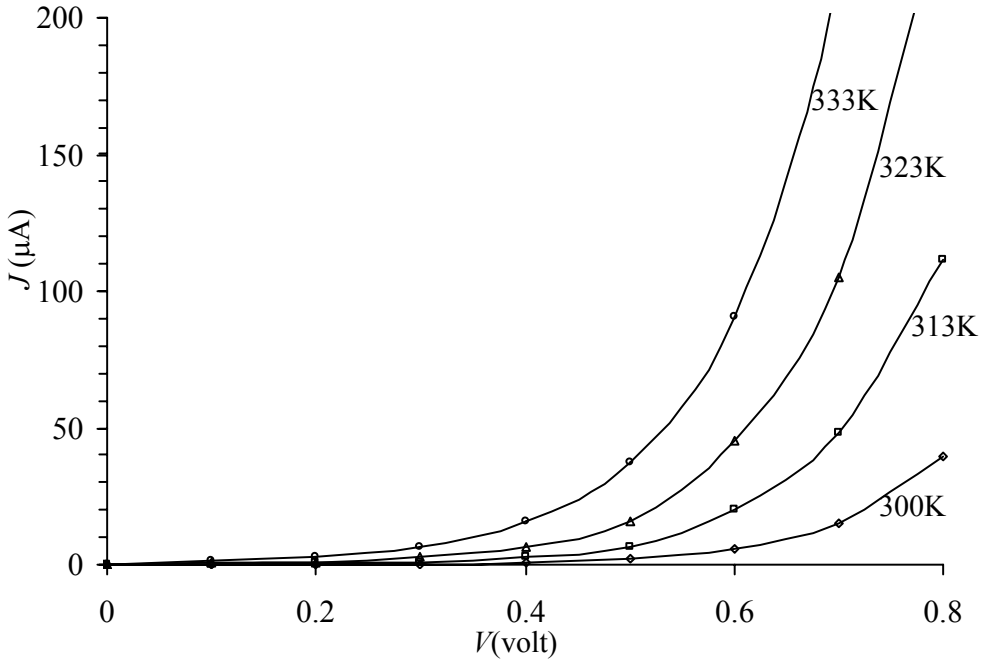

Figure 7.14: *J-V* characteristics of a typical Ni-(n)ZnSe junction (No: N3) in dark at different temperatures (doping concentration 9.7×10^{14} cm^{-3} and junction area=0.01 cm^2)

The saturation current density at different temperatures of the junction were obtained from $\ln[J/(1-e^{-qV/kT})]$ vs V plots for each temperature. Figure 7.15 shows the linear portions of the $\ln[J/(1-e^{-qV/kT})]$ vs V plots of a typical Ni-(n)ZnSe junction at different temperatures. The saturation current density and ideality factor at different temperatures of a typical junction calculated from these plots are given in Table 7.07. The ideality factor (n) has been observed to be nearly of same value while the saturation current density J_0 is found to increase with increase of temperature.

The calculated values of J_0 at different temperatures (T) were used to draw $\ln(J_0/T^2)$ vs T^{-1} plots. The figure 7.16 shows such a plot for a typical Ni-(n)ZnSe junction. The value of the effective Richardson constant A^* was calculated from the intercept on the vertical axis of the Richardson plot and the barrier height (ϕ_b) of the junction was estimated from the slope. Table 7.07 shows the value of A^* and barrier heights of a typical junction as-prepared and after annealing. The barrier heights measured from the Richardson plots, were found to be in the range of 0.723 eV to 0.729 eV. The barrier heights have been observed to increase on annealing the junctions.

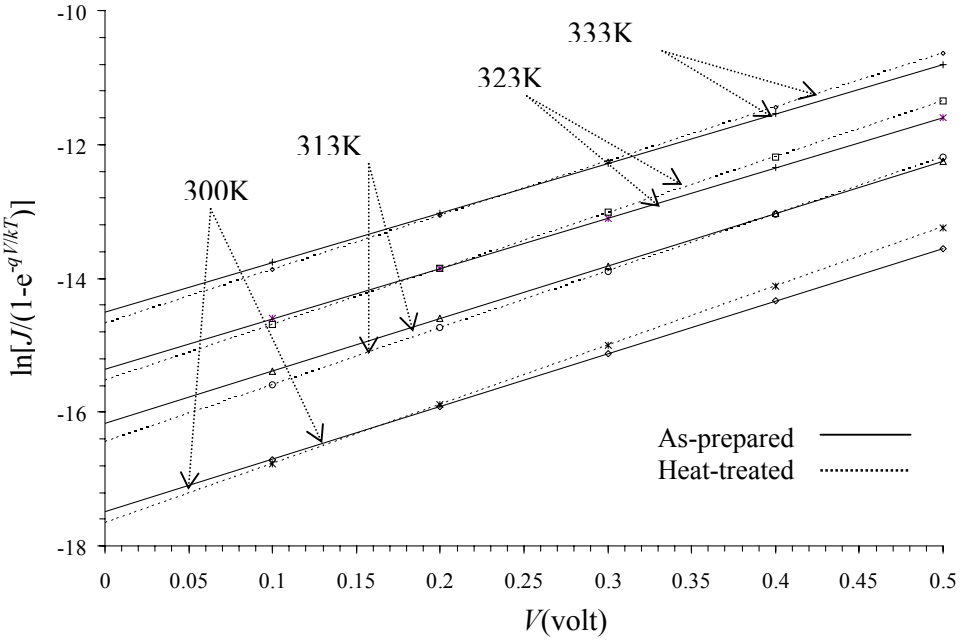

Figure7.15: $\ln[J/(1-e^{-qV/kT})]$ vs V plots of a typical Ni-(n)ZnSe junction (No: N3) (N_D=9.7×10^{14} cm^{-3}) at different temperatures

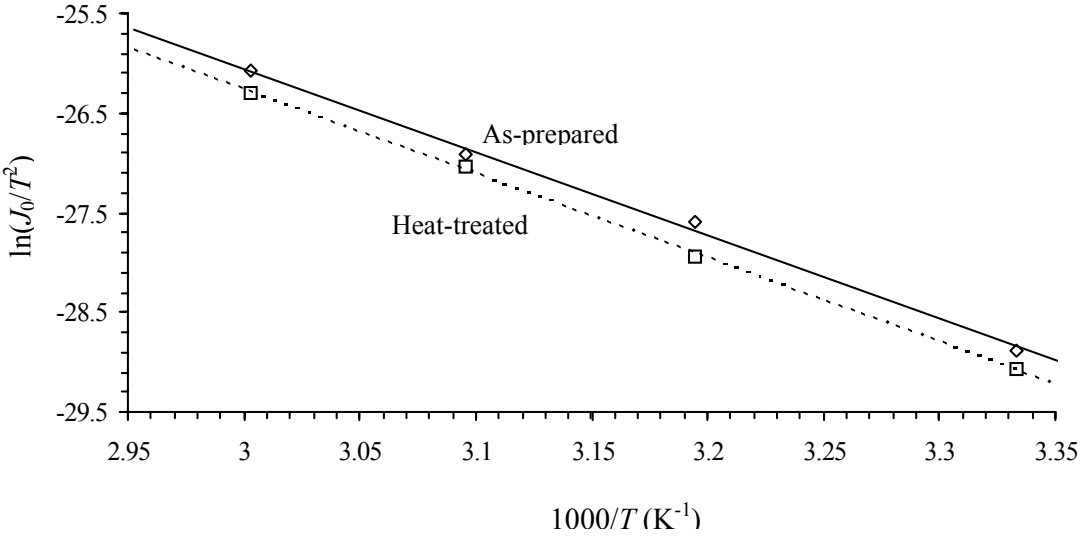

Figure7.16: $\ln(J_0/T^2)$ vs T^{-1} plots of a typical Ni-(n)ZnSe junction (No: N3) (N_D=9.7×10^{14} cm^{-3})

Table 7.07: Some parameters of as-prepared and heat-treated Ni-(n)ZnSe Schottky barrier junctions (No: N3) of Area=0.01 cm^{-2} (N_D=9.7×10^{14} cm^{-3}) at different temperatures in dark from *J-V* plots

Temperature (K)	Ideality factor *N*		Saturation current density J_0 ($nAcm^{-2}$)		Richardson constant A^* ($A\ cm^{-2}K^{-2}$)		Barrier height (eV)	
	As-prepared	Heat-treated	As-prepared	Heat-treated	As-prepared	Heat-treated	As-prepared	Heat-treated
300K	4.90	4.37	26	21	40	38.5	0.724	0.728
313K	4.72	4.35	95	72			0.729	0.729
323K	4.77	4.35	215	181			0.725	0.727
333K	4.70	4.3	502	421			0.723	0.728

From the study it is found that the *J-V* characteristics of Ni-(n)ZnSe Schottky barrier junctions are of rectifying in nature. This indicates the existence of barrier between the films of Ni and (n)ZnSe of the fabricated structures. The reverse current does not saturate.

The diode ideality factors have been found to be 4.89 to 7.39 which were found to reduce to 4.36 to 6.87 on heat treatment of the devices. The series resistance estimated was found to be 3.5 MΩ to 36.5 MΩ. The series resistance of the junctions of higher doping concentration was found to be less and also found to be lowered on heat treatment. The saturation reverse current density also found to increase from 26 $nAcm^{-2}$ to 502 $nAcm^{-2}$ with the increase of temperature from 300K to 333K. The barrier height measured from the values of J_0 at different temperatures, was found to be 0.723 eV to 0.729 eV. The barrier height of the junctions has been found to increase with doping concentrations.

Heat treatment of the devices lowers the diode ideality factor and increases the barrier heights. The reverse saturation current density of the annealed devices was found less than the unannealed devices.

7.5 Discussions and conclusions:

The current-voltage characteristics of the fabricated Au-(n)ZnSe and Ni-(n)ZnSe Schottky barrier junctions have been studied. The rectifying natures of the *J-V* characteristics of the junctions, indicate the existence of barriers at the junctions.

The reverse current does not saturate. This may be due to the voltage dependence of barrier height and also may result from the onset of thermoionic field emission with applied bias. At lower doping levels the application of a few volts can cause the barrier to become thin enough for tunneling to takes place [369]. It is quite possible that more than one of these mechanisms may operate simultaneously.

The diode ideality factors of both structures have been found to be within 3.53 to 7.4. There may be variety of causes [41], which lead *n* to exceed unity. Some of the main causes are:

(i) The presence of interfacial layer and image force affect the barrier and therefore the effective current with applied voltage,

(ii) Recombination of electrons and holes due to surface states, defects etc gives rise to component of current with *n* greater than unity in addition to thermoionic emission current. At higher bias, there may be increase in *n* because of drift and diffusion in the barrier region.

(iii) Due to tunneling effect, at lower forward bias, the current becomes larger than otherwise expected,

(iv) The high series resistance causes the actual voltage drop across the barrier region to be less than the voltage applied to the terminals of the diode.

The series resistance of both the types of junctions was found to be of the order of MΩ. The large value of series resistance is due to various types of defects which were crept into the film during film preparation and also due to low doping concentration. The series resistance of the junctions of higher doping concentration was found less. Introduction of any insulating layer between electrode and semiconductor also contributes to the series resistance. In the present case, some interfacial layer was developed due to breaking of vacuum in between the deposition of metal (Au or Ni) and (n)ZnSe. Heat treatment of the devices reduces the defects of the film and also makes more intimate contacts between the electrodes and semiconductor by thermally removing the insulating layer. Therefore series resistance of the device is found to be lowered on heat treatment.

The *J-V* characteristics of the junctions were also studied at different temperatures. The thermal generation of extra carriers causes a gradual rise of forward current at elevated temperatures. The variation of the saturation reverse current density J_0 of the junctions with temperature indicates that the current transport mechanism is dominated by the thermoionic emission process [370].

The barrier heights measured from *J-V* characteristics, for Au/Ni-(n)ZnSe Schottky barrier junctions were found to be within 0.714 eV to 0.820 eV (Table 7.02 & 7.05). The lower value of barrier height is due to the presence of interfacial layer. In polycrystalline semiconductor thin films, the constituent atoms at the grain boundary are disordered and hence there are large numbers of defects due to incomplete atomic bonding (dangling bond). This may result the existence of surface states [371]. In our case, the barrier heights have been found to be less dependent on work function of the barrier metal Au or Ni. These may be due to the effect of surface states of the semiconductor [372]. Similar behavior was observed in other II-VI semiconductors including ZnSe [373].

Heat treatment of the devices lowers the diode ideality factor and increases the barrier heights. The reverse saturation current density of the annealed devices was found less than the unannealed devices. This improvement is thought to be mainly due to formation of more intimate contact at metal-semiconductor interface on heat treatment, avoiding any surface irregularities, which can cause deviation from Schottky behavior. Heat treatment also removes interfacial layer and reduces the interface state densities.

The barrier heights measured from C^{-2}-*V* plots (Table 7.01) have been observed to be higher than the barrier heights measured from *J-V* measurements (Table 7.02 and Table 7.05). Due to the presence of interfacial layer, the capacitance of the Schottky barrier is increased and thereby measured built-in voltage is found more. Therefore the barrier height of a Schottky barrier with interfacial layer obtained from *C-V* method gives higher value than the actual value [321]. Further the *C-V* method essentially gives the flat-band barrier heights which are larger than those obtained from *J-V* plots, image force lowering being ignored in the former method.

7.6 Studies of Current-Voltage characteristics of Au-(n)ZnSe and Ni-(n)ZnSe junctions under illumination:

7.6.1 Photovoltaic measurements:

For studying photovoltaic effect special arrangements were made to expose the sample to the light of desired intensity and wave lengths at room temperature (300K). The details of the arrangement have been given in chapter 4.

7.6.2 Studies of Photovoltaic Effect in Au-(n)ZnSe junctions

The Figure 7.17 shows the *J-V* characteristics of a few typical Au-(n)ZnSe junctions at room temperature under illumination of intensity 50 mW/cm^2. The *J-V* curves fall in the fourth quadrant as has been discussed in chapter 3. The junctions have been found to exhibit very poor photovoltaic effect. The open-circuit voltage (V_{oc}) was obtained from the intercepts on the voltage axis and short-circuit current (J_{sc}) was obtained from the intercept on the current axis. The value of fill factor (*FF*) and efficiency calculated from the relation (3.66 and 3.67) have been shown in Table 7.08. The photovoltaic performance of the junctions was found to be improved after heat treatment of the devices.

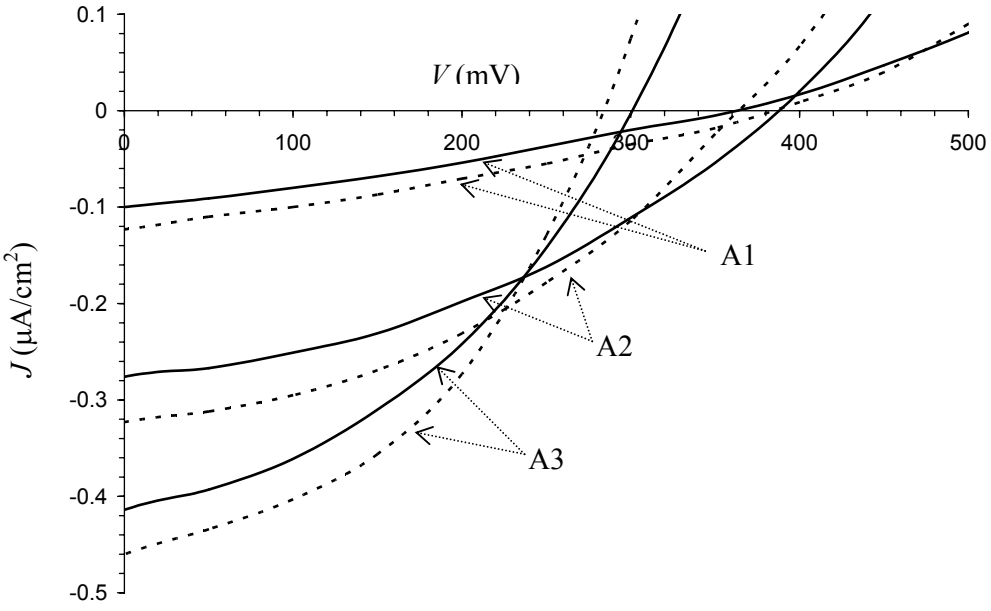

Figure 7.17: *J-V* plots under illumination of as-prepared (solid curve) and heat-treated (dotted curve) Au-(n)ZnSe Schottky barrier junctions of different doping concentrations: A1=1.4×10^{14} cm^{-3}, A2=4.8×10^{14} cm^{-3} and A3=9.7×10^{14} cm^{-3}

Table 7.08: Photovoltaic parameters of as-prepared and heat-treated Au-(n)ZnSe Schottky barrier junctions of area=0.01cm^2 for different doping concentrations

Junction number	Doping concentration N_D (10^{14}cm^{-3})	Short-circuit current density J_{sc} (μA/cm^2)		Open-circuit voltage V_{oc} (mV)		Fill factor *FF*		Efficiency (%)	
		As-prepared	Heat-treated	As-prepared	Heat-treated	As-prepared	Heat-treated	As-prepared	Heat-treated
A1	1.4	0.10	0.123	360	380	0.30	0.30	0.02	0.03
A2	4.8	0.275	0.32	390	365	0.37	0.39	0.08	0.09
A3	9.7	0.42	0.46	300	280	0.40	0.44	0.09	0.11

7.6.3 Diode parameters of Au-(n)ZnSe Schottky barrier junctions under illumination:

To measure the diode ideality factor n and reverse saturation current J_o of the junctions under illumination, J_{sc} and V_{oc} of the junctions were measured from the *J-V* curves under three different levels of illumination (Fig. 7.18(A)). The photovoltaic cell follows the relation (3.63) as discussed in chapter 3.7.2 [374],

$$J_{sc} = J_0\left[\exp\left(\frac{qV_{oc}}{nkT}\right)-1\right]. \qquad (3.63)$$

Therefore, when ln J_{sc} versus V_{oc} is plotted, it will be a straight line as per relation

$$\ln J_{sc} = \ln J_0 + \frac{qV_{oc}}{nkT}. \qquad (3.64)$$

Figure 7.18(B) shows ln J_{sc} versus V_{oc} plot of a typical junction. From the slope and intercept of the plots for each junction, the diode ideality factor n and reverse saturation current density J_o under illumination were calculated and have been given in the table 7.09. Comparing the values of diode parameters in dark (from table 7.02) and under illumination (table 7.09) for the same junction, the diode ideality factors n are observed to decrease under illumination. The saturation current density J_o is found to increase under illumination.

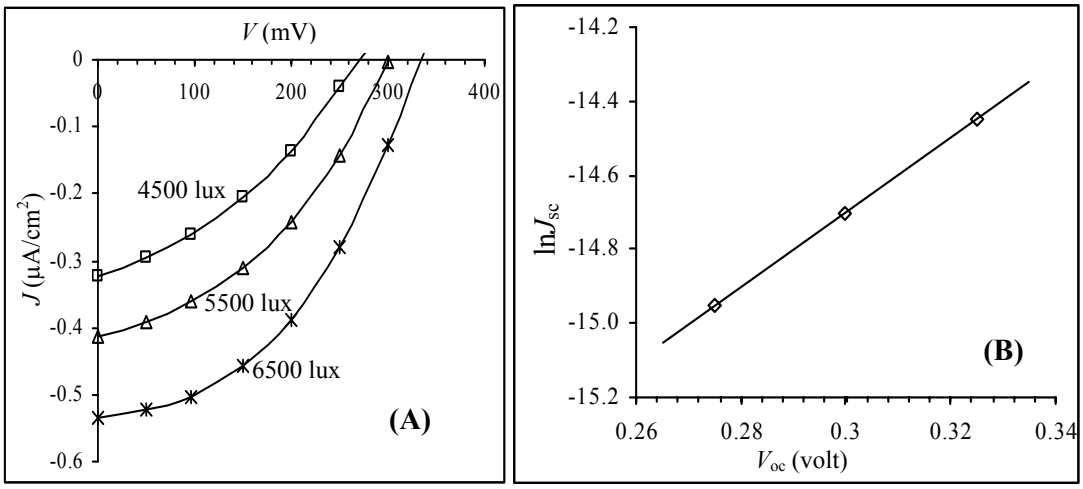

Figure 7.18: (A) *J-V* plots for three different intensities of illumination and (B) ln J_{sc} versus V_{oc} plot for a typical Au-(n)ZnSe Schottky barrier junction (A3) of doping concentration 9.7×10^{14} cm^{-3}.

Table 7.09: Ideality factor and saturation current density under illumination of as-prepared and heat-treated Au-(n)ZnSe Schottky barrier junctions of area=0.01cm^2 for different doping concentrations

Junction number	Doping concentration N_D ($10^{14}cm^{-3}$)	Under illumination			
		Ideality factor *n*		Saturation current density J_o (nA/cm^2)	
		As-prepared	Heat-treated	As-prepared	Heat-treated
A1	1.4	7	6.4	12	11
A2	4.8	6	5.3	16	15
A3	9.7	3.65	3.6	20	18

7.6.4 Studies of Photovoltaic Effect in Ni-(n)ZnSe junctions

Photovoltaic characteristics of three Ni-(n)ZnSe junctions at room temperature under illumination of intensity 50 mW/cm^2 are shown in Figure 7.19. The junctions have exhibited very poor photovoltaic effect, though it is improved on increasing the doping concentration. The photovoltaic performance of the junctions was found to be slightly improved after heat treatment of the devices. Some photovoltaic parameters of a few Ni-(n)ZnSe Schottky barrier junctions have been given in Table 7.10.

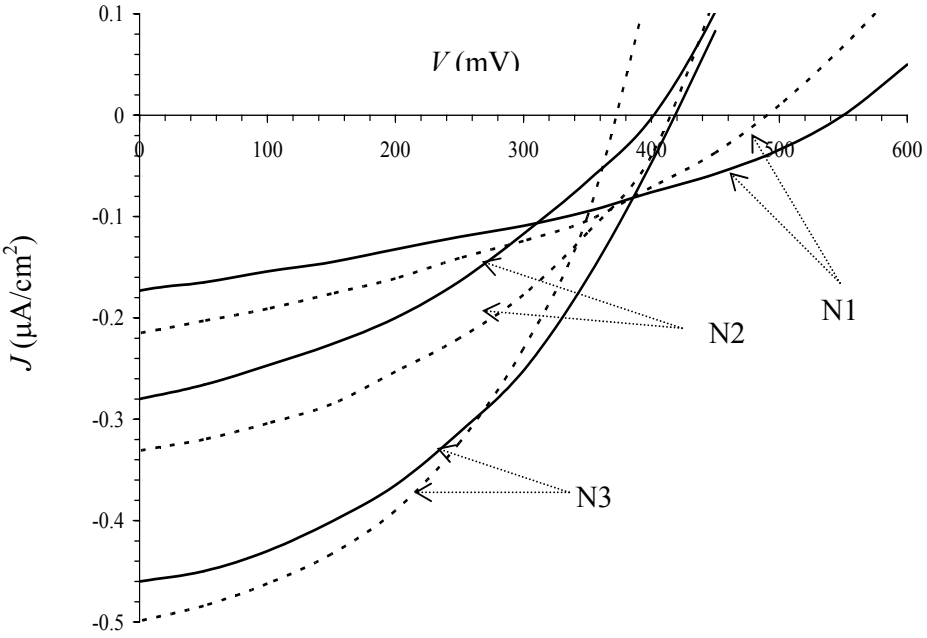

Figure 7.19: *J-V* plots under illumination of as-prepared (solid curve) and heat-treated (dotted curve) Ni-(n)ZnSe Schottky barrier junctions of different doping concentrations [1.4×10^{14} cm^{-3}(N1), 4.8×10^{14} cm^{-3} (N2) and 9.7×10^{14} cm^{-3} (N3)]

Table 7.10: Photovoltaic parameters of as-prepared and heat-treated Ni-(n)ZnSe Schottky barrier junctions of area=0.01cm^2 for different doping concentrations

Junction number	Doping concentration N_D (10^{14}cm^{-3})	Short-circuit current density J_{sc} (μA/cm^2)		Open-circuit voltage V_{oc} (mV)		Fill factor *FF*		Efficiency (%)	
		As-prepared	Heat-treated	As-prepared	Heat-treated	As-prepared	Heat-treated	As-prepared	Heat-treated
N1	1.4	0.17	0.22	550	490	0.31	0.34	0.05	0.07
N2	4.8	0.28	0.33	400	410	0.37	0.41	0.08	0.11
N3	9.7	0.46	0.50	410	370	0.42	0.44	0.16	0.17

7.6.5 Diode parameters of Ni-(n)ZnSe Schottky barrier junctions under illumination:

To measure the diode ideality factor n and reverse saturation current J_o of the junctions under illumination, J_{sc} and V_{oc} of the junctions were measured at three different levels of illumination (Fig. 7.20(A)). Then ln J_{sc} versus V_{oc} plots for each junction were plotted (Fig 7.20(B)) and from the slope and intercept of the respective plots the diode ideality factor n and reverse saturation current density J_o under illumination were calculated as discussed in section 7.4.3. The diode ideality factor n and reverse saturation current J_o of a few junctions under illumination have been given in the table 7.11. Comparing the values of diode parameters in dark (from table 7.05) and under illumination for the same junction, the diode ideality factors n of junction are observed to decrease under illumination. The saturation current density J_o is found to increase under illumination.

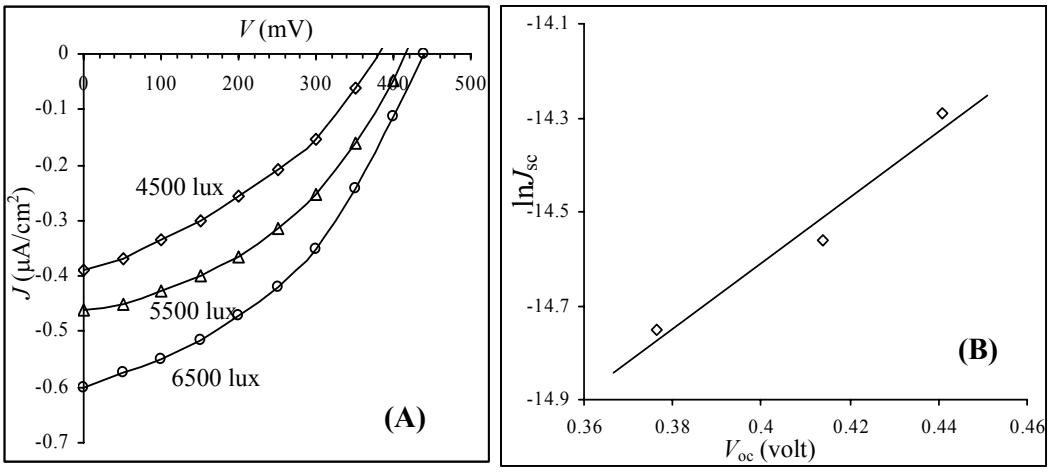

Figure 7.20: (A) *J-V* plots under illumination for three different intensity of illumination and (B) ln J_{sc} versus V_{oc} plot for a typical Ni-(n)ZnSe Schottky barrier junction (N3) of doping concentration 9.7×10^{14} cm^{-3}.

Table 7.11: Ideality factor and saturation current density under illumination of as-prepared and heat-treated Ni-(n)ZnSe Schottky barrier junctions of area=0.01cm^2 for different doping concentrations

Junction number	Doping concentration N_D ($10^{14}cm^{-3}$)	Under illumination			
		Ideality factor *n*		Saturation current density J_o (nA/cm^2)	
		As-prepared	Heat-treated	As-prepared	Heat-treated
N1	1.4	7.3	6.6	12	11
N2	4.8	5.6	4.9	16	15
N3	9.7	4.7	4.2	28	18

7.6.6 Discussions on Photovoltaic effect:

The Au-(n)ZnSe and Ni-(n)ZnSe Schottky barrier junctions were studied under illumination. Both the junctions have been found to exhibit photovoltaic effect. Very low photovoltages with low value of fill-factors have been observed for these junctions. There are various factors responsible for the poor photovoltaic performance, such as high defect density, presence of interfacial layer, low doping concentration etc [41, 375]. The nearly linear nature of the *J-V* curve under illumination implies the existence of very high series resistance in the junctions, which also causes poor photovoltaic effect.

The open circuit voltage (V_{oc}) and short circuit current (I_{sc}) are strongly dependent on the series resistance (R_s) as well as on diode ideality factor (n) as per the well known equations [375]

$$V_{oc}=(nkT/q)\ln[(I_{sc}/I_0)+1]$$

$$I_{sc}=I_0[\exp\{q(V-IR_s)/nkT\}-1]-I$$

where, I is the total output current and I_0 is the diode saturation current. In our case the higher value of series resistance reduces the short-circuit current and hence the open- circuit voltage also. Very low photo voltages with low value of fill factors have been observed in these junctions due to higher value of diode ideality factors. In the polycrystalline films, the grain boundary potential may affect the series resistance and open circuit voltage of solar cell [376]. Due to this grain boundary effect, recombination of photo generated carriers takes place at grain boundary and hence the short-circuit current is reduced [376, 377]. Besides the affect of high series resistance and grain boundary effect, there are various factors responsible for the poor photovoltaic performance, such as high defect density, presence of interfacial layer and low doping concentration. The increase of doping concentration of the semiconducting films slightly improves the photovoltaic performance of the devices. The junctions with ZnSe film of doping concentration 9.7×10^{14} cm^{-3} have been observed to exhibit good photovoltaic effect. It is expected that the junction will act as an efficient photovoltaic device if concentration is increased above it. In the present case it was not possible to increase doping concentration beyond 10^{14} cm^{-3} by coevaporation. Improvement of photovoltaic performance was also observed in heat-treated devices. This is mainly due to lowering of series resistance and improvement of diode quality.

The diode ideality factor under illumination of both Au-(n)ZnSe and Ni-(n)ZnSe junctions has been found to decrease upon illumination while the saturation current density has been observed to increase under illumination. This is due to the generation of more carriers under illumination. Similar type of changes were observed by other workers with other Schottky barrier junctions [375, 378].

CHAPTER 8

Studies on ITO/(p)Si, (n)ZnSe/(p)CdTe and (n)ZnSe/(p)Si Heterojunctions

In this chapter, results of the studies on electrical properties and photovoltaic effect of ITO/(p)Si, (n)ZnSe/(p)CdTe and (n)ZnSe/(p)Si junctions have been presented. All the compound semiconductors of these junctions except Si were vacuum deposited thin films. In case of Si, p-type single crystal Si wafers were used. These junctions are heterojunctions as two semiconductors used to form a structure possess different band gap energies. Different junction parameters such as diode ideality factor, reverse saturation current density, series resistance, short-circuit current, open-circuit voltage etc. of these junctions were determined from current voltage characteristics and also from C^{-2}-V plots. Photovoltaic effect on *I-V* characteristics of these junctions were also studied at room temperature. The details of the preparation of the heterojunctions and experimental arrangement for measuring *J-V* characteristics are discussed in chapter 4. The background theories of heterojunctions have been discussed in chapter 3.

8.1 Studies on ITO/(p)Si heterojunctions

For the preparation of a ITO/(p)Si heterojunctions, Si wafers were used whose specifications were: boron-doped (p-type), orientation (100), resistivity 10-20 ohm cm, thickness 500-550μm and area 1.5x1.5 cm^2. Initially, the (p)Si wafer was etched chemically by hydrofluoric acid and then washed. Al electrodes was vacuum deposited on one side of this wafer to make ohmic contact and then ITO film of thickness 2400Å was deposited on the other side, thus making a ITO/(p)Si-Al structure. Several junctions were prepared on the same Si wafer by depositing several Al electrodes. During deposition the Si substrate was kept at a temperature of 593K. Counter electrodes of Al were vacuum deposited over ITO films for making ohmic contacts to ITO films. Thus structures of the type Al-ITO/(p)Si-Al were obtained. Before deposition of counter-electrodes for measurements, ITO films as well as the junction structures were annealed for one hour at 593K temperature. This was done in

order to improve the conductivity and transparency of the ITO films and to improve the junction quality as reported in our earlier study [379].

8.1.1. Current-voltage characteristics

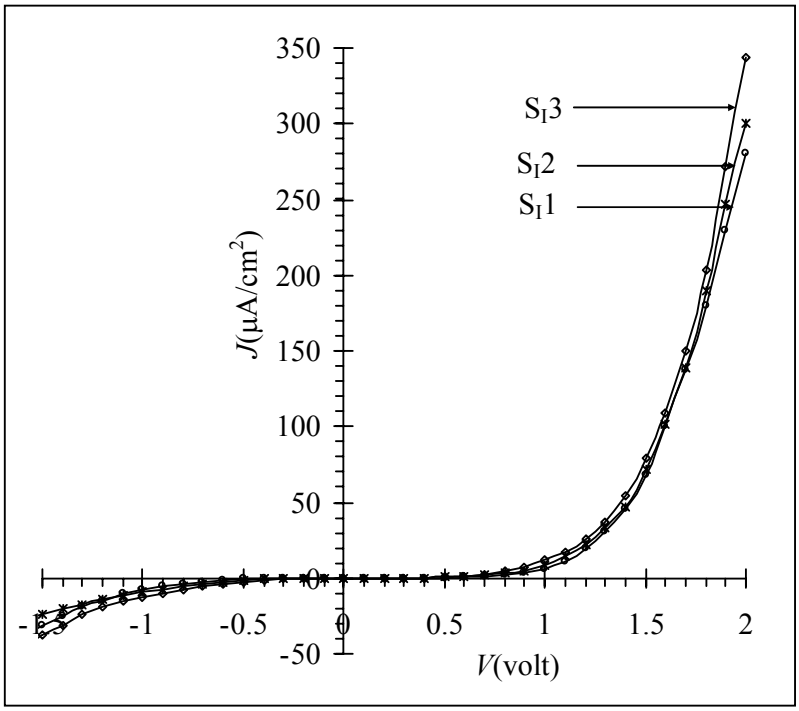

Figure 8.01: *J-V* characteristics of three ITO-(p)Si junctions at room temperature(300K) in dark.

The *J-V* characteristics of a few typical ITO/(p)Si junctions in dark have been shown in figure 8.01. The curves show rectifying nature of a diode in the forward direction. In reverse bias the current increases slowly with voltage and did not show any tendency of saturation. Under the forward bias the current increases exponentially with voltage and followed the standard diode equation (3.56)

$$J = J_0 \exp(qV / nkT)\left[1 - \exp\left(-qV / kT\right)\right]$$

where, J is the current density of a diode for bias voltage V at temperature T (K), n is the diode ideality factor and J_0 is the saturation current density. Other quantities have their usual meanings.

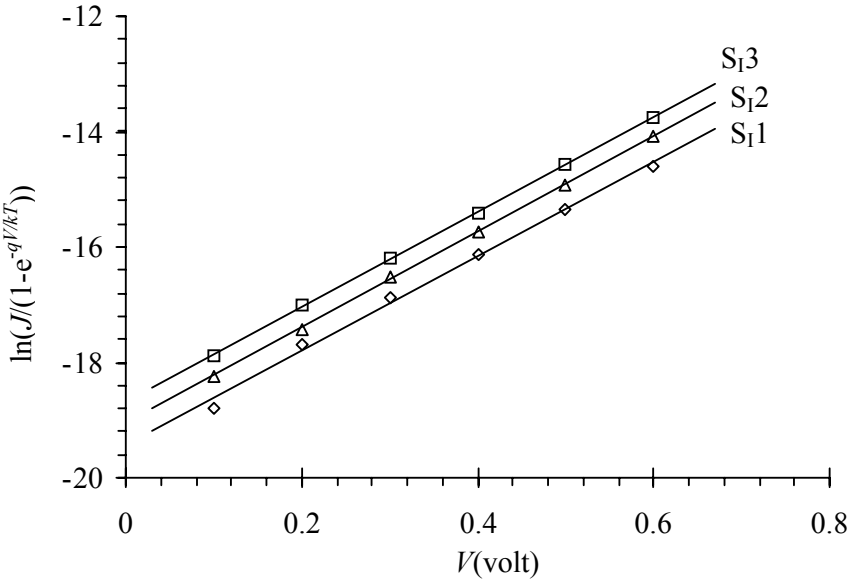

Figure 8.02: ln[J/{1-exp(-qV/kT)}] vs V curves of three ITO-(p)Si junctions at room temperature (300K) in dark.

Figure 8.02 shows linear region of ln[J/{1-exp(-qV/kT)}] vs V plots for a few typical ITO-(p)Si junctions in dark at room temperature. The ideality factor (n) and the saturation current density (J_0) of the junctions were calculated from the slope and intercept of these plots (Figure 8.02) respectively. The estimated values of ideality factor and saturation current density for three junctions are tabulated in Table 8.01. The ideality factor has been found to be within 4.65 to 4.71 and the reverse saturation current density was found in the range of 3.6 nA/cm^2 to 6.7 nA/cm^2.

8.1.2 Effect of Series Resistance:

For bias voltage greater than 0.6 V, the ln$I$-V plots of the junctions have been observed to deviate from linearity (Figure 8.03). This is due to presence of series resistance (R_s) associated with the neutral region of the diode. For this series resistance, the current of the diode is proportional to exp[q(V-IR_s)/kT –1], instead of obeying the ideal condition as discussed earlier.

The series resistance estimated from I vs ΔV plots (Figure 8.04) of the diodes are tabulated in Table 8.01. The series resistance for these typical ITO-(p)Si diodes is found to be more than kilo-ohm.

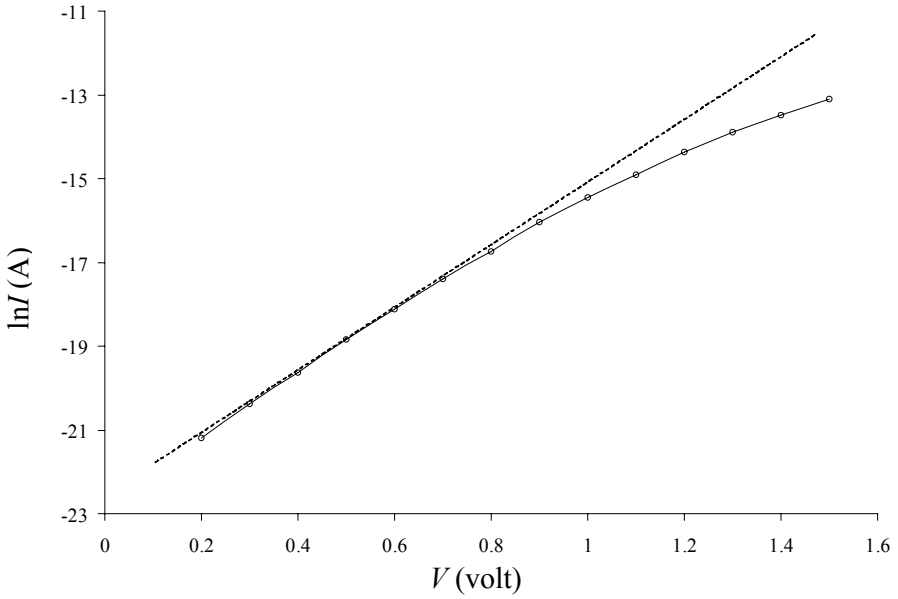

Figure 8.03: ln$I$ vs V plots at room temperature in dark of a typical ITO-(p)Si junction of junction area A=0.03 cm^2, showing the deviation from linearity

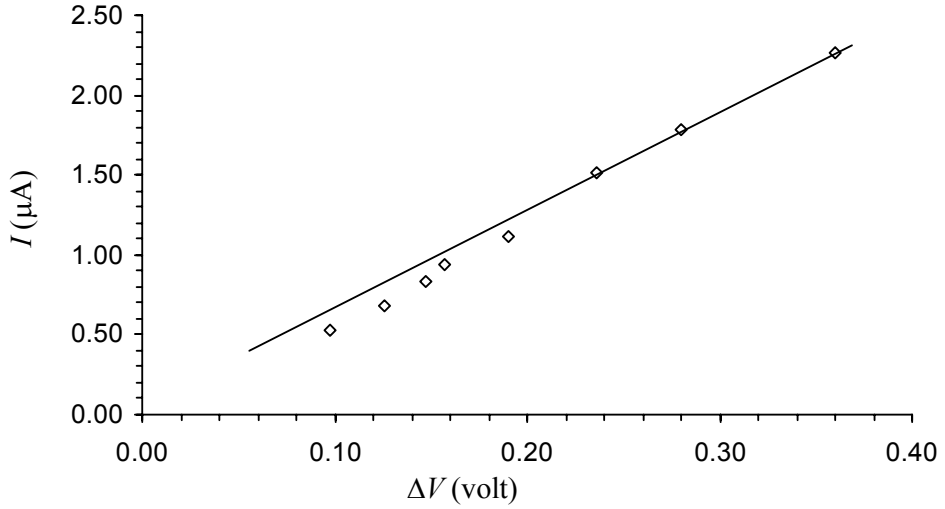

Figure 8.04: I vs ΔV plots at room temperature in dark of a typical ITO-(p)Si junction (S_I1) of junction area A=0.03 cm^2.

8.1.3 Temperature dependence of *J-V* characteristics of ITO-(p)Si junctions (in dark)

The temperature dependence of *J-V* characteristics of the junction has been studied within the temperature range 300K to 333K. Figure 8.05 shows *J-V* curves of a typical ITO-(p)Si junction in dark under forward bias at various temperatures. The saturation current density at a temperature of the junction was obtained from $\ln[J/(1-e^{-qV/kT})]$ vs V plot

for that temperature (Figure 8.06). The saturation current density found from intercept and ideality factor found from the slopes of $\ln[J/(1-e^{-qV/kT})]$ vs V plot at different temperatures of a typical junction are given in Table 8.02. The ideality factor (n) was found to be of nearly same while the saturation current density is found to increase with increase of temperature from 300K to 333K.

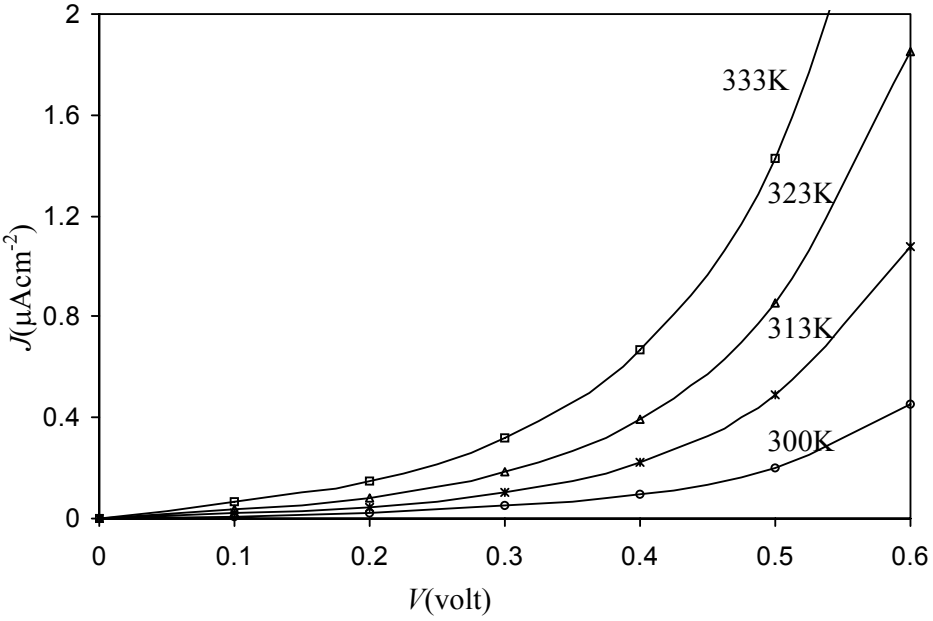

Figure 8.05: J-V plots (for forward bias) of a typical ITO-(p)Si junction (Sample No: S_I1) in dark at different temperatures (N_a= 5×10^{16} cm^{-3})

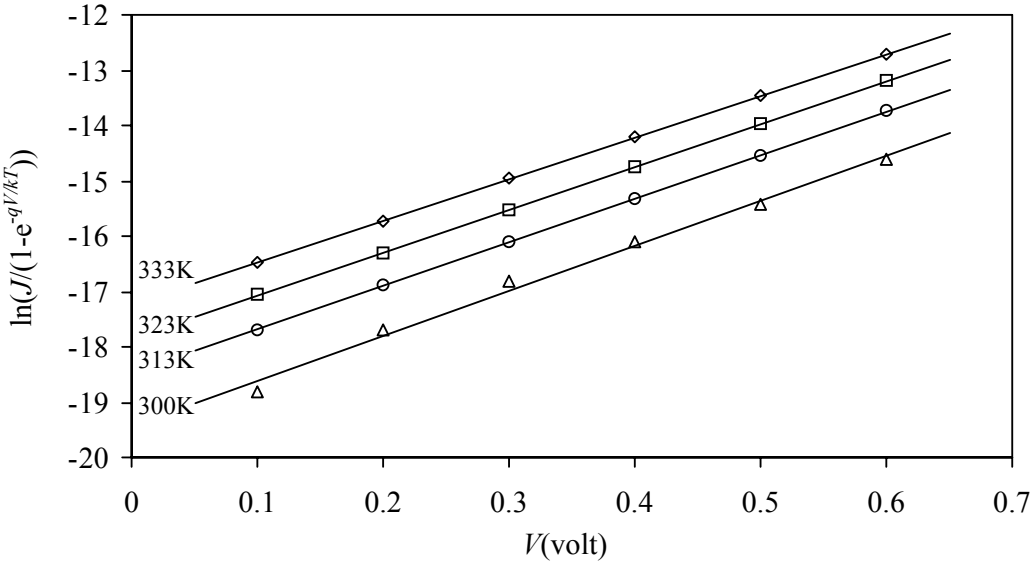

Figure8.06: $\ln[J/(1-e^{-qV/kT})]$ vs V plots of a typical ITO-(p)Si junction (Sample No: S_I1) (N_a= 5×10^{16} cm^{-3}) at different temperatures

Using the calculated values of J_0 for different temperatures, $\ln(J_0/T^2)$ vs T^{-1}, the Richardson's plots were drawn. For all the junctions the plots have been found straight line. This implies that the Schottky theory of thermoionic emission is applicable for these junctions which follows the relation (3.54),

$$J_0=A^*T^2e^{-q\phi_b/kT}$$

where, ϕ_b is the barrier height of the junction, A^* is the effective Richardson constant and T is the temperature. The figure 8.07 shows such a plot for a typical ITO-(p)Si junction.

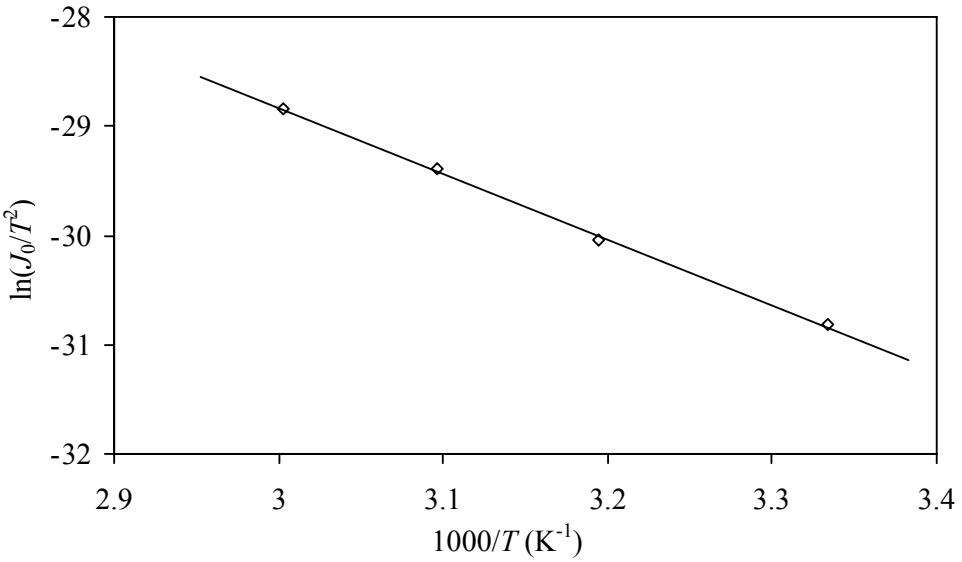

Figure 8.07: $\ln(J_0/T^2)$ vs T^1 plots of a typical ITO-(p)Si junction (sample no: S_I1)

From the slopes of the Richardson's plots, the barrier heights of the junctions were estimated. The barrier heights of three typical junctions measured from current-voltage characteristics are given in Table 8.01. The average value of the barrier height of three junctions has been found to be 0.52 eV.

8.1.4 Capacitance-voltage characteristics:

The C^{-2}-V plots for three junctions have been drawn at frequency 1KHz (Fig. 8.08) under reverse bias condition. The carrier concentration of Si and the built-in potential at the junction are estimated respectively from the slope and the intercept of C^{-2}-V plots of the junction under reverse bias condition using the following relation (3.46),

$$C^{-2} = \left(2 \Big/ q\varepsilon_s N_d \right)\left(V_{bi} + V_r - kT \Big/ q \right)$$

Here V_{bi} is the built-in potential at zero bias which is equal to V_i+kT/q, where V_i=−V_{bi}+kT/q is the negative intercept on the V_r axis and ε is the permittivity of Si. The barrier height is calculated from the measured value of V_{bi} using the relation $\phi_b = V_{bi} + \xi$ as discussed in previous chapter (section 7.2). The value of the difference between Fermi level and the bottom of the conduction band (ξ) is found after knowing the value of effective density of states in conduction band (N_c) at room temperature. For (p)Si the value of N_c is 1.04×10^{19} cm^{-3} [380]. The average barrier height obtained for three junctions from C^{-2}-V plots is about 0.55 eV.

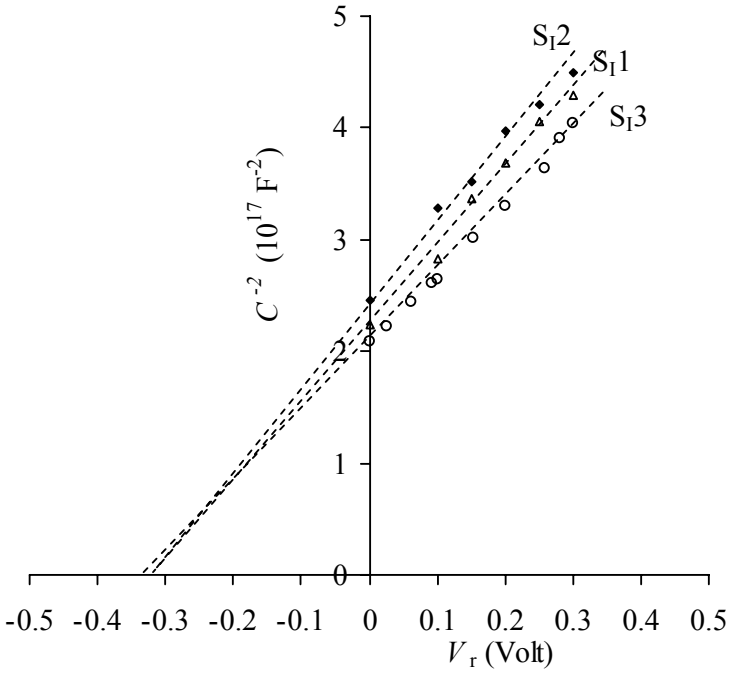

Figure 8.08: C^{-2}-V_r(reverse) plots for three ITO-(p)Si junctions (N_a= 5×10^{16} cm^{-3}) at room temperature (300K) in dark .

Table8.01: Junction parameters of three typical ITO-(p)Si junctions of doping concentration (N_a=5×10^{16}cm^{-3}) at room temperature (300K)

Junction number	Junction area (cm^2)	Ideality factor n	Saturation current density J_0(nA/cm^2)	Series resistance R_s (KΩ)	Barrier height ϕ_b (eV)	
					From J-V study	From C-V study
S_I1	0.030	4.71	4	156	0.520	0.556
S_I2	0.035	4.65	5	177	0.522	0.546
S_I3	0.038	4.70	7	172	0.525	0.556

Table 8.02: Saturation current density, and ideality factor of a typical ITO-(p)Si junction (S_I1) of Area=0.03 cm^{-2} (N_a= 5×10^{16} cm^{-3}) at different temperatures in dark

Temperature (K)	Ideality factor n	Saturation current density J_0 (nAcm^{-2})	Barrier height ϕ_b (eV)
300	4.76	4	0.520
313	4.70	9	0.521
323	4.65	18	0.520
333	4.62	33	0.520

8.1.5 Photovoltaic effect:

The ITO-(p)Si junctions were studied at room temperature (300K) for their photovoltaic performances under white light. Fig.8.09 shows *J-V* curves of three typical junctions when illuminated by white light of intensity 50 mW/cm^2. Nearly linear nature of the curves implies the existence of a large series resistance. Table 8.03 shows the open-circuit voltage, short-circuit current and fill-factor of a typical junction. Very low values of open-circuit voltage and short-circuit currents have been observed in these junctions.

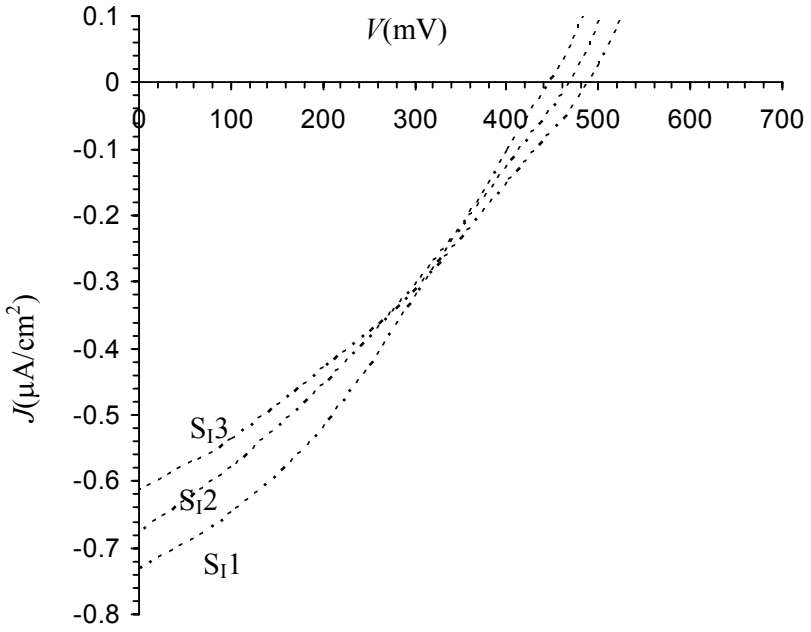

Figure 8.09: Photovoltaic effect of three typical ITO-(p)Si junctions under white light of intensity 50 mW/cm^2

Table 8.03: Some photovoltaic parameters of three typical ITO-(p)Si junctions (N_a= 5×10^{16} cm^{-3}) at room temperature (300K)

Junction number	Junction area (cm^2)	Open-circuit voltage (mV)	Short-circuit current density (μA/cm^2)	Fill factor *FF*
S_I1	0.030	435	0.73	0.33
S_I2	0.035	455	0.67	0.31
S_I3	0.038	475	0.61	0.32

8.1.6 Summary on the studies of (n)ITO-(p)Si heterojunctions:

From the plots of current-voltage characteristics of prepared (n)ITO/(p)Si junctions it is observed that the junctions are rectifying in nature. The barrier exists at the junction between (n)ITO and (p)Si. The reverse current does not saturate.

It has been observed that *J-V* curves are functions of electrode area. The reverse saturation current density of ITO/(p)Si junction is found to increase from 4 nA/cm^2 to 7 nA/cm^2 (Table 8.01) on increasing the junction area from 0.03 cm^2 to 0.038 cm^2. The diode ideality factor of the junctions was found to be in between 4.65 to 4.71.

ITO, being highly degenerate semiconductor, exhibits metallic character of high conductivity and therefore it has been found to form Schottky Barrier with (p)Si. The average barrier height of the ITO/(p)Si junction obtained from *J-V* characteristics is 0.52 eV. The barrier height measured from *C-V* study was found to be more than the value obtained from *J-V* characteristics.

The prepared ITO/(p)Si junctions show high series resistance (156 KΩ to 177 KΩ). The large value of series resistance is contributed by the high sheet resistance of ITO layer, though the highly conducting Si wafer of doping concentration 5×10^{16} cm^3 was used. Also the interfacial oxide layer has offered some resistance.

All the prepared ITO/(p)Si structures were also studied for their photovoltaic performance under light of intensity 50 mW/cm^2. The junctions exhibited photovoltaic effect with very low photovoltaic conversion efficiency and low value of fill factor (0.32 to 0.37). The short-circuit current of ITO/(p)Si junctions were found to be 6.7 $\mu A/cm^2$.

8.2. Studies on (n)ZnSe-(p)CdTe heterojunctions

For using as photovoltaic converter the CdTe was taken as the absorber semiconductor because of its optimum energy gap for solar energy conversion and ZnSe was used as window material due to its wide band gap. Aluminium was found to give good ohmic contact to n-type ZnSe films. Au was used as the ohmic contact to p-type CdTe films. The details of junction preparation and measurement procedure have been presented in chapter 4. For current-voltage measurement of (n)ZnSe/(p)CdTe, Au film deposited on the glass substrate was used as the lower electrode and an Al film deposited on ZnSe film was used as the upper electrode making the junction structure as Al-(n)ZnSe/(p)CdTe-Au. Nine heterojunctions of equal area (0.01 cm^2) on same substrate were simultaneously prepared in the same vacuum cycle.

8.2.1. Current-voltage characteristics

Figure 8.10 shows the *J-V* characteristics of a typical junction in dark at room temperature (298K). The junctions exhibited rectifying characteristics. The current-voltage characteristics of the junctions were also studied at elevated temperature up to 333K. The figure 8.11 shows the *J-V* plots of a typical junction at different temperatures under forward bias.

Assuming thermoionic emission over the heterojunction barrier to be dominant mechanism, current density – voltage relation is given by the relation (3.60) [327],

$$J = A^* T^2 q V_{bi} \exp\left(\frac{-qV_{bi}}{kT}\right)\left(1-\frac{V}{V_{bi}}\right)\left[\exp\left(\frac{qV}{kT}\right)-1\right]$$

$$= J_0\left(1-\frac{V}{V_{bi}}\right)\left[\exp\left(\frac{qV}{kT}\right)-1\right] \qquad (3.60)$$

where, $J_0 = \frac{qA^*TV_{bi}}{k}\exp\left(-\frac{qV_{bi}}{kT}\right)$ is the reverse saturation current density, V_{bi} is the built-in potential of the junction.

Using the general diode equation, $J = J_0 \exp\left(\frac{qV}{nkT}\right)$, the diode ideality factor (n) and reverse saturation current density (J_0) of the junction were calculated from slope and intercept of ln$J$ vs V plot. Figure 8.12 shows the linear region of ln$J$ vs V plots for a typical junction at room temperature and elevated temperatures. The ideality factor and reverse saturation current density so calculated for a typical junction at room temperature as well as at elevated temperature are tabulated in Table

8.04. The ideality factor is found to be 4 to 5 within the temperature range 298K to 333K.

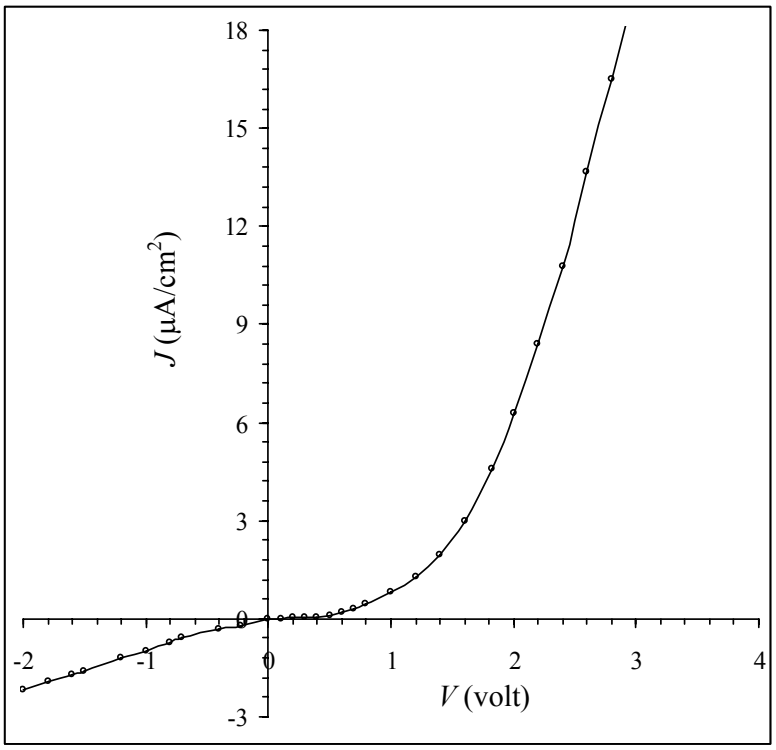

Figure 8.10: *J-V* characteristics of a typical (n)ZnSe/(p)CdTe junction (N_a= 8×10^{15} cm^{-3}, N_d= 9.7×10^{14} cm^{-3}) in dark at room temperature (298K).

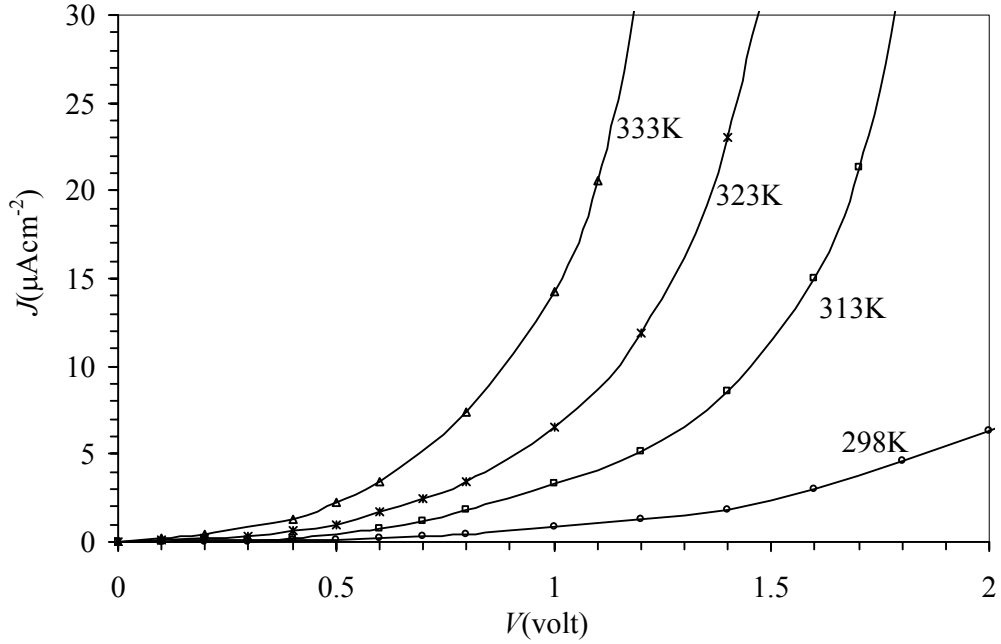

Figure 8.11: *J-V* plots of a typical (n)ZnSe/(p)CdTe junction (N_a= 8×10^{15} cm^{-3}, N_d= 9.7×10^{14} cm^{-3}) at dark at different temperatures (junction area=0.01 cm^2)

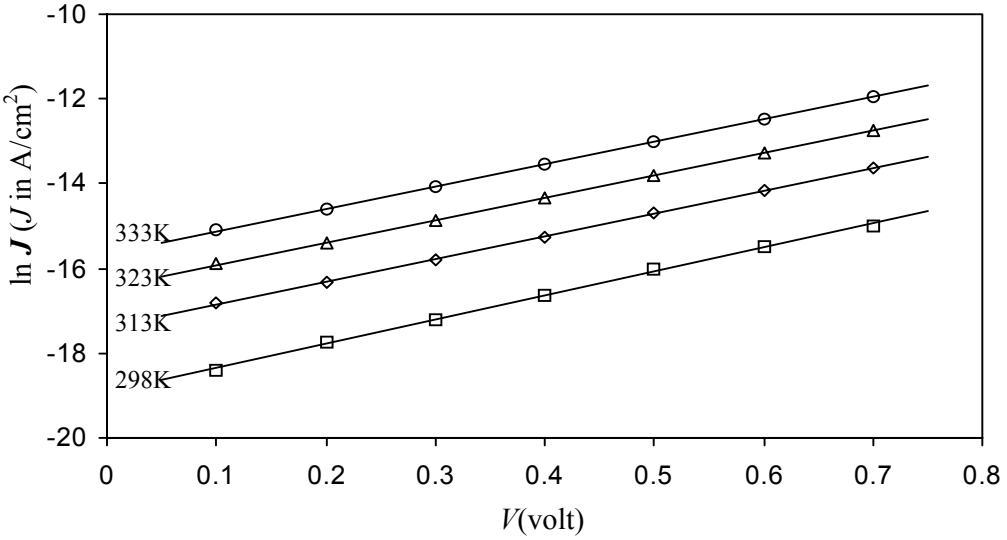

Figure 8.12: ln$J$ vs V curves of a typical (n)ZnSe/(p)CdTe junction (N_a= 8×10^{15} cm^{-3}, N_d= 9.7×10^{14} cm^{-3}) in dark at different temperatures.

From the estimated values of J_0 for different temperatures, ln(J_0/T) vs T^{-1} graph is plotted for the junction (Figure 8.13). From the figure it is seen that the plot is a straight line, which indicates that the current transport is controlled by the thermoionic emission process and follows the relation (3.60). From the slope of the plot, the built-in potential V_{bi} of the junction was estimated. The built-in potential of a typical (n)ZnSe/(p)CdTe junction measured from current-voltage characteristics is given in Table 8.04. The built-in potential of the junction (0.77 eV) has been found to be independent of temperature.

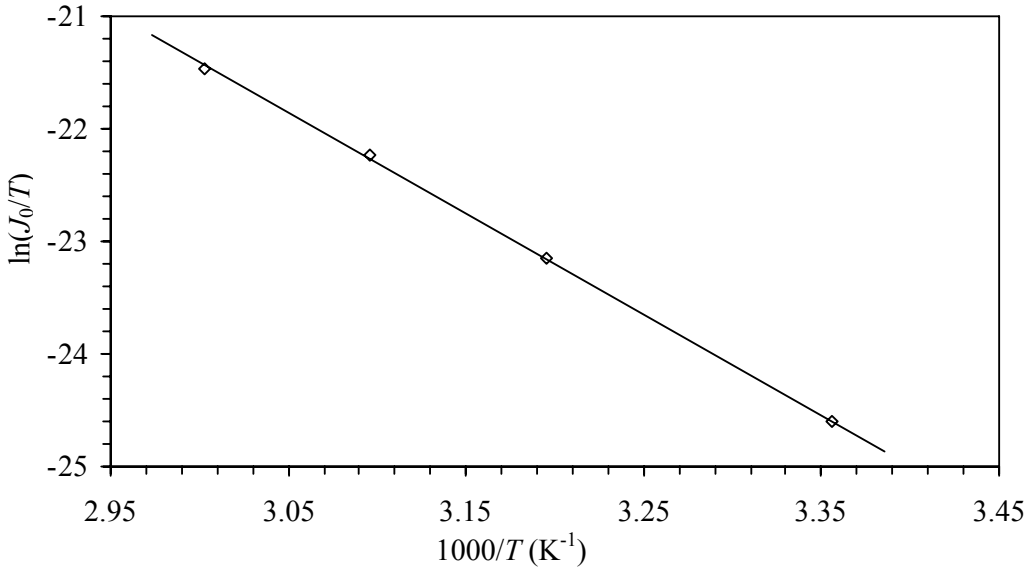

Figure8.13: ln(J_0/T) vs T^{-1} plots of a typical (n)ZnSe/(p)CdTe junction (N_a= 8×10^{15}cm^{-3}, N_d= 9.7×10^{14} cm^{-3}) in dark

Table 8.04: Some junction parameters of a typical (n)ZnSe/(p)CdTe junction in dark at different temperatures (N_a= 8×10^{15} cm^{-3}, N_d= 9.7×10^{14} cm^{-3})

Temperature (K)	Ideality factor n	Saturation current density J_0 (nAcm^{-2})	Series resistance (M-ohm)	Built in potential V_{bi} (eV)	
				From J-V	From C-V
298	6.88	6	16	0.77	0.79
313	6.87	27	-	0.77	-
323	6.77	72	-	0.77	-
333	6.57	158	-	0.77	-

8.2.2 Effect of Series Resistance:

For bias voltage greater than 0.8 V, the ln$I$ vs V plots of the junctions have been observed to deviate from linearity (Figure 8.14). Here I is the total current following through the junction. This deviation reveals the presence of series resistance (R_s) associated with the neutral regions of the semiconductor layers of the (n)ZnSe and (p)CdTe.

The series resistance estimated from I vs ΔV plots (Figure 8.15) of the diode shows that this device possesses series resistance as high as 20 M-ohm. In the present case, the large value of series resistance is contributed by the highly resistive CdTe and ZnSe layer and the resistance offered by the interfacial layer.

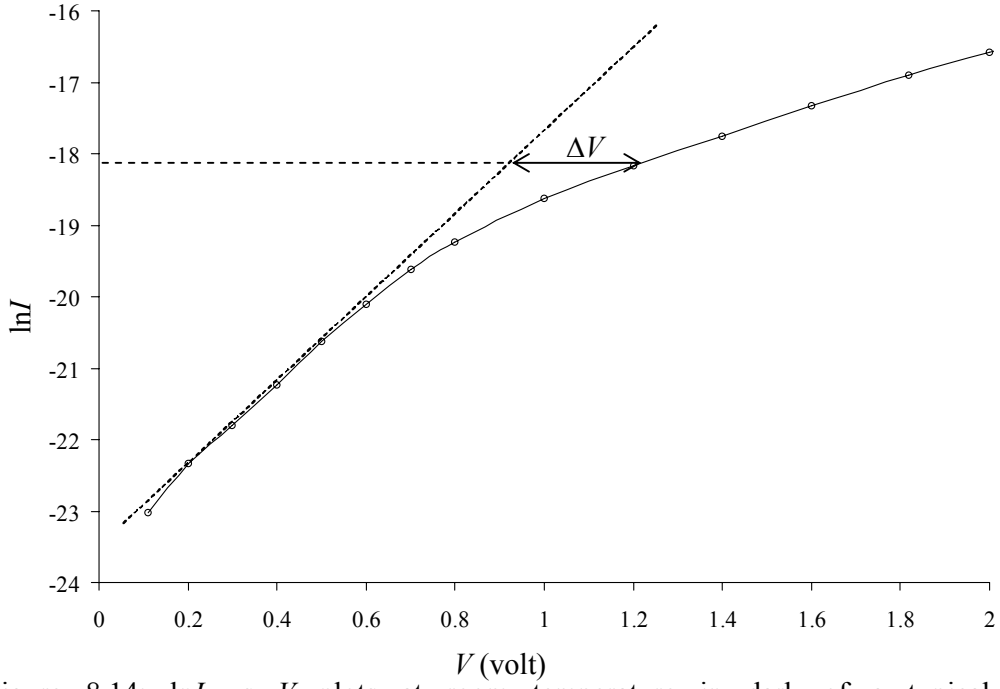

Figure 8.14: ln$I$ vs V plots at room temperature in dark of a typical (n)ZnSe/(p)CdTe junction (N_a= 5×10^{16} cm^{-3}, N_d= 9.7×10^{14} cm^{-3}).

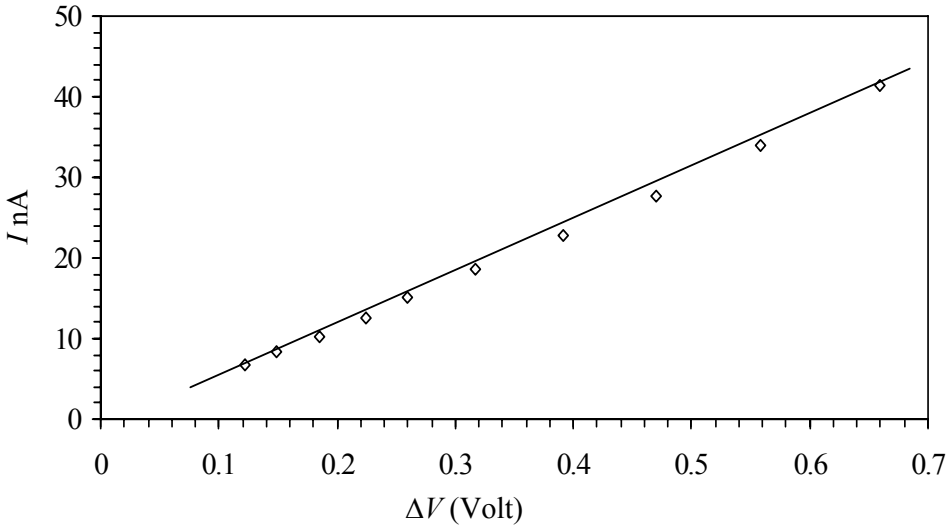

Figure 8.15: I vs ΔV plots at room temperature in dark of a typical (n)ZnSe/(p)CdTe junction.

8.2.3 Capacitance-voltage characteristics:

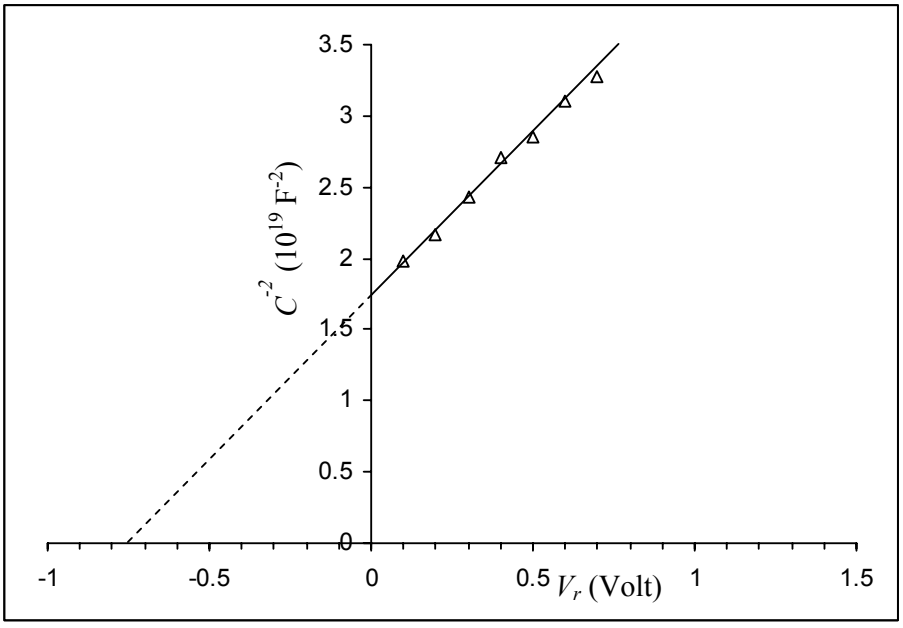

Figure 8.16: C^{-2} vs V_r(reverse) plots of a typical (n)ZnSe/(p)CdTe junction at room temperature in dark .

The C^{-2} vs V_r plots at frequency 1 KHz for a typical junction has been shown in Fig. 8.16. The built-in potential (V_{bi}) at the junction was estimated from the intercept (V_i) of C^{-2} vs V_r plots using the relation (3.46) as discussed in previous section 8.1.4. The built-in potential obtained for this junction is nearer to 0.79 eV.

8.2.4 Photovoltaic effect:

The (n)ZnSe/(p)CdTe junctions were studied for their photovoltaic performances under light intensity 50 mW/cm^2. The *J-V* curve (Fig.8.17) under illumination reveals the photovoltaic effect of the junction. Nearly linear nature of the curve implies the existence of a large series resistance. The open circuit voltage of the junction was found to be 470 mV and short circuit current density 2.1 μA/cm^2

and maximum power output 3.67×10^{-4} mW/cm^2 with fill factor 0.37. The efficiency of the cell is found very low, 0.2%.

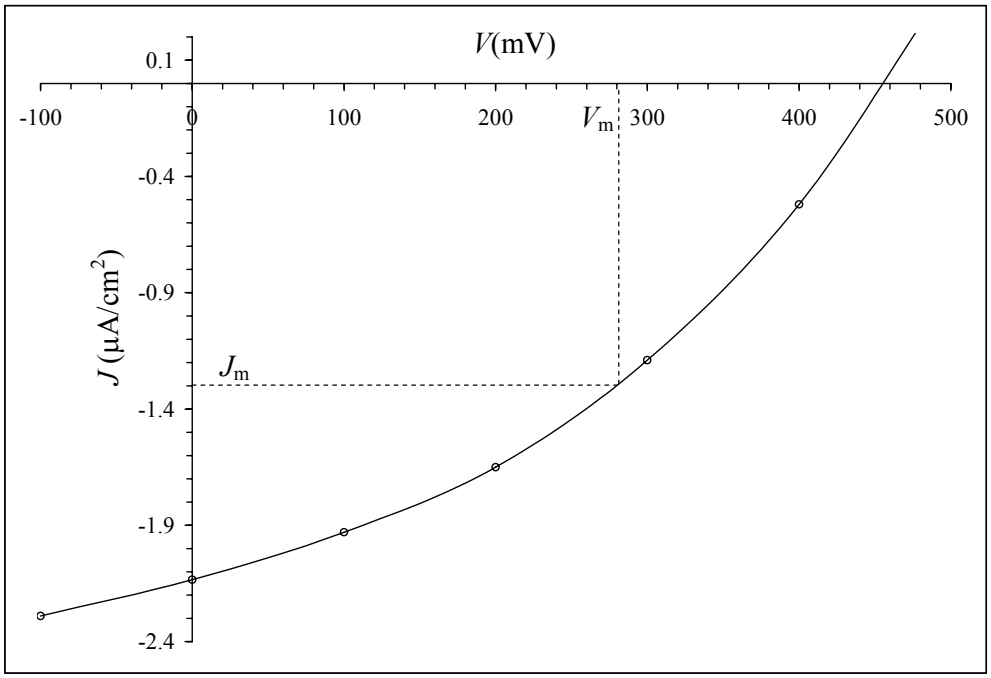

Figure 8.17: Photovoltaic effect of a typical (n)ZnSe/(p)CdTe junction under light of intensity 50 mW/cm^2

Diode parameters under illumination:

To measure the diode ideality factor n and reverse saturation current J_o of the junction under illumination, relation (3.63),

$$J_{sc} = J_0\left[\exp\left(\frac{qV_{oc}}{nkT}\right)-1\right]$$

was used. For this purpose, J_{sc} and V_{oc} of the junctions were measured at three different levels of illumination (Fig. 8.18(A)). Then $\ln J_{sc}$ versus V_{oc} plot for the junction (Figure 8.18(B)) was plotted and from the slope and intercept of the plots the diode ideality factor n and reverse saturation current density J_o under illumination were calculated. Some diode parameters of a typical (n)ZnSe/(p)CdTe heterojunction under illumination have been given in the table 8.05. Comparing the values of diode parameters in dark (from table 8.04) and under illumination for the same junction, the

diode ideality factor is observed to decrease under illumination, while the saturation current density J_o is found to increase under illumination.

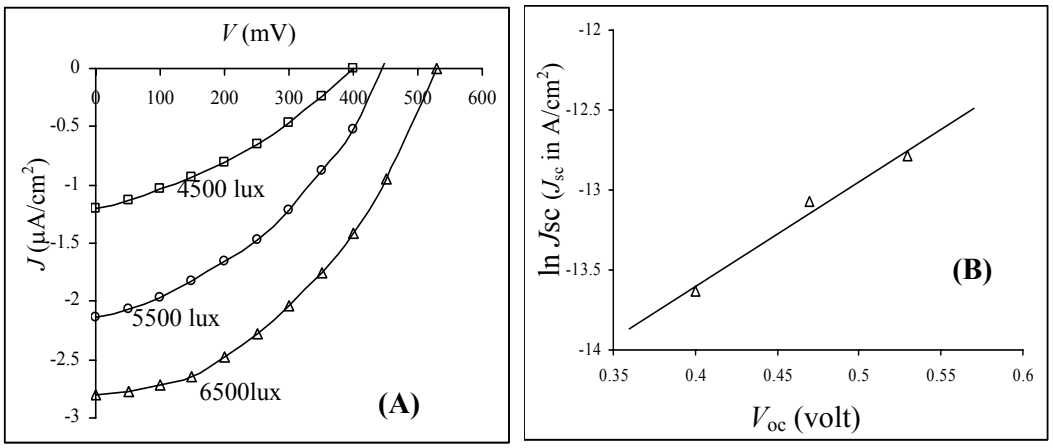

Figure 8.18: (A) *J-V* plots under illumination for three different intensity of illumination and (B) ln J_{sc} versus V_{oc} plot for a typical (n)ZnSe/(p)CdTe junction

Table 8.05: Some photovoltaic parameters of a typical (n)ZnSe/(p)CdTe junction at room temperature (298K)

Open-circuit voltage (mV)	Short-circuit current density ($\mu A/cm^2$)	Maximum power output (mW/cm^2)	Fill factor (%)	Efficiency (%)	Ideality factor *n*	Saturation-current density J_0 (nA/cm^2)
470	2.1	3.64×10^{-4}	38	0.2	5.9	90

Table 8.05 shows the open-circuit voltage, short-circuit current, fill-factor, ideality factor and reverse saturation current density of a typical junction.

8.2.5: Spectral response

The spectral response of the (n)ZnSe/(p)CdTe junction was studied in the wavelength range 400nm-950 nm using a monochromator. Figure 8.19 shows the short-circuit current spectral response of a typical (n)ZnSe/(p)CdTe junction. The maximum short-circuit current was obtained corresponding to the wavelength about 840nm which is well within the visible region. The value of the band edge calculated from the highest peak was found to be 1.47eV which implies that the absorption is mostly within CdTe layer of the structure.

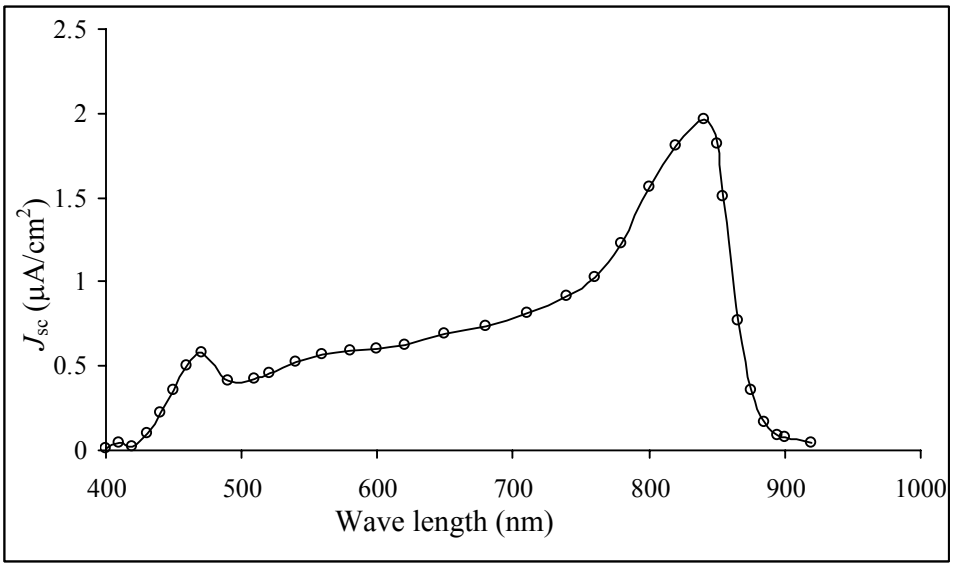

Figure 8.19: Short-circuit current spectral characteristics of a typical (n)ZnSe/(p)CdTe junction

8.2.6 Summary on the studies of (n)ZnSe-(p)CdTe heterojunctions:

The rectifying current-voltage characteristics of the fabricated (n)ZnSe/(p)CdTe junction reveals the formation of barrier at the junction between the films of (n)ZnSe and (p)CdTe.

Diode ideality factor and reverse saturation current density at 298K for a typical (n)ZnSe/(p)CdTe heterojunction has been found to be 6.9 and 6 $nAcm^{-2}$ (Table 8.04) respectively. The ideality factor has been found to decrease with increase in temperature while the reverse saturation current density increases. The built-in potential of the junction measured from *J-V* characteristics is found to be 0.77 eV and is independent of temperature (Table 8.04). The built-in potential measured from *C-V* study was found to be 0.79 eV.

The junction shows high series resistance (16 MΩ). The large value of series resistance is contributed by the high resistance of thermally deposited CdTe layer and low conducting ZnSe layer respectively. In the present case it was not possible to increase the doping concentration of Al-doped ZnSe film beyond $10^{14}cm^{-3}$. Also the interfacial oxide layer has offered some resistance.

The prepared (n)ZnSe/(p)CdTe structure exhibited photovoltaic effect under illumination. Photovoltaic conversion efficiency of the junctions was found very low. The short-circuit current and open-circuit voltage of the (n)ZnSe/(p)CdTe junction are found to be 2.1 $\mu A/cm^2$ and 470mV respectively. Under illumination, the diode ideality factor of the (n)ZnSe/(p)CdTe heterojunction is decreased to 5.9 while the saturation current density is increased to 90 nA/cm^2 due to generation of extra carriers under illumination.

From the studies of spectral response of the junction in the visible region, maximum short-circuit current was obtained at the wave length (840nm) corresponding to band edge 1.47eV. This implies that the absorption is mostly within CdTe layer of the structure.

8.3 Studies of (n)ZnSe/(p)Si heterojunctions:

The (n)ZnSe/(p)Si heterojunctions were prepared by depositing Al-doped ZnSe films on p-type silicon wafer by thermal evaporation. The Al electrodes were deposited onto back surface of silicon wafers by vacuum evaporation prior to the deposition of ZnSe film for ohmic contact. The metal gold electrodes were vacuum deposited onto ZnSe film through a suitable mask making the structures of the form Al-(p)Si/(n)ZnSe-Au. The details of preparation of the junctions have been discussed in chapter 4.

8.3.1 Current-voltage characteristics:

The *J-V* characteristics of a typical (n)ZnSe/(p)Si junction in dark is shown in Fig 8.20. The junction exhibited rectifying characteristics with soft reverse current indicating the existence of a barrier. The *J-V* characteristics of the prepared junction have been studied in dark within temperature range from 298K to 333K. The temperature dependence of *J-V* characteristics for forward bias has been shown in Fig.8.21. At higher bias, the current have been observed to increase more rapidly as the temperature was increased.

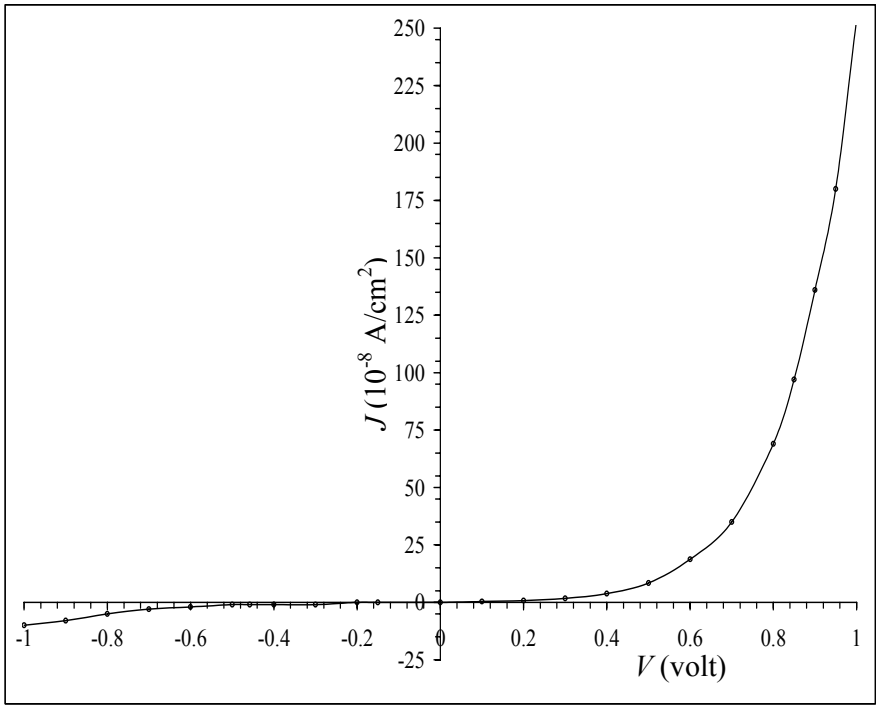

Figure 8.20: *J-V* characteristics of a typical (n)ZnSe/(p)Si junction in dark at room temperature (298K)

The current density of an ideal diode can be represented by (3.56) [378]

$$J = J_0 \exp(qV/nkT)\left[1 - \exp\left(-qV/kT\right)\right]$$

where, J_0 is the reverse saturation current density and n is the diode ideality factor.

Fig 8.22 shows ln [J/ (1-e $^{-qV/kT}$)] vs V plot for a typical junction in dark at different temperatures. The ideality factors (n) and saturation current density (J_0) were calculated from the slopes and intercepts of these plots respectively. Table 8.06 shows the values of diode ideality factor, saturation current density at different temperatures. The saturation current density J_0 was found to vary from 1.56×10^{-9} A/cm^2 to 35.3×10^{-9} A/cm^2 with increase in temperature from 298K to 333K. The diode ideality factor was found to be 4.87 at room temperature and found to decrease slightly with increasing temperature.

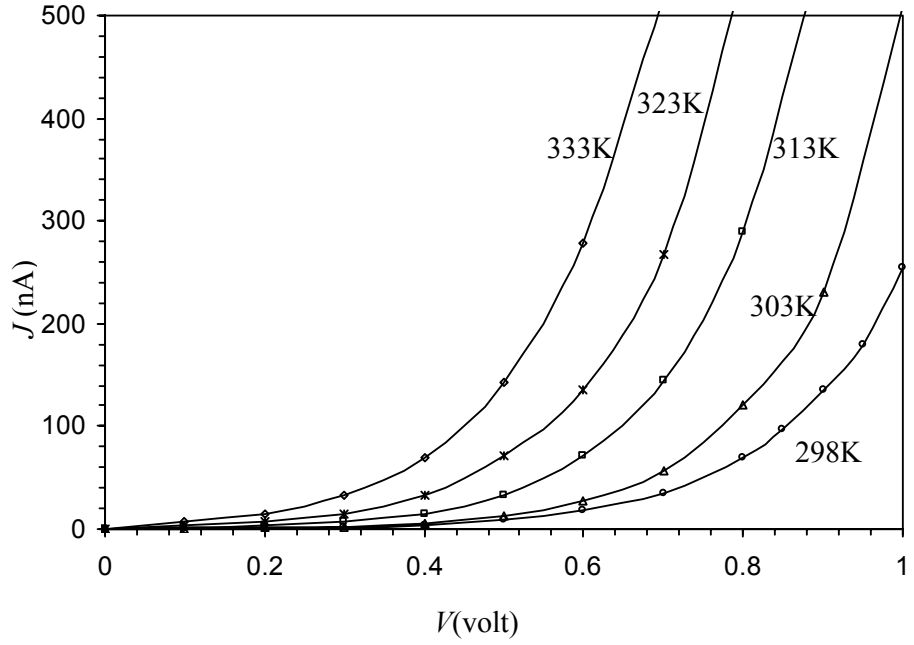

Figure 8.21: J-V plots (forward current) of a typical (n)ZnSe/(p)Si at different temperatures

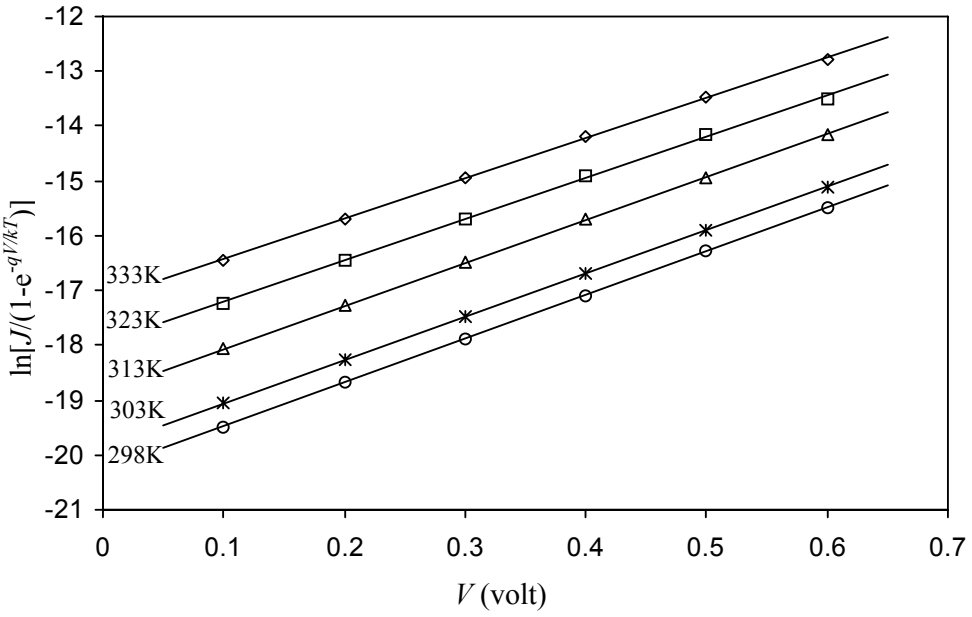

Figure 8.22: ln[$J/(1-e^{-qV/kT}$)] Vs V plots of a typical (n)ZnSe/(p)Si junction at different temperatures

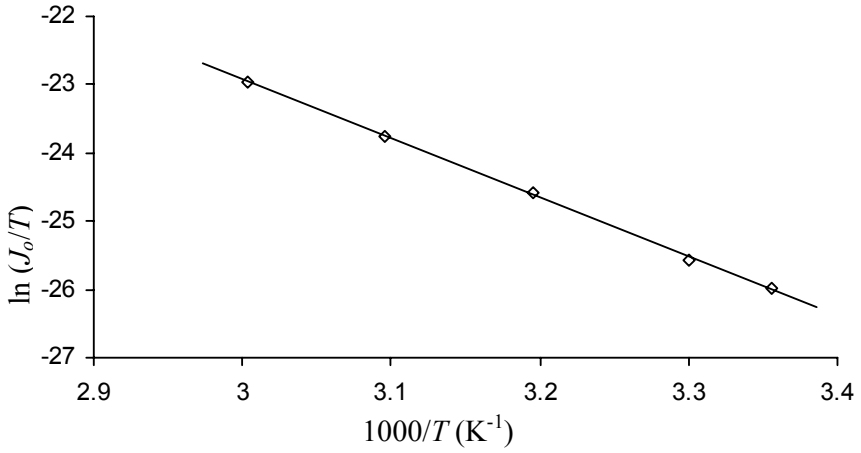

Figure 8.23: ln(J_0/T) vs T^{-1} plot of a typical (n)ZnSe/(p)Si junction

From the measured values of J_0 at different temperatures, a plot of ln(J_0/T) versus T^{-1} has been drawn (Fig 8.23). This plot shows a straight line. This indicates that the current transport process follows the relation (3.60) as discussed in the previous section (8.2.1),

$$J_0 = \frac{qA^*TV_{bi}}{k}\exp\left(-\frac{qV_{bi}}{kT}\right)$$

The values of built-in potential (V_{bi}) calculated from these plots are tabulated in Table 8.06. The built-in potential is about 0.744 eV.

Table 8.06: Some parameters of the (n)ZnSe/(p)Si junction at different temperatures

Temp (K)	Ideality factor(n)	Saturation current density $J_o(10^{-9}\text{A/cm}^2)$	Built-in potential (eV)	Series Resistance R_S (MΩ)
298	4.87	1.6	0.744	2.2
303	4.84	2.4		
313	4.73	6.6		
323	4.76	15.7		
333	4.74	35.4		

8.3.2 Effect of series resistance (R_S) :

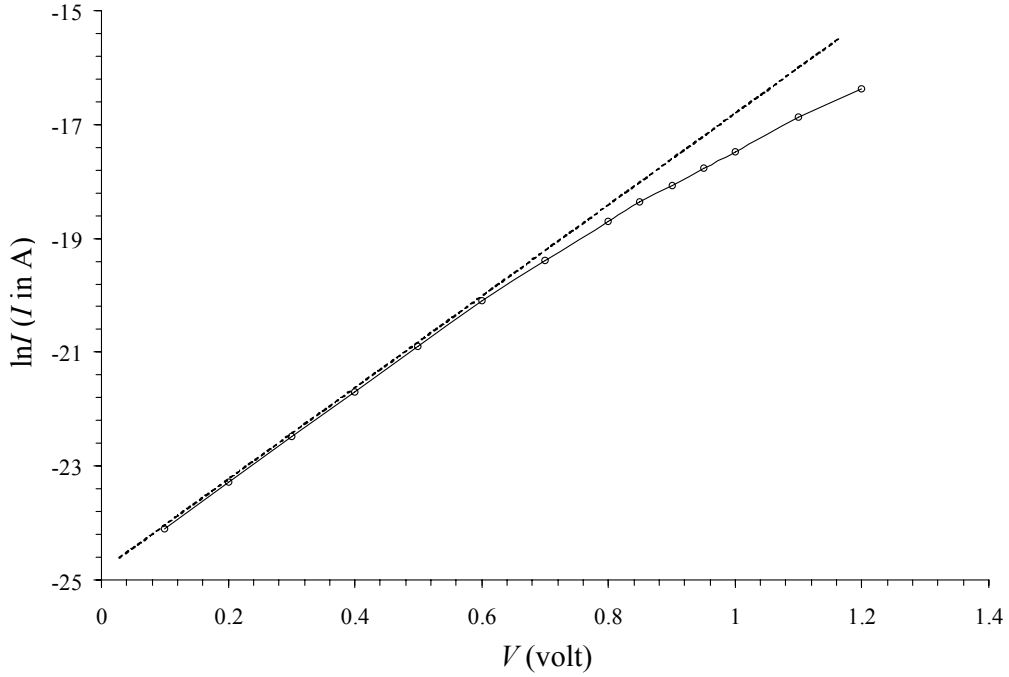

Figure 8.24: ln$I$ vs V plot at room temperature in dark of a typical (n)ZnSe/(p)Si junction of junction area A=0.01 cm^2.

Due to presence of series resistance, the ln*I*-*V* plots for the (n)ZnSe/(p)Si have been observed to deviate from linearity at higher forward voltages (Figure 8.24). Here I is the total current following through the junction. The series resistance R_s for a typical junction in dark was calculated from the I vs ΔV plot (Figure 8.25) where ΔV is the voltage due to series resistance. The value of R_s of a typical (n)ZnSe/(p)Si junction was found to be about 2.2 MΩ.

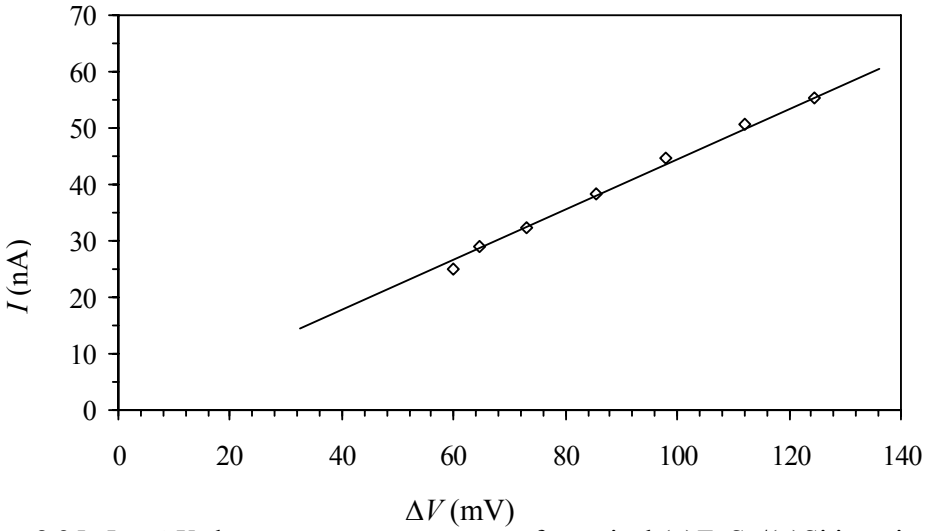

Figure 8.25: I vs ΔV plots at room temperature of a typical (n)ZnSe/(p)Si junction of junction area A=0.01 cm^2 in dark.

8.3.3 Capacitance- Voltage Measurement:

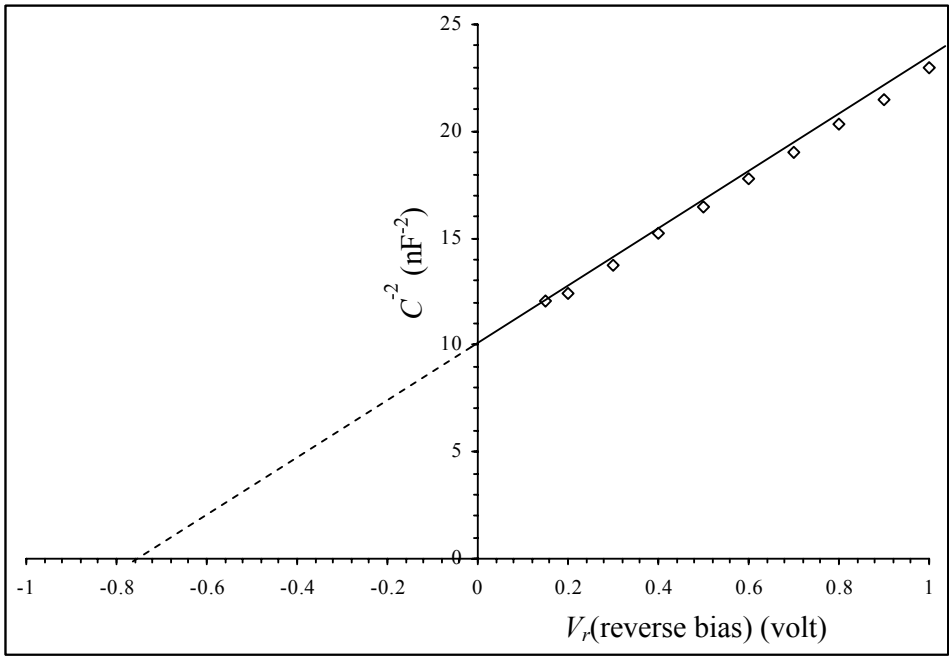

Figure 8.26: C^{-2} vs V_r (reverse bias) plot of a (n)ZnSe/(p)Si junction

The *C-V* measurements were performed on the junctions at room temperature. The C^{-2}-*V* plot for a junction has been drawn at frequency 1KHz (Fig 8.26). The carrier concentration of Si was calculated from the slope of C^{-2}-*V* plots of the junction under reverse bias condition as discussed in the previous sections. The carrier concentration evaluated from the slope was of the order of 10^{16} cm^{-3}. The barrier height measured from this plot is found to be 0.774 eV. This value of barrier height measured from C^{-2}-*V* plot has been observed to be higher than the value obtained from *J-V* plot (table 8.06).

8.3.4 Photovoltaic Effect

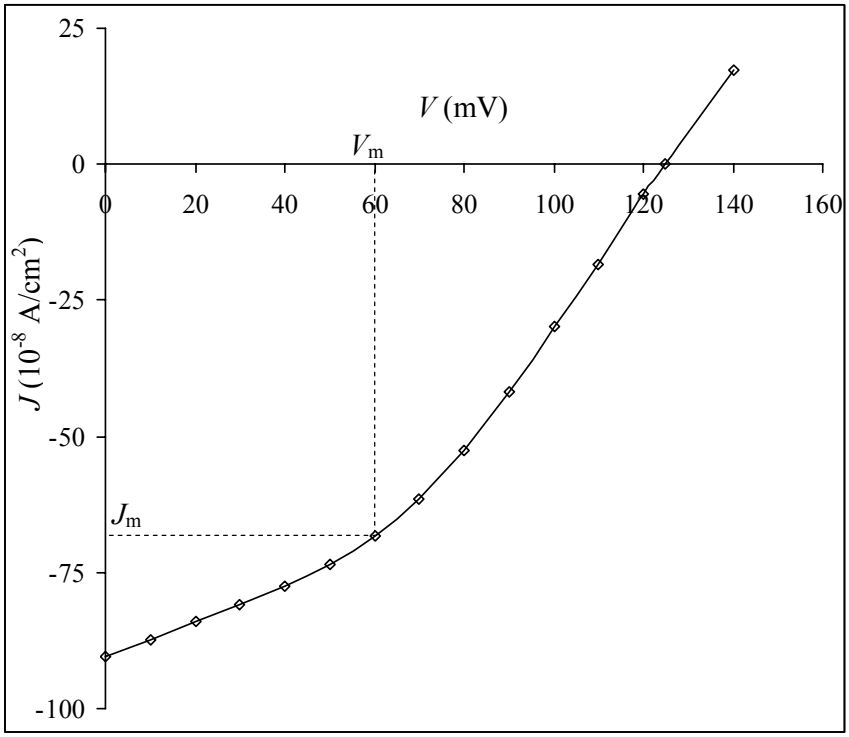

Figure 8.27: Photovoltaic effect of a typical (n)ZnSe/(p)Si junction under 50mW/cm^2 light intensity

The (n)ZnSe/(p)Si junction was studied for its photovoltaic performances. Fig.8.27 shows *J-V* curve under illumination of a typical junction for photovoltaic effect at room temperature. Nearly linear nature of the curve implies the existence of a large series resistance. Table 8.07 shows the open-circuit voltage, short-circuit current and fill-factor of a typical junction.

Table 8.07: Some photovoltaic parameters of a typical (n)ZnSe/(p)Si junction at room temperature (298K)

Incident light intensity	Short-circuit current density J_{sc} (10^{-8}Acm^{-2})	Open-circuit voltage (mV)	J_m (10^{-8}A/cm^2)	V_m (mV)	Fill-factor *FF*
50 mW/cm^2	90.5	125	61	70	0.38

8.3.5 Summary on the studies of (n)ZnSe-(p)Si heterojunctions:

The current-voltage study of (n)ZnSe/(p)Si junction has showed rectifying characteristics with soft reverse current. The ideality factor of the junction is found to be greater than unity and the reverse current does not saturate.

The ideality factor and saturation current density of the junction were also studied at different temperatures. The diode ideality factor has been found to decrease from 4.87 to 4.74 (Table 8.06) when the temperature is raised from room temperature (298K) to 333K. But due to thermal generation of carriers, the saturation current density has been found to increase from 1.56 nA/cm^2 to 35.4 nA/cm^2 at those temperatures. The variation of saturation current density with temperature has followed the thermoionic emission mechanism. The built-in potential calculated from $\ln(J_0/T)$ vs T^{-1} plot is 0.744 eV. The built-in potential measured from *C-V* study was found to be 0.774 eV. Similar to other thin film junctions, the prepared (n)ZnSe-(p)Si junction showed high series resistance. The series resistance of the junction is found to be 2.2 MΩ.

The (n)ZnSe/(p)Si) junction has exhibited photovoltaic effect in their *J-V* characteristics under illumination. Photovoltaic conversion efficiency of the junction is found very low with low value of fill-factor (0.38). The short-circuit current and open-circuit voltage of a typical (n)ZnSe/(p)Si junction is found to be 90.5×10^{-8} A/cm^2 and 125 mV respectively.

8.4 Comparative study and discussions of ITO/(p)Si, (n)ZnSe/(p)CdTe and (n)ZnSe/(p)Si Heterojunctions:

The (n)ITO/(p)Si, (n)ZnSe/(p)CdTe and (n)ZnSe/(p)Si heterojunctions have been prepared by thermal evaporation method and some junction parameters and photovoltaic parameters of the junctions have been studied. Out of them ITO/(p)Si is a Schottky Barrier junction and other two are simple anisotype heterojunction. All the prepared junctions have exhibited rectifying behaviour with soft reverse current. Nonsaturating reverse current implies that the barrier height is lowered with reverse bias voltage. The effect of interfacial layer also contributed to high reverse current.

The diode parameters of the junctions have been measured from the current-voltage characteristics of the junctions. A comparative look of different parameters of three junctions has been shown in Table 8.08. In all the studied junctions the ideality factor is found to be greater than unity. As discussed in chapter 7 (section 7.5), the presence of interfacial layer, image force lowering of built-in potential, recombination of electrons and holes in depletion region and tunneling effect are the main reasons [381] for ideality factor to be greater than unity.

The barrier height or built-in potential of three junctions have been calculated from *J-V* characteristics and also from *C-V* study. The barrier height of (n)ITO/(p)Si, and built-in potential of (n)ZnSe/(p)CdTe and (n)ZnSe/(p)Si heterojunctions, measured from *J-V* characteristics are found to be 0.525 eV, 0.77eV and 0.744 eV respectively. In all the cases barrier height or built-in potential measured from *C-V* study are found to be more than the values obtained from *J-V* characteristics. Due to presence of interfacial layer, the capacitance of the junction is increased and thereby measured built-in voltage is found more. Therefore the barrier height of a junction with interfacial layer obtained from *C-V* method gives higher value than the actual value. Further the *C-V* method essentially gives the barrier height at zero bias voltage, which is larger than those obtained from *J-V* plots.

All the studied junctions show high series resistance. The series resistance of ITO/(p)Si junction is found about 156 KΩ while, the series resistance of (n)ZnSe/(p)Si and (n)ZnSe/(p)Si junctions are found about 16 MΩ and 2.2 MΩ respectively. In all the cases the high series resistance is mainly contributed by the

thermally deposited low conducting ZnSe or CdTe layer. Also the interfacial oxide layer has offered some resistance.

Table 8.08: Comparative look of (n)ITO/(p)Si, (n)ZnSe/(p)CdTe and (n)ZnSe/(p)Si heterojunctions at room temperature

Junction	Doping concen-tration (cm^{-3})	Diode ideality factor n	Saturation current density (nA/cm^2)	Series resistance KΩ	Barrier height (ϕ_b) / built-in potential (V_{bi}) (eV)	Photo-voltaic performance (Fill-factor)
(n)ITO-(p)Si	$N_d=6\times10^{18}$ $N_a=5\times10^{16}$	4.7	7	172	ϕ_b = 0.525	0.32
(n)ZnSe-(p)CdTe	$N_d=9\times10^{14}$ $N_a=8\times10^{15}$	6.88	6	16000	V_{bi}= 0.77	0.38
(n)ZnSe-(p)Si	$N_d=9\times10^{14}$ $N_a=5\times10^{16}$	4.87	1.6	2200	V_{bi}= 0.744	0.38

All the three types of prepared heterojunctions, (n)ITO/(p)Si, (n)ZnSe/(p)CdTe and (n)ZnSe/(p)Si, exhibited photovoltaic effect under illumination. Photovoltaic conversion efficiencies of all the three junctions are found very low with low values of fill-factor. In case of (n)ZnSe-(p)CdTe and (n)ZnSe-(p)Si junctions poor photovoltaic response is due to high series resistance, while the low value of barrier height may

reduce the performance of (n)ITO-(p)Si junction. Also the polycrystalline nature of films with small grain size resulting in increased recombination losses causes the poor photovoltaic performance in all junctions. The short-circuit current of ITO/(p)Si, (n)ZnSe/(p)CdTe and (n)ZnSe/(p)Si junctions were found to be 6.7 $\mu A/cm^2$, 2.1 $\mu A/cm^2$ and 9.05 $\mu A/cm^2$ respectively. The low values of short-circuit current for all junctions are due to higher value of diode ideality factors. In the polycrystalline films, the grain boundary potential may affect the series resistance and open circuit voltage of solar cell [41]. Due to this grain boundary effect, recombination of photo generated carriers takes place at grain boundary and hence the short-circuit current is reduced [41, 376]. The recombination of photogenerated carriers at the interface states, low doping concentration and low barrier height are also responsible for low photovoltaic performance of the junctions [382]. The high defect density in thermally evaporated ITO or ZnSe or CdTe layers also affect the photovoltaic performance of the devices. Also the counter electrodes of the prepared devices were not so thin enough to allow the whole light to penetrate through it. A part of the incident spectrum is reflected and a part is transmitted through the counter electrode which does not match with the bandgaps of the semiconductors used for making junctions. All these factors reduce the efficiency of the junctions to act as photovoltaic converter.

CHAPTER 9

Overall Conclusions from the present studies

In this present study electrical and optical properties of thin films and junctions of two semiconductors have been studied. The films are: Zinc Selenide (ZnSe) and Indium Tin Oxide (ITO), both doped and undoped. The junctions are: (1) Au-(n)ZnSe and Ni-(n)ZnSe Schottky barrier junctions and, (2) (n)ITO-(p)Si, (n)ZnSe-(p)CdTe and (n)ZnSe-(p)Si heterojunctions. All the films as well junctions were prepared by vacuum evaporation technique.

Structural studies by XRD indicate the polycrystalline nature of the films. The data are in good agreement with JCPDS (Joint Committee on Powder Diffraction Standard) file data with their respective code. The average grain sizes of ZnSe and ITO films prepared at their optimum growth condition were found to be 488 Å and 298 Å respectively. The results are in good agreement with the reported values. From XRD spectra of ZnSe films, the stress, strain and dislocation density of the prepared films were calculated and these values were found to be minimum at substrate temperature 453K to 573K during deposition of the films.

The compositional analysis was performed by X-ray Fluorescence Spectra (XRFS) and EDAX (Energy dispersive X-ray Analyzer) and the films were found to be stoichiometric.

The topography of the surfaces of the prepared films of ZnSe and ITO were studied from the SEM photographs for both unannealed and annealed films. The films were found to be continuous on the glass substrates and the annealed films deposited at higher substrate temperatures were fairly uniform and polycrystalline. The grain sizes and distribution of the grains in the films were observed to be uniform. There were no macroscopic defects like void, pinhole, peeling or cracks. The featureless surface morphology of the annealed films exhibit very low optical scattering losses and therefore they will be suitable for optoelectronic applications.

The results of the studies of ohmic contact to the semiconductor films, resistivity measurements at room temperature as well as elevated temperatures, photoconductive rise and decay, effect of light on resistivity, optical constants such as absorption coefficients, refractive indices (real and imaginary), complex dielectric constants, optical energy band gap, transmittance, absorbance measurements of both the semiconductor films have been discussed in respective sections of Chapter 5 and Chapter 6.

In the present study, the undoped ZnSe films was found to posses very high resistivity in the range of 10^6 ohm-cm) at room temperature, while its resistivity was found to decrease to 3.6×10^4 ohm-cm when it was doped with Al to a doping concentration 9.7×10^{14} cm^{-3}. The ITO film prepared at substrate temperature of 593K showed resistivity 160 ohm-cm at room temperature. Both the films exhibited temperature dependence of conductivity. The ln□ versus T^{-1} plots of ZnSe films showed three distinct slopes; two in low temperature range and other at higher temperature range from which activation energies and energy band gap were calculated. These values were found to vary with doping concentration. A study on the effect of illumination on ZnSe films were carried out. Both resistivity and photocurrent were found to be functions of illumination. From photoconductivity rise and decay, trap depths of the prepared ZnSe film were found to be 0.72 eV.

The optical parameters such as transmittance, reflectance, absorbance, refractive index, extinction coefficient etc were measured for both the films of ZnSe and ITO from their respective transmittance spectra recorded by a UV-visible spectrophotometer. The high transmittance of annealed films of ZnSe indicates that the film can be used as "window layer" in the photovoltaic device. Moreover, high transmittance and high conductivity of ITO film make it suitable for using as transparent conducting oxide (TCO). The refractive index of ZnSe films was found in the range of 2.5 to 2.65 at 500nm wavelength and that for ITO film is found about 1.9 for 500nm wave length. The results are in good agreement with earlier reported values. The increase of imaginary part of refractive index (extinction coefficient) k, (and so imaginary part of dielectric constant), towards the IR spectrum of both the films indicates that static (dc) electrical conductivity increases towards the IR spectrum. Also the very low value of extinction coefficient for both the films, confirms the high transparency of the films.

Optical band gaps of both the semiconductor films were determined from $(\square h\square)^2$ versus $h\square$ plots. For ZnSe film of thickness 4150Å prepared at substrate temperature of 453K, the band gap was found to be 2.62eV and that for ITO film of thickness 3350 Å prepared at substrate temperature of 593K was found to be 3.55eV. The band gap energy found from optical absorption coefficient of films prepared under the same conditions has been observed to be slightly greater than the energy gap obtained from temperature dependence of conductivity.

From the studies it is observed that the film properties of both the thermally deposited ZnSe and ITO films depend on the preparation condition and post deposition annealing of the films. From the studies of structural properties, it can be concluded that the substrate temperatures 453K and annealing of the films at 473K for 1 hour are the suitable optimum growth conditions to thermally prepare good quality polycrystalline thin films. The films prepared at this temperature were found nearly stoichiometric and uniform without any macroscopic defects with high transparency for visible light. These growth conditions and parameters were set as optimum growth conditions for preparing ZnSe thin films and for preparation of Schottky barriers and heterojunctions with ZnSe for studying their electrical and optical properties in the present case. Similarly, from the study of electrical properties of ITO films it is concluded that high conductivity with high transmittance ITO films can be prepared by thermal deposition method by maintaining the substrate temperature at 593K and post deposition annealing of the film at 593K in air for one hour. These films were polycrystalline in nature and uniform without any macroscopic defects. The films were transparent for visible range. Therefore, for junction preparation with ITO films, in the present case, substrate temperature was maintained at 593K during deposition of films followed by annealing of the deposited films at 593K for one hour.

Special attention was given in the junction preparation and their studies. In chapter 7, results of studies on Au-(n)ZnSe and Ni-(n)ZnSe Schottky barrier junctions with discussions have been presented. The junction parameters such as diode ideality factor, reverse saturation current density, barrier height of vacuum deposited Au-(n)ZnSe and Ni-(n)ZnSe Schottky barrier junctions have been determined from current-voltage characteristics. For illuminated junctions, short-circuit current, open-circuit voltage, fill factor and both ideality factor and saturation current density under illumination have also been calculated.

Capacitance of both the junctions was measured under reverse bias condition. The doping concentrations of Al-doped ZnSe films obtained from C^{-2}-V plots of three sets of junctions were 1.4×10^{14}cm^{-3}, 4.8×10^{14} cm^{-3}and 9.7×10^{14} cm^{-3}. The average barrier heights obtained from C^{-2}-V plots were observed to be 0.865 eV and 0.785 eV for Au-(n)ZnSe and Ni-(n)ZnSe Schottky barrier junctions respectively.

Both Au-(n)ZnSe and Ni-(n)ZnSe Schottky barrier junctions showed rectification behaviour with soft reverse saturation currents. In the present case it was not possible to overcome the formation of interfacial layer because in between deposition of two films, vacuum had to be broken. Therefore the presence of interfacial layer has affected the *J-V* characteristics of the prepared junctions. The diode ideality factors of both the junctions were found to be much greater than unity. The diode ideality factor was found to decrease and reverse saturation current density was found to increase with doping concentration of the ZnSe film of the junctions. This means that by increasing the doping concentration of the semiconductor film, diode of good quality can be achieved. But in the present case, by the process of co-evaporation, the doping concentration could not be achieved beyond 9.7×10^{14} cm^{-3}. The junctions were also studied after annealing the whole devices in vacuum at 373K for 10 minutes and the diode quality was found to be improved. This may be due to the improvement in the contact between the electrodes and semiconductor after thermal removal of interfacial layer. The barrier height of the junctions was calculated from *J-V* characteristics also. The barrier height measured from *J-V* characteristics of Au-(n)ZnSe junction with doping concentration 9.7×10^{14} cm^{-3} was found to be 0.817 eV while that for Ni-(n)ZnSe junction of same doping concentration was 0.724eV. The low value of barrier height was due to the presence of interfacial layer. In polycrystalline semiconductor thin films, the constituent atoms at the grain boundary are disordered and hence there are large numbers of defects due to incomplete atomic bonding (dangling bond). This may result the existence of surface states. In our case, the barrier heights were found to be less dependent on work function of the barrier metal Au or Ni. These may be due to the effect of surface states of the semiconductor. Similar behavior was observed in other II-VI semiconductors including ZnSe.

Both types of the vacuum deposited junction exhibited high series resistance. The series resistances of Au-(n)ZnSe and Ni-(n)ZnSe junctions (for 9.7×10^{14} cm^{-3}

doping concentration) were found to be 1.7 M□ and 3.5 M□ respectively. Heat treatment of the device reduces the defects of the semiconducting film and reduces the resistance offered by interfacial insulating layer, and the series resistance of the device thus is lowered on heat treatment.

Photovoltaic characteristics of Au-(n)ZnSe and Ni-(n)ZnSe Schottky barrier junctions have also been studied. Both type of junctions exhibited photovoltaic effect. Very low photovoltages with low value of fill factors have been observed for these junctions. The nearly linear nature of the *J-V* curve under illumination implies the existence of very high series resistance in the junctions, which causes poor photovoltaic effect. The short-circuit current, open-circuit voltage and fill-factor for Au-(n)ZnSe junction of doping concentration 9.7×10^{14} cm^{-3} were found to be 0.42 □A/cm^2, 300mV and 0.40 respectively and those for Ni-(n)ZnSe junction with same doping concentration were found to be 0.46 □A/cm^2, 410mV and 0.42 respectively. The higher value of ideality factor, presence of high defect density in the thermally deposited ZnSe film, presence of interfacial layer, low doping concentration etc are the other causes for poor photovoltaic performance of both the junctions.

Under illumination, the diode ideality factors of both Au-(n)ZnSe and Ni-(n)ZnSe Schottky barier junctions were found to decrease, while the saturation current density for both the junctions were observed to increase, which was due to the generation of more carriers under illumination.

In Chapter 8, results of studies on (n)ITO-(p)Si, (n)ZnSe-(p)CdTe and (n)ZnSe-(p)Si heterojunctions with discussions have been presented. All the studied junctions exhibited rectifying characteristics. ITO being highly degenerate, has been found to form Schottky barrier with (p)Si. Diode ideality factor for a typical (n)ITO-(p)Si junction has been found to be 4.7 with reverse saturation current density 7 nA/cm^2 and barrier height 0.525 eV. The values of barrier heights obtained from *C-V* curves have been found to be more than the values obtained from *J-V* characteristics at different temperatures. The current-voltage curves were characterised by high series resistance of the order of KΩ (156 KΩ to 172 KΩ). All the prepared ITO/(p)Si structures exhibited photovoltaic effect with very low photovoltaic conversion efficiency and low value of fill-factor. The linear nature of the photovoltaic characteristics with low fill-factor (0.32) was due to the presence of high series resistance. Very low value of short-circuit current (0.61 to 0.73 μA/cm^2) and open-

circuit voltage (435 to 475 mV) observed in these ITO/(p)Si junctions was due to higher value of diode ideality factor also.

The ideality factor of vacuum deposited (n)ZnSe-(p)CdTe heterojunction was also found more than unity (6.88). The saturation current density and the built-in potential of the junction at room temperature measured from current-voltage characteristics were found to be 6 $nAcm^{-2}$ and 0.77 eV respectively. The series resistance contributed by the highly resistive CdTe and ZnSe layer of the junction was found to be very high (16 MΩ). The junction exhibited low photovoltaic performance. The open-circuit voltage of the junction was found to be 470 mV and short-circuit current density 2.1 $\mu A/cm^2$ and maximum power output 3.67×10^{-4} mW/cm^2 with fill-factor 0.38. The efficiency of the cell was found very low, 0.2%. The short-circuit current spectral response of the (n)ZnSe/(p)CdTe junction was also investigated. The maximum short-circuit current was obtained corresponding to the wavelength about 840nm (photon energy=1.47eV), which implies that the absorption was mostly within CdTe layer of the structure. The diode ideality factor of the junction under illumination was observed to decrease, while the saturation current density J_o of it was found to increase under illumination.

From the rectifying current-voltage characteristics of the (n)ZnSe-(p)Si heterojunction, the diode ideality factor was found to be 4.87 with built-in potential 0.744 eV. The series resistance of this junction was also found very high (2.2 MΩ). The high series resistance of this junction was due to the low conducting ZnSe film. The *J-V* curve of the (n)ZnSe/(p)Si junction was studied for its photovoltaic performances under illumination. Nearly linear nature of this plot implies the existence of a large series resistance in the junction. Very low photovoltage (about 125 mV) with low short-circuit current density (9.05 $\mu A/cm^2$) has been observed in the junction.

From the studies, it is observed that the thermally deposited Au-(n)ZnSe, Ni-(n)ZnSe, (n)ITO-(p)Si, (n)ZnSe-(p)CdTe and (n)ZnSe-(p)Si junctions are of rectifying nature with high ideality factor and high series resistance. There are great potentiality to prepare Schottky barrier junctions and heterojunctions with ZnSe and ITO by thermal evaporation method by improving their diode quality after proper doping, annealing, reduction of interfacial layer and passivation of surface states etc.

REFERENCES

1. K. L. Chopra; *Thin Film Phenomena*; Robert E. Krieger Publishing Company, Huntington, New York (1969).
2. L. I. Maissel and R Glang (eds); *Hand Book of Thin Film and Technology*, Mc Graw Hill Com., New York,1970.
3. K. L. Chopra and L. K. Malhotra, "*Thin Film Technology and Applications"*, (1985) (Tata-Mc-Graw Hill, New Delhi).
4. Joachim P. Kloock, Yulia G. Mourzina, Jürgen Schubert and Michael J. Schöning, A "First Step Towards a Microfabricated Thin-Film Sensor Array on the Basis of Chalcogenide Glass Materials", *Sensors* 2002*,* **2***,* 356-365.
5. www.solarcell.dk
6. C. Cavaco, M. van Kampen, L. Lagae, G. Borghs, "Focus Section: A room-temperature electrical field–controlled magnetic memory cell", *J. Mat. Res.*, (2007) **22** 2111.
7. Lita, A.E.; Rosenberg, D.; Nam, S.; Miller, A.J.; Balzar, D.; Kaatz, L.M.; Schwall, R.E., "Tuning of tungsten thin film superconducting transition temperature for fabrication of photon number resolving detectors", *Applied Superconductivity, IEEE Transactions on* **15**, (2005) 3528 – 3531.
8. Shinya Maenosono, Ceco Danov Dushkin, Soichiro Saita and Yukio Yamaguchi, "Optical Memory Media Based on Excitation-Time Dependent Luminescence from a Thin Film of Semiconductor Nanocrystals", *Jpn. J. Appl. Phys.,* **39** (2000) 4006-4012.
9. Junichi Kimura *et al,* "Near-field optical recording on a CdSe nanocrystal thin film", 2003 *Nanotechnology* **14** 69-72.
10. Stephen, John R and Rajanna, K and Dhar, Vivek and Kumar, Kalyan KG and Nagabushanam, S (2004) Thin-Film Strain Gauge Sensors for Ion Thrust Measurement. *IEEE Sensors Journal* **4** 373 -377.

11. C.L. Johnson; K.D. Wise; J.W. Schwank, "A thin-film gas detector for semiconductor process gases", *International Electron Devices Meeting, 1988. Technical Digest*., 1988 662 – 665.

12. Pierre G. Verly, "Design of a Robust Thin-film Interference Filter for Erbium-doped Fiber Amplifier Gain Equalization", *Applied Optics*, **41**, 3092-3096 (2002).

13. K. Koc, F. Z. Tepehan and G. G. Tepehan, "Antireflecting coating from Ta_2O_5 and SiO_2 multilayer films", *J. Mat. Sc.*, **40** (2005) 1363-1366.

14. Aicha A. R. Elshabini-Riad, Fred D. Barlow, *Thin film Technology Hand Book*, McGraw Hill Professional, New York, 1998.

15. S. M. Sze; *Physics of Semiconductor Devices* (2nd Edition) Wiley Eastern Ltd., New Delhi (1987) p245.

16. W. Schottky, "Halbleitertheorie der Sperrcchicht", *Naturewiss*, **26** (1938), 843

17. Mott N. F., "Note on the contact between a metal and an insulator or semiconductor", *Proc. Cambr. Philos. Soc.*, **34** (1938) 568.

18. H. K. Henisch, *Rectifying Semiconductor Contacts*, (Oxford: Cladrendon Press, 1957).

19. M. M.Atalla, *Prc. Munich Symp. On Microelecronics (Munich: Oldenburge)*, 1966 pp123-157.

20. Yu-Zung Chiou, Yan-Kuin Su, Shoou-Jinn Chang, Jone F. Chen, Chia-Sheng Chang, Sen-Hai Liu, Yi-Chao Lin and Chin-Hsiang Chen, "Transparent TiN Electrodes in GaN Metal–Semiconductor–Metal Ultraviolet Photodetectors", *Jpn. J. Appl. Phys.,* **41** (2002) 3643-3645.

21. Tetsuka Tsutomu, Okajima Shigeki, Kawahata Kazuo, Fujita Junji, "Application of a Schottky Barrier Diode Mixer to a 118.8 μm Laser lnterferometer" *Jpn. J. Appl. Phys. Pt. 2*, **24**, (1985) L593-L595.

22. Chen, C.H. Chang, S.J. Su, Y.K. Chi, G.C. Chi, J.Y. Chang, C.A. Sheu, J.K. Chen, J.F., "GaN metal-semiconductor-metal ultraviolet photodetectors with transparent indium-tin-oxide Schottky contacts", *Photonics Technology Letters, IEEE* **13** (2001) 848-850.

23. Shepherd, F.D., Jr. Yang, A.C., "Silicon Schottky retinas for infrared imaging", *International Electron Devices Meeting, 1973* **19** (1973) 310- 313.

24. Chih-Tangn Sah, *Fundamentals of Solid State Electronics*, World Scientific (Electronic book- www.worldscibook.com) (1991).
25. Boylestad and Nashelsky, Electronic Devices and Circuit Theory, Pentice Hall of India, New Delhi (2003).
26. S. M. Sze; *Physics of Semiconductor Devices* (2nd Edition) Wiley Eastern Ltd., New Delhi (1987) p820.
27. Baliga, B.J., "The pinch rectifier: A low-forward-drop high-speed power diode", *IEEE Electron Devices Letter*, **5** (1984) 194-196.
28. W. Shockley W, U. S. Patent, **2569**, (1951) 347.
29. A. I. Gubanov, *Zh. Tekh. Fiz*, **21** (1951) 304; *Zh. Eksp. Teor. Fiz*., **21** (1951) 721.
30. H. Kroemer, "Theory of wide-gap emitter for Transistor", *Proc. IRE*, **45** (1957) 1535.
31. Harald Böttner, Gang Chen, and Rama Venkatasubramanian, "Theme Article - Aspects of Thin-Film Superlattice Thermoelectric Materials, Devices, and Applications", *Material Research Society Bulletin*, **31** 2006.
32. A. G. Milnes and D. L. Feucht, *Heterojunctions and Metal-Semiconductor Junctions*, Academic, New York, 1972.
33. B. L. Sharma and R. K. Purohit, *Semiconductor Heterojunctions*, Pergamon, London, 1974.
34. R. S. Muller and R. Zuleeg, "Vapor-Deposited, Thin-Film Heterojunction Diodes", *J. App. Phys.,* 35 (1964) 1550-1556.
35. W. A. Gutierrez and H. L. Wilson, "A CdSe-ZnSe Thin Film Rectifier", *Procceedings of IEEE*, **53** (1965) 749.
36. F. V. Shallcross, *RCA Rev.*, December, 1967, pp569-684.
37. C. J. Moore and D. E. Brodie, "A ZnSe-ZnTe Amorphous Heterojunction", *Appl. Phys. Lett.*, **34** (1979) 78-79.
38. F. Pfisterer and H. W. Schock, "ZnTe-CdS thin film photovoltaic cells", *J. Cryst. Growth*, **59** (1982) 432.
39. J. Gunal and M. E. Ozsan, "Te/CdS Thin Film Diodes", *Thin Solid Films*, **113** (1984) 189-197.

40. J. Touskova, D. Kindl and J. Kovanda, "Preparation and Fundamental Properties of CdS-CdTe heterojunctions", *Thin Solid Films.*, **214** (1992) 92-98.

41. P. C. Sarmah, "*The Studies of a few (n)CdTe Films and Ag/Al-(n)CdTe Junctions Prepared by rf Sputtering*", PhD Thesis, Gauhati University (India) 1995.

42. S. C. K. Misra, M. K. Ram, S. S. Pandey, B. D. Malhotra, and Subhas Chandra, "Vacuum-deposited metal/polyaniline Schottky device", *Appl. Phys. Lett.*, **61** (1992) 1219-1221.

43. R. Venugopal, B. K. Reddy, D. R. Reddy, "Preparation and Characterisation of CdTe/$ZnSe_xCdS_{1-x}$ Heterojunctions", *Materials Chem. Phys.*, **55** (1998) 36-43.

44. N.I.Aly, A.A.Akl, A.A.Ibrahim, and A.S.Riad, "Carrier Transport Mechanisms of a-GaAs/ n-Si Heterojunctions", *Egypt. J. Solids,* **24**, 245-254 (2001).

45. M. Rami, E. Benamar, M. Fahoume, F. Chraibi and A. Ennaoui, "Effect of Heat Treatment with $CdCl_2$ on the Electrodeposited CdTe/CdS Heterojunction", *M. J. Condensed Matter* **3** (2000) 66-70.

46. S Mridha and D Basak**,** "Investigation of a p-CuO/n-ZnO thin film heterojunction for H_2 gas-sensor applications" *Semicond. Sci. Technol.* **21** (2006) 928-932.

47. E. I. Adieovich, Yu. M. Yuabov, G. R. Yagudaev, "Investigation of n-CdS-p-CdTe Thin Film Heterojunctions", *Physica Status Solidi* (a), 6**,** (2006) **311 – 322.**

48. G. Hema Chandra, O. M. Hussain, S. Uthanna and B. Srinivasulu Naidu, "Characterization of p-$AgGa_{0.25}In_{0.75}Se_2$/n-$Zn_{0.35}Cd_{0.65}S$ polycrystalline thin film heterojunctions", *Materials Science and Engineering* B, **86,** (2001) 60.

49. C. Weichsel, O. Pagni and A. W. R. Leitch, "Electrical and hydrogen sensing characteristics of Pd/ZnO Schottky diodes grown on GaAs", *Semicond. Sci. Technol.*, **20** (2005) 840-843.

50. G. Wary, T. Kachary and A Rahman, "Electrical and Optical Properties of (n)ZnO/(p)CdTe Heterojunction and Its Performance as a Photovoltaic Converter", *International Journal of Thermophysics,* **27** (2006) 332-346.

51. W. D. Gill and R. H. Bube, "Photovoltaic Properties of Cu_2S-CdS Heterojunctions", *J. Appl. Phys.,* **41** (1970) 3731-3738.

52. A. L. Fahrenbruch, Valery Vasilchenko, F. Buch, Kim Mitchell and R. H. Bube, "II-VI Photovoltaic Heterojunctions for Solar Energy Conversion", *Appl. Phys. Lett*. **25** (1974) 605-608.

53. F. Buch, A. L. Fahrenbruch and R. H. Bube, "Photovoltaic Properties of n-CdSe/p-ZnTe Heterojunctions", *Appl. Phys. Lett.*, **28** (1976) 593-595.

54. T. L. Chu, S. S. Chu, C. Ferekides, C. Q. Wu, J. Britt and C. Wang, "13.4% Efficient Thin Film CdS/CdTe Solar Cells", *J. Appl. Phys.*, **70** (1991) 7608-7612.

55. S. N. Alamri and A. W. Brinkman, "The Effect of the Transparent Conductive Oxide on the Performance of Thin Film CdS/CdTe Solar Cells", *J. Phys. D*, **33** (2000) L1-L4.

56. Habibe Bayhan, "Tunneling-Enhanced Recombination in Polycrystalline CdS/CdTe Solar Cells", *Turk J. Phys.*, **30** 109-114 (2006).

57. M. Purica, E. Budianu, E. Rusu, P. Arabadji, "Electrical Properties of the CdS/InP Heterostructures for Photovoltaic Applications", *Thin Solid Films*, **511-512** (2006) 468-472.

58. S. Venkatachalam, D. Mangalaraj, Sa. K. Narayandass, K. Kim, J. Yi, "Influence of Substrate Temperature on the Structural, Optical and Electrical Properties of Zinc Selenide (ZnSe) Thin Films", *J. Phys. D Appl. Phys* **39** (2006) 4777-4782.

59. II-VI Semiconductor Materials and their Applications, Edited by Maria C. Tamargo, (Taylor and Francis, New York), 2002.

60. R. M. Park, M. B. Troffer, C. M. Rouleau, J. M. DePuydt and M. A. Haase, "p-type ZnSe by nitrogen atom beam doping during molecular beam epitaxial growth", *Appl. Phys. Lett.*, **57** (1990) 2127-2129.

61. R. M. Park and M. B. Troffer, "Noncontact Electrical Characterization of Low-resistivity p-type ZnSe:N Grown by Molecular Beam Epitaxy", *Appl. Phys. Lett*. **59** (1991) 1896-1898.

62. G. D. Brownline, Z. Zhu, G. Horsburgh, T. Steele, P. J. Thompson, J. M. Wallace, K. A. Prior, B. C. Cavenett, "Photoluminescence excitation

Specroscopic Studies of Nitrogen Doped ZnSe", *J. Crystal Growth* **159** (1996) 321-324.

63. Y. Kawakami, T.Ohnakado, M. Tsuka, S. tokudera, Y. Ito, Sz. Fuzita and Sg. Fujita, "p-type ZnSe grown by molecular beam epitaxy with remote microwave plasma of n2", *J. Vac. Sci. Technol.* B **11** (1993) 2057-2061.
64. Deutsch T F, *J. Phys. Chem. Solids* **34** (1973) 2091.
65. Chu C C, Ng T B, Han J, Hua G C, Gunshor R L, Ho E, Warwick E L, Kolodiejski L A and Nurmikko A V *Appl. Phys. Lett.* **69** (1996) 602.
66. E. Masetti, M. Montecchi, and M. P. da Silva, *Thin Solid Films,* **234**, (1993) 557.
67. M. Bedir, M. Oztas, O. F. Bakkaloglu and R. Ormanci, "Investigations on Structural, Optical and Electrical Parameters of Spray Deposited ZnSe thin Films With Different Substrate Temperature", *Eur. Phys J. B"*, **45** (2005) 465-471.
68. A. P. Samantilleke, I. M. Darmadasa, K. A. Prior, K. L. Choy, J. Mei, R. Bacewicz, A, Wolska, "Development of Optoelectronic Devices using Electrochemically Grown Thin ZnSe Layers", *J. Mater. Sci. Mater. Electron.*, **12** (2001) 661-666.
69. M. A. Haase, J. Qiu, J. M. DePuydt, and H. Cheng, "Blue-green laser diodes", *Appl. Phys. Lett.* **59** (1991) 1272-1274.
70. E. Kato, H. Noguchi, M. Nagai, H. Okuyama, S. Kijima, and A. Ishibashi, "Significant progress in II-VI blue-green laser diode lifetime", *Electronics Letters*, vol. **34**, (1998) 282-284.
71. S. L. Chuang, N. Nakayama, A. Ishibashi, S. Taniguchi, and K. Nakano, "Degradation of II-VI blue-green semiconductor lasers," *Journal of Quantum Electronics*, vol. **34**, (1998). 851-857.
72. N. Nakayama, S. Itoh, K. Nakano, H. Okuyama, M. Ozawa, A. Ishibashi, M. Ikeda, and Y. Mori, "Room temperature continuous operation of blue-green laser diodes", *Electron. Lett.,* **29,** (1993) 1488.
73. A. Nouhi, R. J. Stirn and A. Hermann, *Proc. 19th IEEE Photovoltaic Specialistst Conf.,* (1987) IEEE, New York, p. 1461.

74. Ji-Beom Yoo, Alan L. Fahrenbruch and Richard H. Bube, "Effect of a thin intermediate zinc selenide layer on the properties of $CuInSe_2$ solar cells", *Solar Cells*, **31** (1991) 171-180.

75. H.J. Hovel, "Switching and Memory in ZnSe-Ge Heterojunctions", *Appl. Phys. Lett.,* **70** (1970) 141-143.

76. Z.C. Huiang, C.K. Wie, I. Na, H. Luo, D.B. Molt and P.K. Slhu, "High performance ZnSe photoconductors", *Electronics Letters* **32**(1996) 1507-1509.

77. E. Monroy, F Omn`es and F Calle, "Wide-bandgap semiconductor ultraviolet Photodetectors", *Semicond. Sci. Technol*. **18** (2003) R33–R51.

78. F. Vigue, A. Bouille, E. Tournie and J. P. Faurie, "ZnSe and ZnMgBeSe Based Schottky barrier Photodetectors for the Blue and Ultraviolet Spectral Range", *Phys. Stat. Sol. A* **180** (2000) 301.

79. F. Vigue, E. Tournib, and J, P. Faurie, "ZnSe-based Schottky barrier photodetectors", *Electron. Lett.,* **36**, (4), (2000) 352-354.

80. E. Monroy1, F Omn`es and F Calle, "Wide-bandgap semiconductor ultraviolet Photodetectors", *Semicond. Sci. Technol*. **18** (2003) R33–R51.

81. Shinji Fujiwara, Taka Chikamura, Osamaru Eguchi, Yukimasa Kuramiito, and Masakazu Fukai, "Photoconductive Properties of Thin-Film Heterojunction ZnSe-$(Zn_{l-x}\ Cd_xTe)_{l-y}(ln_2Te_3)_y$", *IEEE T'ransactions on Elecron Devices*, ED-**30**, (6) **,** (1983) 706-711.

82. Y. Tsujimoto and M. Fukai, "Electoluminescence from ZnSe-ZnTe Heterojunction Diodes", *Japan J. Appl. Phys.*, **6** (1967) 1024-1025.

83. Masakazu Kobayashi, Naoki Mino, Konagai and Kiyoshi Takahashi, "Effects of Indium diffusion on the properties of ZnSe:Mn dc thin film electroluminescenct devices", *J. Appl. Phys.,* **57** (1985) 2905-2908.

84. M. Aven, D. T. F. Marple and B. Segll, "Some Electrical properties of ZnSe", *J. Appl. Phys*. **32** (1961) 2261-2265.

85. G. B. Stringfellow and R. H. Bube, "Photoelectronic Properties of ZnSe Crystals", *Phys. Rev.* **171** (1968) 903-915.

86. G. B. Stringfellow and R. H. Bube, "Radiative Pair Transitions in p-type ZnSe:Cu Crystals", *J. Appl. Phys*. **39** (1968) 3657-3661.

87. R Markowski, M Piacentinit, D Debowskat, M Zimnal-Starnawskat, F Lamas, N ZemaJJ and A Kisielf, "Electronic structure of zincblende ZnSe: theory and experiment", *J. Phys.: Condens. Matter* **6** (1994) 3207-3219.

88. D. T. F. Marple, "Electron Effective Mass in ZnSe", *J. Appl. Phys*. **35** (1964) 1879-1882.

89. G. Jones and J. Woods, "The Electrical Properties of Zinc Selenide", *J. Phys. D*. **9** (1976) 799-810.

90. J. R. Cutter and J. Woods, "The Anomalous Photovoltaic Effect in Zinc Selenide", *J. Phys. D*. **8** (1975) 314-321.

91. I. Strzalkowski, S. Joshi and C. R. Crowell, "Dielectric Constant and its temperature Dependence for GaAs, CdTe and ZnSe", *Appl. Phys. Lett*. **28** (1976) 350-352.

92. M. Yamaguchi and A. Yamamoto, *Jap. J. Appl. Phys.,* **16** (1977) 77-84.

93. A. W. Livingstone, K. Turvey and J. W. Allen, *Solid St. Electron.* **16** (1977) 351-356.

94. T. Ido, M. Kato, A. Yoshida and M. Ieda, "Heat treatment effects on blue electroluminescence in ZnSe", *J. Phys. D*, **11**, (1978) L5.

95. Shashi Bhushan, "Photoconductivty of ZnSe Crystals", *J. Mater. Sci. Lett.*, **6** (1987) 591-592.

96. V A Gnatyuk**, "**Photoconductivity of ZnSe crystals under high excitation rates**",** *Semicond. Sci. Technol.* **15** (2000) 523–528.

97. S. Cho, P. T. Ho, J. Goldhar, and H. Lee, "Photoconductivity in ZnSe under high electric fields", *IEEE J. Quantum Electron.,* **30** (1994) 1489.

98. S Myhajlenko, J L Batstone, H J Hutchinson and J W Steeds, "Luminescence studies of individual dislocations in II-VI (ZnSe) and III-V (InP) semiconductors", *J. Phys. C: Solid State Phys.*, **17** (1984) 6477-6492.

99. M Isshiki and K Masumoto, "The change in the photoluminescence spectra of Cu- doped ZnSe single crystals caused by heat treatment**",** *J. Phys. C: Solid State Phys*. **21** (1988) 2771-2777.

100. H. Wang, K. S. Wong, B. A. Foreman, Z. Y. Yang, and G. K. L. Wong, "One- and two-photon-excited time-resolved photoluminescence investigations of bulk and surface recombination dynamics in ZnSe" , *J. Appl. Phys* (1998) **83**, 4773-4776.

101. S. Bhaskar, P.S. Dobal, B. K. Rai and R. S. Katiyar, "Photolumnescence study of deep levels in Cr-doped ZnSe", *J. Appl. Phys.* **85** 1999 439-443.

102. S. Fujita, H. Mimoto, and T Noguchi, 'Photoluminescence in ZnSe grown by liquid epitaxy from Zn-Ga solution', *J. Appl. Phys.,* 1979, **50,** (2), pp. 1079-1087.

103. J. A. Tuchman, Z. Sui, S. Kim, and I. P. Herman, 'Photoluminescence of ZnSe/ZnMnSe superlattices under hydrostatic pressure', *J. Appl. Phys.,* 1993**, 13,** pp. 7730.

104. A. Kamata and T. Moriyama, 'Luminescence properties of nitrogen ion implanted ZnSe after thermal annealing', *Appl. Phys. Lett.,* 1995, **67,** pp. 1751-1753.

105. M. Yamaguchi, A. Yamamoto, and M. Kondo, "Photoluninenscence of ZnSe single crystals diffused with group III element", *J. Appl. Phys.,* 1977, **48,** pp. 5237-5244.

106. B. A. Morgan, K. M. Ring and K. L. Kavanagh, "Au/ZnSe Contacts Characterized by Ballistic Electron Emission Microscopy", *J. Appl. Phys*. **79** (1996) 1532-1535.

107. T. Yao, M. Ogura, S. Matsuoka and T. Morishita, "High-quality ZnSe Thin Films Grown by Molecular beam Epitaxy", *Appl. Phys. Lett*. **43** (1983) 499-501.

108. B. Ullrich, "Comparison of the Photocurrent of ZnSe/InSe/Si and ZnSe/Si Heterojunctions", *Mater. Sci. Engg.*, **B56** (1998) 69-71.

109. M. Lazzarino, G. Scarel, S. Rubini, G. Bratina, A. Bonanni, L. Sorba, A. Franciosi, "Schottky Barrier Tunability in Al/ZnSe Intrerfaces", *J. Cryst. Growth*, **184/185** (1998) 193-198.

110. T. L. Chu, S. S. Chu, G. Chen, J. Britt, C. Ferekides and C. Q. Wu, "Zinc Selenide Films and Heterojunctions", *J. Appl. Phys*. **71** (1992) 3865-3869.

111. Chi Tsar Hsu, Kuin Su, Tien Shai Wu, Meiso Yokoyama, "Electric field effect on ZnSe films prepared by metal organic chemical vapor deposition", *Jap. J. Appl. Phys.*, **33** (1994) 161-163.

112. A. Rumberg, Ch. Sommerhalter, M. Toplak, A. Jager-Waldau, M. Ch. Lux-Steiner, "ZnSe thin films grown by CVD for CIGS", *Thin Solid Films*, **361-362** (2000) 172-176.

113. P. Besomi, K. Christianson and B. W. Wessels, “Photovoltaic Properties of ZnSe/GaAs Heterojunctions”, *Thin Solid Films*, **87** (1982) 113-118.

114. E. J. Bawolek and B. W. Wessels, “Electrical Properties of n-n ZnSe/GaAs Heterojunctions”, *Thin Solid Films*, **131** (1985) 173-183.

115. C.T. Hsu , Y.J. Lin, Y.K. Su and M. Yokoyama, “Growth of ZnSe thin films on ITO/glass substrates by low pressure metalorganic chemical vapor deposition”, *Journal of Crystal Growth* ,**125** (1992) 420—424.

116. E. Guziewicz, M. Godlewski, K. Kopalko, E. Lusakowska, E. Dynowska, M. Guziewicz, M. M. Godlewski and M. Phillips, “Atomic Layer Deposition of Thin Films of ZnSe-Structural and Optical Characterization”, *Thin Solid Films*, **446** (2004) 172-177.

117. K. Kopalko, M. Godlewski, E. Guziewicz, E. Lusakowska, W. Paskowicz, J. Domagala, E. Dynowska, A. Szczerbakow, A. Wojcik, M. R. Philips, “Monocrystalline thin Films of ZnSe and ZnO Grown by Atomic Layer Epitaxy”, *Vacuum*, **74** (2004) 269-172.

118. C. Natarajan, M. Sharon, C. L. Clenent, M. N. Spallart, *Thin Solid Films*, **237** (1994) 118.

119. G. Riveros, H. Gomez, R. Henriquez, R. Schrebler, R. E. Marotti, E.A. Dalchiele, “Electodeposition and Characterization of ZnSe Semiconductor Thin Films”, *Sol. Energy Mater. Sol. Cells*, **70** (2001) 255-268.

120. S. Soundeswaran, O. Senthil Kumar, R. Dhanasekaran, P. Ramasamy, R. Kumeresen, M. Ichimura, “Growth of ZnSe Thin Films by Electrocrysallization Technique”, *Mater. Chem. Phys.*, **82** (2003) 268-272.

121. A. P. Samantilleke, M. H. Boyle, J. Young, I. M. Darmadasa, “Electrodeposition of n-type and p-type ZnSe Thin Films for Applications in Large Area Optoelectronic Devices”, *J. Mater. Sci. Mater. Electron.*, **9** (1998) 289-290.

122. I. M. Darmadasa, A. P. Samantilleke, J. Young, M. H. Boyle, R. Bacewicz, A, Wolska, “Electrodeposited p-type and n-type ZnSe Layers for Light Emitting Devices and Multi-Layer Tandem Solar Cells”, *J. Mater. Sci. Mater. Electron.*, **10** (1999) 441-445.

123. K. C. Sharma, R. P. Sharma and J. C. Garg, "Opto-electronic properties of chemical bath deposited polycrystalline non-stoichiometric zinc selenide films', *Ind. J. Pure & Appl. Phys*, **28**, (1990) 539-541.

124. G. N. Chaudhari, S. D. Sathaye, Prabhat Singh, V. J. Rao, V. Manorama, R. S. Bhide, S. V. Bhoraskar, "Studies on thin films of ZnSe prepared by a chemical deposition Method", *J. Material Sc. Lett.*, **11** (1992) 1097– 1099.

125. G N Chaudhari, S Manorama and V J Rao, "Studies on thin films of ZnSe on GaAs prepared by a chemical deposition method", *J. Phys. D Appl. Phys*., **25** (1992) 862464.

126. C. D. Lokhande, P. S. Patil, H. Triutsch, A. Ennaoui, " ZnSe Thin Films by Chemical Bath Deposition Method", *Sol. Energy Mater. Sol. Cells*, **55** (1998) 379-393.

127. R. B. Kale, C. D. Lokhande "Influence of Air Annealing on the Structural, morphological, optical and Electrical Properties of Chemically Deposited ZnSe Thin Films", *Appl. Surf. Sci.*, **252** (2005) 929-938.

128. R. Kumaresan, M. Ichimura and E. Arai, "Photochemical Deposition of ZnSe Polycrystalline Thin Films and Their Characterization", *Thin Solid Films*, **414** (2002) 25-30.

129. M. Oztas, M. Bedir, O.F. Bakkaloglu and R. Ormanci, "Effect of Zn:Se Ratio on the Properties of Sprayed ZnSe Thin Films", *ACTA PHYSICA POLONICA A* **107** (2005) 525-534.

130. R. B. Kale, C. D. Lokhande, " Room Temperature Deposition of ZnSe Thin Films by Successive Ionic Layer Adsorption and Reaction (SILAR) Method", *Mat. Res. Bull.*, **39** (2004) 1829-1839.

131. C. Falcony, F. Sanchez-Sinencio, J. S. Heiman, O. Zelaya and C. Menezes, "Polycrystalline zinc selenide films deposited by a low-temperature close-spaced vapor-transport method", *J. Appl. Phys.* **56** (1984) 1752-1756.

132. J. M. Pawlikowski, "Preparation and Characterization of Close-spaced Vapour transport Thin Films of ZnSe for Heterojunction solar cells", *Thin Solid Films*, **127** (1985) 9-27.

133. H. S. Reehal, J. M. Gallego and C. B. Edwards, *Appl. Phys. Lett.,* **40** (1982) 258.

134. A. Pizzo, M. A. Tagliente, L. Caneve, S. Scaglione, *Thin Solid Films*, **368** (2000) 8.

135. G. Perna, V. Capozzi, M. C. Plantamura, A. Minafra, P. F. Biagi, S. Orlando, V. Marotta, A. Gardini, "Structural and Optical Properties of Pulsed Laser-deposited ZnSe Films", *Appl. Surf. Sci.*, **186** (2002) 521-526.

136. G. Perna, V. Capozzi, M. C. Plantamura, A. Minafra, P. F. Biagi, M. Pallara, S. Orlando, V. Marotta, A. Gardini, "Structural and Optical Properties of ZnSe Films Deposited on Crystalline Al_2O_3 Substrate by Laser Ablation technique", *Appl. Surf. Sci.*, **208-209** (2003) 582-588.

137. P Poulopoulos, S Baskoutas, V Karoutsos, M Angelakeris and N K Flevaris, "Growth and optical absorption of thin ZnSe films", *J. of Physics: Conference Series* **10** (2005) 259–262.

138. Li Yan and John A. Woollam, "Oxygen plasma effects on optical properties of ZnSe films", *J. Vac. Sci. Technol.* A **20**, (2002) 693-701.

139. Pradip K. Kalita, B. K. Sarma and H. L. Das, "Effect of substrate Temperature on Photo-Electronic Properties of Thermally Evaporated ZnSe Thin Films", *Indian J. Phys.*, **74A** (2000) 283-285.

140. Pradip K. Kalita, B. K. Sarma and H. L. Das, "Structural Characterization of Vacuum Evaporated ZnSe Thin Films", *Bull. Mater. Sci.*, **23** (2000).

141. C. K. De, N. K. Mishra and T. B. Ghosh, "Preparation and structural characterization of ZnSe thin films by X-ray diffraction technique", *Indian J. Phys*. **69A** (1993) 261.

142. C. K. de and N. K. Mishra, "X-ray diffraction analysis of lattice defects of ZnSe thin films deposited at different substrate temperatures", *Indian J. Phys*. **71A** (1997) 535.

143. S. Venkatachalam, D. Mangalaraj, Sa. K. Narayandass, K. Kim, J. Yi, "Structure, Optical and Electrical Properties of ZnSe Thin Films", *Physica B*, **358** (2005) 27-35.

144. L.M. Caicedo, G. Cediel, A. Dussan, J.W. Sandino, C. Calderón, G. Gordillo, "Study of Optical, Morphological and Structural Properties of ZnSe Thin Films Deposited by Evaporation", *Physica status solidi (b)* **220** (2000) 249-253.

145. E. E. Khawaja, S. M. A. Durrani, A. B. Hallak, M. A. Salim and M. Sakhawat Hussain, "Density of Thin vapour-Deposited films of Zinc Selenide", *J. Phys. D*. **27** (1994) 1008-1013.

146. G. K. M. Thutupalli and S.G. Tomlin, "The Optical Properties of Thin Film of Cadmium and Zinc Selenides and Tellurides", *J. Phys. D*. **9** (1976) 1639-1646.

147. A. L. Dawar, P. K. Shishodia, G. Chauhan, C. Jagadish, S. K. Kapoor and P. C. Mathur, " Effect of Hydrogen Annealing on Structural and Optical properties of ZnSe Thin Films", *J. Crystal Growth* **100** (1990) 281-285.

148. M. El Sherif, F. S. Terra, S. A. Khodier, "Optical Characteristics of Thin ZnSe Films of Different Thickness", *J. Mater. Sci. Mater. Electron.*, **7** (1996) 391-395.

149. B. P. Singh, V. Singh, L. Kumar, P. Dwivedi and T. P. Sharma, "Spectroscopic study of vacuum evaporated crystalline Zinc Selenide thin films", *Asian J. Phys.* **11** (2002) 199-203.

150. S. T. Lakshmikumar, A. C. Rastogi, "Noval two-stage Selenization Process for the Preparation of ZnSe Films", *Thin Solid Films*, **299** (1995) 150-153.

151. S. Gogoi and K. Barua,"DC Conduction Mechanism and Dielectric Properties of Dry-Air Stabilised ZnSe Films", *Indian J. Phys.*, **56A** (1982) 47-54.

152. G. I. Rusu, M. E. Popa, G. G. Rusu and Iulia Salaoru, "On The Electronic Transport Properties of polycrystalline ZnSe Films", *Appl. Surf. Sci.*, **218** (2003) 222-230.

153. A. A. El-Shazly, M. A. Kenawy, H. T. El-Shair, M. M. El-Nahass and H. S. Soliman, " Anomalous Photovoltaic Effect in Thin Film of ZnSe obliquely Deposited in Vacuum", *J. Phys. D*. **16** (1983) 1967-1976.

154. K. N. Verma, D. P. Saha and S Singh, "Polycrystalline ZnSe under solar illumination", *Indian J. Pure and Applied Phys*. **39** (2001) 271.

155. G. A. ANTCLIFFET, " Electroluminescence of evaporated ZnS and ZnSe films", *Brit. J. Appl. Phys*., **16** (1965) 1467-1476.

156. B. K. Shin, Y. S. Park and D. C. Look, "Electrical Characteristics of Al-implanted ZnSe", *Appl. Phys. Lett*. **24** (1974) 435-436.

157. T Yao, Y. Makita and S. Maekawa, "Molecular beam epitaxial growth of low resistivity ZnSe films", *Appl. Phys. Lett.,* **35** (1979) 97.

158. Paul Besomi and Bruce W. Wessels, “High conductivity heteroepitaxial ZnSe films”, *Appl. Phys. Lett.*, **37** (1980) 955-957.

159. D M Chiu, “Electrical properties of n-type ZnSe : I and ZnSe : I : In single crystals”, *J. Phys. D: Appl. Phys.*, **16** (1983) 2281-2295.

160. Julio Aranovich, Alan L Fahren and Richard H Bube, “High Conductivity ZnSe films”, *J. Appl. Phys*. **49** (1978) 2584.

161. F. Kitagawa, T. Mishima and K. Takahashi, “Near band edge Luminescence in ZnSe grown from Gallium Solution”, *J. Electrchem Soc*.,**126** (1979) 341.

162. F. Kitagawa, T. Mishima and K. Takahashi, “Molecular beam epitaxial growth of ZnTe and ZnSe”, *J. Electrchem Soc*.,**127** (1980) 937.

163. M. G. M. Choudhury, M.R. Islama, M.M. Rahmana, M.O. Hakima, M.K.R. Khana, K.J. Kaob, G.R. Lai, “PREPARATION AND CHARACTERIZATION OF ZnSe:Al THIN FILMS”, *Acta Physica Slovaca*, vol. **54** No. 4, (2004) 417-425.

164. D. C. Oh, J. H. Chang, T. Takai, J. S. Song, J. J. Kim, K. Godo, Y. G. Park, K. Shindo, T. Yao, “Electrical properties of highly Al-doped ZnSe grown by molecular beam epitaxy”, *Procceedings of IEEE*, (2002) 685-386.

165. Z. Ali, A. K. S. Aqili, A. Maqsood, S. M. J. Akhtar, “Properties of Cu-doped Low Resistive ZnSe Films Deposited by Two-sourced Evaporation”, *Vacuum*, **80** (2005) 302-309.

166. R. J. Robinson and Z. K. Kun, *Appl. Phys. Lett.* **27** (1975) 74-76.

167. A A Qidwai and J Woods, “Photocapacitance and defect levels in gallium-doped zinc selenide”, *J . Phys. C: Solid State Phys*., **16** (1983) 6789-6797.

168. I. L. Kuskovsky, Y. Gu, C. Tian, G. F. Neumark, S. P. Guo, W. Lin, O. Maksimov, M. C. Tamargo, A. N. Alyoshin and V. M. Belous, “Heavily p-Type Doped ZnSe and ZnBeSe”, *Phys. Stat. Sol. (b)* **229** (2002) 385-389.

169. H. Wolf, A. Burchard, M. Deicher, T. Filz, A. Jost, St. Lauer, R. Magerle, V. Ostheimer, W. Pfeiffer and Th. Wichert, “Doping of ZnSe, ZnTe and CdTe with Group V Elements”, 19th International Conference on Defects in Semiconductors, Sedai, Japan, 23-28 July 1995.

170. B. L. VanMil, A.J. Ptak, Lihua Bai, N. C. Giles, T. H. Myers, Y. Xu, K. Meehan and L. Wang, “Growth and Characterization of Cr-doped ZnSe and ZnTe by Molecular Beam Epitaxy”.

171. Toshiyuki Ido, Hideo Goto, “Doping Efficiency of Sb in ZnSe Grown by MOVPE”, 10th European Workshop on MOVPE, Lecce (Italy) 8-11 June 2003.

172. A W Brinkman and D L Kirk, “The role of thermal annealing in changing the interfacial microstructure of Ge-ZnSe heterojunctions”, *J. Phys. D: Appl. Phys.,* **10**, (1977) 499-508.

173. P. Besomi and B. W. Wessels, “Deep Level Defects in Au/ZnSe Schottky Diode”, *Electronic Lett.*, 16 (1980) 794-795.

174. R. Coratger, C. Girardin, J. Beauvillain, I. M. Dharmadasa, A. P. Samanthilake, J. E. F. Frost, K. A. Prior and B. C. Cavenett, “Schottky barrier Formation at metal/n-ZnSe Inerfaces and Characterization of Au/n-ZnSe by Ballistic Electron Emission Microscopy”, *J. Appl. Phys*. **81** (1997) 7870-7875.

175. K Schull, W Spahn, V Hock, U Lunz, M Ehinger, W Faschinger and G Landwehr, “Non-metal in situ and ex situ ohmic Contacts to n-ZnSe”, *Semicond. Sci. Technol.*, **12** (1997) 485-489.

176. A. Saidane, “Chemical Reaction and Interdiffusion at ZnSe-(Indium Tin Oxide) Interface”, *Thin Solid Films*, **121** (1984) 51-59.J.

177. D. Seghier and H. P. Gislason, “Effect of the interface on the electrical properties of ZnSe/GaAs heterojunctions grown by molecular beam epitaxy”, *Appl. Phys. Lett.*, **71** (1997) 2295-2297.

178. U. Blieske, T. Kampschulte, A. Bauknecht, M. Saad, J. Sollner , A. Krost, K. Schatke, M. Ch. Lux-Steiner, “n-ZnSe/p-GaAs HETEROJUNCTION SOLAR CELLS”, *Proc. 26th PVSC IEEE*, (1997) 939-942.

179. D. Seghier and H. P. Gislason, “The Observation of Persistent Photoconductivity in N-doped p-type ZnSe/GaAs Heterojunctions”, *J. Phys. D*. **32** (1999) 369-373.

180. M. J. Kim, H. S. Lee, J. Y. Lee, T. W. Kim, K. H. Yoo, M. D. Kim, “Effect of thermal annealing on the surface, optical, and structural properties of *p*-type ZnSe thin films grown on GaAs (100) substrates”, *J. Material Sc.*, **39** (2004) 323– 327.

181. M. D. Kim, H. S. Park and T. W. Kim, “Effect of Hydrogenetion and Thermal Annealing on the Electrical Properies of Au-p-ZnSe/n-GaAs diodes”, *J. Mater. Sci. Lett.*, **18** (1999) 467-469.

182. J. Nurnberger, W. Faschinger, R. Schmitt, M. Korn, M. Ehinger, and G. Landwehr, "Optimization of p-contacts on ZnSe diodes", *Appl. Phys. Lett*., **70** (10), (1997) 1281-1283.

183. F Vigue, P. de Mierry, J.-P. Faurie, E. Monroy, F. Calle and E Mufioz "High detectivity ZnSe-based Schottky barrier photodetectors for blue and near-ultraviolet spectral range", *ELECTRONICS LETTERS*, **36** (9) (2000) 826-827.

184. A. Gerhard, J. Nurnberg, K. Schull, V. Hock, C. Schumacher, M. Ehinger, and W. Faschinger, 'ZnSe-based MBE-grown photodiodes', *J. Crystal Growth,* 1998, **184/185,** pp. 1319-1323.

185. D. L. Dreifus, B. P. Sneed, J. W. Cook, Jr., and J.F. Schetzina, R.M. Kolbas, "ZnSe Field Effect Tansistor", *Appl. Phys. Lett.,* **57** (1990) 1663-1665.

186. H. Ohnishi and Y. Hamakawa, "Thin film electroluminescent cell with the low-threshold voltage of n-Ge-ZnSe:Mn^{2+}-indium-tin oxide structure", *J. Appl. Phys.*, **51** (1980) 2937-2939.

187. S. Rubini, B. Bonanni, E. Pelucchi, A. Franciosia, A. Garulli, A. Parisini, Y. Zhuang and G. Bauer and V. Holy, "ZnSe/CdTe/ZnSe heterostructures", *J. Vac. Sci. Technol.* B **18** (2000) 2263-2270.

188. S Darwishy, A S Riady and H S Soliman, "Electrical conductivity and the effect of temperature on photoconduction of n-ZnSe/p-Si rectifying heterojunction cells", *Semicond. Sci. Technol.*, **11** (1996) 96-102.

189. S. Venkatachalam, R. T. Rajendra Kumar, D. Mangalaraj, Sa. K. Narayandass, K. Kim, J. Yi, "Optoelectronic Properties of $Zn_{0.52}Se_{0.48}$/Si Schottky Diodes", *Solid State Electronics*, **48** (2004) 2219-2223.

190. S. Venkatachalam, D. Mangalaraj, Sa. K. Narayandass, S. Velumani, P. Schabes-Retchkiman, J. A. Ascencio, "Structural studies on vacuum evaporated ZnSe/p-Si Schottky diodes", *Mat. Chem. Phys.,* **103** (2007) 305-311.

191. W. S. Lour, and C. C. Chang,: 'VPE grown ZnSe/Si PIN-like visible photodiodes', *Solid-State Electronics,* 1996, **39,** (9), pp. 1295-1298.

192. C. C. Chang, and S. J. Lii, 'Fabrication of ZnSe/Si PIN photodiode by IR furnace chemical vapor deposition', *Solid State Electronics,* 1998, **42,** (5), pp. 8.817-822.

193. C. C. Chang and K.T.Wu, "Fabrication of n-ZnSe/p-Si/n-Si heterojunction phototransistor using IR furnace chemical vapour deposition and its optical properties analysis", *IEE Proc.-Optoelectron.*, **147,** (2000) 104-108.

194. F. Buch, A. L. Fahrenbruch and R. H. Bube, "Photovoltaic Properties of Five II-VI Heterojunctions", *J. Appl. Phys.*, **48** (1977) 1596-1602.

195. A. J. Nelson, "Photoemission investigation of the ZnSe/CdTe heterojunctisn band discontinuity", *J. Appl. Phys.* **78** (1995) 2537-2540.

196. P. Mahawala, S. Vekkalanka, S. Jeedigunta, C. S. Ferekides and D. L. Morel, "Transparent Contact Development for CdSe Top Cells in High Efficiency Tandem Structure", Photovoltaic specialist conference, 2005.

197. G. Gordillo. C. Calderbn and H. Infante, "CdTe THIN FILM SOLAR CELLS WITH ZnSe BUFFER LAYER", *IEEE* (2002) 644-647.

198. Larry C. Olsen, F.William Addis, David Greer , Wenhua Lei and Fuad Abulfotah, "NON-CADMIUM ZnO/CIS AND ZnSe/CIS SOLAR CELLS", *Proc. 1st WCPEC* (1994) 194-197.

199. Yasutoshi OHTAKE, Katsumi KUSHIYW, Akira YAMADA and Makoto KONAGAI, "DEVELOPMENT OF ZnO/ZnSe/CuIn~.,Ga,Se~THIN-FILM SOLAR CELLS WITH BAND GAP OF 1.3 TO 1.5 e V" *Proc. 1st WCPEC* (1994) 218-221.

200. Chang, S.J. Lin, T.K. Su, Y.-K. Chiou, Y.Z. Wang, C.K. Chang, S.P. Chang, C.M. Tang, J.J. Huang, B.R. , "ITO/Homoepitaxial ZnSe/ITO MSM Sensors With Thermal Annealing", *Sensors Journal, IEEE*, **6** (2006) 945- 949.

201. K. L. Chopra, S. Major and D. K. Pandya, "Transparent Conductors - A Status Review", *Thin Solid Films*, **102**, 1983, pp. 1 – 46.

202. K. L. Chopra and S. Major, "Transparent Conducting Oxide Films", *Thin Film Technology and Applications"*, (1985) 224-236 (Tata-Mc-Graw Hill, New Delhi).

203. T. Minami, "Transparent Conducting Oxide Semiconductors for Transparent Electrodes", *Semicond. Sci. Technol.*, **20** (2005) S35-S44.

204. Vinod K. Jain, "Indium-Tin Oxide Layers and Their Application in SIS Solar Cell Technology", *Physics of Solar Cells.*, 1st Edn S.C. Jain, S. Radhakrishna, and T. R. S. Reddy, eds. (International Council of Scientific Unions, Madras, India) (1984) p111-126.

205. T. Margalith, O. buchinsky, D. A. Cohen, A. C. abare, M. Hansen, S. P. denBaars and L. A. Coldren, "Indium Tin Oxide Contacts to Gallium Nitride optoelectronic Devices", *Appl. Phys. Lett*. **74** (1999) 3930-3932.

206. C S Chang, S J Chang, Y K Su, Y C Lin, Y P Hsu, S C Shei, S C Chen, C H Liu and U H Liaw, "InGaN/GaN light-emitting diodes with ITO p-contact layers prepared by RF Sputtering", *Semicond. Sci. Technol*., **18** (2003) L21–L23.

207. P. Nath and R. F. Bunshah, "Preparation of In_2O_3 and Tin-Doped In_2O_3 Films by a Novel Activated Reactive Evaporation Technique", *Thin Solid Films*, **69**, 1980, pp. 63 -68.

208. J. C. C. Fan, F. J. Bachner and G. H. Foley, "Effect of Oxygen Partial Pressure During Deposition on Properties of r.f. Sputtered Sn-Doped In_2O_3 Films", *Applied Physics Letters*, **31**(11), 1977, pp. 773 – 775.

209. R. G. Dhere, T. A. Gessert, L. L. Schilling, A. J. Nelson, K. M. Jones, H. Aharoni and T. J. Coutts, "Electro-Optical Properties of Thin Indium Tin Oxide Films: Limitations on Performance", *Solar Cells,* **21** (1987) 281 – 290.

210. L Kerkache, A Layadi, E Dogheche and D R emiens, "Physical properties of RF sputtered ITO thin films and annealing effect", *J. Phys D*, **39**, (2006) 184.

211. A. K. Kulkarni, Kirk H. Schulz, T. S. Lim, M. Khan, "Dependence of the Sheet Resistance of Indium Tin Oxide Thin Films on Grain Size and Grain Orientation Determined from X-ray Diffraction Techniques", *Thin Solid Films*, **345** (1999) 273-277.

212. T. Mizrah and D. Adler, "Operation of ITO/Si Heterojunction Solar Cells", *Appl. Phys. Lett.*, **29** (1976) 682-684.

213. K. Sreenivas, T. Sudersena Rao, Abhai Mansingh, Subhash Chandra, "Preparation and characterization of rf sputterd indium tin oxide films", *J. Appl. Phys*. **57** (1985) 384-392.

214. John C. C. Fan, Frank J. Bachner and George H. Foley, "Effect of O_2 pressure during deposion on properties of rf sputtered Sn doped In_2O_3 films", *Appl. Phys Lett.*, **31** (1977) 773-775.

215. J. Szczyrbowski , A. Dietrich , H. Hoffmann, "Optical and electrical properties of RF-sputtered indium-tin oxide films", *Physica Status Solidi,* (a) **78** (2006) 243 – 252.

216. A. I. P. Theuwissen and G. J. Declerck, “Optical and Electrical Properties of Reactive D. C. Magnetron-Sputtered In_2O_3:Sn Films”, *Thin Solid Films*, **121** (1984) 109-119.

217. Swati Ray, R. Banerjee, N. Basu, A. K. Batabyal and A. K. Barua, “ Properties of tin doped indium oxide films prepared by magnetron sputtering”, *J. Appl. Phys*., **54** (1983) 3497-3501.

218. J. Dutta and S. Ray, “Variations in Structural and Electrical Properties of Magnetron- Sputtered Indium Tin Oxide Films with Deposition Parameters”, *Thin Solid Films*, **162** (1-2), 1988, pp. 119 – 127.

219. J. Touskova, J. Kovanda, L. Dobiasova, V. Parizek, P. Kielar, “Sputtered Indium Tin Oxide Substrates for CdS-CdTe Solar Cells”, *Sol. Energy Mater Sol Cell.*, **37** (1995) 357-365.

220. T. Neubert, F. Neumann, K. Schiffmann, P. Willich, A. Hangleiter, “Investigations on oxygen diffusion in annealing processes of non-stoichiometric amorphous indium tin oxide thin films”, *Thin Solid Films* **513** (2006) 319.

221. R X Wang, C D Beling, S Fung1, A B Djuri¡si´c, C C Ling, C Kwong and S Li , “Influence of annealing temperature and environment on the properties of indium tin oxide thin films, *J. Phys D*, **38**, (2005) 2000.

222. P Manivannan and A Subrahmanyam, “Studies on the electrical and optical properties of reactive electron beam evaporated indium tin oxide films”, *J. Phys D*, **26**, (1993) 1510.

223. H. J. Krokoszinski and R. Oesterlein, “Post-Deposition Annealing Effects in Electron-Beam-Evaporated Indium Tin Oxide Thin Films”, *Thin Solid Films*, **187** (1990) 179-186.

224. Tom Feng, Amal K. Ghosh and Chrles Fishman, “Efficient electron-beam deposited ITO/n-Si solar cells”, *J. Appl. Phys.,* **50** (1979) 4972-4974.

225. K. S. Ramaih, V. Sundara raja, A K. Bhatnagar, R. D. Tomlinson, R. D. Pilkington, A. E. Hill, S. J. Chang, Y. K. Su and F. S. Juang, “Optical, Structural and Electrical Properties of Tin Doped Indium Oxide Thin Films Prepared by Spray-Pyrolysis Technique”, *Semicond. Sci. Technol.*, **15** (2000) 676-683.

226. V. Vasu and S. Subrahmanyam, "Photovoltaic Properties of Indium Tin Oxide (ITO)/Silicon Junctions Prepared by Spray Pyrolysis- Dependence on Oxidation Time", *Semicond. Sci. Technol.*, **7** (1992) 320-323.

227. H. Kobayashi, T. Ishida, Y. Nakato and H. Tsubomura, " Mechanism of Carrier Transport in Highly Efficient Solar Cells Having Indium Tin Oxide/Si Junctions", *J. Appl. Phys.*, **69** (1991) 1736-1743.

228. A. K. Sexena, S. P. Singh, R. Thangaraj and O. P. Agnihotri, "Thickness Dependence of the Electrical and Structural Properties of In_2O_3:Sn Films", *Thin Solid Films*, **117** (1984) 95-100.

229. W. Siefert, "Properties of Thin In_2O_3 and SnO_2 Films Prepared by Corona Spray Pyrolysis, and a Discussion of the Spray Pyrolysis Process", *Thin Solid Films*, **121** (1984) 275-282.

230. H. Haitjema and J. J. Ph. Elich, "Physical properties of pyrolytically sprayed tin-doped indium oxide coatings", *Thin Slid Film*, **205** (1991) 93-100.

231. B. Radha Krishna, T. K. Subramanyam, S. Uthana, B. S. Naidu and P. J. Reddy, 'Preaparation and characterization of reactive evaporated Indium Tin Oxide films", *The Physics of Disorded Materials* Edited by M. P. Saxena, N. S. Saxena & Deepika Bhandari, (1997), 224-228, NISCOM, New Delhi, India.

232. H. L. Ma, D. H. Zhang, P. Ma, S. Z. Win, S. Y. Li., "Preparation and properties of transparent conducting indium tin oxide films deposited by reactive evaporation", *Thin Solid Films*, **263** (1995) 105.

233. N. Balasubrarnanian and A Subrahrnanyarn, "Electrical and optical properties of reactivelyevaporated indium tin oxide (ITO) films- dependence on substrate temperature and tin concentration", *J. Phys D*, **22**, (1989) 206.

234. S. Noguchi and H Sakata, "Electrical properties of Sn-doped In_20_3 films prepared by reactive evaporation", *J. Phys D*, **14**, (1981) 1523.

235. H. U. Habermeter, "Properties of Indium Tin Oxide thin films prepared by reactive evaporation", *Thin Solid Films*, **80**, (1981) 157.

236. N. Balasubramanian and A. Subrahmanyam, "Effect of substrate temperature on the electrical and optical properties of reactively evaporated indium tin oxide films, *Mater. Sc. Engg.* B **1** (1988) 279-281.

237. A. Salehi, "The Effect of Deposition Rate and Substrate Temperature of ITO thin films on Electrical and Optical Properties", *Thin Solid Films*, **324** (1998) 214-218.

238. J. L. Yao, S. Hao and J. S. Wilkinson, "Indium Tin Oxide Film by Sequential Evaporation", *Thin Solid Films*, **189** (1990) 227-233.

239. Mamoru Mizuhashi, "Electrical Properties of Vacuum-Deposited Indium Oxide and Indium Tin Oxide", *Thin Solid Films*, **70** (1980) 91-100.

240. H. Kim, J. S. Horwitz, A. Pique, C. M. Gilmore and D. B. Chrisey, "Electrical and Optical Properties of Indium Tin Oxide Thin Films Grown by Pulsed Laser Deposition", *Appl. Phys. A*, **69** (1999) S447-S450.

241. Hiroyuki Tomonaga, Takeshi Morimoto, "Indium-tin oxide coatings via chemical solution deposition", *Thin Solid Films*, **392** (2001) 243

242. Bruce Mayer, "Highly Conductive and Transparent films of Tin and Fluorine Doped Indium Oxide Produced by APCVD", *Thin Solid Films*, **221** (1992) 166-182.

243. E. Kawamata and K. Ohshima, "Transparent Conducting In_2O_3 Films Prepared by Thermal Decomposition of $InCl_3$", *Jpn. J. Appl. Phys.*, **18** (1979) 205-206.

244. Masatoshi Higuchi, Shinichiro Uekusa, Ryotaro Nakano and Kazuhiko Yokogawa, "Postdeposition Annealing Influence on Sputtered Indium Tin Oxide Film Characteristics", *Jpn. J. Appl. Phys.,* **33** (1994) 302-306.

245. R. B. H. Tahar, T. Ban, Y. Ohya and Y. Takahashi, "Tin Doped Indium Oxide Thin Films: Electrical Properties", *J. Appl. Phys*, **83** (1998) 2631-2645.

246. M. Buchanan, J. B. Webb and D. F. Williams, "The Influence of Target Oxidation and Growth Related Effects on the Electrical Properties of Reactively Sputtered Films of Tin-Doped Indium Oxide", *Thin Solid Films*, **80**, 1981, pp. 373 – 382.

247. M. Higuchi, S. Uekusa, R. Nakano and K. Yokogawa, "Post-Deposition Annealing Influence on Sputtered Indium Tin Oxide Film Characteristics", *Japanese Journal of Applied Physics*, **33**, 1994, pp. 302 – 306.

248. J. Bregman, Y. Shapira and H. Aharoni, "Effects of Oxygen Partial Pressure During Deposition on the Properties of Ion-Beam-Sputtered Indium-Tin Oxide Thin Films", *Journal of Applied Physics*, **67**(8), 1990, pp. 3750 – 3753.

249. J. B. DuBow, D. E. Burk and J. R. Sites, "Efficient photovoltaic heterojunctions of indium tin oxides on silicon", *Appl. Phys Lett.* **8** (1976) 494-496.

250. J. C. Manifacier and L. Szepessy, "Efficient sprayed In_2O_3:Sn n-type silicon heterojunction solar cell", *Appl. Phys Lett.*, **31** (1977) 459-462.

251. K. S. Sree Harsha, K. J. Bachmann, P. H. Schmidt, E. G. Spencer and F. A. Thiel, "n-indium tin oxide/p-indium phosphide solar cells", *Appl. Phys. Lett.*, **30** (1977) 645-646.

252. L. Gupta, A. Mansingh and P. K. Srivastava, "Band Gap Narrowing and the Band Structure of Tin Doped Indium Oxide Films", *Thin Solid Films*, **176**, 1989, pp. 33 – 44.

253. L. Holland; Vacuum Deposition of Thin Films, Chapman& Hall Ltd, 1970 p 1-135.

254. K. L. Chopra; Thin Film Phenomena; Robert E. Krieger Publishing Company, Huntington, New York (1969) p10-22.

255. A. Goswami; Thin Film Fundamentals, New Age International (p) Ltd., New Delhi (1995), p4-20.

256. V. Dutta, "*Thin Film Technology and Applications"*(Eds K. L. Chopra and L. K. Malhotra), (1985) (Tata-Mc-Graw Hill, New Delhi) p5-13.

257. L. I. Maissel and R Gang (eds); Hand Book of Thin Film and Technology, Mc Graw Hill Com., New York,1970 pI-92.

258. K. L. Chopra; Thin Film Phenomena; Robert E. Krieger Publishing Company, Huntington, New York (1969) p18.

259. A. Goswami; Thin Film Fundamentals, New Age International (p) Ltd., New Delhi (1995), p18.

260. K. Wasa, "*Thin Film Technology and Applications"*(Eds K. L. Chopra and L. K. Malhotra), (1985) (Tata-Mc-Graw Hill, New Delhi) p27-50.

261. K. L. Chopra; Thin Film Phenomena; Robert E. Krieger Publishing Company, Huntington, New York (1969)p23-43.

262. A. Goswami; Thin Film Fundamentals, New Age International (p) Ltd., New Delhi (1995), p21-31.

263. V. D. Vankar, "*Thin Film Technology and Applications"*(Eds K. L. Chopra and L. K. Malhotra), (1985) (Tata-Mc-Graw Hill, New Delhi) p14-26.

264. K. L. Chopra; Thin Film Phenomena; Robert E. Krieger Publishing Company, Huntington, New York (1969)p43-51.
265. A. Goswami; Thin Film Fundamentals, New Age International (p) Ltd., New Delhi (1995), p31-35.
266. I. Langmuir, *Physik Z.,* **14**, 1273 (1913).
267. L. Holland; Vacuum Deposition of Thin Films, Chapman& Hall Ltd, 1970 p185.271
268. W. L. Bond; *Jour. Opt. Soc. Am.,* **44**, 1954, 429.
269. H. Maye and H. Gohre, *Proc. North West German Phys. Soc.,* 1962.
270. L. S. Palatnik and Y. F. Komnik, *Sov. Phys. Doklady (Eng. Trans.)* **4**, 1959 p663.
271. B. Lewis and F. Champbell, *J. Vacuum Sci. Technol*., **4**, 1967 p209.
272. C. A. Neugebaner, Hand Book of Thin Film and Technology, L. I. Maissel and R Gang (eds); Mc Graw Hill Com., New York,1970 Ch-8.
273. D. Walton, *Phil. Mag.*, **7** 1962 p1671.277
274. D. Walton, T. Rhodin and R. W. Rollins, *J. Chem. Phys.*, **38** 1968 p2698.278
275. B. Lewis, *Thin Solid Films*, **1** 1967 p85.
276. J. P. Hirth and K. L. Moazed, *Physics of Thin Films*, G. Hass and R. E. Thurn (Eds), Academic Press Inc., New York, 1967 p97.
277. D. W. Pashley, *Thin Films*, Am. Soc. Metals, Metal Park, Ohio, 1964 p59.
278. G. A. Basset, Condensation and Evaporation of Solids, E. Ruther et. al. (Eds.), Gordon and Beach Science Publishers Inc., New York, 1964 p521.
279. D. W. Pashley, M. J. Stowell, M. H. Jacobs and T. J. Law, *Phil. Mag.*, **10** 1964 p127.
280. D. W. Pashley, (Review), *Adv. Phys.*, 14 1965 p361.
281. B. W. Sloope and C. O. Tiller, *J. Appl. Phys.* **36** 1965 p3174; **33** 1962 p3458; **32** 1961 p1331.
282. C. Kittel, "*Introduction to Solid State Physics*", (5th Edition) Wiley Eastern Ltd., New Delhi (1979)
283. J. B. Nelson and D. P. Riley; "An experimental investigation of extrapolation methods in the derivation of accurate unit cell dimensions of crystals", *Proc. Phys. Soc., (London)* **57**, 1945, 160.

284. H. P. Klug and L. E. Alexander; "*X-Ray Diffraction Procedures*", John Wiley & Sons, Inc, N. Y., 1954, Chap 9, p 512.

285. K. L. Chopra; *Thin Film Phenomena*; McGraw Hill Book Company, , New York (1969) p270

286. R. Stokes, and A. J. C. Wilson, "The Diffraction of X rays by Distored Crystal Aggregates-I", *Proc. of Physical Society*, LVI, 3 (1944) 174-181.

287. N. Mozumdar, "Photoconductivity Processes of and Structural Characteristics in Polycrystalline ZnTe Thin Films", PhD Thesis, Gauhati University (India) 2006 p48.

288. G. B. Williamson and W. H. Hall, *Acta. Metall*. **1** 22 (1953).

289. E. Lifshim, *X-ray Characterization of Materials*, Wiley, Newyork 1999 p37.

290. Mario Birkholz, *Thin film Analysis by X-ray Scattering* Wiley-VCH, Weinhein 2006 p123.

291. S. Sen, S. K. Halder and S. P. Sen Gupta; *Jour. Phys. Soc., Japan***, 38(6),** 1975, 1643-1645.

292. Neil Broderick, *Solid State Electronics*, (Electronic book) 2003 p47-48.

293. Leonid V. Azaroff, "*Introduction to Solids*" (Tata McGraw-Hill Pub. Co., New Delhi) (1987) p325.

294. J. Dekker, *Solid State Physics*, Macmillan India Limited, New Delhi (2000) p329, 312, 305-318.

295. H. M. Rosenberg, *Low temperature Solid State Physics*. Oxford Clarendon Press, 1995, 218.

296. S. M. Sze, *Semiconductor Devices- Physics & Technology*, John Willey & Sons, New York (1985) p22.

297. Jacques I. Pankove, "*Optical Processes in Semiconductors*", (Dover Publications Inc., New York) (1971) p34.

298. Richard H. Bube, "*Photoconductivity of Solids*", (John Wiley & Sons, Inc., New York) (1960) p211-214.

299. F. Abeles, *Optical Properties of Solids*, North Holand Publishing Co., (1972) p23.

300. M. Born and E. Wolf, *Principle of Optics*, Pergamon, Oxford, (1975) Chap 2.

301. R. Swanepoel, "Determination of the thickness and Optical constants of Amorphous Silicon", *J. Phys. E.* **16** (1983) 1214-1222.

302. R. Swanepoel, "Determination of surface roughness and optical constants of inhomogenous amrphorus silicon films", *J. Phys. E.* **17** (1984) 896-903.

303. J. C. Manifacier, J Gasiot and J P Fillard, "A simple method for the determination of the optical constants *n, h* and the thickness of a weakly absorbing thin film", *Journal of Physics E: Scientific Instruments* **9** (1976) 1002-1004.

304. E Marquez, J Ramirez-Malo, P Villares, R Jimbnez-Garay, P J S Ewen and A E Owen, "Calculation of the thickness and optical constants of amorphous arsenic sulphide films from their transmission spectra", *J. Phys. D*, **25** (1992) 535-541.

305. Jacques I. Pankove, "*Optical Processes in Semiconductors*", (Dover Publications Inc., New York) (1971) p94.

306. F. A. Jenkins, H. E. White, *Fundamentals of Optics*, McGraw Hills Book Co, New York, (1957) 468.

307. K. L. Chopra; *Thin Film Phenomena*; Robert E. Krieger Publishing Company, Huntington, New York (1969) 734.

308. K. L. Chopra; *Thin Film Phenomena*; Robert E. Krieger Publishing Company, Huntington, New York (1969) 729.

309. P. S. Ivanov, *Introduction to Solid State Electronics*, Mir Publishers, Moscow (1984)385-387.

310. Richard H. Bube, "*Photoconductivity of Solids*", (John Wiley & Sons, Inc., New York) (1960) 276, 404.

311. J. Millman and C. C. Halkias, "*Integrated Electronics*", Tata McGraw-Hill Publishing Co. Ltd., New Delhi 1991 p53.

312. E. H. Rhoderick, "*The Physics of Schottky Barriers*", J Phy D, **3** (1970) 1153-1167.

313. E. H. Rhoderick, *Metal semiconductor contacts* (Oxford: Clarendon Press) (1978) p131.

314. S. M. Sze; *Physics of Semiconductor Devices* (2nd Edition) Wiley Eastern Ltd., New Delhi (1987) p27.

315. W. Shockley, "On the Surface States Associated with a Periodic Potential", *Phys. Rev*, **56** (1939) 317-323.

316. J. Bardeen, "Surface States and Rectification at a Metal Semi-Conductor Contact", *Phys. Rev.*, **71** (1947) 717-727.

317. M. Cowley and S. M. Sze, "Surface States and Barrier Height of Metal-Semiconductor Systems", *J. Appl. Phys.*, **36** (1965) 3212-3220.
318. E. H. Rhoderick, *Metal semiconductor contacts* (Oxford: Clarendon Press) (1978) p31-32.
319. S. M. Sze; *Physics of Semiconductor Devices* (2nd Edition) Wiley Eastern Ltd., New Delhi (1987) p251.
320. E. H. Rhoderick, *Metal semiconductor contacts* (Oxford: Clarendon Press) (1978) p123 & p136.
321. Bart Van Zeghbroeck, "*Principles of Electronic Devices*" (Electronic Book) (1996) p3.11
322. M. Cowley, *J. Appl. Phys.*, **37** (1966) 3024.
323. S. M. Sze; *Physics of Semiconductor Devices* (2nd Edition) Wiley Eastern Ltd., New Delhi (1987) p271.
324. H. K. Henisch, *Rectifying Semiconductor Contacts* (Oxford: Clarendon Press) (1957) p221
325. V. L. Rideout, *Thin Solid Films*, **48** 1978 p261.
326. E. H. Rhoderick, *Metal semiconductor contacts* (Oxford: Clarendon Press) (1978) p87.
327. S. M. Sze; *Physics of Semiconductor Devices* (2nd Edition) Wiley Eastern Ltd., New Delhi (1987) p126.
328. Charles E. Backus (Edtd), *Solar Cells*, IEEE Press, 1975, p8.
329. S. M. Sze; *Physics of Semiconductor Devices* (2nd Edition) Wiley Eastern Ltd., New Delhi (1987) p821.
330. S. M. Sze; *Physics of Semiconductor Devices* (2nd Edition) Wiley Eastern Ltd., New Delhi (1987) p793.
331. R. K. Kotnala and N. P. Singh, *Essentials of Solar Cell*, Allied Publishers Pvt. Ltd., (New Delhi) 1986 p86-90.
332. R. Brown; in L. I. Maissel and R. Glang (eds) *Hand Book of Thin Film Technology*, Mc Graw Hill, N Y,1970 chap 6-1.
333. B. Tareev; *Physics of Dielectric Materials*, Mir publisher, Moscow, 1975, p 46.
334. L. Holland; *Vocuum Deposition of Thin Films*. Chapmann and Hall Ltd., London, 1963, p 100.

335. S. Tolansky; *Multiple beam Interferomerty of surfaces and films*, Oxford Uni. Press, London, N Y, 1948.

336. S. Tolansky; *Surface Microtopography*, Wiley (Interscience) N Y, 1960, p 62-68.

337. S. Tolansky; *An Introduction to Interferometry*, Longmanns, Green and Co. Ltd., London, p 165-172.

338. W. A. Pliskin and S. J. Zanin; in L. I. Maissel and R. Glang (eds) *Hand Book of Thin Film Technology,* Mc Graw Hill, NY,1970 chap 11-1.

339. K. L. Chopra; *Thin Film Phenomena*, McGraw Hill Book Co., New York, 1969, p 101-105.

340. W. R. Runyem, *Semiconductor measurements and Instrumentation*, (Mc Graw Hill Book Company, New York, 1975) p. 144.

341. Moutinho H R, Al-Jassim M M, Abulfotuh F A, Levi D H, Dippo P C, Dhere R G and Kazmerski, 1997, *Proceedings of the 26th IEEE Photovoltaic Specialist Conference*, IEEE California.

342. JCPDS X-ray powder file data (Data file 05–0522).

343. Y. P. Venkata Subbaiah, P. Prathap, M. Devika and K. T. R. Reddy, *Physica B*, **365** (2005) 240.

344. B. Maiti, P. Gupta S. Choudhuri and A. K. Pal; Thin Solid Films **234** (1994) 104-111.

345. L. I. Maissel and R Gang (eds), *Hand Book of Thin Film and Technology*, Mc Graw Hill Com., New York,1970 chapter 12.

346. El-Kadry N, Ashour A and Mahmoud S A, 1995 *Thin Solid Films* **269**, 112.

347. S. M. Sze; *Physics of Semiconductor Devices* (2nd Edition) Wiley Eastern Ltd., New Delhi (1987) p396.

348. R. Sahai and A. G. Milnes, "Heterojunction Solar Cell Calculations", *Solid state Electronics*, **13** (1970) 1289-1299.

349. M. Aven and J. S. Prener; "*Physics and Chemistry of II-VI Compounds*", North-Holland Publishing Company-Amsterdam, (1967) p598, 603, 604.

350. J. I. Pankove, *Optical process in Semiconductors*, Dover publications, Inc, New York, (1971), 10, 22, 36, 90, 94.

351. P. K. Kalita, B. K. Sarma and H. L. Das; *Ind. Jour. Pure and Appl. Phys*., **37**, 1999, 885.

352. L. Kindleysides and J. Wood; *Jour. Phys. D: Appl. Phys.*, **3**, 1970, 451.

353. A. Serpi; *Jour. Phys. D*: Appl. Phys., **9**, 1976, 1881.

354. R. H. Bube; *Photoconductivity of Solids*, Wiley, N. Y., 1960, p 273.

355. S. M. Ryvkin; *Photoelectric effects in Semiconductors*, Consultants Bureau, N. Y., 1969,Chap 5&6, P 88-155.

356. BN Srivastava and S Singh, *Indian J. Pure. Appl. Phys.*, **8**(1970)716.

357. J. T. Randall and M. H. F. Wilkins; *Proc. Roy. Soc.* **A 184** (1945) 366.

358. G. Wary and A. Rahman, "Optical and electrical properties of transparent CdTe films prepared by evaporation and rf sputtering", *Proc. of 6th Asian Thermophysical properties conference , India (2001)*, 597-584.

359. C. Baban, G. I. Rusu and P. Prepelita, "On the optical properties of polycrstalline CdSe thin films" *J. Optoelectr. Adv. Mater*., 2005, **7**, 817-821.

360. G. I. Rusu, M. E. Popa, G. G. Rusu and Iulia Salaoru,, *Appl. Surf. Sci.*, **218** (2003) 222.

361. Lalitha S, Sathyamoorthy R, Senthilarasu S, Subbarayan A and Natarajan K, 2004 *Sol. Energ. Mat.. Sol. cell,* **82**, 187.

362. B. Bozzini, C. Lenardi and N. Lovergine; *Materials of Chemistry and Physics*, **66** (2-3), (2000) 219-228.

363. P. Thilakan, J. Kumar, *Phys. Status Solidi*, A Appl Res., **160** (1997) p97.

364. F. M. Amanullah, K. J. Pratap, V. Hari Babu, *Thin Solid Films*, **254** (1995) p28.

365. M.Mizuhashi, *Thin Solid Films*, **70** (1980) p91.

366. G. Khlyap, M. Andrukhiv, "New Heterostructures n-PbS/n-ZnSe: Long Term Sability of Electrical Characteristics", *Cryst. Res. Technol.*, **34** 1999 751.

367. S. M. Sze, *Physics of Semiconductor Devices*, 2nd Edn, (Willey Eastern Ltd, New Delhi, 1986), 17, 849.

368. E. H. Rhoderik, *Metal semiconductor contacts* (Clarendon Press, Oxford, 1978) p. 7.

369. E. H. Rhoderik, *Metal semiconductor contacts* (Clarendon Press, Oxford, 1978) p. 96.

370. S. M. Sze, *Physics of Semiconductor Devices*, 2nd Edn, (Willey Eastern Ltd, New Delhi, 1986), p.259.

371. J. M. Pawlikoski, *Thin Solid Films*, **190**, 39 (1990).

372. J. Bardeen, *Phys. Rev.*, **71**, 717 (1947).

373. I. M. Dharmadasa, *Prog. Crystal Growth and Charact.,* **36**, 249 (1998).

374. O. Vigil-Galan, A. Arias-Carbajal, R. Mendoza-Perez, G. Santana-Rodriguez, and A. Morales-Acevedo, "Improving the efficiency of CdS/CdTe solar cells by varying the thiourea/CdCl2 ratio in the CdS chemical bath", *Semicond. Sci. Technol.*, **20** (2005) 819-822.

375. G. Wary, T. Kachary and A. Rahman, *International Journal of Thermophysics,* **27**, 332 (2006).

376. Ting L. Chu and Shirley S. Chu, *Sol Stat. Electron.*, **38**, 533 (1995).

377. J. Dutta, D. Bhattacharyya, S. Chaudhuri and A. K. Pal, *Sol. Energy Mat. And Solar Cells*, **36**, 357 (1995).

378. G. C. Wary, "Optical and electronic properties of CdTe, CdS and ITO transparent films and their junctions", PhD Thesis, Gauhati University (India) 2006.

379. S. Chaliha, M. N. Borah, P. C. Sarmah and A. Rahman, "Optical and Electrical properties of Indium Tin Oxide", *Proc. of the 6th Asian Thermophysical Properties Conference* (Guwahati), p750-754, (2001).

380. S. M. Sze, *Physics of Semiconductor Devices*, 2nd Edn, (Willey Eastern Ltd, New Delhi, 1986), 17, 850.

381. H. K. Henisch, *Semiconductor Metal Contacts* (Oxford: Clarendon Press) (1984), 88

382. S. M. Sze, *Physics of Semiconductor Devices*, 2nd Edn, (Willey Eastern Ltd, New Delhi, 1986), p.806.

LIST OF PAPER PUBLISHED

A. Published in International Journals:

1. "Study of Au, Ni-(n)ZnSe Thin Film Schottky Barrier Junctions" Sumbit Chaliha, Mothura Nath Borah, P. C. Sarmah, and A. Rahman, *International Journal of Thermophysics* (in press) (2009), (online on 23rd January 2009).
2. "Effect of substrate temperature on structural properties of thermally evaporated ZnSe thin films", Sumbit Chaliha, M. N. Borah, P. C. Sarmah and A. Rahman, *Journal of Optoelectronics and Advanced Materials* Vol. **10** No. 2 p427-433 (2008).
3. "Effect of substrate temperature on structural properties of thermally evaporated ZnSe thin films of different thickness", Sumbit Chaliha, M. N. Borah, P. C. Sarmah and A. Rahman, *Journal of Physics:Conference seriess* Vol. **114** 012048 (2008).
4. "Optical and electrical properties of thermally evaporated ZnSe thin films", Sumbit Chaliha, M. N. Borah, P. C. Sarmah and A. Rahman, *Indian Journal of Physics*, **82**(3) p303-310 (2008).
5. "A study of current-voltage characteristics of ITO/(p)Si heterojunctions", S. Chaliha, M. N. Borah, P. C. Sarmah and A. Rahman, *Indian Journal of Physics*, **82**(5) p595-601 (2008).
6. "Synthesis and Characterization of Nanocrystalline CdS Thin Films in PVA Matrix", R. Devi, P. K. Kalita, P. Purkayastha, S. Chaliha and B. K.Sharma, *Journal of Scientific Conference Proceedings*, Vol. **1** pp.65-71 (2009).
7. "Studies on current-voltage characterisics of ITO/(n)CdSe heterojunctions", Mothura Nath Borah, S. Chaliha, P. C. Sarmah and A. Rahman, *Journal of Optoelectronics and Advanced Materials* Vol. **10** No. 10 p2793-2799 (2008).
8. "Electrical and optical properties of thinfilm (n)CdSe/(p)CdTe heterojunction and its performance as a photovoltaic converter", Mothura N. Borah, S. Chaliha, P. C. Sarmah and A. Rahman, *Journal of Optoelectronics and Advanced Materials* Vol. **10** No. 6 p1333-1339 (2008).

9. "Effect of substrate temperature on structural properties of thermally evaporated CdSe thin films of different thickness", Mothura N. Borah, S. Chaliha, P. C. Sarmah and A. Rahman, *Optoelectronics and Advanced Materials- Rapid Communications* Vol. **2** No. 6 p. 342-348 (2008).
10. "Electrical properties of thermally evaporated doped and undoped CdSe thin films", M. N. Borah, S. Chaliha, P. C. Sarmah and A. Rahman, *Indian Journal of Pure and Applied Physics*, **45** pp687-691 (2007).

B. Published in International and National Conference Proceedings:

1. "Current-voltage characteristics of Au-(n)ZnSe Schottky barrier", Sumbit Chaliha, M. N. Borah, P. C. Sarmah and A. Rahman, *Proc. of the DAE Solid State Physics Symposium* (India), **53**, (2008).
2. "Chemically prepared CdSe thin films at different bath temperatures", D. Gogoi, S. Chaliha, and C. R. Dutta, *Proc. of the DAE Solid State Physics Symposium* (India), **53**, (2008).
3. "Study of Au, Ni-(n)ZnSe Thin Film Schottky Barrier Junctions", Sumbit Chaliha, M. N. Borah, P. C. Sarmah and A. Rahman, *Proceedings of the 8th Asian Thermophysical Properties Conference,* August 21-24, 2007, Kyushu University, Japan.
4. "The structural and optical properties of Thermally Evaporated ZnSe Thin Films of Different thickness at Different Substrate temperature", Sumbit Chaliha, M. N. Borah, P. C. Sarmah and A. Rahman, *Proceedings of the 8th Asian Thermophysical Properties Conference* August 21-24, 2007, Kyushu University, Japan.
5. "Electrical and Optical Properties of Thin Film (n)CdSe/(p)CdTe Heterojunction and its Performance as a Photovoltaic Converter", M. N. Borah, S. Chaliha, P. C. Sarmah and A. Rahman, *Proceedings of the 8th Asian Thermophysical Properties Conference* August 21-24, 2007, Kyushu University, Japan, p.. (2007).
6. "Some optical parameters of thermally evaporated ZnSe thin films prepared at different substrate temperatures", S. Chaliha, M. N. Borah, P. C. Sarmah and A. Rahman, in *Contemporary Optics and Optoelectronics* (proceedings of 33rd Optical Society of India symposium) p168 (2007).

7. "Current-voltage characteristics of Ag-(n)CdSe Schottky junction", M. N. Borah, S. Chaliha, P. C. Sarmah and A. Rahman, *Proc. of the DAE Solid State Physics Symposium* (India), **52**, (2007) p957-958.
8. "Current-Voltage Characteristics of Ni-(n)ZnSe Schottky Barriers", S. Chaliha, M. N. Borah, P. C. Sarmah and A. Rahman, in *Advanced Material Science* (Proceengs of the National Conference on Recent Advances in Material Science, Sept 27-29, 2006, Kurukshetra Unversity, Kurukshetra) p297 (2006).
9. "Electrical and Optical Properties of Thin Film Al-(n)CdSe-ITO structure", M. N. Borah, S. Chaliha, P. C. Sarmah and A. Rahman, in *Advanced Material Science* (Proceengs of the National Conference on Recent Advances in Material Science, Sept 27-29, 2006, Kurukshetra Unversity, Kurukshetra) p285 (2006).
10. "Electrical properties of pure and Ag-doped CdSe thin films prepared by vacuum evaporation", M. N. Borah, S. Chaliha, P. C. Sarmah and A. Rahman, *Proc. of 51st Annual Technical Session of Assam Science Society* (Guwahati), **7** p181-186 (2006).
11. "Current –Voltage Characteristics of thermally evaporated ZnSe/p-Si Schottky barrier junctions", S. Chaliha, M. N. Borah, P. C. Sarmah and A. Rahman, *Proc. of 51st Annual Technical Session of Assam Science Society* (Guwahati), **7** p173-180 (2006).
12. "Electrical and optoelectrical properties of thermally evaporated Ag-doped CdSe films", M. N. Borah, S. Chaliha, P. C. Sarmah and A. Rahman, *Proc. of the DAE Solid State Physics Symposium* (India), **51**, (2006) p439.
13. "Electrical and optoelectrical properties of thermally evaporated Cu-doped ZnSe film", S. Chaliha, M. N. Borah, P. C. Sarmah and A. Rahman, *Proc. of the DAE Solid State Physics Symposium* (India), **50**, p395-396, (2005).
14. "Current-Voltage Characterisics of Al-(n)CdSe-Ag, Ni, Sn Junctions", M. N. Borah, S. Chaliha, P. C. Sarmah and A. Rahman, *Proc. of XIII International Workshop on The Physics of Semiconductor Devices* (New Delhi) p116-119, (2005).
15. "Optical and Electrical properties of Indium Tin Oxide", S. Chaliha, M. N. Borah, P. C. Sarmah and A. Rahman, *Proc. of the 6th Asian Thermophysical Properties Conference* (Guwahati), p750-754, (2001).